

STRUCTURE REFINEMENT, OPTICAL AND DIELECTRIC PROPERTIES OF
METAL PYROPHOSPHATE GROUPS



A THESIS SUBMITTED IN PARTIAL FULFILLMENT
OF THE REQUIREMENT FOR THE DEGREE OF
DOCTOR OF PHILOSOPHY IN NANOSCIENCE AND NANOTECHNOLOGY
COLLEGE OF NANOTECHNOLOGY
KING MONGKUT'S INSTITUTE OF TECHNOLOGY LADKRABANG
2016

KMITL-2016-NT-D-001-001

This material is reserved for educational use only, not allowed for commercial use.

Forbidden to modify the content, and cite the document when use.

การศึกษารายละเอียดโครงสร้าง สมบัติทางแสงและสมบัติไดอิเล็กทริกของสาร
กลุ่มโลหะไพโรฟอสเฟต

STRUCTURE REFINEMENT, OPTICAL AND DIELECTRIC PROPERTIES OF
METAL PYROPHOSPHATE GROUPS



วิทยานิพนธ์นี้เป็นหนึ่งของการศึกษาตามหลักสูตรปริญญาปรัชญาดุษฎีบัณฑิต
สาขาวิชาโนวิทยาและนาโนเทคโนโลยี
วิทยาลัยนาโนเทคโนโลยีพระจอมเกล้าลาดกระบัง
สถาบันเทคโนโลยีพระจอมเกล้าเจ้าคุณทหารลาดกระบัง
พ.ศ. 2559

KMITL-2016-NT-D-001-001

This material is reserved for educational use only, not allowed for commercial use.

Forbidden to modify the content, and cite the document when use.



COPYRIGHT 2016

COLLEGE OF NANOTECHNOLOGY

KING MONGKUT'S INSTITUTE OF TECHNOLOGY LADKRABANG

This material is reserved for educational use only, not allowed for commercial use.

Forbidden to modify the content, and cite the document when use.

หัวข้อวิทยานิพนธ์	การศึกษารายละเอียดโครงสร้าง สมบัติทางแสงและสมบัติไดอิเล็กทริกของสารกลุ่มโลหะฟอสเฟต
นักศึกษา	นายรัตน์ ไบตาเฮ
รหัสประจำตัว	53670105
ปริญญา	ปรัชญาดุษฎีบัณฑิต
สาขาวิชา	นาโนวิทยาและนาโนเทคโนโลยี
พ.ศ.	2559
อาจารย์ที่ปรึกษาวิทยานิพนธ์	รศ.ดร.นราธิป วิทยาการ

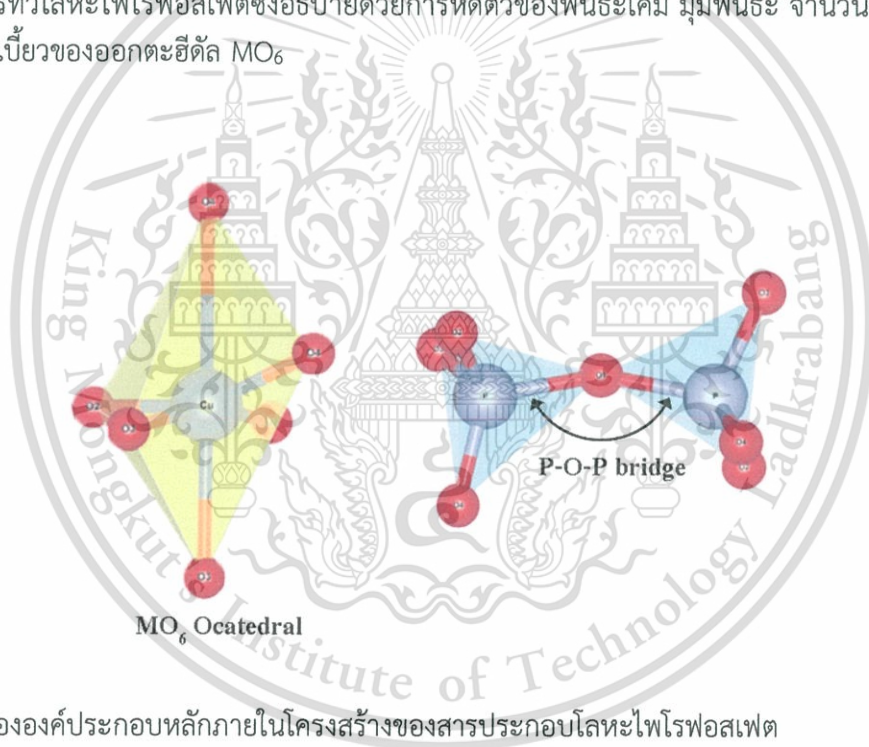
บทคัดย่อ

งานวิจัยนี้ได้นำเสนอกลไกการเกิดเฟส รายละเอียดโครงสร้างผลึก สมบัติทางแสง และสมบัติไดอิเล็กทริกของสารประกอบโลหะฟอสเฟต ($M_2P_2O_7$ เมื่อ $M = Cu, Zn$ และ Mg) โดยการศึกษา รายละเอียดโครงสร้างผลึกใช้วิธี Rietveld refinement เป็นหลัก อีกทั้งงานวิจัยนี้ได้ทำการศึกษาความสัมพันธ์ระหว่างโครงสร้างผลึก สมบัติทางแสง และสมบัติไดอิเล็กทริกของสารประกอบโลหะฟอสเฟตอีกด้วย

การศึกษากลไกการเกิดเฟสและการเปลี่ยนแปลงอัตราส่วนอะตอมระหว่าง Cu ต่อ Zn ในผลึก $Cu_{(2-x)}Zn_xP_2O_7$ เมื่อ $x \approx 1$ ซึ่งได้ทำการสังเคราะห์ด้วยวิธีปฏิกิริยาสถานะของแข็งและทำการเผาแคลไซน์ที่อุณหภูมิ 400 500 600 700 และ 800°C เพื่อศึกษาการเปลี่ยนแปลงอัตราส่วนอะตอมระหว่าง Cu ต่อ Zn ของการเกิดผลิตภัณฑ์สุดท้ายในรูป $CuZnP_2O_7$ โดยเทคนิคที่ใช้การวิเคราะห์การเปลี่ยนแปลงอัตราส่วนอะตอมประกอบด้วยเทคนิคการดูดกลืนรังสีเอ็กซ์ การเลี้ยวเบนรังสีเอ็กซ์ รามานสเปกโตรสโคปี อินฟราเรดสเปกโตรสโคปี รวมทั้งเทคนิคทางความร้อน การศึกษาการเปลี่ยนแปลงเฟสที่เป็นไปอย่างเป็นระบบ พบว่าของผสมเชิงซ้อนมีส่วนทำให้เกิดปฏิกิริยาที่อุณหภูมิต่างๆ โดยสารมัธยันตร์ที่เกิดขึ้นประกอบด้วย $Cu_2P_2O_7$, $CuP_2O_7 \cdot 2NH_3 \cdot 3H_2O$, $Zn_2P_2O_7$ และ $Zn_2P_2O_7 \cdot 3H_2O$ ร้อยละการลดลงของสารมัธยันตร์ $CuP_2O_7 \cdot 2NH_3 \cdot 3H_2O$ มีความสัมพันธ์โดยตรงกับการเพิ่มขึ้นของผลิตภัณฑ์สุดท้าย การเปลี่ยนแปลงองค์ประกอบของ Cu ต่อ Zn ใน $Cu_{(2-x)}Zn_xP_2O_7$ ในช่วงอุณหภูมิ 400-600°C เมื่อ $x \approx 1$ มีความสัมพันธ์แบบเชิงเส้นอย่างชัดเจนกับอุณหภูมิการเกิดปฏิกิริยา การยืนยันการเกิดสารละลายสถานะของแข็งระหว่างอะตอม Cu และ Zn ในโครงสร้างของผลิตภัณฑ์สุดท้าย $CuZnP_2O_7$ ทำการศึกษาด้วยเทคนิค EXAFS fitting และยังทำให้ทราบถึงสิ่งแวดล้อมรอบๆ อะตอมอีกด้วย

ส่วนที่สองในงานวิจัยนี้เป็นการศึกษาความสัมพันธ์ระหว่างโครงสร้างผลึกกับสมบัติทางแสง การศึกษาการสังเคราะห์สารประกอบทวิโลหะฟอสเฟต $Cu_{(2-x)}M_xP_2O_7$ เมื่อ $x = 0.50 - 1.50$ ด้วยวิธีปฏิกิริยาสถานะของแข็งเพื่อเป็นข้อมูลในการเกิดเฟสแบบสารละลายของแข็ง พิกเอกลักษณะของเฟสปีต้า สามารถวิเคราะห์ด้วยเทคนิครามานสเปกโตรสโคปีซึ่งปรากฏพิกในช่วงเลขคลื่น $1200-1250 \text{ cm}^{-1}$ ภายใต้การเปล่งแสง UV/Vis การวิเคราะห์การสั่นของหมู่ไอออน $P_2O_7^{4-}$ ซึ่งประกอบด้วยอนุมูล O-P-O และสะพานเชื่อม P-O-P รวมทั้งการประมาณค่าการยืดหดของพันธะ M-O อาศัยการวิเคราะห์สเปกตรัม

ด้วยเทคนิครามานและอินฟราเรดสเปกโตรสโคปี การแทนที่อะตอม Cu ด้วยอะตอม Zn และ Mg ลงในโครงสร้างของ $\text{Cu}_2\text{P}_2\text{O}_7$ พบว่าค่าคงที่ไดอิเล็กทริกของสารตัวอย่างมีค่าใกล้เคียงกัน แต่อย่างไรก็ตามค่าคงที่ไดอิเล็กทริกมีการลดลงเล็กน้อยสอดคล้องกับการเพิ่มขึ้นของสัดส่วน x สีของสารตัวอย่างที่สัดส่วน $x = 0.00 - 1.50$ มีสีค่อนข้างเขียว และที่สัดส่วน $x = 2.00$ สารตัวอย่างเป็นสีขาว พิกัดสีบน CIE chromaticity ของ $\text{Cu}_{(2-x)}\text{M}_x\text{P}_2\text{O}_7$ เมื่อ $x = 0.50 - 1.50$ มีการเลื่อนจากตำแหน่ง (0.312, 0.358) เป็น (0.324, 0.364) ซึ่งสอดคล้องกับความยาวคลื่นของการมองเห็นสีจาก 506 เป็น 542 nm และสำหรับสัดส่วน $x = 0.00$ เป็น 562 nm จากการศึกษาพบว่าปรากฏการณ์ทั้งสมบัติไดอิเล็กทริกและสมบัติทางแสงเป็นผลมาจากการเปลี่ยนแปลงโครงสร้างผลึกซึ่งเกี่ยวข้องกับกลุ่มไอออน $\text{P}_2\text{O}_7^{4-}$ และออกตะฮีดรอลของ M-O_6 ด้วยการศึกษารายละเอียดโครงสร้างด้วยวิธี Rietveld refinement พร้อมทั้งสนับสนุนความถูกต้องด้วยผลจากการวิเคราะห์ Exafs fitting นอกจากนี้ งานวิจัยนี้ยังชี้ให้เห็นถึงการเชื่อมโยงความสัมพันธ์ระหว่างโครงสร้างผลึกและสมบัติไดอิเล็กทริก รวมทั้งความสัมพันธ์ระหว่างโครงสร้างผลึกกับสมบัติทางแสงของสารทวิโลหะไพโรฟอสเฟตซึ่งอธิบายด้วยการหดตัวของพันธะเคมี มุมพันธะ จำนวนกลุ่มไอออน และการบิดเบี้ยวของออกตะฮีดรอล MO_6



ภาพแสดงสององค์ประกอบหลักภายในโครงสร้างของสารประกอบโลหะไพโรฟอสเฟต

คำสำคัญ: โลหะไพโรฟอสเฟต กลไกการเกิดเฟส เรทเวลดรีไฟน์เมนต์ การเกิดสี สมบัติไดอิเล็กทริก

Thesis Title	Structure refinement, optical and dielectric properties of metal pyrophosphate groups
Student	Rattanaï Baitahe
Student ID	53670105
Degree	Doctor of philosophy
Program	Nanoscience and nanotechnology
Year	2016
Thesis Advisor	Assoc.Prof.Dr.Naratip Vittayakorn

ABSTRACT

This research presented the phase formation, crystal structure, optical and dielectric properties of metal pyrophosphate ($M_2P_2O_7$; $M = Cu, Zn, \text{ and } Mg$ atoms) compound. Rietveld refinement was used to investigate the crystal structure of the compound. The relationship between crystal structure, optical and dielectric properties of metal pyrophosphate compounds was studied in this research.

To investigate the phase formation and evolution of Cu:Zn partials in binary metal pyrophosphate, $Cu_{(2-x)}Zn_xP_2O_7$; $x=1$ powders were prepared by the solid state reaction method and subsequently calcined at 400, 500, 600, 700, and 800 °C in order to study Cu:Zn partial evolution to the final $CuZnP_2O_7$ product. Synchrotron X-ray absorption, X-ray diffraction, Raman, FT-IR spectroscopy, and Thermogravimetry analysis were used in this investigation. Phase evolution of the reaction products was investigated systemically. The results showed that complicated mixtures contributed to the reaction of synthesis temperature. The reaction comprised $3CuO \cdot 2P_2O_5 \cdot 0.3NH_3 \cdot 0.2H_2O$, $Cu_2P_2O_7$, $Zn_2P_2O_7$, and $Zn_2P_2O_7 \cdot 3H_2O$ intermediates. Decreasing percentage of $3CuO \cdot 2P_2O_5 \cdot 0.3NH_3 \cdot 0.2H_2O$ intermediates was related directly to an increasing final product. Cu:Zn contents changed in $Cu_{(2-x)}Zn_xP_2O_7$ in the temperature range of 400-600°C, when $x \approx 1$ clearly was related linearly to the reaction temperature. The final product was confirmed by EXAFS fitting spectra as solid solution between the Cu and Zn atom in the $CuZnP_2O_7$ structure, and it indicated environment around metal atoms.

The correlate between crystal structure and optical properties were investigated in the second part of the thesis. The binary metal pyrophosphates, $Cu_{(2-x)}M_xP_2O_7$; $x = 0.50 - 1.50$, were synthesized by solid state reaction in order to obtain information on solid solution phase formation. Under UV/Vis light emission, characteristic peaks of β -phase

were detected in the range of 1,200-1,250 cm^{-1} for Raman spectra. The $\text{P}_2\text{O}_7^{4-}$ ion, analyzed by vibration, carries the O-P-O radical, P-O-P bridge, and approximate M-O bond stretching and was identified using Raman and Fourier transform infrared (FT-IR) spectra. The dielectric constant (ϵ_r) of samples shows a similar value when Cu^{2+} was replaced by Zn^{2+} and Mg^{2+} in the $\text{Cu}_2\text{P}_2\text{O}_7$ structure. However, a slightly decreasing ϵ_r still showed when composition x increased. The colour of samples as a function of $x = 0.00 - 1.50$ exhibits a greenish hue, except for the composition $x = 2.00$, which presents a colourless powder. The CIE chromaticity coordinates of $\text{Cu}_{(2-x)}\text{Zn}_x\text{P}_2\text{O}_7$; $x = 0.50$ to 1.50, shifted from (0.312, 0.358) to (0.324, 0.364), which corresponds to the visible wavelength that shifted from about 506 to 542 nm, and 562 nm for $x = 0.00$. The phenomena of both dielectric and optical properties resulted from the changing crystal structure of the respective $\text{P}_2\text{O}_7^{4-}$ cluster and octahedral M-O₆ site. Investigation of the crystal structure used Rietveld refinement analysis, with support from the extended X-ray absorption fine structure (EXAFS) fitting technique. Furthermore, this study revealed the relationships between structure and dielectric property, and correlations to structure and optical property of binary metal pyrophosphates which were clarified by shrinking chemical bonding, bond angle, number of clusters, and distortion of octahedral MO₆.

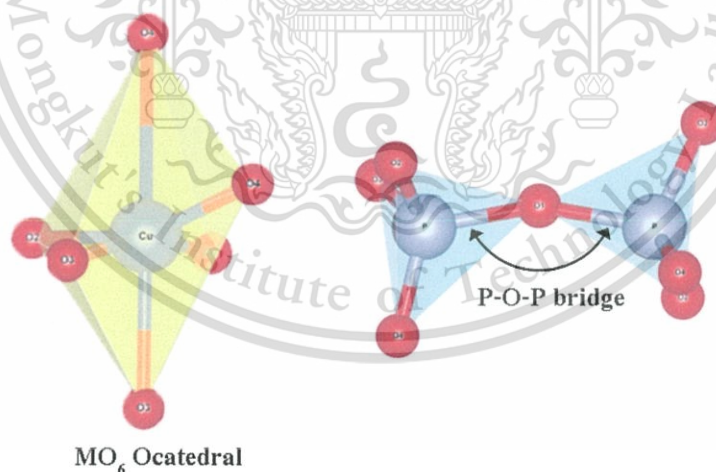


Illustration of two main structure of metal pyrophosphates compound

Keywords: metal pyrophosphates, phase formation, Rietveld refinement analysis, color, dielectric properties.

This material is reserved for educational use only, not allowed for commercial use.

Forbidden to modify the content, and cite the document when use.

ACKNOWLEDGEMENT

This thesis had been accomplished in the Electroceramics Research Laboratory (ECRL), College of Nanotechnology, King Mongkut's Institute of Technology Ladkrabang, Bangkok, Thailand.

First of all, I would like to thank Assoc.Prof.Dr.Naratip Vittayakorn, my research supervisor for the valuable suggestions, good supervisions, and all support he has given me throughout my education.

I would like to acknowledge Dr. Chanapa Kongmard, Department of Material, Faculty of Science, Kasetsart University for useful advice and constructive recommendations Ritveld refinement.

Finally, I am very grateful to my parents and my family for their support, understanding, and encouragement throughout my educational life.

Rattanaï Baitahe

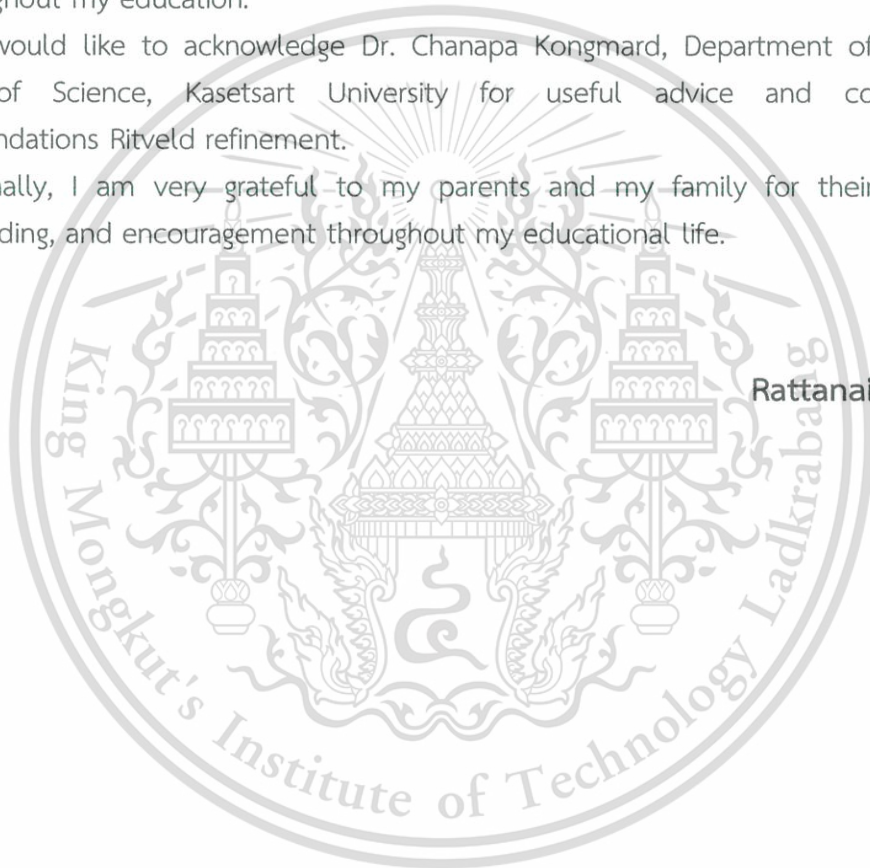


TABLE OF CONTENTS

	Page No.
THAI Abstract	i
ENGLISH Abstract	iii
Acknowledgement	v
Table of Contents	vi
List of Tables	x
List of Figures	xi
Abbreviations and Symbols	xiv
CHAPTER 1 INTRODUCTION	1
1.1 Overview	1
1.2 Scope of this work	4
1.3 Objective of this work	5
REFERENCE	6
CHAPTER 2 LITERATURE REVIEW	9
2.1 Phosphates compound	9
2.2 Candidate materials	11
2.2.1 Possibility of solid solution	12
2.3 Synthetic and functional group analysis	14
2.3.1 Synthetic	14
2.3.2 Functional group analysis	19
2.3.2.1 Fourier transform infrared spectroscopy (FTIR)	22
2.3.2.2 Raman scattering spectroscopy (Raman)	24
2.4 Physical properties	28
2.4.1 Dielectric properties	28
2.4.1.1 Frequency Dependence of Polarization	31
2.4.1.2 Dielectric constant	34
2.4.2 Optical properties	35
2.4.2.1 Color of matter	42

TABLE OF CONTENTS

	Page No.
2.4.2.2 Color conversion theory	43
2.5 Phase formation and evolution	45
2.6 Structure refinement	49
2.6.1 X-ray diffraction (XRD)	49
2.6.1.1 Rietveld refinement analysis	52
2.6.1.2 Rietveld refinement method	53
2.6.1.3 Agreement factors of Rietveld refinement	56
2.6.2 X-ray absorption spectroscopy (XAS)	57
2.6.2.1 Theory of X-ray absorption spectroscopy	58
2.6.3 Prediction of crystal structure bond strength	62
2.7 The crystal structure of metal pyrophosphate group	64
REFERENCE	72
CHAPTER 3 EXPERIMENTAL PROCEDURES	77
3.1 Phase formation and mechanism of reaction	77
3.2 Synthesis of metal pyrophosphate	81
3.3 Sample characterization	82
3.3.1 Functional group analysis	82
3.3.2 Phase formation	84
3.3.3 Structure refinement	86
3.3.4 Dielectric properties	87
3.3.5 Optical properties	89
REFERENCE	91
CHAPTER 4 PHASE FORMATION AND EVOLUTION OF Cu:Zn PARTIALS IN BINARY METAL PYROPHOSPHATES $\text{Cu}_{2-x}\text{Zn}_x\text{P}_2\text{O}_7$; $x \approx 1$	92
4.1 Introduction	92
4.2 Experimental procedure	93

TABLE OF CONTENTS

	Page No.
4.3 Results and Discussion	94
4.3.1 Functional group analysis	94
4.3.2 Mechanism of phase formation	98
4.3.3 Atomic evolution	104
4.4 Summary	109
REFERENCE	111
CHAPTER 5 CORRELATION BETWEEN THE CHROMATICITY, DIELECTRIC PROPERTIES AND STRUCTURE OF THE BINARY METAL PYROPHOSPHATES, $\text{Cu}_{(2-x)}\text{Zn}_x\text{P}_2\text{O}_7$	
	114
5.1 Introduction	114
5.2 Experimental procedure	116
5.3 Results and Discussion	117
5.4.1 Functional group analysis	117
5.4.2 Dielectric and optical properties	123
5.4.3 Structure analysis	125
5.4 Summary	136
REFERENCE	138
CHAPTER 6 DIELECTRIC PROPERTIES AND CHARACTERIZATIONS OF BINARY $\text{Cu}_{(2-x)}\text{Mg}_x\text{P}_2\text{O}_7$ PYROPHOSPHATES	
	141
6.1 Introduction	141
6.2 Experimental procedure	143
6.3 Results and Discussion	144
6.3.1 Functional group analysis	144
6.3.2 Crystal structure analysis	145
6.3.3 Dielectric properties	150
6.3.4 Correlation between structure and dielectric properties	151

TABLE OF CONTENTS

	Page No.
6.4 Summary	153
REFERENCE	155
CHAPTER 7 CONCLUSIONS	157
7.1 General Conclusions	157
APPENDIX	
CURICULUM VITAE	



LIST OF TABLES

Table No.	Page No.
2.1 Generally used nomenclature of phosphate compound	10
2.2 Summary of data on the pyrophosphates in this study	12
2.3 Crystallographic information for the predicted solid solution of all samples	13
2.4 Summary of the characteristics, advantages and disadvantages of some common methods used in the preparation of condensed inorganic solids, taken from the references	18
2.5 Summary of electromagnetic radiation	20
2.6 Observed vibrational frequencies of ions in the pyrophosphate species	27
2.7 Absorbed and transmitted color	43
2.8 The mathematical definitions of peak profile functions	55
2.9 The structural model of the single metal pyrophosphate, $\text{Cu}_2\text{P}_2\text{O}_7$	67
2.10 The structural model of the single metal pyrophosphate, $\text{Mg}_2\text{P}_2\text{O}_7$	68
2.11 The structural model of the single metal pyrophosphate, $\text{Zn}_2\text{P}_2\text{O}_7$	69
2.13 The structural model of the binary metal pyrophosphate, CuMP_2O_7	71
3.1 Specifications of the starting materials used in this study	77
4.1 Approximation of percentage by weigh from XRD results	102
4.2 Comparison values between the proposed TGA and XRD mass loss	106
4.3 Results obtained by EXAFS fitting analysis	109
5.1 Vibrational assignment of the samples	122
5.2 Bond angle and bond length from Rietveld refinement for samples	128
5.3 The approximate grouping of M-O bonding and bond strength of samples	130
5.4 Bond length from EXAFS fitting for the samples	133
5.5 The evolution of average bond length, octahedral volume, and distortion index of samples	135
5.6 Approximate wavelength of energy absorption	135
6.1 Lattice parameters of $\text{Cu}_{(2-x)}\text{Mg}_x\text{P}_2\text{O}_7$; $x = 0.00 - 2.00$ calculated from XRD data	146
6.2 Energy positions of the absorption edges observed for measured samples	148
6.3 Relative permittivity and dielectric loss of samples	149
6.4 Bond angle, M-O stretching position, and average bond length of samples	152
7.1 Summary of all factors on the pyrophosphates in this study	159

LIST OF FIGURES

Figure No.	Page No.
1.1 Crystal structure of $\text{Cu}_2\text{P}_2\text{O}_7$ at a low temperature	4
2.1 A graphical representation of the electromagnetic spectrum	19
2.2 Typical vibrational stretching and bending modes	21
2.3 Transitions for the scattering process: IR absorption, Rayleigh, Stokes and anti-Stokes scattering	25
2.4 Normal modes of PO_4^{3-} ion vibration	27
2.5 Frequency dependence of polarization processes	32
2.6 The five equivalent 3d orbitals	36
2.7 Separation of the orbitals into two sets is called the ligand-field splitting parameter, Δ , where the subscript, O, signifies octahedral complexes	38
2.8 Jahn-Teller distortions for an octahedral complex	40
2.9 Illustration of tetragonal distortion (elongation) in an octahedral complex	41
2.10 Wavelengths of colors and complementary colors	42
2.11 Summarized method of color and bond length relation	44
2.12 Example of a typical thermogram	45
2.13 Illustration of Bragg's law	50
2.14 Components of a typical XRD pattern of powder	52
2.15 Example of a typical Rietveld refinement plot	55
2.16 Typical X-ray absorption spectrum	58
2.17 The EXAFS phenomenon; outgoing photoelectron of the X-ray absorbed atom and backscattering photoelectron from the adjacent atom	59
2.18 The EXAFS phenomenon The $\chi(k)$ EXAFS (top), and the k -weight EXAFS, $k^2\chi(k)$ (bottom)	61
2.19 Basic cluster in ground metal pyrophosphates	65
2.20 Two types of $\text{P}_2\text{O}_7^{4-}$ cluster structures	65
2.21 The crystal structure of α - $\text{Cu}_2\text{P}_2\text{O}_7$ projected in 3 dimensions	67
2.22 The crystal structure of α - $\text{Mg}_2\text{P}_2\text{O}_7$ projected in 3 dimensions	68
2.23 The crystal structure of α - $\text{Zn}_2\text{P}_2\text{O}_7$ projected in 3 dimensions	70
2.24 The crystal structure of CuMP_2O_7 projected in 3 dimensions	71
3.1 The processing route for the mechanism of reaction	78

LIST OF FIGURES

Figure No.	Page No.
3.2 Thermogravimetry system	79
3.3 X-ray absorption spectroscopy	80
3.4 FT-IR spectrophotometer	83
3.5 Raman spectrophotometer	84
3.6 X-ray diffractometer	85
3.7 Fullprof program page	87
3.8 Dielectric measurement system	88
3.9 Image staked SONY IMX214 CMOS sensor	89
3.10 CIE chromaticity diagram	91
4.1 Raman spectra of $\text{Cu}_{(2-x)}\text{Zn}_x\text{P}_2\text{O}_7$; $x \approx 1.00$, subsequently calcine at 400, 500, 600, 700, and 800°C	96
4.2 FTIR spectra of $\text{Cu}_{(2-x)}\text{Zn}_x\text{P}_2\text{O}_7$; $x \approx 1.00$, subsequently calcine at 400, 500, 600, 700, and 800°C	97
4.3 XRD patterns of $\text{Cu}_{(2-x)}\text{Zn}_x\text{P}_2\text{O}_7$; $x \approx 1.00$, subsequently calcine at 400, 500, 600, 700, and 800°C	99
4.4 Plots of the relationship of the atomic partial, Cu:Zn, versus reaction temperature	105
4.5 TG/DTG of CuZnP_2O_7 precursor powder	106
4.6 Experiment (Black line) and fitted EXAFS data (Red line) at Cu and Zn K-edge of CuZnP_2O_7	108
5.1 FT-IR spectra of $\text{Cu}_{(2-x)}\text{Zn}_x\text{P}_2\text{O}_7$; $x = 0.00 - 2.00$	119
5.2 Raman spectra of $\text{Cu}_{(2-x)}\text{Zn}_x\text{P}_2\text{O}_7$; $x = 0.00 - 2.00$	121
5.3 Dielectric constant plots of $\text{Cu}_{(2-x)}\text{Zn}_x\text{P}_2\text{O}_7$; $x = 0.00 - 2.00$	124
5.4 CIE chromatic coordinates of $\text{Cu}_{(2-x)}\text{Zn}_x\text{P}_2\text{O}_7$; $x = 0.00 - 2.00$	125
5.5 Rietveld refinement patterns of $\text{Cu}_{(2-x)}\text{Zn}_x\text{P}_2\text{O}_7$; $x = 0.00 - 2.00$	127
5.6 The approximate grouping of M-O bonding of $\text{Cu}_{(2-x)}\text{Zn}_x\text{P}_2\text{O}_7$; $x = 0.00 - 2.00$	129
5.7 EXAFS fitting curves of $\text{Cu}_{(2-x)}\text{Zn}_x\text{P}_2\text{O}_7$; $x = 0.00 - 2.00$	132
5.8 Summary of crystal field splitting in $\text{Cu}_{(2-x)}\text{Zn}_x\text{P}_2\text{O}_7$; $x = 0.00 - 1.50$	136
6.1 Raman spectra of $\text{Cu}_{(2-x)}\text{Mg}_x\text{P}_2\text{O}_7$; $x = 0.00 - 2.00$	145
6.2 XRD patterns of $\text{Cu}_{(2-x)}\text{Mg}_x\text{P}_2\text{O}_7$; $x = 0.00 - 2.00$	146
6.3 XANES spectra of $\text{Cu}_{(2-x)}\text{Mg}_x\text{P}_2\text{O}_7$; $x = 0.00 - 2.00$	149

LIST OF FIGURES

Figure No.	Page No.
6.4 Plots of the relative permittivity and loss of $\text{Cu}_{(2-x)}\text{Mg}_x\text{P}_2\text{O}_7$; $x = 0.00 - 2.00$	151
6.5 EXAFS patterns of $\text{Cu}_{(2-x)}\text{Mg}_x\text{P}_2\text{O}_7$; $x = 0.00 - 2.00$	153



ABBREVIATIONS AND SYMBOLS

$A_{\phi,h}$	Absorption correction
C	Number of constraints
E	Applied field vector
EN	Electronegativity
F	Local field
FWHM	Full Width at Half Maximum
$F_{\phi,h}$	Structure factor
$F_{(hkl)\alpha}$	Structure factor for the reflection, hkl , of phase α
I_0	Incident beam intensity
$I_{(hkl)\alpha}$	Reflection intensity of hkl in phase α
$Lp_{\phi,h}$	Lorentz-polarization factor
m	Mass of the two nuclei
M_{hkl}	Multiplicity of the reflection, hkl , of phase α
$M_{\phi,h}$	Multiplicity factor of the h^{th} reflection
N	Number of observations
N_i	Number of dipoles per unit volume
O	Lorentz-polarization (and monochromator) correction
P	Polarization vector
P_e	Electronic polarization
P_i	Ionic polarization
P_0	Orientalional polarization.
r	Distance from specimen to detector
R	Total distance between the two atoms
R_{exp}	Expected R-factor
R_p	Profile R-factor
R_w	Weighted profile R-factor
R_0	Bond length of a unit cell
S	Bond strength or bond valence of length
S_0	Ideal bond strength of length
s_{ϕ}	Scale factor of the phase
$T_{\phi,hi}$	Temperature factor

ABBREVIATIONS AND SYMBOLS

ν	Coordination number
V_{α}	Volume of the unit cell of phase α
w_i	Weighting factor ($w_i=1/y_i^{\text{obs}}$)
y_i^b	Background intensity
y_i^{calc}	Calculated intensity point i
y_i^{obs}	Observed intensity
Z	The number of formula units per unit cell
α_e	Electronic polarizability
α_i	Ionic polarizability
α_o	Orientalional or dipolar polarizability
α_s	Space charge polarizability
$\delta(\text{OPO})$	Bending vibrations
Δ_o	Octahedral crystal field splitting energy
ϵ	Static dielectric constant of the medium
ϵ_r	Dielectric permittivity
$\Omega_{i,\phi,h}$	Reflection profile function
λ	X-ray wavelength
μ	Reduced mass
μ_s	Linear absorption coefficient of the specimen
ν_1	Symmetric stretching
ν_2	Symmetric Bending
ν_3	Asymmetric stretching
ν_4	Asymmetric Bending
ν_{α}	Volume fraction of phase α
χ	Susceptibility
ψ	Wave function
$2\theta_m$	Diffraction angle of the monochromator
$\langle S_{\text{M-O}} \rangle$	Bond strength
$\langle V_{\text{M-O}} \rangle$	Bond valence

CHAPTER 1

INTRODUCTION

1.1 Overview

Metal phosphates with open-framework structures are of great interest and the subject of a broad study, due to their potential applications as fertilizer, pigments in artist's paints, biomaterials, batteries, anti-corrosive pigments in metal, fire retardant substance and catalysts [1-4]. They are being researched widely, due to their structural variability, and their structure type has been reported with a general formula, including metal hydrogen phosphate hydrate form ($M(H_2PO_4)_2 \cdot nH_2O$, $MHPO_4 \cdot nH_2O$; $n=1, 2, 3, \dots$), metal ammonium phosphate hydrate form ($MNH_4PO_4 \cdot nH_2O$), metal phosphate anhydrate form ($M_3(PO_4)_2$), metal cyclo-tetraphosphate form ($M_2P_4O_{12}$), and metal pyrophosphate form ($M_2P_2O_7$). Anhydrous pyrophosphate salts of divalent metal ions in metal phosphate compounds are found to assume a rather wide range of electrical applications such as Li-ion rechargeable batteries, low temperature co-fired ceramics (TTCC), and wireless communication materials [5-8], but phase transition often occurs when the temperature increases or decreases. As a result, dielectric properties of the devices change. These compounds appear in two phases: low- and high temperature. In the low-temperature (α) phase, pyrophosphate ions are in staggered conformation with a bent P–O–P bridge ($<180^\circ$), while the pyrophosphate ions in the high-temperature (β) phases have a linear P–O–P bridge (180°) [9]. In a previous work, Kim et al. [10] reported two important factors, which caused polarization in the structure. This shifted O atoms in the collinear P–O–P bridge, and moved M^{2+} ions in the octahedral MO_6 . However, few details of the structure were related in their study. Each pyrophosphate displayed a reversible phase transformation, and in each case the room temperature form was in the α phase. The modified structure for restraining reversible phase transformation led to stabilized properties when its temperature changed.

This material is reserved for educational use only, not allowed for commercial use.

Forbidden to modify the content, and cite the document when use.

Most researches of metal phosphate groups usually concentrate on four principal stories, including 1) synthesis and characterization [11-13], 2) kinetics and thermodynamics of reaction [14-16], 3) property measurement of materials [17, 18], and 4) refinement of the crystal structure [8, 13]. However, the study for linking the relationship between crystal structure and their properties is often highly unpredictable and not completely understood. Recently, crystal structure refinement has been needed for a greater understanding of crystallization processes [19]. The difference of these compounds causes variance in phosphate ion numbers in the polymerization reaction of phase formation, and arrangement of atoms in the crystal structure. Furthermore, varied crystal structures have different material properties. Therefore, the structural refinement of metal phosphates has been investigated extensively by using different techniques.

Recently, important techniques have allowed the changes in crystal structure, microstructure and phase composition to follow the use of X-ray absorption spectroscopy (XAS), Mossbauer spectroscopy, and Neutron diffraction spectroscopy, with the processes analyzed by powerful methods. Nevertheless, these techniques have problems regarding the number of instruments that are very few worldwide, and come at a high operation cost. The general X-ray diffraction (XRD) technique is a well-established analytical method for investigating crystallography, geology, chemistry, petrology, natural sciences, material science, and the pharmaceutical industry. Earlier, the application of XRD was confined mostly to the field of 'conventional' applications such as definition of micro-structural analysis and unit-cell parameters [20] of materials, using diffraction 'line profiles' [21] and qualitative phase analysis (e.g., estimation of unknown or new crystalline phases). In 1967, the Rietveld method [22] was introduced originally as a structural refinement method for collecting powder data. Later, the method evolved into a general structural refinement technique. Therefore, collected data from XRD and the Rietveld refinement process were selected for use in characterizing the crystal structure of metal phosphates in this research.

The α - $\text{Cu}_2\text{P}_2\text{O}_7$ pyrophosphate structure is shown in Figure 1.1, and it represents metal pyrophosphate compound before structural modification [23]. This compound is a

layered structure that consists of CuO_6 octahedral sheets and separated by $[\text{P}_2\text{O}_7]^{4-}$ ion layers. The cations are found in irregular octahedral coordination with oxygen atoms, as shown in Figure 1. The major distortion from regularity includes two elongated metal oxygen atoms, which lie bonded almost perpendicular to the b axis. The two remaining pairs of oxygen ligands lie above and below this plane, and rotate in opposite directions from their 'regular' position nearby the b axis. These octahedral cations share edges to form a pseudo-hexagonal network, extendable in the (001) plane. Adjacent sheets of these octahedral cations are joined by pyrophosphate anions, which consist of corner shared PO_4^{3-} tetrahedral, form $\text{P}_2\text{O}_7^{4-}$ clusters that share two of their terminal oxygen atoms on each side with one sheet, and a third with the adjacent sheet. The P-O-P angle is approximately 157° , the central P-O bond 1.576 \AA , and the average terminal P-O bond 1.525 \AA , when they are not corrected from the effects of thermal motion. The single metal $\alpha\text{-Cu}_2\text{P}_2\text{O}_7$ compound shows a rather low sintering temperature of about 800°C , which can save energy in ceramic sintering processes. Furthermore, the reversible phase transformation is simply ($C2/c \leftrightarrow C2/m$), with a low temperature in the range of $75\text{-}100^\circ\text{C}$ [24]. Thus, a modified structure of binary metal pyrophosphates has been based on $\alpha\text{-Cu}_2\text{P}_2\text{O}_7$ compound.

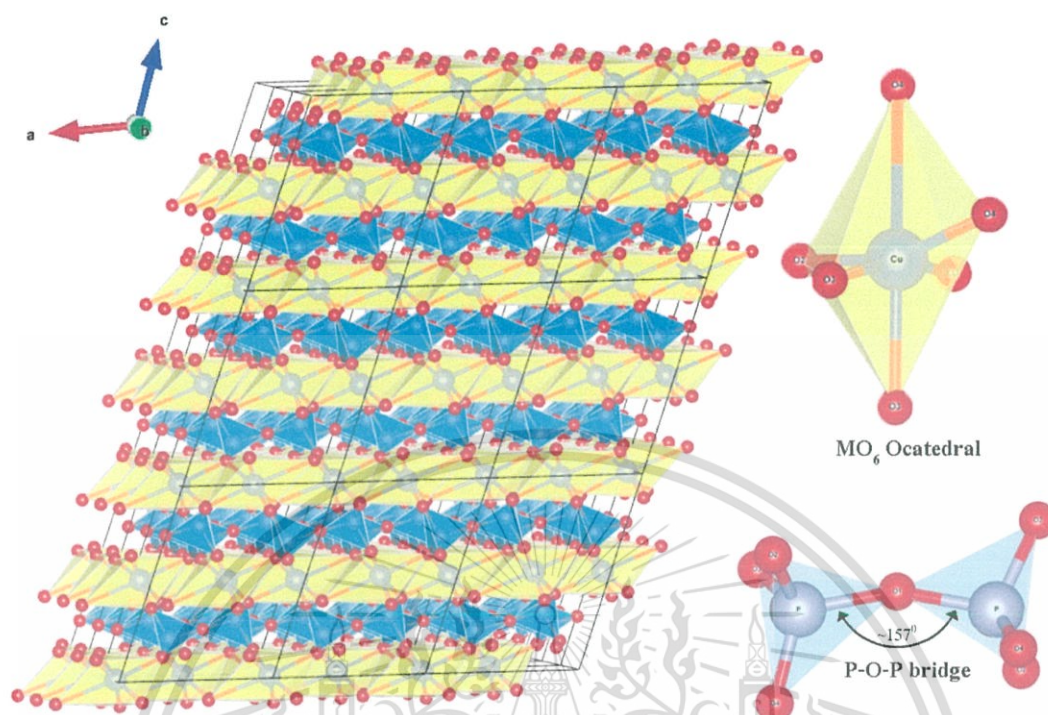


Figure 1.1 Crystal structure of $\text{Cu}_2\text{P}_2\text{O}_7$ at a low temperature.

1.2 Scope of this work

This work describes the relationship between crystal structures by using the effects of bond length, bond angle, bond strength, number of P-O-P clusters, average bond length, and distortion of the MO_6 octahedral site and dielectric properties of single metal pyrophosphates, as well as modified structured binary metal pyrophosphate compounds. In addition, it reveals the correlations of structure with optical property. These samples are considered to be of a largely different crystal structure for observing the difference after structural modification. The influence of a changing crystal structure after modification, and changing properties were investigated. The Zn^{2+} in the $\text{Zn}_2\text{P}_2\text{O}_7$ form and Mg^{2+} in the $\text{Mg}_2\text{P}_2\text{O}_7$ form were selected, due to their having the same crystal system, but they had a slightly different ionic radii (Cu^{2+} : 0.73 Å, Mg^{2+} : 0.72 Å, and Zn^{2+} :

0.74 Å) [25]. These ions were used to stabilize the β -phase of $\text{Cu}_2\text{P}_2\text{O}_7$ when freezing the dielectric constant of samples at all working temperatures. The dielectric property of samples was determined using an LCR meter, and the optical property was studied by CIE chromaticity coordinate analysis. Details of the crystal structure were identified by the XRD technique and refined by the Rietveld refinement method. These results were supported by extended X-ray absorption fine structure (EXAFS) fitting analysis, Raman spectroscopy, and Fourier transform-infrared spectroscopy (FT-IR). Morphology and grain size of the pellets were investigated by scanning electron microscope (SEM).

1.3 Objective of this work

This research focused on the synthesis of single metal pyrophosphates, and modified binary metal pyrophosphates in order to fulfill the following objective:

1.3.1 To synthesize single metal pyrophosphates (α - $\text{Cu}_2\text{P}_2\text{O}_7$, α - $\text{Mg}_2\text{P}_2\text{O}_7$, α - and $\text{Zn}_2\text{P}_2\text{O}_7$), and modify binary metal pyrophosphates ($\text{Cu}_{(2-x)}\text{Zn}_x\text{P}_2\text{O}_7$ and $\text{Cu}_{(2-x)}\text{Mg}_x\text{P}_2\text{O}_7$).

1.3.2 To study the mechanism of phase formation and evolution of Cu:Zn particles in $\text{Cu}_{(2-x)}\text{Zn}_x\text{P}_2\text{O}_7$; $x \approx 1$.

1.3.3 To investigate the dielectric properties of the samples.

1.3.4 To investigate the optical properties (colour) of the samples.

1.3.5 To determine the crystal structure of the samples by the Rietveld refinement method and confirm by EXAFS fitting, Raman spectroscopy, and FT-IR results.

1.3.6 To relate between the crystal structure and dielectric property, and the crystal structure and optical property.

REFERENCE

- [1] Lapina LM: Metal Ammonium Phosphates and Their New Applications. Russian Chemical Reviews. 1968;37: 693.
- [2] Bian JI, Kim DW, Hong KS: Microwave dielectric properties of $A_2P_2O_7$ (A = Ca, Sr, Ba; Mg, Zn, Mn). Japanese Journal of Applied Physics Part 1-Regular Papers Short Notes & Review Papers. 2004;43: 3521-3525.
- [3] Bian JJ, Kim D, Hong KS: Microwave dielectric properties of $(Zn_{1-x}Mn_x)_2P_2O_7$. Journal of Materials Science. 2005;40: 1801-1803.
- [4] Wenwei W, Yanjin F, Xuehang W *et al.*: Preparation via solid-state reaction at room temperature and characterization of layered nanocrystalline $NH_4MnPO_4 \cdot H_2O$. Journal of Physics and Chemistry of Solids. 2009;70: 584-587.
- [5] Forsyth JB, Wilkinson C, Paster S *et al.*: The magnetic structure of cobalt diphosphate $Co_2P_2O_7$. Journal of Physics: Condensed Matter. 1989;1: 169-178.
- [6] Pang H, Yan Z, Wang W *et al.*: Template-free controlled fabrication of $NH_4MnPO_4 \cdot H_2O$ and $Mn_2P_2O_7$ micro-nanostructures and study of their electrochemical properties. International Journal of Electrochemical Science. 2012;7: 12340-12353.
- [7] Pang H, Yan Z, Ma Y *et al.*: Cobalt pyrophosphate nano/microstructures as promising electrode materials of supercapacitor. Journal of Solid State Electrochemistry. 2013;17: 1383-1391.
- [8] Hou L, Lian L, Li D *et al.*: Facile synthesis of $Co_2P_2O_7$ nanorods as a promising pseudocapacitive material towards high-performance electrochemical capacitors. RSC Advances. 2013;3: 21558-21562.
- [9] Calvo C: The crystal structure and phase transitions of β - $Zn_2P_2O_7$. Canadian Journal of Chemistry. 1965;43: 1147-1153.
- [10] Kim CH, Yim HS: The effect of tetravalent metal on dielectric property in ZrP_2O_7 and TiP_2O_7 . Solid State Communications. 1999;110: 137-142.

- [11] Boonchom B, Baitahe R: Synthesis and characterization of nanocrystalline manganese pyrophosphate $Mn_2P_2O_7$. *Materials Letters*. 2009;63: 2218-2220.
- [12] Xiao ZW, Hu GR, Peng ZD *et al.*: Solid state synthesis and characterization of iron(II) pyrophosphate $Fe_2P_2O_7$. *Chinese Chemical Letters*. 2007;18: 1525-1527.
- [13] Bensalem A, Ahluwalia M, Vijayaraghavan TV *et al.*: Synthesis of amorphous $MgHPO_4 \cdot x(R)$ [R = Ethanol; Ethylene glycol] in anhydrous media. *Materials Research Bulletin*. 1997;32: 1473-1483.
- [14] Brandová D, Trojan M, Arnold M *et al.*: Mechanism of dehydration and condensation of $CuHPO_4 \cdot H_2O$. *Journal of thermal analysis*. 1988;34: 1449-1454.
- [15] Brandová D, Trojan M, Paulik F *et al.*: Mechanism of dehydration of $ZnHPO_4 \cdot H_2O$. *Journal of thermal analysis*. 1987;32: 1923-1928.
- [16] Boonchom B, Baitahe R, Kongtaweelert S *et al.*: Kinetics and Thermodynamics of Zinc Phosphate Hydrate Synthesized by a Simple Route in Aqueous and Acetone Media. *Industrial & Engineering Chemistry Research*. 2010;49: 3571-3576.
- [17] Jouini A, Gâcon JC, Ferid M *et al.*: Luminescence and scintillation properties of praseodymium poly and diphosphates. *Optical Materials*. 2003;24: 175-180.
- [18] Yang T, Lin J: Hydrothermal syntheses and low temperature magnetic behaviors of $ACo_3(P_2O_7)_2$ (A=Ca, Sr, Ba, Pb). *Journal of Solid State Chemistry*. 2013;198: 1-5.
- [19] Braga D: Inorganic crystal engineering: a personal perspective. *Journal of the Chemical Society, Dalton Transactions*. 2000: 3705-3713.
- [20] Langford JI, Daniél L: Powder diffraction. *Reports on Progress in Physics*. 1996;59: 131.
- [21] Kapoor K, Lahiri D, Rao SVR *et al.*: X-ray diffraction line profile analysis for defect study in Zr-2.5% Nb material. *Bulletin of Materials Science*. 2004;27: 59-67.
- [22] Rietveld H: Line profiles of neutron powder-diffraction peaks for structure refinement. *Acta Crystallographica*. 1967;22: 151-152.
- [23] Robertson BE, Calvo C: The crystal structure and phase transformation of α - $Cu_2P_2O_7$. *Acta Crystallographica*. 1967;22: 665-672.
- [24] Calvo BERaC: Crystal structure of β - $Cu_2P_2O_7$. *Canadian Journal of Chemistry*. 1968;46.

- [25] Shannon R: Revised effective ionic radii and systematic studies of interatomic distances in halides and chalcogenides. *Acta Crystallographica Section A*. 1976;32: 751-767.



This material is reserved for educational use only, not allowed for commercial use.

Forbidden to modify the content, and cite the document when use.

CHAPTER 2

LITERATURE REVIEW

2.1 Phosphates compound

In general, phosphates are salts of monophosphoric acid H_3PO_4 and various other condensed and polymeric forms [1]. Phosphate materials can be classified into three main categories: monophosphates, condensed phosphates, and ultraphosphates [2]. Monophosphates are salts derived from H_3PO_4 and are the simplest phosphates, with an isolated PO_4^{3-} tetrahedron as the anionic unit, and an O/P ratio of 4:1. They are the widest family of phosphates; and all natural phosphates are monophosphates. Substituted phosphates also can be included in the phosphate family, where one or more types of oxygen in the PO_4 tetrahedron have been substituted, for example, PO_3H (phosphonate), PO_3S (triphosphate) and PO_3F (fluorophosphates) [1, 2].

Condensed phosphates (also known as oligophosphates) have a P-O-P bridge within the anionic unit and are built from corner sharing tetrahedral PO_4 . The P-O-P bonds are formed in various different processes, with the simplest being via a condensation reaction, where water is eliminated. This P-O-P bond is susceptible to hydrolysis in acidic conditions when heated, and is therefore considered less stable than monophosphates. The O/P ratio in condensed phosphates is less than 4:1, as a direct consequence of oxygen loss during their formation. There are 2 different geometries observed in condensed phosphates: polyphosphates and cyclic phosphates [3]. Polyphosphates are formed when a condensation reaction occurs, forming linear chains of tetrahedral phosphates, which share one or two of their oxygen atoms. The anionic unit in this geometry corresponds to the general formula $[\text{P}_n\text{O}_{(3n+1)}]^{(n+2)-}$, where n is the number of tetrahedral phosphates. Diphosphates, also known as pyrophosphates, are the simplest polyphosphate, where n = 2. These, together with triphosphates and infinite chain materials are studied most of all among polyphosphates, and were first discovered by Berzelius [4]. Discrete polyphosphates, where n > 4, are rare. Pyrophosphates can take the general formulae of

$M^IV P_2O_7$, $M_2^{II} P_2O_7$, $M^I M^{III} P_2O_7$, $M_2^I M^{II} P_2O_7$ and $M_4^I P_2O_7$; M = cation element. Acidic anions also are known within these categories, such as $H_2P_2O_7^{2-}$, which is characterized by strong hydrogen bonding between anions. This leads to ribbons, planes and infinite chains. Cyclic phosphates (or cyclophosphates) have an anionic unit ring, and a general formula of $[P_n O_{3n}]^{n-}$, where $n \leq 3$. In this geometry, each phosphate tetrahedron shares 2 oxygen atoms with its neighbor, thus giving an O/P ratio of 3:1.

Ultraphosphates, in contrast to polyphosphates and cyclic phosphates, are branched: meaning the anionic unit contains tetrahedral phosphate that shares 3 of its oxygen atoms, which can form various different geometries such as three dimensional networks, infinite ribbons and layers [5], or finite groups. Ultraphosphates undergo hydrolysis rapidly due to triply linked tetrahedral, and so they are somewhat unstable. The general anionic formula for ultraphosphates is $[P_{(n+2)} O_{(3n+5)}]^{n-}$. There has been much confusion in the naming of condensed phosphates over the years. Therefore, it is helpful to summarize. Table 2.1 shows the nomenclature generally used today.

Table 2.1 Generally used nomenclature of phosphate compound

Number of tetrahedral	Name
2	Pyrophosphates or diphosphates
3	Tripolyphosphates or triphosphates
4	Tetrapolyphosphates or tetraphosphates
5	Pentapolyphosphates or pentaphosphates
<20	Oligophosphates
Very large or infinite chains	Long chain phosphates or meta phosphates

2.2 Candidate materials

The group of metal pyrophosphate compounds ($M_2P_2O_7$; M = metal element) was used for many applications such as pigment, biomedical cements, chelating agents, corrosion-resistant coatings, high-quality fertilizers, glass ceramics, and microwave dielectric materials [6-8]. Pyrophosphate compounds have appeared to possess a relatively low sintering temperature as well as good dielectric loss properties [6], which correspond to a crystal structure. Metal pyrophosphates within the family of phosphates can show low sintering temperature and phenomena of coloration, which depend on the type and occupancy of cations in a structure. The pyrophosphates of divalent Cu^{2+} , Zn^{2+} and Mg^{2+} cations have an isostructural high-temperature phase, termed traditionally as β -phases, which undergo a reversible transition to α -phase on cooling [9, 10]. They are a monoclinic system within the $C2/m$ space group. However, these pyrophosphates are different in structure at low-temperature and they require a different sintering temperature. The literature review found that the pyrophosphate of the copper cation, $Cu_2P_2O_7$, can be transitioned reversibly to α -phase at a much lower temperature than other compounds. The reversible phase transition was simple due to the α - and β -phases being close to the crystal structure [$C2/c$ (15) \rightarrow $C2/m$ (12)]. Additionally, the $Cu_2P_2O_7$ compound can be shown at a low sintering temperature and with a colorful pigment (green tone), while the pyrophosphate of Zn^{2+} and Mg^{2+} cations exhibit colorless powder. The pertinent features of these structures are summarized in Table 2.2.

Table 2.2 Summary of data on the pyrophosphates in this study [11, 12]

Compound	<i>a</i> (Å)	<i>b</i> (Å)	<i>c</i> (Å)	β (°)	Space group	Transition temp. (°C)	Sinter temp. (°C)	Color
α -Cu ₂ P ₂ O ₇	6.876	8.113	9.162	109.54	<i>C2/c</i>	~90	700	green
β -Cu ₂ P ₂ O ₇	6.827	8.118	4.576	108.85	<i>C2/m</i>			green
α -Mg ₂ P ₂ O ₇	13.198	8.295	9.072	104.90	<i>B2₁/c</i>	~70	1100	white
β -Mg ₂ P ₂ O ₇	6.494	8.280	4.522	103.80	<i>C2/m</i>			white
α -Zn ₂ P ₂ O ₇	20.068	8.259	9.099	106.35	<i>I2/c</i>	~140	900	white
β -Zn ₂ P ₂ O ₇	6.610	8.290	4.510	105.40	<i>C2/m</i>			white

2.2.1 Possibility of solid solution

A solid solution is formed when two metals are completely soluble in a liquid state and also solid state. In other words, when homogeneous mixtures of two or more kinds of atoms (of metals) occur in the solid state, they are known as solid solutions. If the atoms of the solvent or parent metal are replaced in the crystal lattice by atoms of the solute metal, then the solid solution is known as substitutional solid solution. Here, the solute atoms have substituted the solvent atoms in an orderly manner on their lattice site. Hume-Rothery [13] formulated certain rules that govern the formation of substitutional solid solutions, and they are as follows:

(a) **Crystal structure factor:** For complete solid solubility, the two elements should have the same type of crystal structure, *i.e.*, both elements should have either F.C.C. or B.C.C. or H.C.P. structure.

(b) **Relative size factor:** As the size (atomic radii) difference between two elements increases, solid solubility becomes more restricted. The difference in atomic radii of two elements should be less than 15 percent for extensive solid solubility. If the relative size factor is more than 15 percent, solid solubility is limited. For example, both silver and lead have F.C.C. structure and the relative size factor is about 20 percent. Therefore, the

solubility of lead in solid silver is about 1.5 percent and the solubility of silver in solid lead is about 0.1 percent. Copper and nickel are completely soluble within each other in all proportions. They have the same type of crystal structure (F.C.C.) and differ in atomic radii by about 2 percent.

(c) **Chemical affinity factor:** Solid solubility is favored when the two metals have less chemical affinity. If the chemical affinity of the two metals is greater, the tendency is towards compound formation. Generally, if the two metals are separated widely in the periodic table, they possess greater chemical affinity and are more likely to form some type of compound instead of solid solution.

(d) **Relative valence factor:** It is found that metal of lower valence tends to dissolve more than metal of higher valence and vice versa.

Table 2.3 Crystallographic information for the predicted solid solution of all samples

Sample	Crystal system	Atomic radii (Å)	EN	Oxidation state
$\text{Cu}_2\text{P}_2\text{O}_7$	Monoclinic	0.73	1.9	2+
$\text{Mg}_2\text{P}_2\text{O}_7$	Monoclinic	0.72	1.31	2+
$\text{Zn}_2\text{P}_2\text{O}_7$	Monoclinic	0.74	1.65	2+

These data show a high possibility of substitutional solid solution between $\text{Cu}^{2+}/\text{Zn}^{2+}$, and $\text{Cu}^{2+}/\text{Mg}^{2+}$ ions in pyrophosphate compound.

2.3 Synthetic and functional group analysis

2.3.1 Synthetic

Metal pyrophosphate compounds are synthesized by a variety of routes, which include the spray pyrolysis, precipitation method; sol-gel process; hydrothermal techniques; microwave processing; and solid state reaction. They provide intimate mixing of the components, thus allowing production of finer particles and high-purity materials.

Spray pyrolysis

The solution-based approach in the preparation of metal pyrophosphate powders is spray pyrolysis, which is an effective technique for obtaining final powders with fine size and regular morphology. The starting solutions can be sprayed ultrasonically into a high-temperature reactor by electrospray or rotary techniques with an inert carrier gas at temperatures ranging from 450 to 650 °C. The precursor solution can be made by dissolving stoichiometric amounts of metal carbonate, oxalate and ammonium dihydrogen phosphate in nitric acid. The as-sprayed fine powders are spherical in shape, but with low crystallinity, therefore, the post-annealing process is necessary at temperatures ranging from 600 to 900 °C in inert or slightly reductive atmosphere. However, the spherical morphology changes during calcination [14].

Precipitation method

Precipitation methods offer the advantages of optimum particle size and ensuring phase purity. Phase pure, homogeneous, and well-crystallized metal pyrophosphate is synthesized by aqueous co-precipitation of metal ion solution and phosphoric acid. After condition of the solution optimizes, metal phosphate hydrates form ($MHPO_4 \cdot nH_2O$ or $MNH_4PO_4 \cdot nH_2O$) and begin to precipitate. Then, the precipitate obtained is calcined at about 500-900°C into metal pyrophosphate compound, and a water molecule and ammonia gas. Sometimes, the precipitating agent competes with the reaction to bring about a final product of $M_3(PO_4)_2 \cdot nH_2O$, which is in the impurity phase, $M_3(PO_4)_2$. The preparation methods need optimum chemical reagent and conditions of single phase synthesis.

Sol-gel processing

Sol-gel synthesis of metal phosphate compounds has attracted much attention recently, due to its many advantages, including high product purity, homogeneous composition, and low synthesis temperature. Low-temperature formation and fusion of apatite crystals have been the main contributions in the sol-gel process, when compared with conventional methods. For instance, temperatures higher than 1,000 °C are usually required for sintering fine crystals prepared by the wet precipitation method, whilst temperatures several hundred degrees Celsius lower than those mentioned above are needed for density of sol-gel metal phosphate compounds. The sol-gel process for preparing metal phosphate compounds usually produces a fine-grain microstructure containing a mixture of nano-to submicron crystals. Furthermore, the high reactivity of sol-gel powder allows a reduction of processing temperature and all degradation phenomena that occur during sintering. The major limitation in applying the sol-gel technique is linked to the possible hydrolysis of phosphates and high cost of raw materials. On the other hand, most sol-gel processes require a strict pH control, vigorous agitation and much time for hydrolysis.

Hydrothermal processing

Hydrothermal chemistry is currently one of the principal methods of synthesis for the preparation of new inorganic materials. There is a pressing need for understanding the formation mechanisms of inorganic materials under hydrothermal conditions, aiding the preparation of new materials in a rational manner and optimizing synthesis conditions for efficient production [15]. The hydrothermal method involves heating solid and liquid reagents with a suitable solvent (usually water) in a sealed vessel at temperatures of up to 250 °C. Although elevated temperatures are used, and pressure is generated in a sealed container, the conditions are much less severe than in traditional ceramic methods of solid-state chemistry. The pressure within the sealed reaction container increases dramatically with temperature, which is rather dangerous.

Microwave processing

Microwave processing is a self-heating process that occurs through absorption of electromagnetic energy [16]. Since microwave energy is absorbed directly by the sample, uniform and rapid heating is achieved within a short period of time, and at temperatures lower than those required for furnace heating. This type of processing has been applied as a novel sintering method for preparing many ceramics. Domestic microwave ovens are inexpensive and convenient, and they require very little energy to operate. Therefore, microwave processing using a domestic oven is presumed to be a very economical synthetic method for producing various inexpensive ceramic powders with homogeneous microstructures and fine grain size. The samples obtained from this method give high electrochemical capacity and good cycle ability, but low purity.

Solid-state reaction

Although sol-gel, hydrothermal, spray pyrolysis, and combustion methods have reportedly synthesized phosphates, the simplest method is solid-state reaction, which can be scaled up easily in large quantities and was chosen for this study. Solid-state synthesis is a conventional method for preparing ceramics, and includes several successive steps of intimate grinding and annealing of the stoichiometric mixture of starting materials. Generally, in the case of metal pyrophosphates, the starting mixture consists of a stoichiometric amount of metal oxides or metal carbonates and a phosphate source of ammonium hydrogen phosphates $[(\text{NH}_4)_2\text{HPO}_4, \text{NH}_4\text{HPO}_4]$. The raw materials were prepared according to stoichiometric amounts, and then the mixture was ground homogeneously in an agate mortar. Thereafter, the mixture was transferred to muffle furnaces in an alumina ceramic crucible and heated at temperatures from 400 to 1,000 °C for 2–24 h [17].

All the samples used in this work were prepared by the conventional solid state synthesis technique, which involves heating (not melting!) mixtures of two or more solids to form the desired solid phase product. Unlike the gas phase and solution reactions, diffusion is usually the limiting factor in solid-solid reactions. The diffusion process can be described by Fick's laws, which are used to solve the diffusion coefficient, D . To obtain good rates of reaction, the diffusion coefficient has to be larger than $10\text{-}12 \text{ cm}^2/\text{s}$. As the

melting point is approached, the diffusion coefficient increases rapidly with temperature. This concept leads to Tamman's rule [18].

The rates of solid state reactions are controlled by two factors:

- (1) The area of contact between solid reactions: this should be maximized using starting reagents with a large surface area, achieved by fine milling of starting reagents (precursors).
- (2) The rate of diffusion: this can be increased by increasing the temperature.

Steps in conventional solid state synthesis:

1. Selecting appropriate starting materials: fine grain powders should be chosen to maximize the surface area. In most cases, a well-defined composition is crucial.
2. Weighing out and mixing together starting materials: starting materials should be weighed precisely with electronic balance at an appropriate stoichiometric ratio. Then, they can be mixed together in an agate mortar and pestle or a ball mill (for large preparations).
3. Pelletizing: pelletizing the mixed precursors can enhance intimate contact of reactants and also minimize contact with the crucible. An organic binder can be used for better binding. For some preparations, 10% solution (by weight, in water) of polyvinyl alcohol was used, with the chemical formula $(C_2H_4O)_n$.
4. Selecting a sample container: when selecting containers, reactivity of the sample container with the precursors used for synthesis, strength, cost and durability should be considered. There is choice from a variety of sample containers made of, (a) ceramic refractories such as Al_2O_3 or ZrO_2/Y_2O_3 , (b) precious metals such as Pt, Au, Ag and Ir, and (c) SiO_2 , Mo, W, etc. (mostly as sealed tubes).
5. Heat treatment: factors influencing the choice of temperature include Tamman's rule and the potential for volatilization.
6. Verifying phase purity: powder diffraction.
7. Improvement: if the reaction is incomplete, the steps from 4 are repeated until the desired phase product is obtained.

Table 2.4 Summary of the characteristics, advantages and disadvantages of some common methods used in the preparation of condensed inorganic solids, taken from the references [25]

Methods	Typical Temperature	Advantages	Disadvantages
Spray pyrolysis	450-650°C	1.) Spherical in shape 2.) Small particle	1.) Low crystallinity 2.) Secondary phases
Precipitation	500-900°C	1.) Simple 2.) Stronger shaped particle 3.) Homogeneous product	1.) Long reaction time 2.) Mixed phases of product 3.) Difficult to condition
Sol-Gel	Step1: Room temperature Step2: 600-1,000°C	1.) Mixing of reagent: homogeneous product	1.) Impurities in the product from the gel precursor 2.) Difficult to control size
Microwave processing	300°C	1.) Simple 2.) Very fast	1.) Impurity 2.) Agglomerated particle
Solid state reactions	600-1000°C	1.) Simple 2.) Single step 3.) Low cost of raw materials 4.) High purity (optimum conditions)	1.) High temperature 2.) Contaminated ball

2.3.2 Functional group analysis

Electromagnetic waves are a form of radiant energy released by certain electromagnetic processes. Visible light is one type of electromagnetic radiation, while other familiar forms are invisible such as X-rays and radio waves. The spectrum of electromagnetic waves is divided into different types, as shown in Figure 2.1.

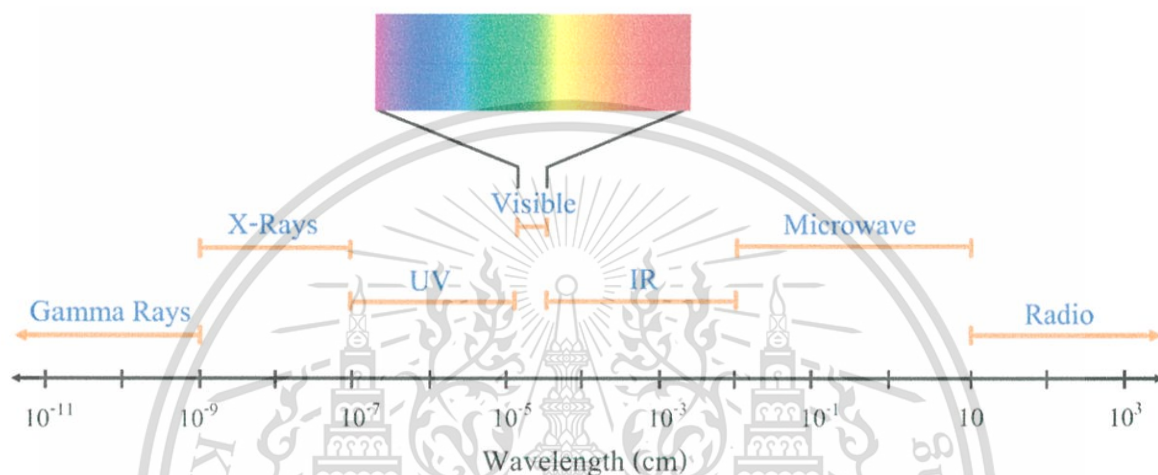


Figure 2.1 A graphical representation of the electromagnetic spectrum.

1. **Gamma radiation:** is generated by radioactive atoms and in nuclear explosions, and used in many medical applications.
2. **X rays:** are high-energy waves, which have great penetrating power and are used extensively in medical applications and weld inspection.
3. **Ultra violet (UV):** is electromagnetic radiation at wavelengths shorter than the violet end of visible light, (400 nm to 10 nm), and is used in fluorescence.
4. **Visible light:** is electromagnetic radiation at wavelengths that the human eye can see. This radiation is perceived as colors ranging from red (longer wavelengths; ~ 700 nanometers) to violet (shorter wavelengths; ~ 400 nanometers).

5. **Infrared radiations:** are electromagnetic waves with wavelengths longer than the red end of visible light and shorter than microwaves (roughly between 1 and 100 microns).
6. **Infrared spectrum:** is divided into three regions: far infrared (in the wavenumber range of $400\text{-}100\text{ cm}^{-1}$), mid infrared (in the wavenumber range of $4,000\text{-}400\text{ cm}^{-1}$), and near infrared (in the wavenumber range $14,285\text{-}4,000\text{ cm}^{-1}$), where wavenumber = $1/\lambda$ (cm). The majority of infrared applications in biological samples employ the mid infrared region [19].
7. **Microwave:** has a longer wavelength (between 1 mm and 30 cm) than visible light.
8. **Radio:** has the lowest frequency and longest wavelength (less than one centimeter to tens and hundreds of meters), and is produced by charged particles moving back and forth.

Table 2.5 Summary of electromagnetic radiation

Region	Wavelength (cm)	Wavenumber (cm^{-1})	Frequency (Hz)	Energy (eV)
Radio	> 10	< 0.1	$< 3 \times 10^9$	$< 10^{-5}$
Microwave	$10 - 0.01$	$0.1 - 100$	$3 \times 10^9 - 3 \times 10^{12}$	$10^{-5} - 0.01$
Infrared	$0.01 - 7 \times 10^{-5}$	$100 - 14285.7$	$3 \times 10^9 - 4.3 \times 10^{14}$	$0.01 - 2$
Visible	$7 \times 10^{-5} - 4 \times 10^{-5}$	$14285.7 - 25000$	$4.3 \times 10^{14} - 7.5 \times 10^{14}$	$2 - 3$
Ultraviolet	$4 \times 10^{-5} - 10^{-7}$	$25000 - 10^7$	$7.5 \times 10^{14} - 3 \times 10^{17}$	$3 - 10^3$
X-rays	$10^{-7} - 10^{-9}$	$10^7 - 10^9$	$3 \times 10^{17} - 3 \times 10^{19}$	$10^3 - 10^5$
Gamma rays	$< 10^{-9}$	$> 10^9$	$> 3 \times 10^{19}$	$> 10^5$

Light can interact with tissue in various ways by absorbing, scattering, reflecting, and so on [20]. The chemical bonds vibrate when the matter absorbs infrared (IR) radiation. Thus, the existence of chemical bonds is a necessary condition for IR absorbance to take place. A molecule absorbs energy, when the intermolecular distance of two or more atoms changes. This is vibrational energy. There are two oscillations of the atoms, which correspond to the normal modes of vibration: stretching and bending.

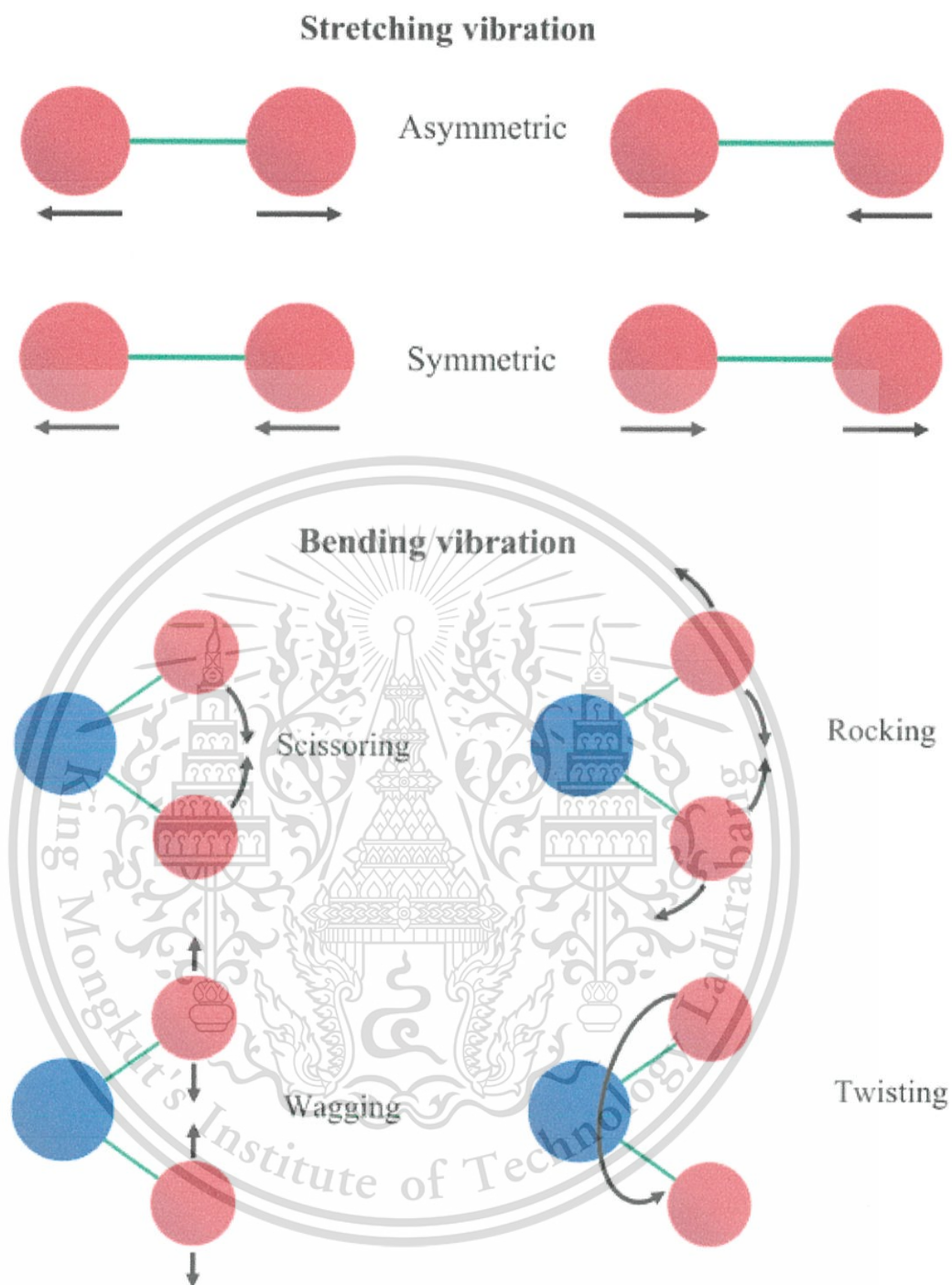


Figure 2.2 Typical vibrational stretching and bending modes.

Stretching is a symmetric or anti-symmetric rhythmical movement along the bond axis. The bending vibration occurs when the bond angle between two atoms, or movement of a group of atoms, changes in relation to the remainder of the molecule. These motions are known as scissoring, wagging, rocking, and twisting. Figure 2.2 shows the stretching and bending modes [19].

The main vibrational spectroscopies [Fourier transform infrared spectroscopy (FTIR) and Raman] are known to be powerful methods in the research of crystalline materials [21]. There are two types of spectroscopy that involve vibrational transitions and rotation. The first is IR spectroscopy, in which transitions between vibrational energy levels of a molecule, induced by absorption of IR radiation, are observed [22]. The second is Raman spectroscopy, which occurs during the scattering of light by molecules [23]. These two methods are used widely to provide information on chemical structures and physical forms, identify substances from characteristic spectral patterns ('fingerprinting'), and determine quantitatively or semi-quantitatively the amount of substance in a sample.

2.3.2.1 Fourier transform infrared spectroscopy (FTIR)

Through quantum mechanical considerations, the vibration of two nuclei in a diatomic molecule can be reduced to the motion of a single particle of the mass, μ , and displacement of q from its position of equilibrium is equal to the change of inter-nuclear distance. The mass, μ , is called the reduced mass and is represented by:

$$\frac{1}{\mu} = \frac{1}{m_1} + \frac{1}{m_2} \quad (2.1)$$

where m_1 and m_2 are the mass of the two nuclei, and displacement of the two atoms from the center of mass can be defined by:

$$\mu \frac{d^2 R}{dt^2} = -kR \quad (2.2)$$

where R is the total distance between the two atoms. Quantum mechanical treatment [24] shows the energy levels given by:

$$E_{vib} = (n+1)h\nu \quad (2.3)$$

where h is Plank's constant, and n is the quantum number, which has only positive integers. In order to absorb a photon and excite it to a higher vibrational state, the molecular energy difference should be equal to the photon energy. This condition can be achieved if the quantum number changes by ± 1 . This condition is known as the selection rule for molecule vibration [25]. The selection rules for vibrational and rotational transitions are [24]:

$$\Delta n = \pm 1, \Delta l = \pm 1 \text{ and } \Delta m = \pm 1 \text{ or } 0. \quad (2.4)$$

For vibrational transitions, the matrix element is calculated as:

$$\varepsilon_{n \rightarrow m} = \left| \int \psi_m^* \bar{\mu} \psi_n dr \right| \quad (2.5)$$

where μ represents the difference between the dipole moment of the ground and excited state. The dipole moment can be written as a Taylor series expansion as follows:

$$\bar{\mu}(r) = \bar{\mu}_0 + \frac{d\bar{\mu}}{dr} r + \frac{1}{2} \left[\frac{d^2 \bar{\mu}}{dr^2} \right] r^2 + \dots \quad (2.6)$$

According to characteristics of the wave function, ψ , the first component of the dipole moment in equation 2.5 contributes to a zero matrix element. In order to obtain a non-zero matrix element, there must be a change in the dipole moment during transition ($d\mu/dr \neq 0$).

IR radiation can be absorbed by a molecule possessing a permanent dipole moment. The frequency of IR radiation has the same values as the frequency of a dipole

moment change. Furthermore, infrared and Raman activity of particular molecules or polyatomic ions depend solely on the point group. It is assumed usually that factor group splitting of molecular or ion vibration in crystals originates essentially from dipole-dipole interaction. Thus, selection rules and symmetry classifications of crystal containing molecular groups are derived from factor group analysis [26]. The symmetric site of molecules in crystals is generally a subgroup of the free molecular point group. A change in the effective site group of molecules affects vibrational behavior by taking the dynamic nature of surrounding molecules into account.

2.3.2.2 Raman scattering spectroscopy (Raman)

Raman scattering is a promising technique for following the change in a chemical environment of metal phosphate structures or molecular species during the course of the reaction. From the fact that Raman bands generally reflect bond lengths and bond strengths, as well as the overall symmetry of molecules, a particular Raman spectrum can be used as a fingerprint for identifying each molecular species present in any state: gas, solution or solid (whether in crystalline or amorphous phase).

The Raman scattering process relies on inelastic scattering of monochromatic and coherent light, known as incident electromagnetic radiation.

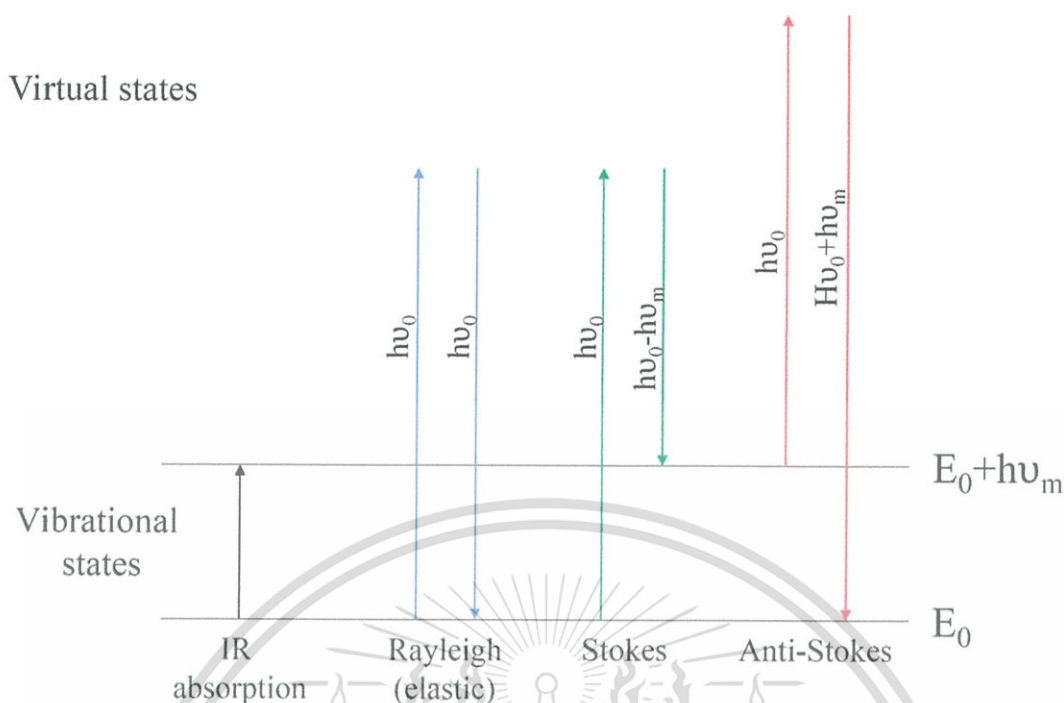


Figure 2.3 Transitions for the scattering process: IR absorption, Rayleigh, Stokes and anti-Stokes scattering.

The effect of Raman involves molecular vibration and must be accompanied by changes of polarizability ellipsoid in either shape or size. When excitation energy is equal to vibration energy, a quantum of radiation may be absorbed or emitted. These phenomena are known as IR absorption and stimulated emission, respectively, whereas, a scattering process generally occurs when the excitation energy is much higher than the vibration energy (Fig. 2.3). A molecule will be excited to a virtual state with an excited light quantum, and relax to an excited state by emitting a secondary light quantum of the same or different energy. Generally, the exciting light quanta are scattered elastically, giving rise to so-called Rayleigh scattering. Inelastic scattering, known as Raman scattering, also was observed, but with more than a million times less probability than Rayleigh scattering. The inelastic interaction of a primary light quantum with a molecule in the vibrational ground state gives Stokes lines, which are a secondary light quantum of lower

energy (or frequency). If a molecule is not in its ground state, the interaction of a primary light quantum may produce a secondary light quantum of higher energy, thus giving anti-Stokes lines. Since the intensity of Rayleigh scattering is several orders of magnitude higher than that of the Raman lines, the use of an intense monochromatic and coherent light, *i.e.* ultraviolet, visible or near IR lasers as exciting sources, is necessary.

Selection rules of IR and Raman activities, and the number of symmetry species, are derived from a correlation of three irreducible representations, namely, for point group symmetry of an isolated molecule, site group symmetry, and unit cell symmetry, which is isomorphous with the factor group [27]. The number of IR-active and Raman-active modes of vibration can be derived from irreducible representations, which can be obtained from crystallographic data. The number of internal modes is equal to $(3n-6)Z$ (Z is the number of formula units per unit cell, and n is the number of atoms in a vibrating unit) [28].

The published FTIR and Raman spectra are assigned on the basis of changes in symmetry through the series, PO_4^{3-} , $\text{P}_2\text{O}_7^{4-}$ and M-O. The nature of phosphate vibrations, pyrophosphates and the metal oxide group can be illustrated, as shown in Table 2.6, which derived from the site group method of Halford [29]. The fundamental normal vibrations (ν_1 , ν_2 , ν_3 , and ν_4 in the Herzberg notation) of the free ion correlate with its vibrations in the crystal. The free PO_4^{3-} ion has four normal vibrational modes of a tetrahedral ion, which are ν_1 symmetric stretching $\nu_s(\text{PO}_3)$; ν_3 asymmetric stretching $\nu_{as}(\text{PO}_3)$; and ν_4 and ν_2 bending $\delta(\text{OPO})$ vibrations. All four modes are Raman active, whereas only ν_3 (asymmetric stretching) and ν_4 (out-of plane bending) are IR active. The ν_3 and ν_4 modes are triply degenerate, ν_2 is doubly degenerate and ν_1 is non-degenerate.

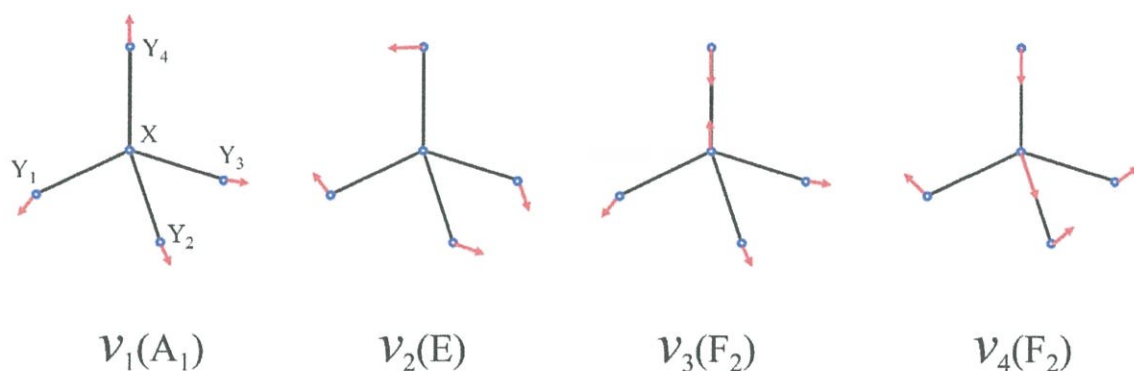


Figure 2.4 Normal modes of PO_4^{3-} ion vibration [30].

Table 2.6 Observed vibrational frequencies of ions in the pyrophosphate species [21, 31]

Ion	Observed frequencies (cm^{-1})	FTIR active	Raman active	Assignment
PO_4^{3-}	1200-1100	vs	vs	$\nu_{\text{as}}(\text{PO}_3)$
	1100-1050	vs	vs	$\nu_{\text{s}}(\text{PO}_3)$
	1050-1000	vs	vs	$\nu_{\text{as}}(\text{PO}_3)$
	650-280	s	s	$\delta(\text{OPO})$
$\text{P}_2\text{O}_7^{4-}$	980-950	s	vw	$\nu_{\text{as}}(\text{POP})$
	760-730	m	w	$\nu_{\text{s}}(\text{POP})$
Metal oxide	260-160	-	w	$\nu(\text{M-O})$
	200-100	-	m	Lattice vibration
	1250-1200	-	w	α -phase characteristic

vw: very weak, w: weak, m: medium, s: strong and vs: very strong

2.4 Physical properties

Some excellent reviews on the properties of metal phosphates deal with structural, morphological, electrochemical, and other physical properties. Nevertheless, little attention has been paid to synthesis procedures. Therefore, this study tried to summarize details for structure-properties of metal pyrophosphate powders, in the hope that it would be of use for understanding the relationship between crystal structure and property research.

2.4.1 Dielectric properties

Electrical insulator materials that prevent the flow of current in an electrical circuit have been used since the beginning of electrical science and technology. Dielectrics are insulating materials that exhibit the property of electrical polarization, thereby modifying the dielectric function of a vacuum.

The first capacitor, known as the Leyden jar, was constructed by Cunaeus and Mussachenbroek in 1745 [32]. However, no studies on the properties of insulating materials were performed until 1837. Faraday published the first numerical measurements of these materials, which he called dielectrics [33]. He found that condenser capacity was dependent on the nature of the material separating the conducting surface. This discovery encouraged further empirical studies of insulating materials, which aimed at maximizing the amount of charge that can be stored by a capacitor. Throughout most of the 19th century, scientists searching for insulating materials for specific applications had become increasingly concerned with the detailed physical mechanism governing the behavior of these materials. In contrast to the insulation aspect, the dielectric phenomena have become more general and fundamental, as they originate from dielectric polarization.

When a dielectric slab is placed in a static electric field, it acquires a surface charge. The polarization so induced arises from the alignment of electric dipoles (if present) and the displacement of positive and negative charges in the dielectric. For an isotropic, linear dielectric, the polarization vector P is proportional and parallel to the applied field vector, E . The electric flux density, or electric displacement, D , is defined by (in cgs units):

$$D = E + 4\pi P = \epsilon E \quad (2.7)$$

where ϵ is the static dielectric constant of the medium. From eq. (2.7), eq. (2.8) follows:

$$\epsilon = 1 + 4\pi\chi \quad (2.8)$$

where χ ($= P/E$) is the susceptibility. Regarding isotropic dielectrics, ϵ and χ are scalar quantities, which are dependent on the molecular properties of the dielectric. The dielectric constant is determined by the polarizabilities of the lattice. The polarizability, α , of an atom (or molecule) is defined by:

$$\mu = \alpha F \quad (2.9)$$

where μ is the electric dipole moment and F is the local, or effective field acting on a given atom. The polarization, P , is defined as the net dipole moment per unit volume, and is given by:

$$P = \sum_i N_i \mu_i = \sum_i N_i \alpha_i F \quad (2.10)$$

where N_i is the number of dipoles per unit volume. The local field, F , at the given lattice site, i , is generally written as:

$$F_i = E + E_{\text{int}} = E + 4\pi \sum_j \phi_{ij} P_j \quad (2.11)$$

where E is the applied field, and E_{int} is the internal field acting on the ion, i , due to the other ion, j , which is expressed usually as a power series in odd powers of polarization. For small field measurements, however, only the first power term in polarization needs

to be considered, as indicated in Eq. (2.11), where ϕ_{ij} is the internal field coefficient, which is a dimensionless quantity that depends on the position of the ion in the lattice.

For anisotropic dielectrics, ϵ , χ and α are tensors, and Eq. (2.7) must be written as:

$$D = \epsilon E \quad (2.12)$$

with components:

$$D_j = \sum_{i=1}^3 \epsilon_{ij} E_i, (i=1,2,3) \quad (2.13)$$

All other quantities follow similarly. When the dielectric is subjected to an alternating field, both D and P vary periodically with time. In general, however, D and P cannot follow the field instantaneously. There will always be inertial and energy dissipation effects (losses) that cause a lag in phase between E and the response of the material. Thus, if:

$$E = E_0 \cos \omega t \quad (2.14)$$

then
$$D = D_0 \cos(\omega t - \delta) \quad (2.15)$$

where δ is the angle loss, which is independent of E_0 , but generally depends on frequency. In the presence of dielectric losses and relaxation effects, ϵ and χ are complex quantities composed of charging (real) and lost (imaginary) components. Thus:

$$\epsilon^* = \epsilon' - i\epsilon'' \quad (2.16)$$

and

$$\chi^* = \chi' - i\chi'' \quad (2.17)$$

The angle loss is given by $\tan \delta = \epsilon'' / \epsilon'$

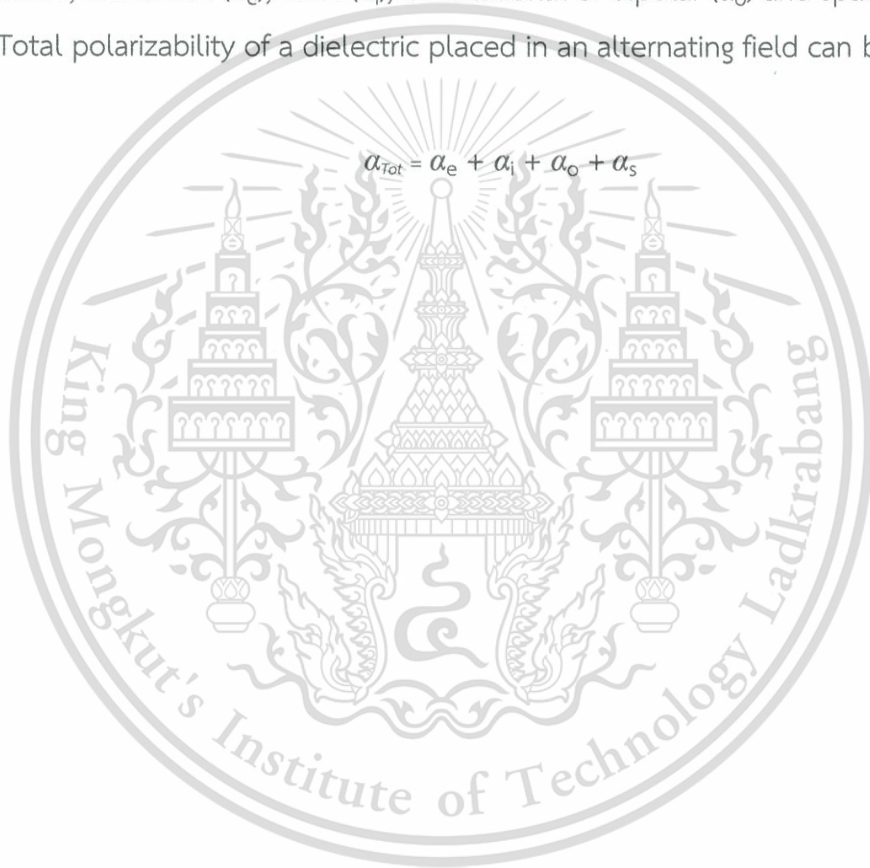
This simply relates to the Q-factor of the dielectric by $Q = 1/\tan \delta$, and is obtained rather directly from the experiment. Then, ϵ' and ϵ'' are related, at any given frequency, by Kramers- Kronig dispersion relations.

2.4.1.1 Frequency Dependence of Polarization

Polarization occurs due to several atomic mechanisms. For example, an atom placed inside an electric field can be considered. The center of a positive charge is displaced along the applied direction of the field, while the center of a negative charge is displaced in the opposite direction, thus, a dipole is produced. When a dielectric material is placed inside an electric field, such dipoles are created in all of the atoms inside. This process of producing electric dipoles, which originate along the field direction, is called polarization in dielectrics. There are several types of polarization mechanisms, and the basic ones are; electronic (α_e), ionic (α_i), orientational or dipolar (α_o) and space charge (α_s) (Fig.2.5). Total polarizability of a dielectric placed in an alternating field can be written as:

$$\alpha_{Tot} = \alpha_e + \alpha_i + \alpha_o + \alpha_s$$

(2.18)



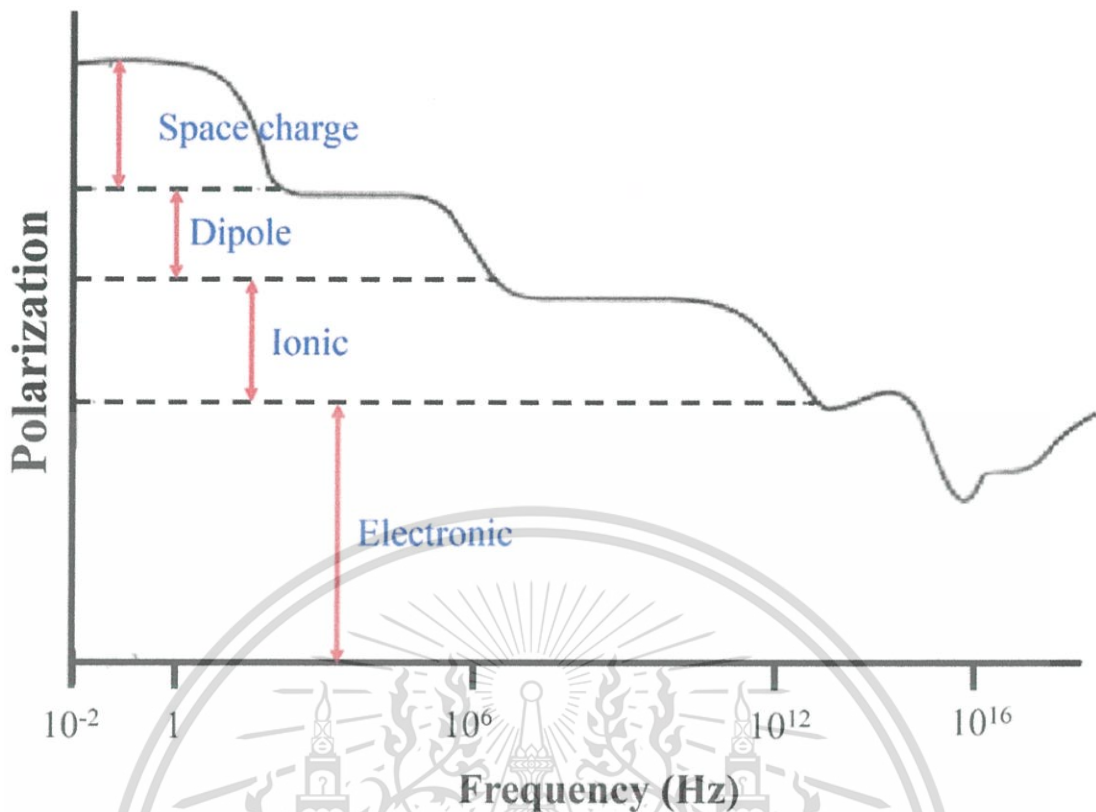


Figure 2.5 Frequency dependence of polarization processes.

Electronic contribution arrives from the displacement of electrons in an atom relative to the deformation of the electron shell around a nucleus by the application of an external electric field. Electronic polarization is extremely rapid. Even when the frequency of the applied voltage is very high in the optical range ($\sim 10^{15}$ Hz), electronic polarization occurs during every cycle of the voltage applied.

Ionic contribution comes from the displacement and deformation of a charged ion with respect to other ions, i.e. ionic polarization is due to the displacement of ions over a small distance, owing to the field applied. Since ions are heavier than electron cloud, the time taken for displacement is longer. The frequency with which ions are displaced is of the same order as the lattice vibration frequency ($\sim 10^{13}$ Hz). This means that ions do not respond to optical frequency, as the time required for lattice vibrations is nearly 100 times

longer than that applied for voltage at an optical frequency. Hence, there is no ionic polarization at optical frequencies. If the frequency of the voltage applied is less than 10^{13} Hz, the ions would respond. Hence, both electronic polarization and ionic polarization respond at 10^{13} Hz.

Orientalional or dipolar polarizability arises when the substance is built of molecules possessing a permanent electronic dipole moment, which may be more or less free to change orientation in the electronic field applied. To clarify, according to Debye, this type of polarization is due to the rotation (orientation) of molecules in polar dielectrics that have a constant dipole moment in direction of the electric field applied. Orientalional polarization is even slower than ionic polarization. The relaxation time for orientational polarization in a liquid is less than that in a solid. For example, it is 10^{-10} s in liquid propyl alcohol, while 3×10^{-6} s in solid ice. Orientalional polarization occurs when the frequency of the voltage applied is in the audio range.

Space charge polarization is the slowest process, as it involves the diffusion of ions over several interatomic distances. The relaxation time for this process is related to the frequency of successful ion jumps under the influence of the field applied, with a typical value being 10^2 Hz. Correspondingly, space charge polarization occurs at lower frequencies (50 – 60 Hz). In considering a dielectric medium placed between two electrodes, with no field applied to the electrode, the positive and negative charges are not separated and the number of charges is fixed. On the other hand, when an electric field is applied, the charges are separated. The positive charges accumulate near the negative electrode. Therefore, a dipole moment is induced due to the displacement of ions. Then, the induced dipole moment per unit volume gives induced polarization, which also is known as interfacial polarization.

In calculating total polarization, space charge polarization is not taken into account, since it occurs as interface and is very small and hence negligible. In addition, the fields are not well defined at interfaces. Therefore, the total polarization vector is given by:

$$P = P_e + P_i + P_o \quad (2.19)$$

where P_e is electronic polarization, P_i ionic polarization and P_o orientational polarization.

2.4.1.2 Dielectric constant

Regarding a unit volume of material containing N atoms, when a dielectric is subjected to the external electric field, E_{ext} , dipole moments are induced inside the material. If P is the dielectric polarization, which is equal to the total dipole moment induced in the material by the electric field, the total polarization is:

$$P = NaE_{\text{local}} \quad (2.20)$$

and the local field can be seen acting on the dipoles as:

$$E_{\text{local}} = E_{\text{Ext}} + 4\pi(P/3) \quad (2.21)$$

where E_{local} is the local electric field, E_{Ext} is the external electric field, and P is polarization.

The dipole moment of the single atom, p , is proportional to the field, $p = \alpha E_{\text{local}}$, where α is electrical polarizability of the atom. The total polarization of an insulator containing N atoms is:

$$\sum_{i=1}^n n_i \alpha_i E_{\text{local}} \quad (2.22)$$

where n_i is the number of i atoms having the polarizabilities, α_i , and being acted on by the local field, E_{local} . Hence, from $\epsilon^* = \epsilon' - i\epsilon''$ equations, the Clausius-Mossotti equation can be obtained by rearranging the terms as follows:

$$\frac{\epsilon_r - 1}{\epsilon_r + 2} = \frac{4\pi}{3} \sum_i n_i \alpha_i \quad (2.23)$$

Expressed polarizabilities are additive, and the additive relation is valid for electronic, ionic and dipolar polarization. Hence, expression can be written in the form of total polarizability. If N is the number of atoms or ions per unit volume, then:

$$\frac{\epsilon_r - 1}{\epsilon_r + 2} = \frac{4\pi}{3} N\alpha \quad (2.24)$$

The above formula gives the Clausius-Mossotti relation.

In other words:

$$\epsilon_r = \frac{3 + 8\pi N\alpha}{3 - 4\pi N\alpha} \quad (2.25)$$

however, $N = 1/V_m$ (V_m : molar volume) which is simplified to:

$$\epsilon_r = \frac{3V_m + 8\pi\alpha}{3V_m - 8\pi\alpha} \quad (2.26)$$

The above expression gives the dielectric constant in relation to the molar volume in \AA^3 , and α gives the total dielectric polarizability of individual ions using Shannon's dielectric polarizability [34].

2.4.2 Optical properties

Color is a property of the coordination complex such as green for $[\text{CoF}_6]^{3-}$, red for $[\text{Co}(\text{NH}_3)_5\text{H}_2\text{O}]^{3+}$, and blue for $[\text{Cu}(\text{NH}_3)_4\text{H}_2\text{O}]^{2+}$. The phenomenon of color can be explained by two theories: the molecular orbital (MO) theory and crystal field theory (CFT) [35, 36]. The MO theory takes a covalent approach, and considers the overlap of d-orbitals with orbitals on the ligands to form molecular orbitals; which is not covered by this research. The CFT takes the ionic approach and considers the ligands as point charges around a positive central metal ion, ignoring any covalent interactions. The negative charge on the ligands is repelled by electrons in the d-orbitals of the metal.

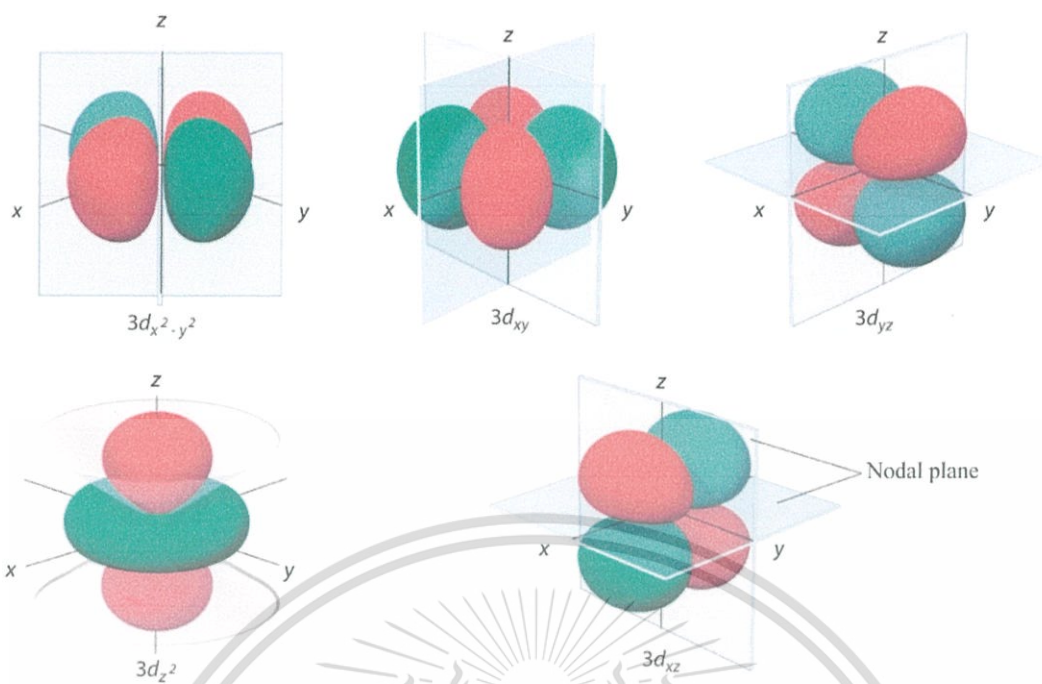


Figure 2.6 The five equivalent 3d orbitals.

Orientation of the d-orbitals, with respect to the ligands around the central metal ion, is important and can be used to explain why the five d-orbitals are not degenerate (= at the same energy).

The concept of the crystal field was first developed by H. A. Bethe in 1929 in order to study the effect of surrounding ions on the electron distribution of a single magnetic ion on a lattice. The CFT has a purely electrostatic approach to bonding within transition metal complexes and was developed to account for spectroscopic properties and coloration of *d*-block metal ions in ionic crystals. The basic idea is that a ligand lone pair is modeled as a point negative charge or part negative charge of an electric dipole that repels electrons in the *d*-orbitals of the central metal ion. The CFT focuses on resultant energy splitting of *d*-orbitals into groups and then using that split to account for the number of unpaired electrons in transition metal complexes. Even though this theory ignores covalent bonding interactions between ligands and central metal ions in transition

metal complexes, it provides a remarkably good qualitative explanation for many of their properties.

Originally, a metal ion in the CFT was thought to be surrounded by a uniform sphere of negative charge with some r radii. This results in elevation of all d orbital energies, but they still remain degenerate. If the negative charge is allowed to collect along the coordinated axes in an octahedral arrangement, electrons in the orbitals pointing along the axes (usually d_{z^2} and $d_{x^2-y^2}$) would be repelled more than those in the orbitals pointing between the axes (usually d_{xy} , d_{yz} and d_{zx}). The former are raised in energy, with the latter lowered relatively to the spherical distribution; and the energy of the two doubly degenerate (e_g) orbitals (d_{z^2} and $d_{x^2-y^2}$) must be raised 1.5 times to equal the three triply degenerate (t_{2g}) orbitals (d_{xy} , d_{yz} and d_{zx}) that are lowered in order to maintain balance. This is named the Barycentre rule [37] and the splitting is named octahedral crystal field splitting energy (Δ_o). The *Gerade* (g) and *Ungerade* (u) are orbitals that do and do not possess a center of symmetry, respectively. The subscript, g , in the t_{2g} and e_g indicates that the orbitals have a center of symmetry in an octahedral field.

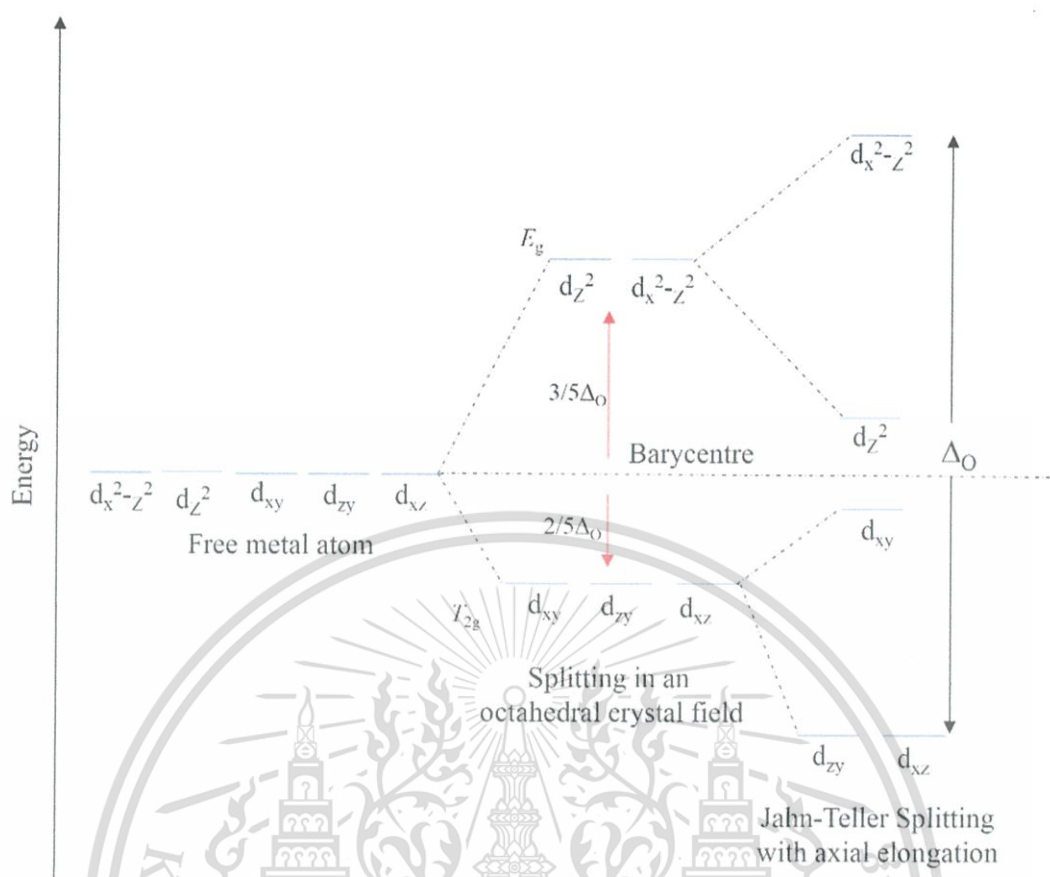


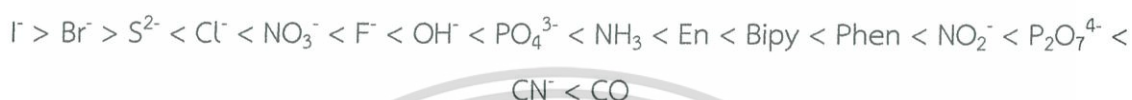
Figure 2.7 Separation of the orbitals into two sets is called the ligand-field splitting parameter, Δ , where the subscript, O, signifies octahedral complexes.

The size of the energy gap between the t_{2g} and e_g levels, Δ_o , depends on 3 factors:

- 1) Oxidation state of the transition metal: as the oxidation state of the transition metal (effectively the charge on the metal) increases, the surrounding ligands are attracted more closely to the metal center, and the orbitals on the ligands interact more strongly with the d -orbitals, and Δ_o increases.
- 2) Row of the transition metal: in continuation from the first to second row of a transition metal triad, an increase of approximately 50% in the size of Δ_o exists, and also another 50% increase from the second to third row. This is due to the fact that while descending,

a transition metal triad the size of the d -orbitals increases ($3d < 4d < 5d$). The larger d -orbitals interact more with the orbitals on the ligands, hence, Δ_o is larger. It should also be noted that the pairing energies for the larger d -orbitals are smaller, which means that low spin configurations are favored.

3) Ligand: the size of Δ_o depends on the ligand(s) present according to the **spectrochemical series**. Ligands generating a weaker ligand field are to the left in the series and those generating a stronger one are to the right.



It is also possible to arrange the metals according to a spectrochemical series. The approximate order is:



A possible explanation for this series is the narrowing ionic radii from left to right across a period in the periodic system, which causes bonding between the ligand and metal central ion in order to increase in strength. This series also is thought to reflect the improved metal-ligand bonding of more expanded $4d$ and $5d$ orbitals, when compared with compact $3d$ orbitals. In general, $4d$ and $5d$ metals have larger Δ_o -values than $3d$ metals. Hence, complexes of these metals generally have the characteristic of electron configurations in strong ligand fields.

In 1937, H. A. Jahn and E. Teller put forward a theorem, which explained some of the distortions observed in transition metal complexes [38]. This became known as the Jahn-Teller theorem, which states:

"For any non-linear molecule in an electronically degenerate state, distortion must occur to lower the symmetry, remove the degeneracy and lower the energy."

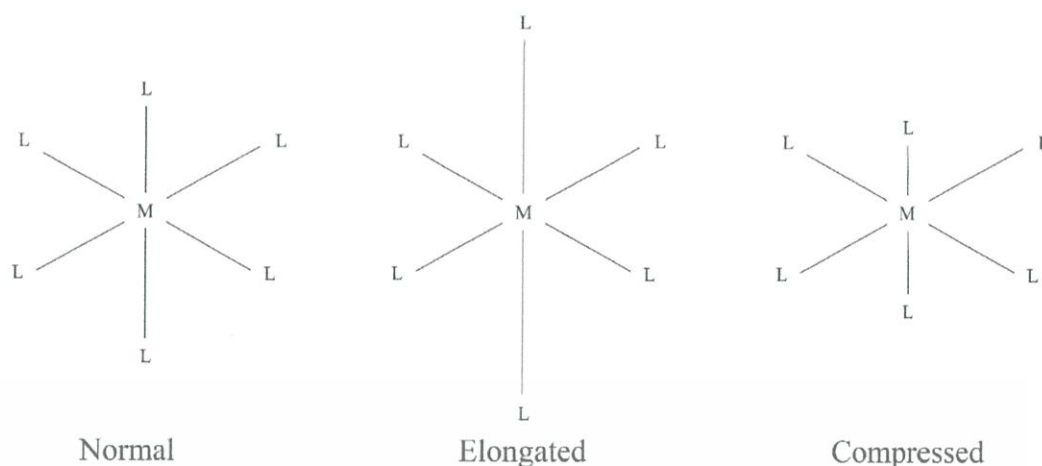


Figure 2.8 Jahn-Teller distortions for an octahedral complex.

This is observed most commonly with transition metal octahedral complexes, however, it can be seen in tetrahedral compounds as well. For a given octahedral complex, the 5d atomic orbitals are split into two degenerate sets when constructing a molecular orbital diagram. These are represented by the symmetry labels: t_{2g} (d_{xz} , d_{yz} , d_{xy}) and e_g (d_{z^2} and $d_{x^2-y^2}$) of the sets. When a molecule possesses a degenerate electronic ground state, it distorts (Jahn-Teller effect) to remove the degeneracy and form a lower energy (and by consequence, lower symmetry) system. The octahedral complex either elongates or compresses the z ligand bonds, as shown in Figure 2.8.

When an octahedral complex exhibits elongation, the axial bonds are longer than the equatorial ones. The reverse applies for compression; when the equatorial bonds are longer than the axial ones. Elongation and compression effects are dictated by the amount of overlap between the metal and ligand orbitals. Thus, this distortion varies greatly depending on the type of metal and ligands. In general, the stronger the metal-ligand orbital interactions are, the greater the chance of a Jahn-Teller effect appearing.

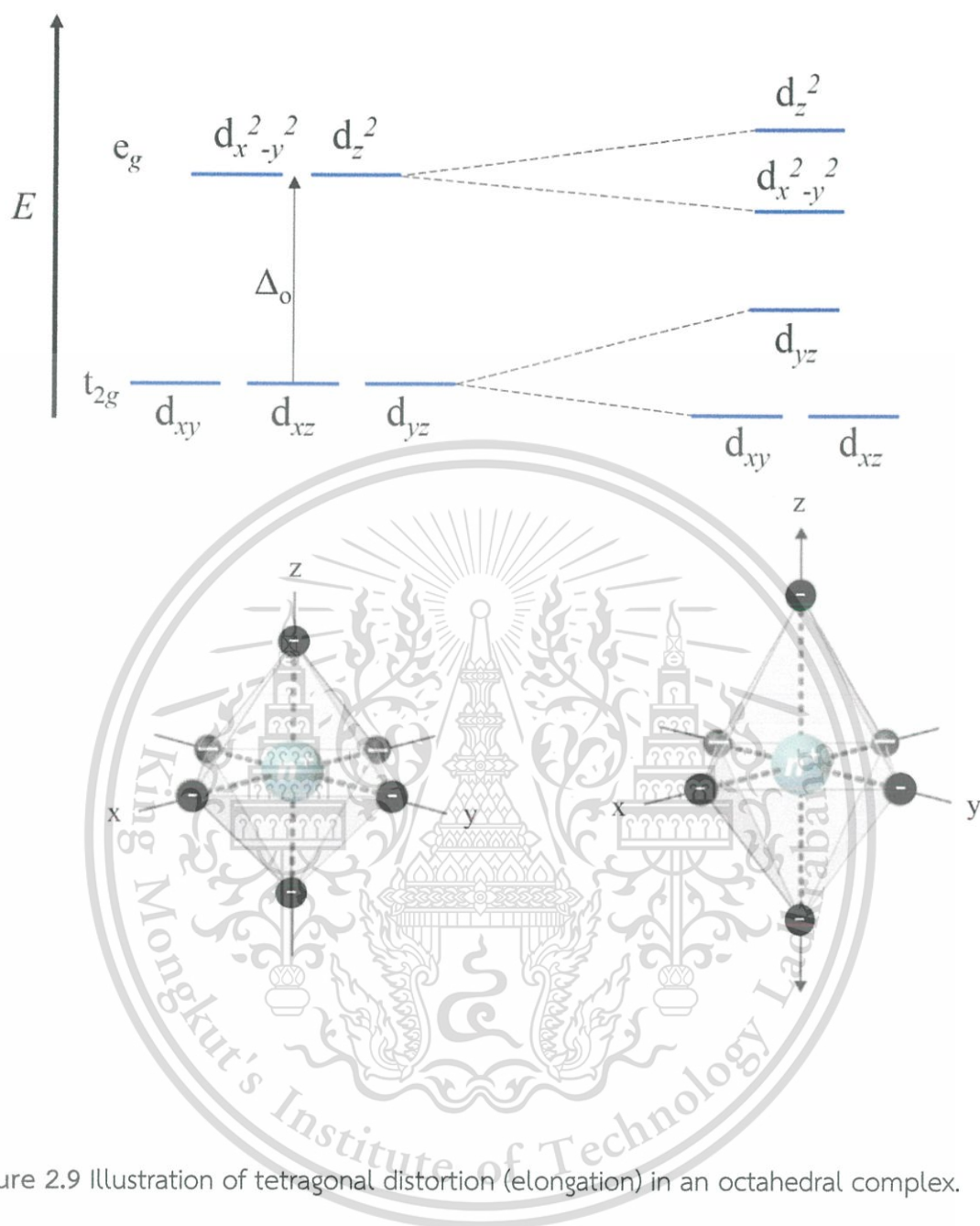


Figure 2.9 Illustration of tetragonal distortion (elongation) in an octahedral complex.

Elongated Jahn-Teller distortions occur when degeneracy is broken by the stabilization (lowering in energy) of d orbitals with a z component, while orbitals without a z component are destabilized (higher in energy), as shown in Figure 2.9.

This is due to d_{xy} and $d_{x^2-y^2}$ orbitals having greater overlap with ligand orbitals, resulting in the orbitals being higher in energy. Since the $d_{x^2-y^2}$ orbital is antibonding, it is expected to increase in energy due to elongation. The d_{xy} orbital is still nonbonding, but is destabilized due to the interactions.

2.4.2.1 Color of matter

Coordination compound complexes are colored because they absorb light in a visible region. The color observed (or transmitted) is complementary to that of the light absorbed. The visible part of the electromagnetic spectrum contains a light wavelength of 380-750 nm. The colored wheel below gives information on the wavelength of different colors and also the complementary color. If light from the yellow-green part of the spectrum is absorbed, the color observed would be a white light with yellow-green subtracted, which is violet.

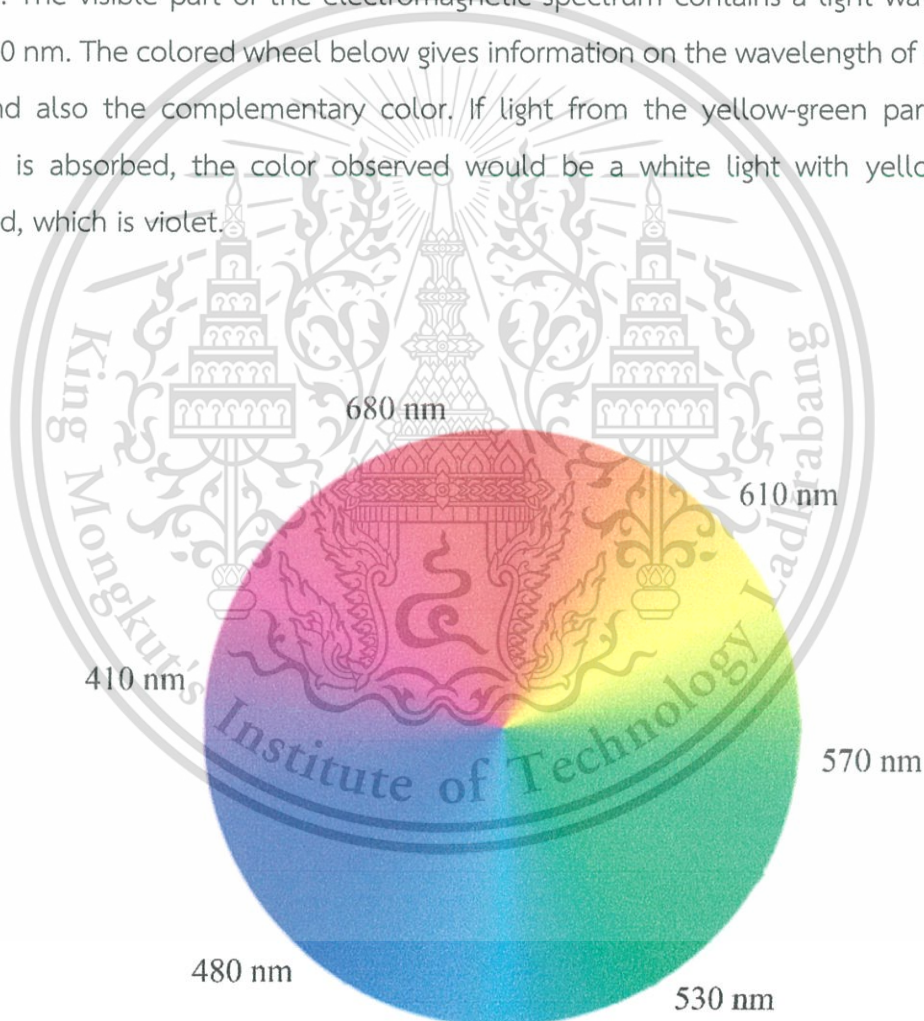


Figure 2.10 Wavelengths of colors and complementary colors.

Table 2.7 Absorbed and transmitted color

Color of light absorbed		Color of light transmitted	
Wavelength ranges (nm)	Color	Color	Wavelength ranges (nm)
380-420	Purple	Yellowish green	500-550
420-440	Bluish purple	Yellow	550-580
470-500	Greenish blue	Red	620-780
500-550	Yellowish green	Purple	380-420
550-580	Yellow	Bluish purple	420-440
580-620	Orange	Blue	440-470
620-780	Red	Greenish blue	470-500

2.4.2.2 Color conversion theory

Digital images are often given in red-green-blue (RGB), but RGB is not always a convenient space for image processing. Splitting RGB colors into their luminance and chrominance, and performing the opposite, are very common operations when it comes to image filtering.

The Yxy encoding is a very good solution, due to its strong physical/perceptual background. It can go from RGB to XYZ (selecting a certain color-space transform matrix), and then from XYZ to Yxy using the following formulas:

$$x = \frac{X}{X+Y+Z} \quad (2.27)$$

$$y = \frac{Y}{X+Y+Z} \quad (2.28)$$

The inverse transform that goes from Yxy to XYZ is given by the following formulas:

$$X = Y \cdot \frac{x}{y} \quad (2.29)$$

$$Z = \frac{X}{x} - X - Y \quad (2.30)$$

The color-space transform matrix that turns RGB values into XYZ ones (and its inverse) is a simple 3x3 affine transform matrix. The exact values of the matrix depend on the color-space working in. For example, the matrix for standard red-green-blue (sRGB) can be found on the Wikipedia sRGB page. Actually, a custom RGB-to-XYZ matrix can be built by defining the xy coordinates of the three primary colors (R, G, and B), and position of the white-point. The Wikipedia sRGB page presents an excellent explanation of this by Ryan Juckett. XYZ colors, and the Yxy encoding have some very interesting practical properties and some of them are illustrated in Figure 2.11.

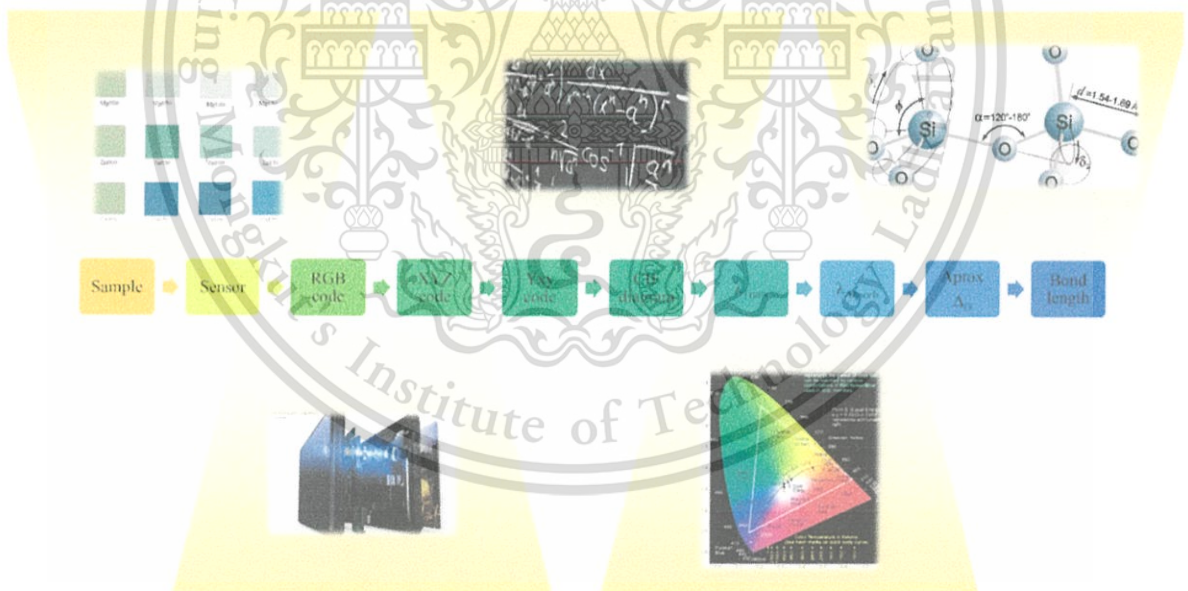


Figure 2.11 Summarized method of color and bond length relation.

2.5 Phase formation and evolution

One of the goals in material science is to understand the mechanism and atomic evolution of phase formation for engineering materials. The thermogravimetry (TG) technique combining X-ray diffraction (XRD) can track the change in a sample when the chemical reacts. TG analysis is a thermal technique available for characterizing the thermal properties of materials such as activation energy (E_a) and the pre-exponential factor (A) [39]. TG is determined as a function of temperature and/or time. The resulting mass-change versus temperature curve (thermogram) provides information concerning thermal stability and composition of the initial sample, thermal stability and composition of any intermediate compounds formed, and composition of residue, if any. The typical thermogram is shown in Figure 2.12.

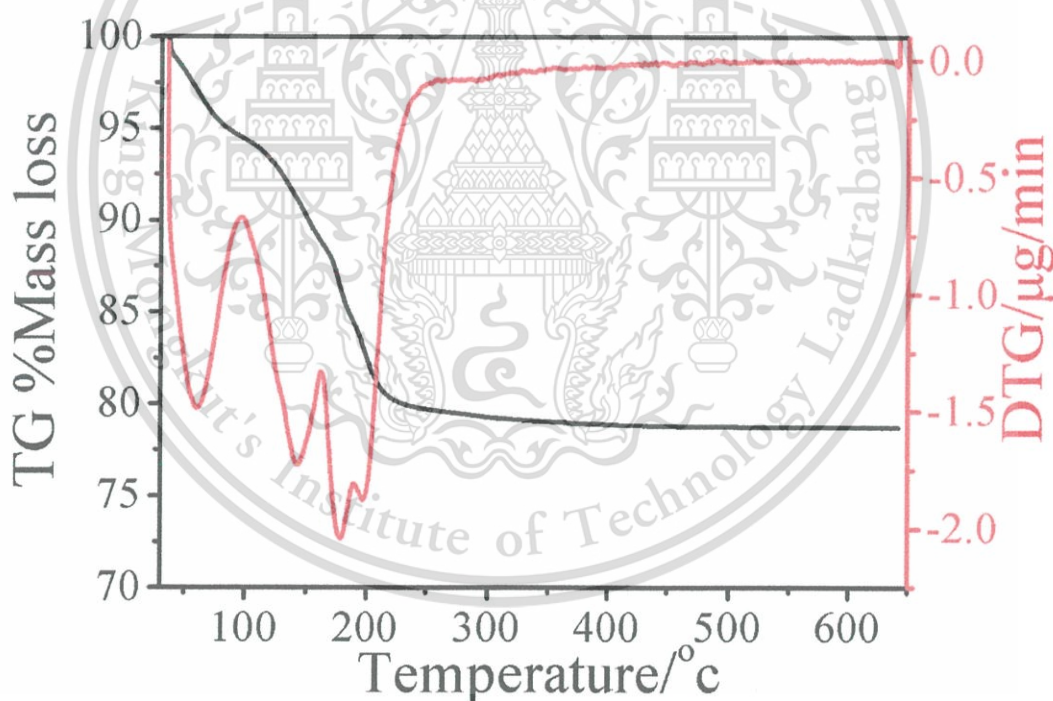
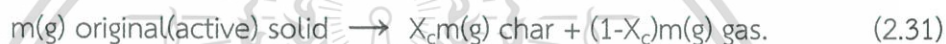


Figure 2.12 Example of a typical thermogram.

The form of the TG curve obtained experimentally is dependent on the interplay of two major factors: (1) the properties of the sample, and (2) the actual experimental conditions used, also called procedural variables. It is possible to predict a theoretical mechanism if the parameters and intermediate substances are known from the XRD result, on the assumption that heat transfer is instantaneous and no temperature gradient exists within the sample.

To explain the thermal decomposition of a solid, the stoichiometry, reaction rate of the decomposing material, and mass conservation need to be appreciated. The model for the process is assumed as follows: the decomposing solid is considered as a perfect mixture of original solid fuel (active species, a) and char (c). The chemical stoichiometry is given as follows:



In derivative thermogravimetry (DTG), the derivative of the mass-change with respect to the time, dm/dt , is recorded as a function of time (t) or temperature (T), or:

$$dm/dt = f(T \text{ or } t) \quad (2.32)$$

In other cases, the derivative of the mass-change with respect to the temperature, dm/dT (dT), is recorded as a function of time (t) or temperature (T):

$$dm/dT = f(T \text{ or } t) \quad (2.33)$$

The resulting curve in both cases is the first derivative of the mass-change curve. A series of peaks are obtained, instead of a stepwise curve, in which the areas under the peaks are proportional to the total mass-change of the sample. A horizontal plateau in the TG curve means $dm/dt = 0$. A maximum in the DTG curve is obtained when the TG curve has an inflection point, where the loss of mass is the quickest.

The intermediate information of a phase can be supported by XRD patterns. This technique can be investigated by both qualitative and quantitative analysis. XRD is often used semi-quantitatively to determine the weight fraction of constituents, which can be identified by comparing integrated intensities of the diffraction peaks with each of the known phases. In addition, complex mixtures containing more than two phases also can be quantified. Even if one phase is amorphous, diffraction can still yield a relative amount of each phase. The diffraction pattern includes information of peak positions and intensity. The peak positions are indicative of the crystal structure and symmetry of the contributing phase. The peak intensities reflect total scattering from each plane in the crystal structure of the phase, and are dependent directly on the distribution of particular atoms in the structure [40]. Thus, intensities are related ultimately to both the structure and composition of the phase. The diffraction intensity equation has been studied many times [41-44], and is summarized below;

$$I_{(hkl)\alpha} = \frac{I_0 \lambda^3}{64\pi r} \left(\frac{e^2}{m_e c^2} \right)^2 \frac{M_{(hkl)}}{V_\alpha^2} |F_{(hkl)\alpha}|^2 \left(\frac{1 + \cos^2(2\theta) \cos^2(2\theta_m)}{\sin^2 \theta \cos \theta} \right)_{hkl} \frac{v_\alpha}{\mu_s} \quad (2.34)$$

where:

$I_{(hkl)\alpha}$ = reflection intensity of hkl in phase α .

I_0 = Incident beam intensity.

r = distance from specimen to detector.

λ = X-ray wavelength.

$(e^2/m_e c^2)^2$ = square of classical electron radius.

μ_s = linear absorption coefficient of the specimen.

v_α = volume fraction of phase α .

M_{hkl} = multiplicity of the reflection, hkl , of phase α .

0 = Lorentz-polarization (and monochromator) correction, $\left(\frac{1 + \cos^2(2\theta) \cos^2(2\theta_m)}{\sin^2 \theta \cos \theta} \right)$.

V_α = volume of the unit cell of phase α .

$2\theta_m$ = diffraction angle of the monochromator.

$F_{(hkl)\alpha}$ = structure factor for the reflection, hkl , of phase α (i.e., the vector sum of scattering intensities of all atoms contributing to that reflection).

In recognizing that many of these terms are consistent for a particular experimental setup, the experimental constant, K_e , can be defined. The constant, $K_{(hkl)\alpha}$, can be defined for a given phase that is in effect equal to the structure factor term for phase α . In substituting the weight fraction (X_α) for the volume fraction, the density of the phase (ρ_α) for the volume, and mass absorption coefficient of the specimen (μ/ρ)_s for the linear absorption coefficient, yields the following equation:

$$I_{(hkl)\alpha} = \frac{K_e K_{(hkl)\alpha} X_\alpha}{\rho_\alpha (\mu/\rho)_s} \quad (2.35)$$

This equation describes the intensity for the peak, hkl , in similar terms to those in phase α . The weight fraction, f_1 , can be described as follows:

$$f_1 = \frac{(I_1^{\text{mix}} / I_1^{\text{pure}}) A_2}{A_1 - (I_1^{\text{mix}} / I_1^{\text{pure}}) (A_1 - A_2)} \quad (2.36)$$

where I_1^{mix} and I_1^{pure} are the phase 1 intensities in the mixture and pure material, respectively, and A_1 and A_2 are the mass absorption coefficients.

2.6 Structure refinement

2.6.1 Introduction of X-ray diffraction (XRD)

Crystalline materials show a three-dimensional periodic arrangement of atoms. The X-rays are electromagnetic waves with a wavelength λ , which is in the range of interatomic distances that allow diffraction to occur. If coherent X-ray radiation hits a crystal, the electrons in its atoms induce vibrations, which cause X-ray emission of the same wavelength as that in initial radiation. In some directions the emitted rays interfere constructively, while in others they cancel each other. William Lawrence Bragg gave clarification of this phenomenon [45]. He described XRD as a reflection of X-rays on atomic layers, the so-called lattice planes, which are comparable to light that is reflected by a mirror. In contrast to light, X-rays can penetrate the material and are therefore reflected on several equivalent planes. In order to obtain constructive interference, the path length difference, which occurs when X-rays hit two parallel lattice planes in the distance, d , has to be a multiple of wavelength λ of the radiation. The difference of path length depends on the angle of incidence θ of the X-rays and the distance, d , of the lattice planes:

$$n\lambda = 2d \sin \theta \quad (2.37)$$

As previously stated, X-rays are emitted by the electrons that are bound to atoms and not reflected by planes. Atoms in succeeding planes are not necessarily placed consecutively. A scheme of such a situation can be seen in Figure 2.13. It has been proven that the Bragg equation also is valid in such cases [46].

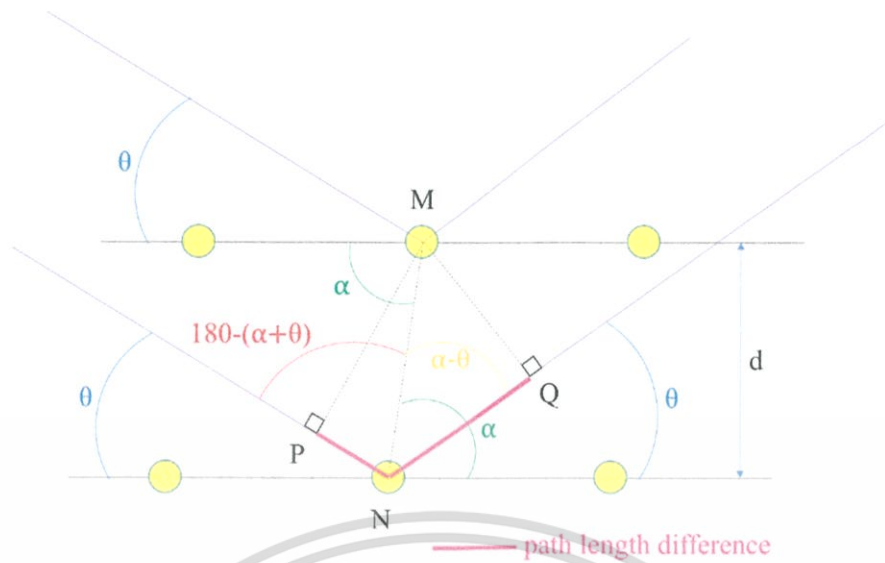


Figure 2.13 Illustration of Bragg's law.

Nevertheless, the difference in path length needs to be a multiple of the wavelength λ . In Figure 2.13, the path length can be described as the two distances, \overline{PN} and \overline{NQ} , which are given by using the distance, \overline{MN} , and the respective angles. This leads to Bloss's equation as follows:

$$n\lambda = \overline{MN} \cos(180^\circ - (\alpha + \theta)) + \overline{MN} \cos(\alpha - \theta) \quad (2.38)$$

$$= \overline{MN} [-\cos(\alpha + \theta) + \cos(\alpha - \theta)] \quad (2.39)$$

$$= 2\overline{MN} [\sin \alpha \sin \theta] \quad (2.40)$$

The distance, \overline{MN} , can be given in terms of the distance, d , of the lattice planes and the angle, α :

$$\overline{MN} = \frac{d}{\sin \theta} \quad (2.41)$$

Use of this equation leads to the Bragg equation:

$$n\lambda = 2d \sin \theta \quad (2.42)$$

That a powder contains small crystallites, ideally of random orientations, is a benefit of powder diffraction, and that is why there are always some crystals that fulfil the Bragg equation. The reflected rays for powders form cones with different apex angles. On a screen perpendicular to direction of the initial beam, the reflected, interfered radiation is located on rings, known as Debye-Scherrer rings. The recorded powder diffraction pattern contains plenty of information about the sample. Position of the peaks, $2\theta_0$, provides information about the crystal system, space group and unit cell dimensions. The integral peak intensities are related to the content of the unit cell. The shape and width of a peak, which is given in terms of the Full Width at Half Maximum (FWHM) or the Integral Breadth² (IB), are influenced by domain size and root mean square micro-strain [47]. Every crystalline material has a characteristic diffraction pattern, allowing for phase identification in a sample. Figure 2.14 shows the components of an XRD pattern of powder. The peak position is determined by the phase symmetry and unit cell parameters. The positions correspond to lattice plane separation distances, as described by the Bragg Equation. Peak position also can be affected by a zero error in the diffractometer. Both instrument and sample effects contribute to the background of an XRD pattern. This can include the sample holder, detector noise, amorphous material and fluorescence of the sample.

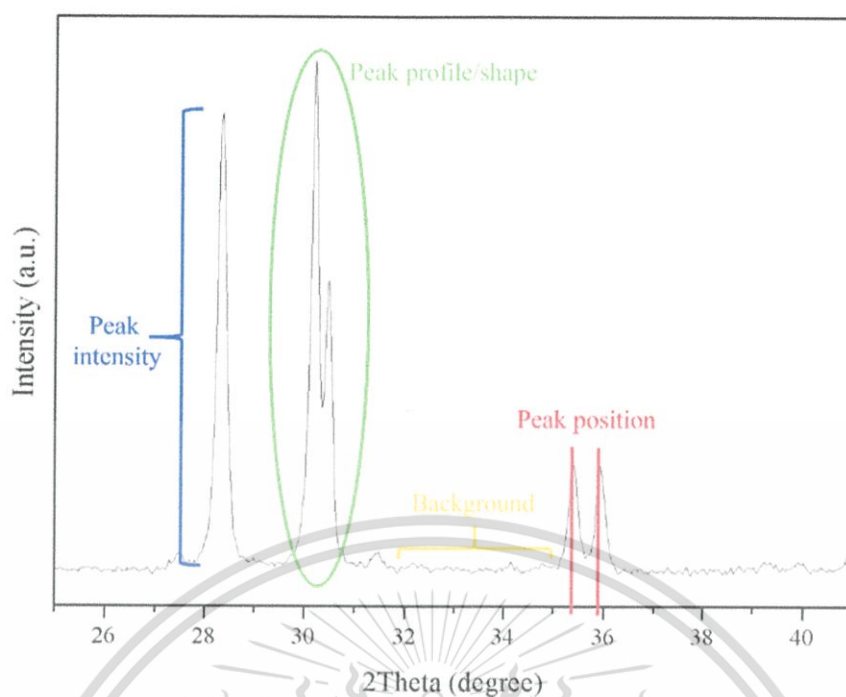


Figure 2.14 Components of a typical XRD pattern of powder.

Nowadays, powder diffraction is used widely for qualitative analysis, quantitative analysis, structure refinement, structure solution and microstructural analysis.

2.6.1.1 Rietveld refinement analysis

The XRD pattern of samples is determined by reflections of given intensity at certain positions. The position, height, and width of these peaks can be used to investigate many characteristics of the material structure. The peak positions corresponding to lattice spacing, and the comparative intensity of the reflections, are indicative of crystalline structures in the case of a 'fingerprint' of the materials. Phase determination can be performed first by comparing the *Powder Diffraction File* (PDF) to a database such as the Inorganic Crystal Structure Database (ICSD), and Joint Committee on Powder Diffraction Standards (JCPDS).

2.6.1.2 Rietveld refinement method

The crystal structure of known materials is refined by using the *Rietveld refinement method*, which was utilized for structural refinement using raw data of both powder X-ray diffraction (PXRD) and powder neutron diffraction (PND). Despite the light source radiation being different while recording data, the refinement method is the same. In all cases, the *best fit* sought is the best least squares fit to all intensities at each step. The quantity minimized in non-linear least squares minimizations is function (M), which summed up all data points as:

$$M = \sum_{i=1}^n w_i (y_i^{obs} - y_i^{calc})^2 \quad (2.43)$$

where w_i is a weighting factor ($w_i = 1/y_i^{obs}$),
 y_i^{calc} is the calculated intensity point i , and
 y_i^{obs} is the observed intensity at equal angular intervals by adjusting model parameters.

A crystal structure model is used to generate a theoretical diffraction pattern that can be matched to the measured profile. The profile was modeled using the integrated intensity at i^{th} step of 2θ by summing up the calculated contributions from the neighboring Bragg reflection, plus the background:

$$y_i^{calc} = \sum_{\phi} S_{\phi} \sum_h M_{\phi,h} \cdot |F_{\phi,h}|^2 \cdot Lp_{\phi,h} \cdot T_{\phi,h} \cdot A_{\phi,h} \cdot \Omega_{i,\phi,h} + y_i^b \quad (2.44)$$

where s_{ϕ} is the scale factor of the phase, ϕ ,

$M_{\phi,h}$ is the multiplicity factor of the h^{th} reflection,

$F_{\phi,h}$ is the structure factor,

$Lp_{\phi,h}$ is the Lorentz-polarization factor,

$T_{\phi,h}$ is the temperature factor (more correctly referred to as the displacement parameter),

$A_{\phi,h}$ is the absorption correction,

$\Omega_{i,\phi,h}$ is the reflection profile function, and
 y_i^b is the background intensity.

The profile function for comparing intensities is performed at every point. It is essential for constructing profile calculation in order to describe the shape of Bragg reflections accurately, i.e. peak shape.

The Lorentzian function of peak shape implies homogeneous broadening by some physical mechanism. The Gaussian function implies a normal distribution, and would be the peak shape expected for a perfect crystal with a single long-range ordering or only instrumental line broadening. The pseudo-Voigt function is a linear approximation of convoluting Gaussian and Lorentzian functions of a peak used for computational purposes. More complicated functions are possible, including those that allow for asymmetric line broadening. Peak broadening may be due also to strain in the sample, which can be incorporated in the refinement model. The profile functions of this thesis are specified in Table 2.8. The peaks are defined by the offset, y_0 , peak center, x_c , peak area, A , FWHM, w , and mixing coefficient, η , which can be refined as a linear function of 2θ .

$$\eta = N_A + N_B(2\theta) \quad (2.45)$$

where N_A and N_B are definable parameters.

The FWHM of powder diffraction is induced by several components including microstructural effects, as stain and size effect; instrumental factors; and the presence of defects. The FWHM (H) can be modeled using the function proposed by Caglioti *et al* [48]:

$$H^2 = U \cdot \tan^2 \theta + V \cdot \tan \theta + W \quad (2.46)$$

The Caglioti U , V and W parameters are all instrument and sample dependent, and the FWHM, w , is related to the Gaussian width, ω , by $\omega = w/\sqrt{\ln(4)}$. The typical Rietveld refinement plot is shown in Figure 2.16.

Table 2.8 The mathematical definitions of peak profile functions

Peak Shape	Function
Lorentzian L(x)	$y = y_0 + \frac{2A}{\pi} \frac{w}{4(x-x_c)^2 + w^2}$
Gaussian G(x)	$y = y_0 + \frac{A}{\omega\sqrt{\pi/2}} e^{-\frac{2(x-x_c)^2}{\omega^2}}$
Pseudo-Voigt	$y = (1-\eta) \cdot G(x) + \eta \cdot L(x)$

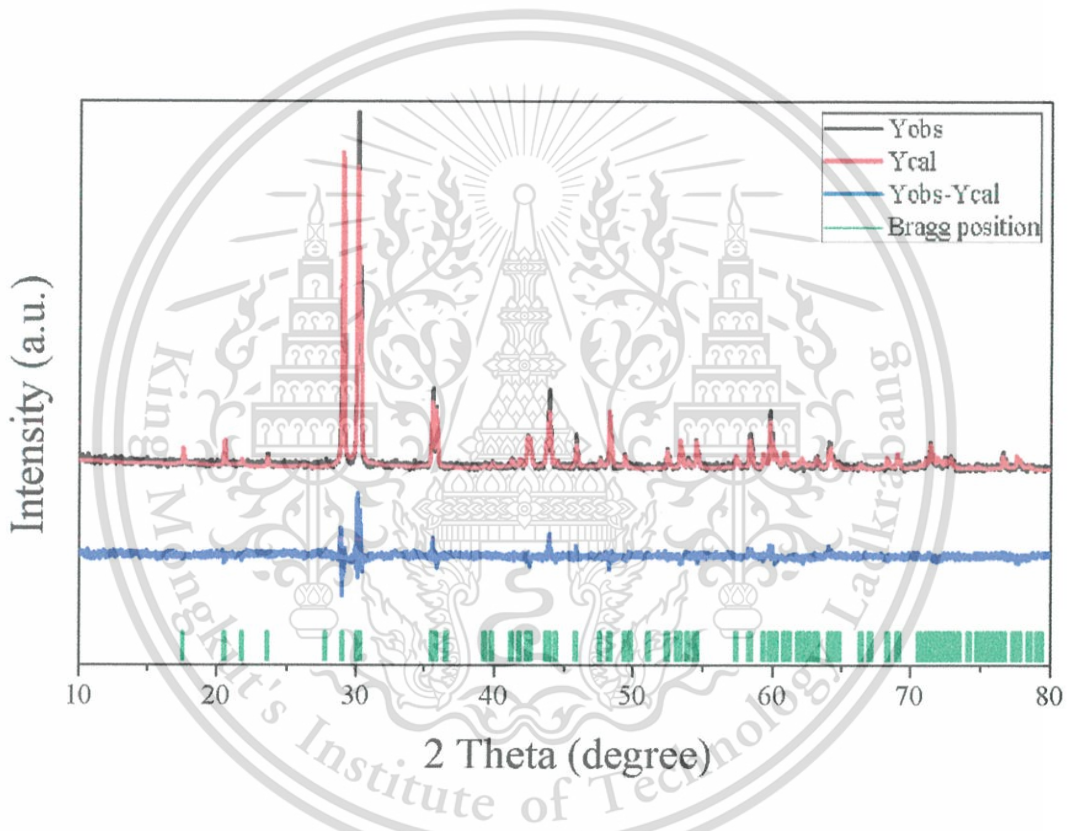


Figure 2.15 Example of a typical Rietveld refinement plot.

The observed intensity data, y_i , are plotted in the upper field as a black line, which represents the c.s.d. counted statistically. The calculated pattern is shown as a red line in the same field. A difference of observed minus calculations is shown in the middle field. The short vertical bars in the lower field indicate the positions of possible Bragg reflections.

2.6.1.3 Agreement factors of Rietveld refinement

Agreement between the calculated and observed profile is considered by the Rietveld refinement of various statistical agreement factors (R-factors), which help to make a quantitative assessment of refinement that includes the profile R-factor, R_p , expected R-factor, R_{exp} , and weighted profile R-factor, R_{wp} [49]. The R_p is defined by the following equation:

$$R_p = \frac{\sum_{i=0}^{n-1} |y_i^{obs} - y_i^{calc}|}{\sum_{i=0}^{n-1} y_i^{obs}} \quad (2.47)$$

The expected R-factor gives a subtracted background measure of the value that would be obtained for a possibly refined based on counting statistics, as follows:

$$R_{exp} = \sqrt{\frac{N - P + C}{\sum_{i=0}^{n-1} w(y_i^{obs})^2}} \quad (2.48)$$

where N is the number of observations,

P is the number of refinable parameters, and

C is the number of constraints.

R_{wp} is the one that reflects the greatest progress in fitting from the mathematical point, because the numerator is the residual being minimized:

$$R_{wp} = \sqrt{\frac{\sum_{i=0}^{n-1} w_i (y_i^{obs} - y_i^{calc})^2}{\sum_{i=0}^{n-1} w_i (y_i^{obs})^2}} \quad (2.49)$$

R_{exp} and R_{wp} can be expressed as a single criterion with a good fit (GOF) or chi-square (χ^2), which is obtained by dividing R_{wp} by R_{exp} :

$$GOF = \frac{R_{wp}}{R_{exp}} = \sqrt{\frac{\sum_{i=0}^{n-1} w_i (y_i^{obs} - y_i^{calc})^2}{M - P}} \quad (2.50)$$

If the nature of fitting in Rietveld refinement analysis has a good fit, the value should be near to unity. The value of R_{wp} must be near the R_{exp} value. The quality of fit also can be approximated visually by examining a plot of the calculated and observed profile fit; for a good fit the difference in lines should be as flat as possible with fluctuations consistent with noise.

2.6.2 X-ray absorption spectroscopy (XAS)

XAS is a widely used procedure for determining the electronic structure and local geometric of matter. The XAS spectrum is especially responsive to the oxidation state, formal coordination number, and distances of the atoms in an instantly selected element environment. XAS can be applied in bulk physical surroundings and different systems. Moreover, it is used usually in an extensive range of scientific fields, including environmental science, catalyst, biology and material science research [50].

The X-ray absorption spectrum can be divided in two parts (Fig. 2.16), XANES or X-ray absorption near-edge spectroscopy, and EXAFS or the extended X-ray absorption fine-structure spectroscopy.

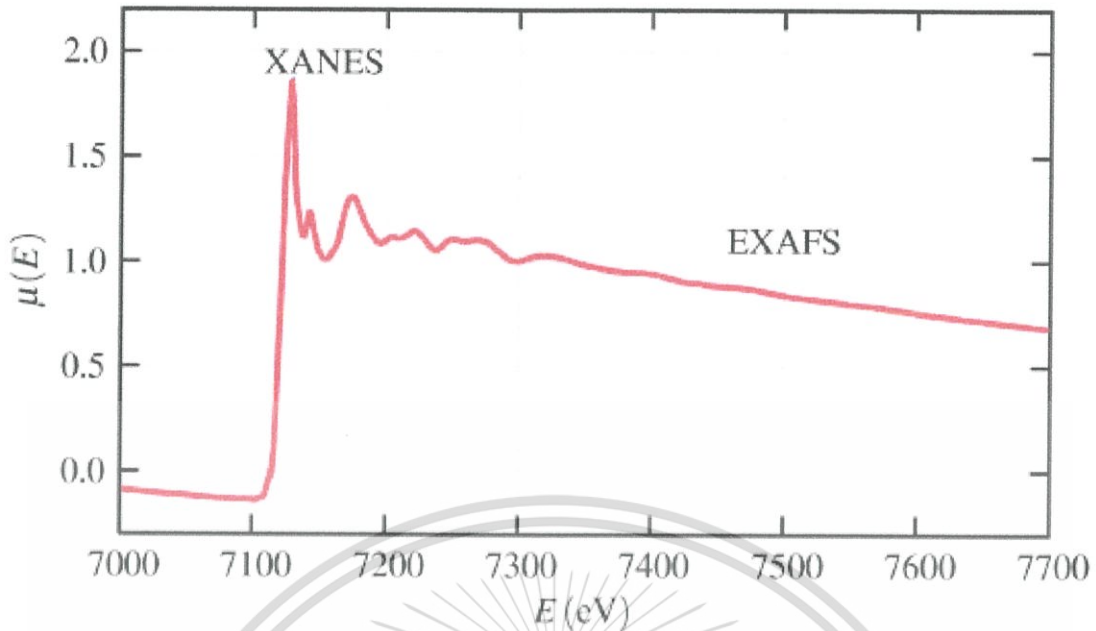


Figure 2.16 Typical X-ray absorption spectrum [50].

It is more a convention than a physical separation, since both have the same origin; but XANES is more responsive to formal oxidation state and coordination number while EXAFS can report the species of the neighbors of the absorbing atom, distances, and coordination number.

2.6.2.1 Theory of X-ray absorption spectroscopy

An X-ray beam travels through material, it is absorbed because the photo-electric effect. This is an interaction between an electron in a quantum core level of an atom and the X-ray photon (Fig. 2.17).

For a particular electron to be excited, the incident energy of the X-ray has to be greater than the binding energy, but due to the nature of X-ray, it is strongly dependent on Z , the atomic number as proposed by this equation:

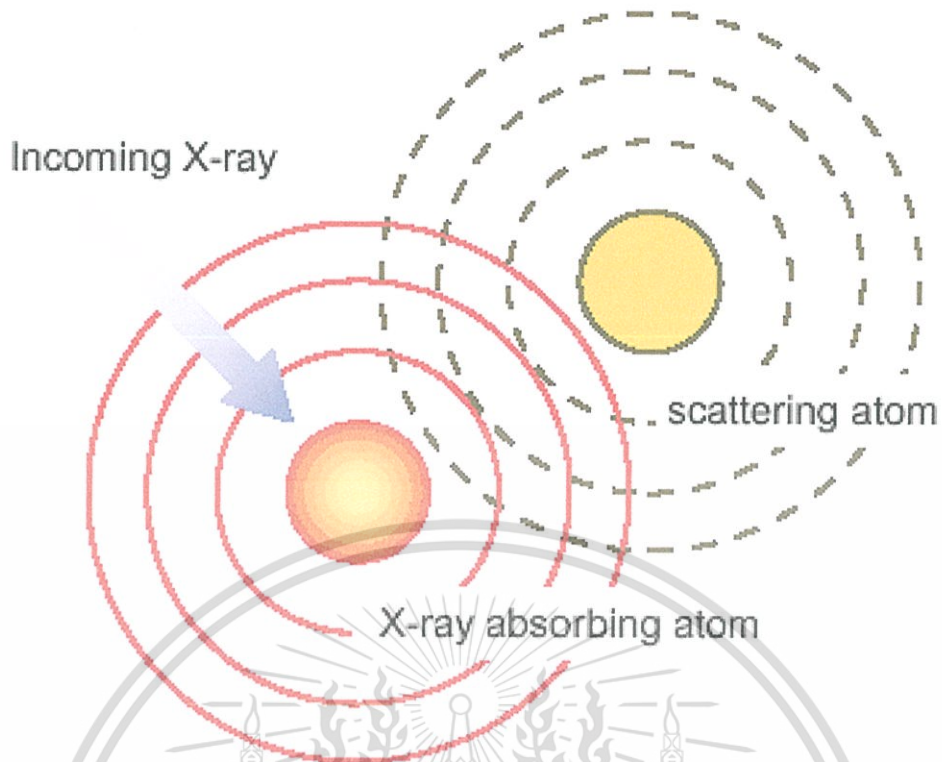


Figure 2.17 The EXAFS phenomenon; outgoing photoelectron of the X-ray absorbed atom and backscattering photoelectron from the adjacent atom [50].

$$\mu = \frac{\rho Z^4}{M_A E^3} \quad (2.51)$$

Where Z is the atomic number of the absorber,
 μ is the absorption coefficient,
 M^A is the atomic mass of the absorber,
 ρ is the sample density,
 E is the X-ray energy.

When the incident X-ray energy matches the binding energy of a core level electron, the absorption rises greatly; it is called the 'absorption edge'. The EXAFS is the measure of change of the absorption coefficient i in function of the energy, just above this

edge. Since every atom has core-level electrons with well-defined binding energies, it allows this technique to be element specific.

The Fourier transform method is a powerful tool for the interpretation of EXAFS. By changing the oscillation into the interatomic distance between the absorber and the scattered (R-space), it gives clear indication about the different coordination spheres around the absorbing atom. Broad peaks visibly correspond to the shell of backscattering atoms, but there is no direct quantification possible since a scattering phase-shift of 0.5 Å is usually present. To obtain quantitative information, a theoretical model is used to fit the experimental data. Many models have been developed for the EXAFS but the simplest theory is the plane wave theory of Lee *et. al.* [51].

$$\chi(\kappa) = \sum_{j=1}^{shells} \frac{N_j}{\kappa R_j} S_0^2 F_j(\kappa) \exp(-2\kappa^2 \sigma_j^2) \exp\left(\frac{-2R_j}{\lambda \kappa}\right) \sin(2\kappa R_j + 2\phi_{abs}(\kappa) + \phi_{scat}(\kappa)) \quad (2.54)$$

where N_j is the number of equivalent backscatterers in each shell,
 S_0^2 is an amplitude reduction factor accounting the absorber multi-excitations,
 $F_j(k)$ is the element specific backscattering amplitude,
 R_j is the interatomic distance between the absorber and the scatterer,
 σ_j^2 is the mean square variation of R_j ,
 λ is the mean-free path,
 $\phi_{abs}(k)$ is the phase shift from the absorber,
 $\phi_{scat}(k)$ is the phase shift from the scatterer.

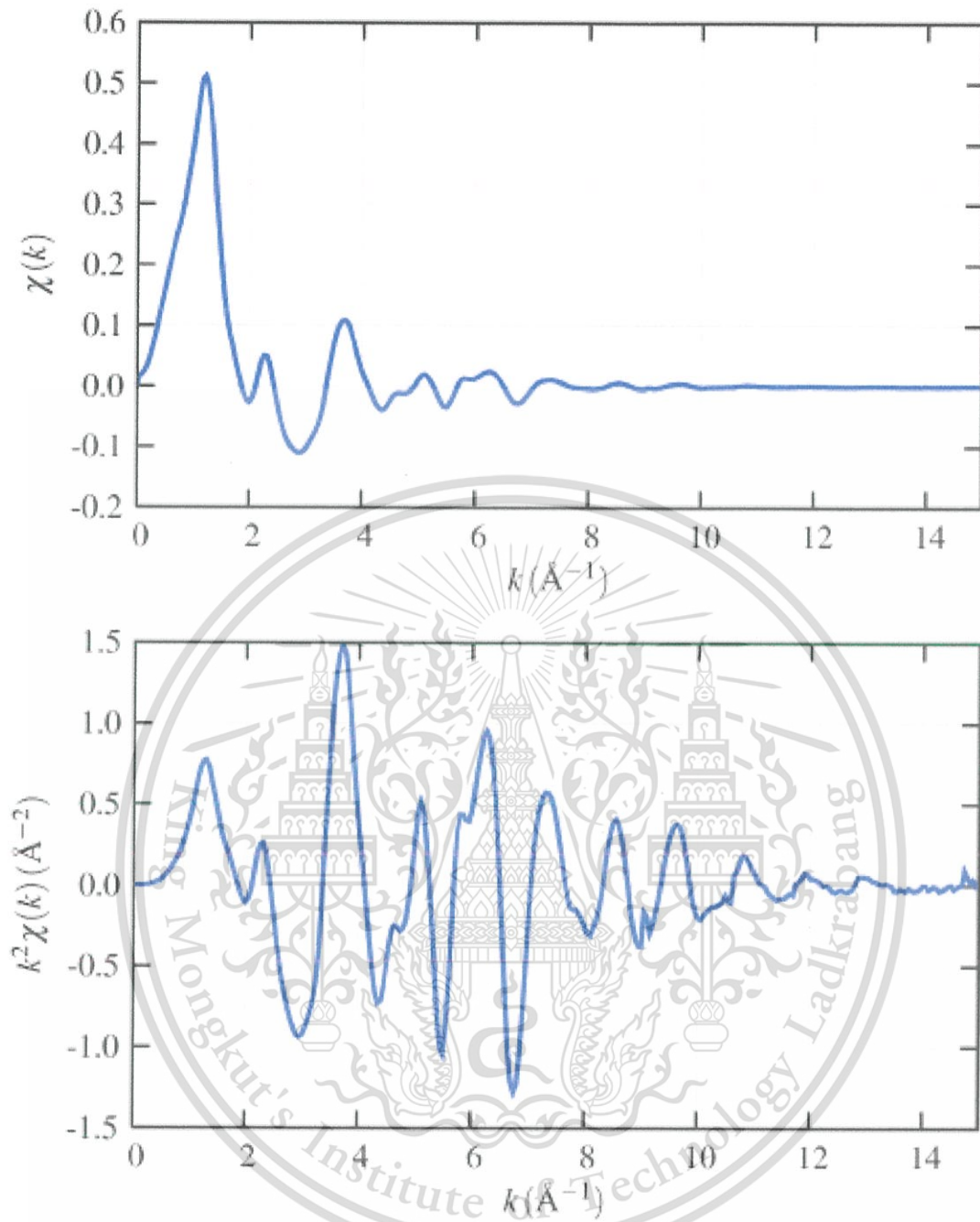


Figure 2.18 The EXAFS phenomenon The $\chi(k)$ EXAFS (top), and the k -weight EXAFS, $k^2\chi(k)$ (bottom) [50].

This model assumes that the outgoing spherical wave can be treated as a plane wave. This approximation considers the backscattering atom to be small compared to the interatomic distance, which is true for most materials. Another assumption which is made is that all backscattering pathways are independent and do not interfere with others. In the EXAFS region, this can be assumed since only a few percent of the total scattering is due to multiple scattering.

2.6.3 Prediction of crystal structure bond strength

For many years structural mineralogists have found Pauling's concept [52] of bond strength, $\langle S_{M-O} \rangle$, and bond valence, $\langle V_{M-O} \rangle$, useful tools in evaluating mineral structures. Recently, the concept has been refined to recognizing the close relationship between bond valence and bond length.

This is a simple but powerful approach for predicting the structure and properties of complex solids and liquids. It can study relationships of bonds between oxygen and As^{5+} , Ge^{4+} , Ga^{3+} , Zn^{2+} , Cu^{2+} , Co^{2+} , Fe^{2+} , Fe^{3+} , Mn^{2+} , Cr^{6+} , V^{5+} , Ti^{4+} , Sc^{3+} , Ca^{2+} , K^+ , S^{6+} , P^{5+} , Si^{4+} , Al^{3+} , Mg^{2+} , Na^+ , B^{3+} , Be^{2+} , Li^+ and H^+ . It is based on the study of a large number of crystal structures and empirical concepts of chemical bonds and atomic valences. The valence of an atom is assumed to distribute between the bonds it forms, and the resulting bond valences correlate well with bond length and other bond properties. Bond valences, determined from experimentally measured bond lengths, are used to calculate atomic valences, which can be used in a number of ways to help in determining and evaluating crystal structures. The properties of bond valence lead to a structure-based scale of Lewis acid and base strength that can be used to predict which structure is likely to be stable and what bonding topologies it might have. Bond valence calculated from bond length can be used through the valence sum rule to calculate experimental atomic valences. Discrepancies between the experimental and theoretical valences may indicate that the structure has not been determined or interpreted correctly.

The concept of bond strength was defined by Pauling. The number of polyhedrons with a common corner can be determined by the use of an extended conception of electrostatic valence. Let z be the electric charge of cation and its coordination number.

The strength of the electrostatic valence bond going to each polyhedron corner of anions around it is defined as:

$$S = \frac{Z}{v} \quad (2.51)$$

where S is the ideal strength of the bond,

Z is the cation valence, and

v is the coordination number.

Brown and Wu proposed a list of values for bond strength parameters [53]:

$$S = S_0 (R/R_0)^{-N} \quad (2.52)$$

where S is the bond strength or bond valence of length, R ,

S_0 is the ideal bond strength of length R_0 ,

R is the observed bond length,

R_0 is the bond length of a unit cell, and

N is the constant difference in each cation-anion pair, and sometimes the cation.

The average bond strength ($\langle S_{P-O} \rangle$) of P^{5+} and O^{2-} in the $[O_3P-O-PO_3]^{4-}$ or $[P_2O_7]^{4-}$ cluster and bond valence sum ($\langle V_{P-O} \rangle$) in the metal pyrophosphate group were calculated according to the procedure of Brown [54]. The average bond strength can be estimated from the average sum of bond valence divided by the average cation coordination numbers, from which bond valence can be defined by:

$$V_{P-O} = \exp\left(\frac{R_0 - R}{B}\right) \quad (2.53)$$

where R is the bond length between P and O atoms. R_0 and B are parameters determined empirically, by which the B parameter must use a universal value for the empirical parameter, B ; $B = 0.37 \text{ \AA}$. This makes a one-parameter model relate to the formal valence,

V , bond length, R , and coordination number, N . Therefore, the sum of the bond valence is defined by:

$$V_i = \sum_j^N \exp\left(\frac{(R_1 - R_{ij})}{0.37}\right) \quad (2.54)$$

In divergence, the average bond strength of a single metal pyrophosphate is smaller than that in binary metal pyrophosphates. Bond energies and force constants decrease with average bond strength. However, determination of a quantitative correlation in the same type of bonding is complex [55].

2.7 The crystal structure of metal pyrophosphate groups

The crystal structure of metal pyrophosphate compound consists of two main parts, which contain six oxygen atoms around a metal atom or an MO_6 octahedral and a $P_2O_7^{4-}$ cluster (Fig. 2.17) that is caused by the polymerization of two $[PO_4]^{3-}$ ions to the $[P_2O_7]^{4-}$ cluster [56, 57]. Two crystallized conformations are known for these phosphates (Fig. 2.18). Firstly, a dichromate type shows that an M radius structure is greater than 0.97 Å such as $Ca_2P_2O_7$, $Sr_2P_2O_7$, $Ba_2P_2O_7$, $Pb_2P_2O_7$ and $Cd_2P_2O_7$ [58]. The $P_2O_7^{4-}$ cluster of eclipsed crystallized conformation in this group is around the center of symmetry and bridging P–O–P, which spread towards each other. Secondly, a thortveitite type shows that an M radius structure is smaller than 0.97 Å such as $M = Cu_2P_2O_7$, $Zn_2P_2O_7$, $Ni_2P_2O_7$, $Mn_2P_2O_7$, $Co_2P_2O_7$ and $Mg_2P_2O_7$. The $P_2O_7^{4-}$ cluster of this type occurs in staggered conformation. On the other hand, the metal pyrophosphate compound was separated by a stable phase at different temperatures, which included α - $M_2P_2O_7$ and β - $M_2P_2O_7$ phases (low and high temperature, respectively) [2].

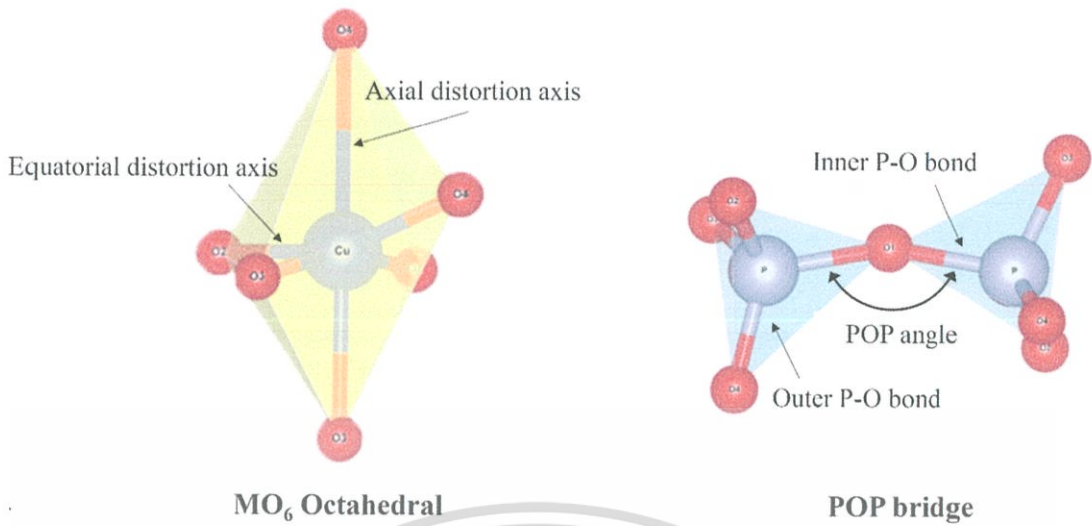


Figure 2.19 Basic cluster in ground metal pyrophosphates.

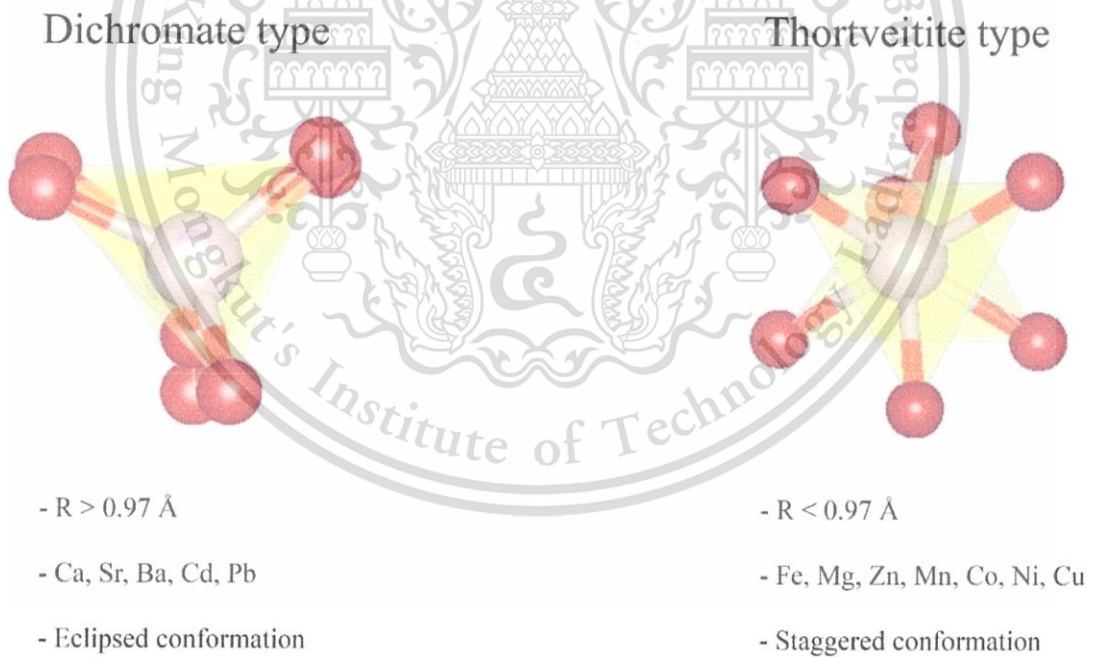


Figure 2.20 Two types of $P_2O_7^{4-}$ cluster structures.

Based α - $\text{Cu}_2\text{P}_2\text{O}_7$ was possibly first identified in 1965 by Robertson *et al.* [9], who described it as a detail of crystal structure and phase transformation. This compound shows a bent P-O-P bond angle of 157° , and the inner and outer P-O bonds of the $\text{P}_2\text{O}_7^{4-}$ anion are 1.58 Å and 1.53 Å, respectively. A phase transformation was found to begin at 70°C and extend to above 100°C , and the average axial $\text{M-O}_{\text{axial}}$ and equatorial $\text{M-O}_{\text{equatorial}}$ bond distances in the octahedral are 2.947 Å and 2.322 Å, respectively. The detail of β - $\text{Cu}_2\text{P}_2\text{O}_7$ or unstable phase of the crystal structure was proposed later [11]. Both crystal structures of $\text{Cu}_2\text{P}_2\text{O}_7$ were solved accurately by XRD spectroscopy, and their atomic coordination is given in Table 2.9 and 2.13.



Table 2.9 The structural model of the single metal pyrophosphate, $\text{Cu}_2\text{P}_2\text{O}_7$, as proposed by Robertson *et al.*

Atom	Wyckoff	X	Y	Z	Occupancy	Biso (\AA^2)	Site symmetry
Cu	8f	-0.0180	0.3132	0.5070	1	1.06	1
P	8f	0.1979	0.0077	0.2060	1	0.83	1
O	4e	0.0000	0.0471	0.2500	1	2.76	2
O	8f	0.3764	-0.0026	0.3625	1	1.61	1
O	8f	0.2213	0.1572	0.1135	1	0.99	1
O	8f	0.1778	-0.1526	0.1189	1	1.53	1

Monoclinic; $C2/c$; $a = 6.8760 \text{ \AA}$, $b = 8.1130 \text{ \AA}$, $c = 9.1620 \text{ \AA}$, $\beta = 109.540^\circ$, $V = 481.667 \text{ \AA}^3$ and $Z = 4$

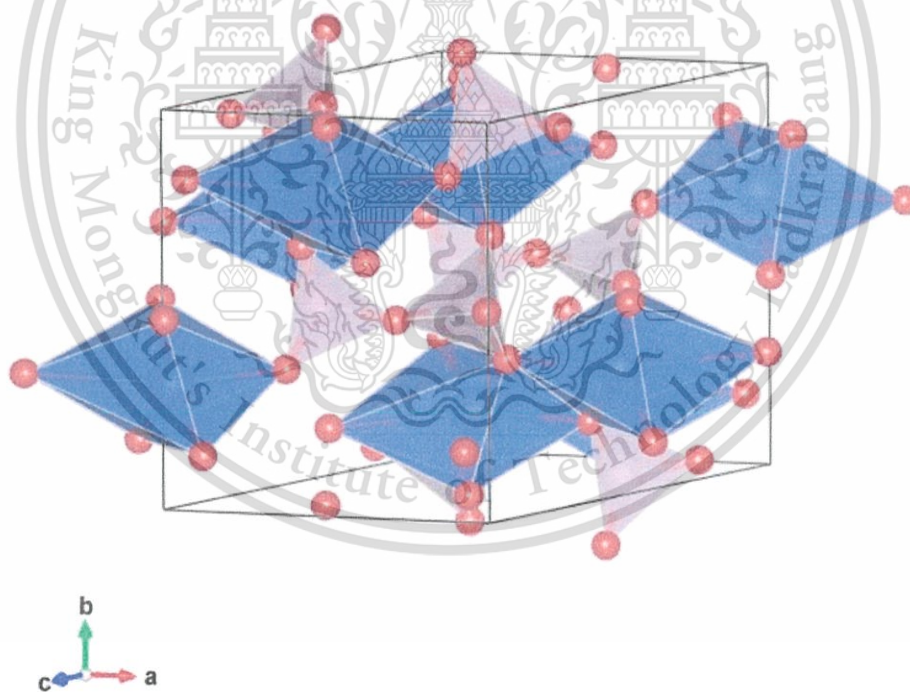


Figure 2.21 The crystal structure of $\alpha\text{-Cu}_2\text{P}_2\text{O}_7$ projected in 3 dimensions (Cu blue, O red in blue octahedral and P purple in purple tetrahedral).

This material is reserved for educational use only, not allowed for commercial use.

Forbidden to modify the content, and cite the document when use.

Table 2.10 The structural model of the single metal pyrophosphate, $Mg_2P_2O_7$, proposed by Calvo [59]

Atom	Wyckoff	X	Y	Z	Occupancy	Biso (\AA^2)	Site symmetry
Mg	4e	0.2496	0.9249	0.1212	1	0.021	1
Mg	4e	0.6986	0.4331	0.8286	1	0.021	1
P	4e	0.9479	0.7644	0.7649	1	0.021	1
P	4e	0.5245	0.7730	0.4683	1	0.021	1
O	4e	0.7290	0.8326	0.5901	1	0.021	1
O	4e	0.3762	0.7611	0.5513	1	0.021	1
O	4e	1.1276	0.7691	0.6999	1	0.021	1
O	4e	1.0113	0.9071	0.8953	1	0.021	1
O	4e	0.9236	0.5963	0.8287	1	0.021	1
O	4e	0.4710	0.8973	0.3203	1	0.021	1
O	4e	0.5998	0.6060	0.4192	1	0.021	1

Monoclinic: $P2_1/c$; $a = 6.9443 \text{ \AA}$, $b = 8.2861 \text{ \AA}$, $c = 9.0438 \text{ \AA}$, $\beta = 113.816^\circ$, $V = 476.078 \text{ \AA}^3$ and $Z = 4$

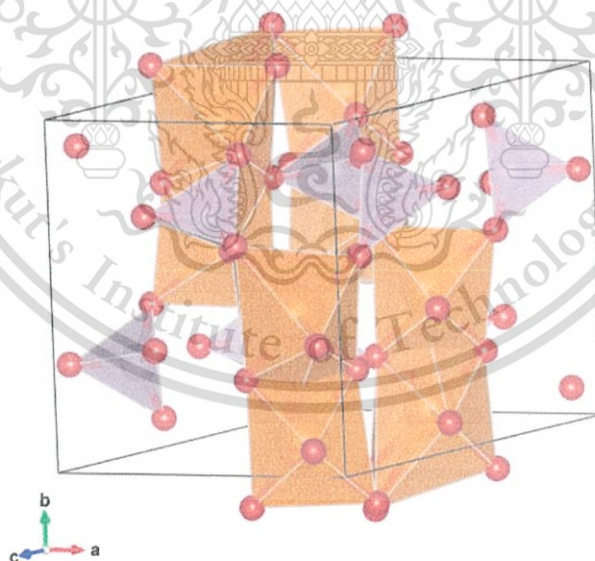


Figure 2.22 The crystal structure of α - $Mg_2P_2O_7$ projected in 3 dimensions (Mg orange, O red in orange octahedral and P purple in purple tetrahedral).

This material is reserved for educational use only, not allowed for commercial use.

Forbidden to modify the content, and cite the document when use.

Table 2.11 The structural model of the single metal pyrophosphate, $Zn_2P_2O_7$, proposed by Robertson *et al* [60]

Atom	Wyckoff	X	Y	z	Occupancy	Biso (\AA^2)	Site symmetry
Zn	8f	0.0130	0.3118	-0.0238	1	0.509	1
P	8f	0.0662	0.0202	0.2042	1	0.320	1
O	4e	0.0000	0.0886	0.2500	1	0.880	2
O	8f	-0.1241	0.0059	0.1437	1	0.470	1
O	8f	-0.0836	0.1574	0.3928	1	0.540	1
O	8f	0.0512	-0.1393	0.1197	1	0.950	1
Zn	8f	0.1635	0.1830	0.0010	1	0.481	1
Zn	8f	0.1824	0.8109	-0.0240	1	0.492	1
P	8f	0.1019	0.5068	0.2842	1	0.326	1
P	8f	0.2388	0.5184	0.2019	1	0.341	1
O	8f	0.1645	0.5564	0.2168	1	0.600	1
O	8f	0.0405	0.4939	0.1422	1	0.310	1
O	8f	0.2895	0.5101	0.3612	1	0.510	1
O	8f	0.0940	0.6513	0.3829	1	0.560	1
O	8f	0.2537	0.6595	0.1090	1	0.640	1
O	8f	0.1179	0.3550	0.3758	1	1.110	1
O	8f	0.2351	0.3576	0.1162	1	0.890	1

Monoclinic: $I2/c$; $a = 20.0680 \text{ \AA}$, $b = 8.2590 \text{ \AA}$, $c = 9.0990 \text{ \AA}$, $\beta = 106.350^\circ$, $V = 1447.096 \text{ \AA}^3$
and $Z = 12$

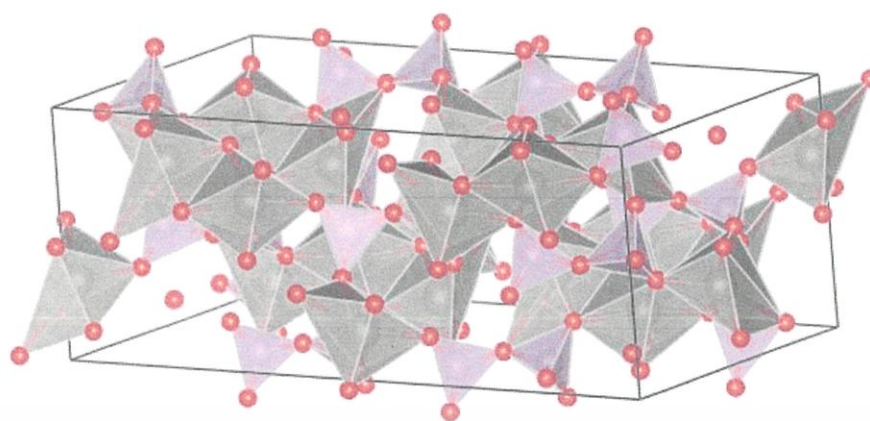


Figure 2.23 The crystal structure of α - $\text{Zn}_2\text{P}_2\text{O}_7$ projected in 3 dimensions (Zn grey, O red in grey octahedral and P purple in purple tetrahedral).

These data were the starting model for single metal pyrophosphate refinement using the Fullprof program. The modified structure model of Robertson *et al* was used for binary metal pyrophosphate refinement, as shown in Table 1.

Table 2.13 The structural model of the binary metal pyrophosphate, CuMP_2O_7 , proposed by Robertson *et al*

Atom	Wyckoff	X	y	Z	Occupancy	Biso (\AA^2)	Site symmetry
Cu	4h	0.0000	0.3092	0.5000	0.5	1.855	2
M	4h	0.0000	0.3092	0.5000	0.5	1.855	2
P	4i	0.2104	0.0000	0.9014	1	1.102	m
O	2a	0.0000	0.0000	0.0000	1	4.467	2/m
O	4i	0.3781	0.0000	0.2167	1	2.049	m
O	8j	0.2262	0.1559	0.7181	1	2.118	1

Monoclinic: $C2/m$; $a = 6.6100 \text{ \AA}$, $b = 8.2900 \text{ \AA}$, $c = 4.5100 \text{ \AA}$, $V = 105.400 \text{ \AA}^3$ and $Z = 2$

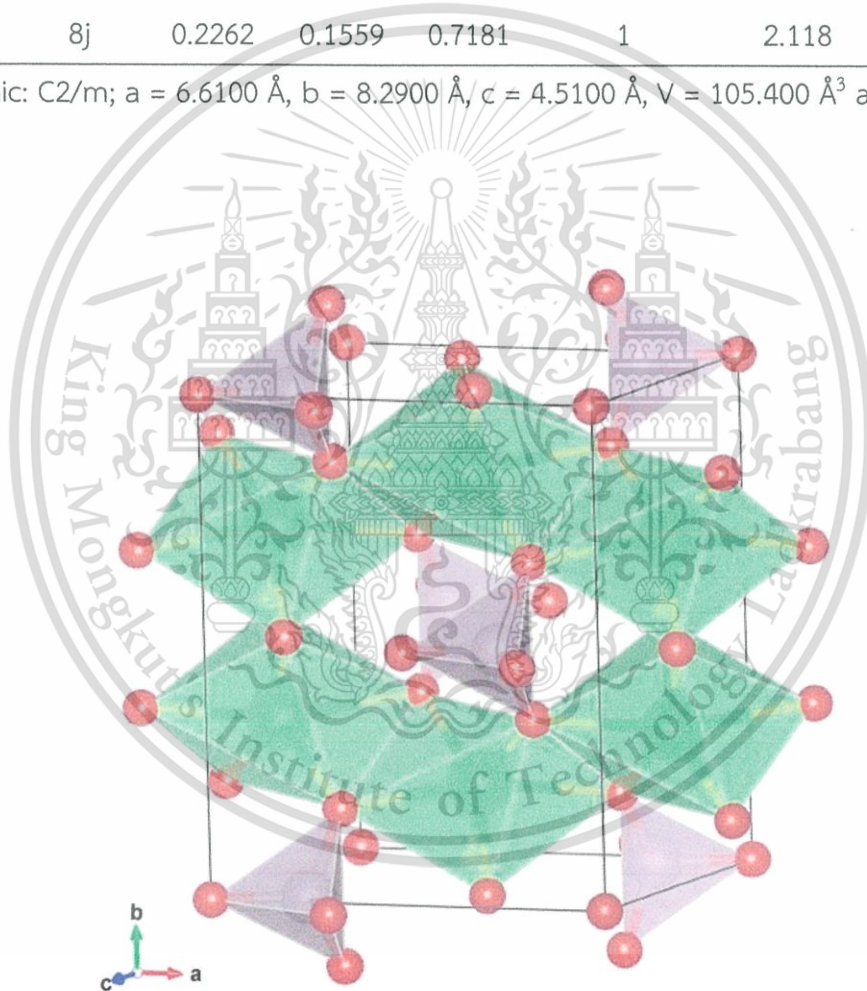


Figure 2.24 The crystal structure of CuMP_2O_7 projected in 3 dimensions (Cations green, O red in green octahedral and P purple in purple tetrahedral).

This material is reserved for educational use only, not allowed for commercial use.

Forbidden to modify the content, and cite the document when use.

References

- [1] A. D. M. T. Averbuch-Pouchot, *Topics in Phosphate Chemistry*, World Scientific Pub Co Inc, 1996.
- [2] A. Durif, *Crystal chemistry of condensed phosphates*, New York, Plenum Press, 1995.
- [3] V. M. V. a. T. V. K. I. S. Kulaev, *The Biochemistry of Inorganic Polyphosphates*, John Wiley & Sons, Ltd., 2006.
- [4] J. Berzelius, " *Ann. Physik*, 54, 31-52 (1816).
- [5] A. Mbarek, M. Graia, G. Chadeyron, D. Zambon, J. Bouaziz and M. Fourati, "Synthesis and crystal structure determination of yttrium ultraphosphate YP5O14", *Journal of Solid State Chemistry*, 182, 509-516 (2009).
- [6] J. I. Bian, D. W. Kim and K. S. Hong, "Microwave dielectric properties of $A_{(2)}P_{(2)}O_{(7)}$ ($A = Ca, Sr, Ba; Mg, Zn, Mn$)", *Jpn J Appl Phys* 1, 43, 3521-3525 (2004).
- [7] J. J. Bian, D. Kim and K. S. Hong, "Microwave dielectric properties of $(Zn_{1-x}Mn_x)_{(2)}P_2O_7$ ", *J Mater Sci*, 40, 1801-1803 (2005).
- [8] W. Wenwei, F. Yanjin, W. Xuehang, L. Sen and L. Shushu, "Preparation via solid-state reaction at room temperature and characterization of layered nanocrystalline $NH_4MnPO_4 \cdot H_2O$ ", *Journal of Physics and Chemistry of Solids*, 70, 584-587 (2009).
- [9] B. E. Robertson and C. Calvo, "The crystal structure and phase transformation of α - $Cu_2P_2O_7$ ", *Acta Crystallographica*, 22, 665-672 (1967).
- [10] C. Calvo, "THE CRYSTAL STRUCTURE AND PHASE TRANSITIONS OF β - $Zn_2P_2O_7$ ", *Canadian Journal of Chemistry*, 43, 1147-1153 (1965).
- [11] B. E. R. A. C. CALVO, "Crystal structure of β - $Cu_2P_2O_7$ ", *Canadian Journal of Chemistry*, 46 (1968).
- [12] J.-J. Bian, D.-W. Kim and K.-S. Hong, "Phase transformation and sintering behavior of $Ca_2P_2O_7$ ", *Materials Letters*, 58, 347-351 (2004).
- [13] W. Hume-Rothery and M. Powell Herbert, in *Zeitschrift für Kristallographie - Crystalline Materials* (1935), Vol. 91, pp. 23.
- [14] M. Konarova and I. Taniguchi, "Preparation of $LiFePO_4/C$ composite powders by ultrasonic spray pyrolysis followed by heat treatment and their electrochemical properties", *Materials Research Bulletin*, 43, 3305-3317 (2008).

- [15] G. T.-K. Fey and T.-L. Lu, "Morphological characterization of LiFePO_4/C composite cathode materials synthesized via a carboxylic acid route", *Journal of Power Sources*, 178, 807-814 (2008).
- [16] M. Higuchi, K. Katayama, Y. Azuma, M. Yukawa and M. Suhara, "Synthesis of LiFePO_4 cathode material by microwave processing", *Journal of Power Sources*, 119–121, 258-261 (2003).
- [17] G. A. Smolenskiĭ and I. E. Chupis, "Ferroelectromagnets", *Soviet Physics Uspekhi*, 25, 475 (1982).
- [18] A. I. Shcherbakov, "Theory of dissolution of binary alloys and the Tamman rule", *Prot Met*, 41, 30-35 (2005).
- [19] P. B. Coleman, *Practical Sampling Techniques for Infrared Analysis*, CRC Press, 1993.
- [20] D. W. Ball, *The basics of spectroscopy*, SPIE Publications, 2001.
- [21] B. C. Cornilsen and R. A. Condrate Sr, "The vibrational spectra of α -alkaline earth pyrophosphates", *Journal of Solid State Chemistry*, 23, 375-382 (1978).
- [22] B. C. Smith, *Fundamentals of Fourier Transform Infrared Spectroscopy*, CRC press, 1996.
- [23] L. J. J., *Modern techniques in Raman spectroscopy*, Chichester ; New York, Wiley, 1996.
- [24] L. I. Schiff, *Quantum Mechanics (Pure & Applied Physics)*, McGRAW Hill International Editions, 1968.
- [25] L. H. D. a. S. E. W. N.B. Colthup, *Introduction to Infrared and Raman Spectroscopy*, Third Edition ed, ACADEMIC PRESS, 1990.
- [26] J. S. Z. John R. Ferraro *Introductory group theory and its application to molecular structure*, Second Edition ed, New York, Plenum Pr, 1975.
- [27] C. R.L., *Molecular symmetry and group theory*, New York, Wiley, 1998.
- [28] B. M. D. Harris D.C., *Symmetry and spectroscopy*, New York, Oxford University Press., 1978.
- [29] J. Xu, D. F.R. Gilson and I. S. Butler, "FT-Raman and high-pressure FT-infrared spectroscopic investigation of monocalcium phosphate monohydrate, $\text{Ca}(\text{H}_2\text{PO}_4)_2 \cdot \text{H}_2\text{O}$ ", *Spectrochimica Acta Part A: Molecular and Biomolecular Spectroscopy*, 54, 1869-1878 (1998).
- [30] V. C. Farmer, *Mineralogical Society Monograph 4: Infrared Spectra of Minerals*, London, Academic Press Inc, 1974.

- [31] K. Pogorzelec-Glaser, A. Pietraszko, B. Hilczer and M. Połomska, "Structure and phase transitions in $\text{Cu}_2\text{P}_2\text{O}_7$ ", *Phase Transitions*, 79, 535-544 (2006).
- [32] P. V. M. Broek, *Introduction Philosophion Naturalem*, Luchtman, Leiden, 1762.
- [33] M. Faraday, "Experimental Researches in Electricity, Fourteenth Series. On the General Nature and Relation of the Electric and Magnetic Forces. [Abstract]", *Abstracts of the Papers Printed in the Philosophical Transactions of the Royal Society of London*, 4, 77-78 (1837).
- [34] I. D. Brown and R. D. Shannon, "Empirical bond-strength-bond-length curves for oxides", *Acta Crystallographica Section A*, 29, 266-282 (1973).
- [35] A. El Jazouli, B. Tbib, A. Demourgues and M. Gaudon, "Structure and colour of diphosphate pigments with square pyramid environment around chromophore ions (Co^{2+} , Ni^{2+} , Cu^{2+})", *Dyes and Pigments*, 104, 67-74 (2014).
- [36] L.-T. Chen, C.-S. Hwang, I. L. Sun and I.-G. Chen, "Luminescence and chromaticity of alkaline earth aluminate $\text{M}_x\text{Sr}_{1-x}\text{Al}_2\text{O}_4:\text{Eu}^{2+}$ (M: Ca, Ba)", *Journal of Luminescence*, 118, 12-20 (2006).
- [37] F. L. Wimmer, "Book Review: Inorganic Chemistry. (Second edition). By D. F. Shriver, P. W. Atkins and C. H. Langford", *Angewandte Chemie International Edition in English*, 34, 599-600 (1995).
- [38] H. A. Jahn and E. Teller, "Stability of Polyatomic Molecules in Degenerate Electronic States. I. Orbital Degeneracy", *Proceedings of the Royal Society of London A: Mathematical, Physical and Engineering Sciences*, 161, 220-235 (1937).
- [39] R. Baitahe, N. Vittayakorn and B. Boonchom, "Study on thermal transformation of $\text{CuHPO}_4 \cdot \text{H}_2\text{O}$ obtained by acetone-mediated synthesis at ambient temperature", *J Therm Anal Calorim*, 110, 625-632 (2012).
- [40] P. Y. Z. Vitalij K. Pecharsky, *Fundamentals of Powder Diffraction and Structural Characterization of Materials*, 2nd ed ed, Springer, 2009.
- [41] H. P. Klug and L. E. Alexander, *X-ray diffraction procedures for polycrystalline and amorphous materials*, 2d ed, New York, Wiley, 1974.
- [42] J. I. Langford and A. J. C. Wilson, "Scherrer after sixty years: A survey and some new results in the determination of crystallite size", *Journal of Applied Crystallography*, 11, 102-113 (1978).
- [43] S. Calvin, S. X. Luo, C. Caragianis-Broadbridge, J. K. McGuinness, E. Anderson, A. Lehman, K. H. Wee, S. A. Morrison and L. K. Kurihara, "Comparison of extended x-ray absorption fine structure and Scherrer analysis of x-ray diffraction as methods

- for determining mean sizes of polydisperse nanoparticles", *Applied Physics Letters*, 87, - (2005).
- [44] D.-M. Smilgies, "Scherrer grain-size analysis adapted to grazing-incidence scattering with area detectors", *Journal of Applied Crystallography*, 42, 1030-1034 (2009).
- [45] W. L. Bragg, in *X-ray and Neutron Diffraction*, edited by G. E. Bacon (Pergamon, 1966), pp. 109-125.
- [46] B. F.D., *Crystallography and Crystal Chemistry*, Washington D. C., Mineralogical Society of America, 1994.
- [47] B. S. J. L. Dinnebier R. E., *Principles of Powder Diffraction*, Cambridge, England, RSC Publishing, 2008.
- [48] G. Caglioti, A. Paoletti and F. P. Ricci, "Choice of collimators for a crystal spectrometer for neutron diffraction", *Nuclear Instruments*, 3, 223-228 (1958).
- [49] B. H. Toby, "R factors in Rietveld analysis: How good is good enough?", *Powder Diffraction*, 21, 67-70 (2006).
- [50] M. Newville, *Fundamentals of XAFS*, USA, University of Chicago, 2004.
- [51] P. A. Lee and J. B. Pendry, "Theory of the extended x-ray absorption fine structure", *Physical Review B*, 11, 2795-2811 (1975).
- [52] L. Pauling, "The principles determining the structure of complex ionic crystals", *Journal of the American Chemical Society*, 51, 1010-1026 (1929).
- [53] I. D. Brown and K. K. Wu, "Empirical parameters for calculating cation-oxygen bond valences", *Acta Crystallographica Section B*, 32, 1957-1959 (1976).
- [54] I. Brown, "Predicting bond lengths in inorganic crystals", *Acta Crystallographica Section B*, 33, 1305-1310 (1977).
- [55] I. Brown, "Chemical and steric constraints in inorganic solids", *Acta Crystallographica Section B*, 48, 553-572 (1992).
- [56] E. Steger and B. Käßner, "Die infrarotspektren von wasserfreien schwermetall-diphosphaten", *Spectrochimica Acta Part A: Molecular Spectroscopy*, 24, 447-456 (1968).
- [57] B. Boonchom and R. Baitahe, "Synthesis and characterization of nanocrystalline manganese pyrophosphate $Mn_2P_2O_7$ ", *Materials Letters*, 63, 2218-2220 (2009).
- [58] M. Weil and B. Stöger, "Crystal chemistry of transition metal diarsenates $M_2As_2O_7$ (M = Mn, Co, Ni, Zn): Variants of the thortveitite structure", *Acta Crystallographica Section B: Structural Science*, 66, 603-614 (2010).
- [59] C. Calvo, "The crystal structure of α - $Mg_2P_2O_7$ ", *Acta Crystallographica*, 23, 289-295 (1967).

- [60] B. E. Robertson and C. Calvo, "Crystal structure of α -Zn₂P₂O₇", *Journal of Solid State Chemistry*, 1, 120-133 (1970).



This material is reserved for educational use only, not allowed for commercial use.

Forbidden to modify the content, and cite the document when use.

CHAPTER 3

EXPERIMENTAL PROCEDURES

The procedures used for the synthesis and subsequent characterization of electrical and optical properties of all the materials produced in this research are discussed in this chapter, including Rietveld refinements of general X-ray diffraction (XRD) patterns and phenomena of the dielectric sample. Furthermore, physical properties were used to correct and confirm structural refinement.

3.1 Phase formation and mechanism of reaction

The study of phase formation, atomic evolution and mechanism of the final pyrophosphate product is necessary, as they are not understood widely and based on powder synthesis. The objective of this study was to investigate the mechanism and each atom evolution of possible single/binary metal pyrophosphate formation in a solid state reaction at different temperatures. In order to investigate the idealism of a fully solid solution, samples were synthesized using traditional solid-state reaction techniques. A high purity metal and phosphate source were used as raw materials, as listed in Table 3.1, together with the suppliers, formula of weights, and percentage of purity.

Table 3.1 Specifications of the starting materials used in this study

Source	Powder	Formula mass	Supplier	Purity (%)
Metal source	CuO	79.54	Sigma-Aldrich	≥99.9
	MgO	40.30	Sigma-Aldrich	≥99.9
	ZnO	81.38	Fluka	≥99.9
Phosphate source	(NH ₄) ₂ HPO ₄	132.05	Aldrich	≥99.0

Stoichiometric mixtures of starting materials were homogenized by ball milling with ZrO_2 media in ethanol for 24 h, and batching was calcined for 2 h at 300, 400, 500, 600, 700, 800 and 900°C. The phase content of the prepared samples was studied by X-ray powder diffraction, with functional group analysis used. Room temperature Fourier transform infrared (FT-IR) and Raman spectra were recorded. Thermal analysis measurements (thermogravimetry, TG; derivative thermogravimetry, DTG) were taken using a Perkin Elmer, Pyris 1 TGA. TG/DTG curves were used to trace the quantity of all intermediate substances in the progress of reaction, with support from XRD patterns, and FT-IR and Raman results.

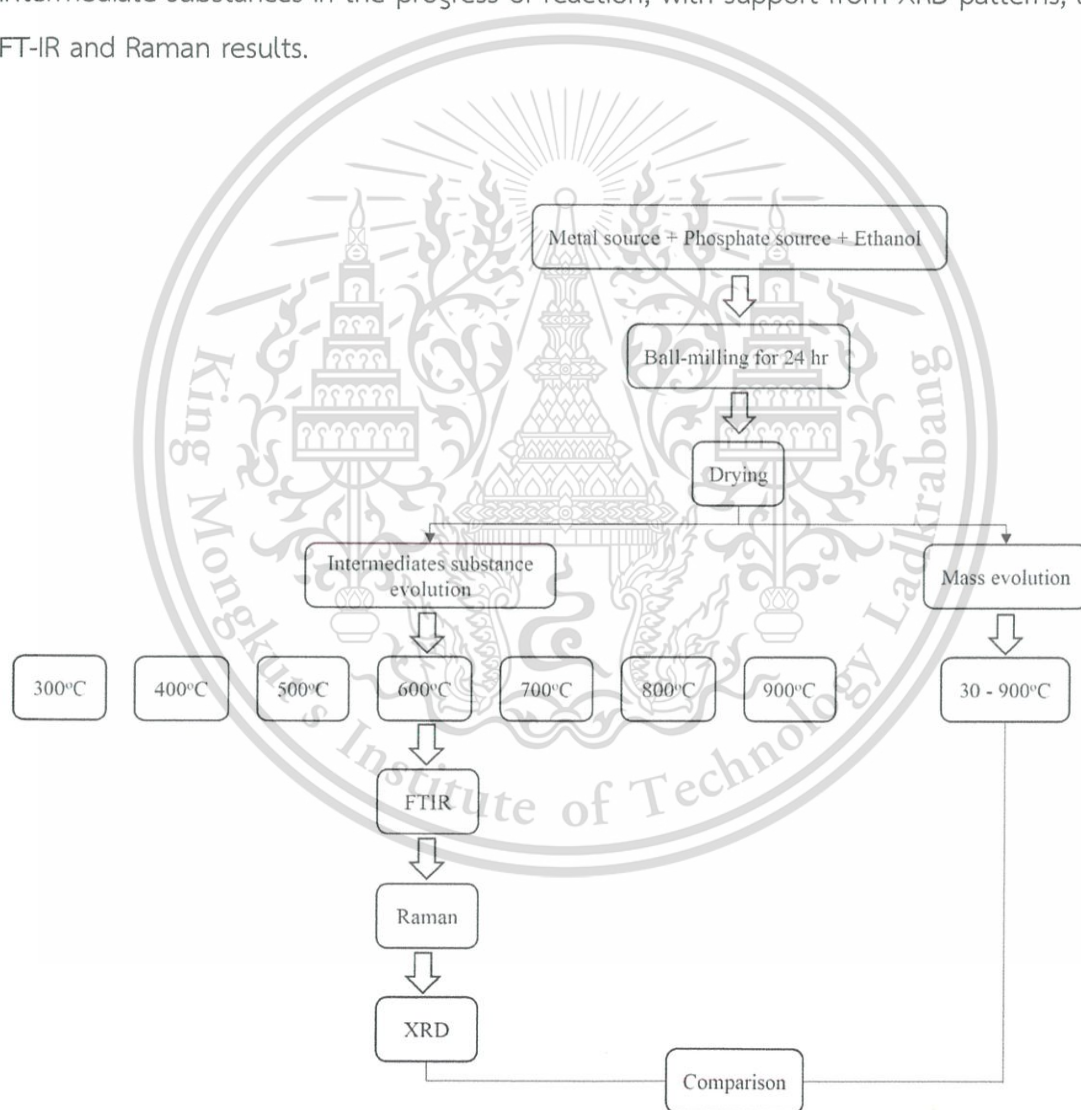


Figure 3.1 The processing route for the mechanism of reaction.

Thermal analysis measurements (thermogravimetry, TG; differential thermogravimetry, DTG; and differential thermal analysis, DTA) were carried out on Pyris Diamond Perkin Elmer apparatus by increasing the temperature from 50 to 800°C, with calcined α -Al₂O₃ powder as the standard reference. The experiments were performed in static air, at heating rates of 5, 10, 15, and 20°C/min⁻¹. An alumina crucible was filled with about 6.0-10.0 mg of sample mass without pressing. In order to know the exact mole number in crystallized water and the effect of its removal, thermal treatment was carried out in TG mode. The basic data of α and T were collected from TG curves at four different heating rates.

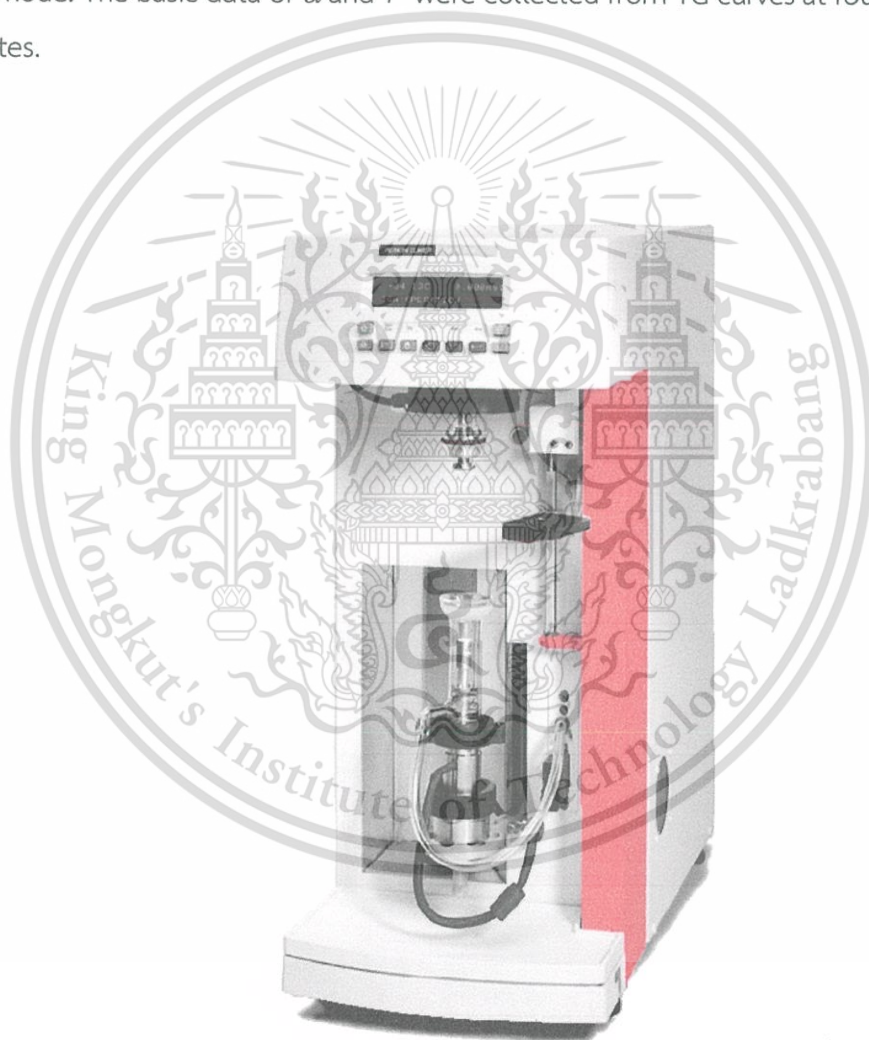


Figure 3.2 Thermogravimetry system [1].

The instrument needed to be more local. X-ray absorption spectroscopy (XAS), using synchrotron radiation, is the most suitable technique for studying local atomic and electronic structures of mixed metal phosphates, such as CuZnP_2O_7 , as well as the use of extended X-ray absorption fine structure (EXAFS) measurements for probing the structure of the final product. Experiments were conducted at room temperature on the beam line (BL8) of the Synchrotron Light Research Institute (SLRI), Nakhon Ratchasima, Thailand, with a double crystal Ge(220) for the EXAFS mono-chromator. X-ray absorption spectra (XAS) at the Cu and Zn K-edge were obtained in transmission mode with air chambers. The XANES and EXAFS spectra analysis was performed using the Athena-Artemis software package [2]. EXAFS data fitting used theoretical backscattering phases and amplitudes calculated with FEFF code [3].

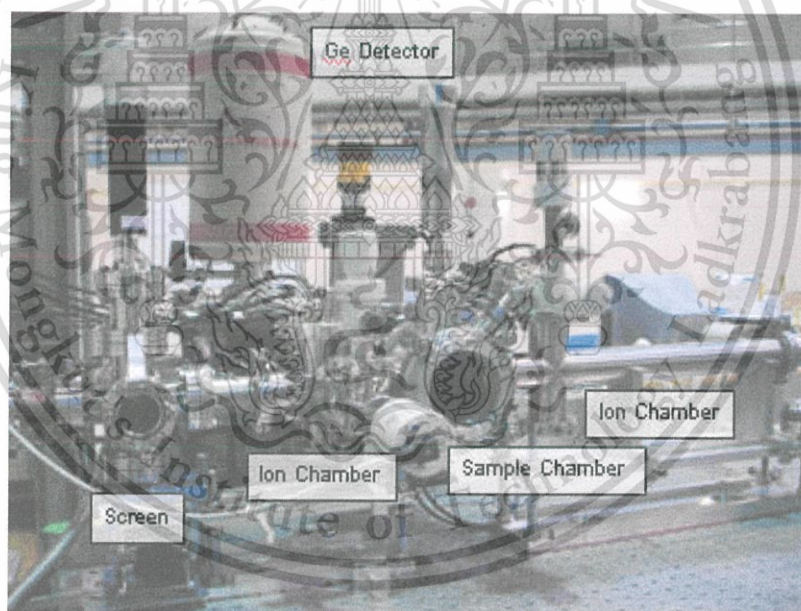


Figure 3.3 X-ray absorption spectroscopy [4].

3.2 Synthesis of metal pyrophosphate

Powders with the single metal pyrophosphates, α -Cu₂P₂O₇, α -Mg₂P₂O₇, and α -Zn₂P₂O₇, and binary metal pyrophosphates, Cu_(2-x)Mg_xP₂O₇, and Cu_(2-x)Zn_xP₂O₇ were synthesized by solid state reaction using reagent-grade metal oxides and ammonium hydrogen phosphate powders. All raw materials were weighed in stoichiometric proportion and then mixed homogeneously for 24 h by vibratory ball milling with stabilized zirconia balls in anhydrous ethanol. The dried powders were calcined in crucibles at 700-1,200°C for 24 h, then vibratory-milled again for 2 h. After that, the calcined powder was sieved and mixed with 5wt% polyvinyl alcohol (PVA) solution and uniaxial pressed into green disks of 10 mm diameter. The sintering temperature was varied between 700–1,250°C for 24 h in order to obtain optimum sintering conditions. In order to eliminate the extrinsic factor of electrical properties such as grain size and density, ceramics with more than 95% theoretical density and near average grain size of each composition were selected for the investigation of electrical properties. The complete reactions were as follows:



and for binary metal pyrophosphates:



3.3 Sample characterization

The following section intends to address the main characterization techniques used to investigate functional group analysis, phase formation, structural refinement, and dielectric and optical properties of the compounds in this study.

3.3.1 Functional group analysis

FT-IR and Raman spectroscopy (Raman) are powerful methods that analyze the chemical bonding of vibrational, rotational and other low-frequency modes in the phosphate system. The vibration group of the samples was examined at room temperature by FT-IR spectroscopy in the range of $3,000\text{--}400\text{ cm}^{-1}$, with eight scans on a Perkin-Elmer Spectrum GX spectrometer and resolution of 4 cm^{-1} . Raman spectra were measured in the wave number range of $100\text{--}1,600\text{ cm}^{-1}$, with eight scans on a Thermo Scientific DXR Raman microscope, using the 532 nm exciting line of an He-Ne laser in order to support the identification of crystal structured ceramics.



Figure 3.4 FT-IR spectrophotometer [5].

This material is reserved for educational use only, not allowed for commercial use.

Forbidden to modify the content, and cite the document when use.

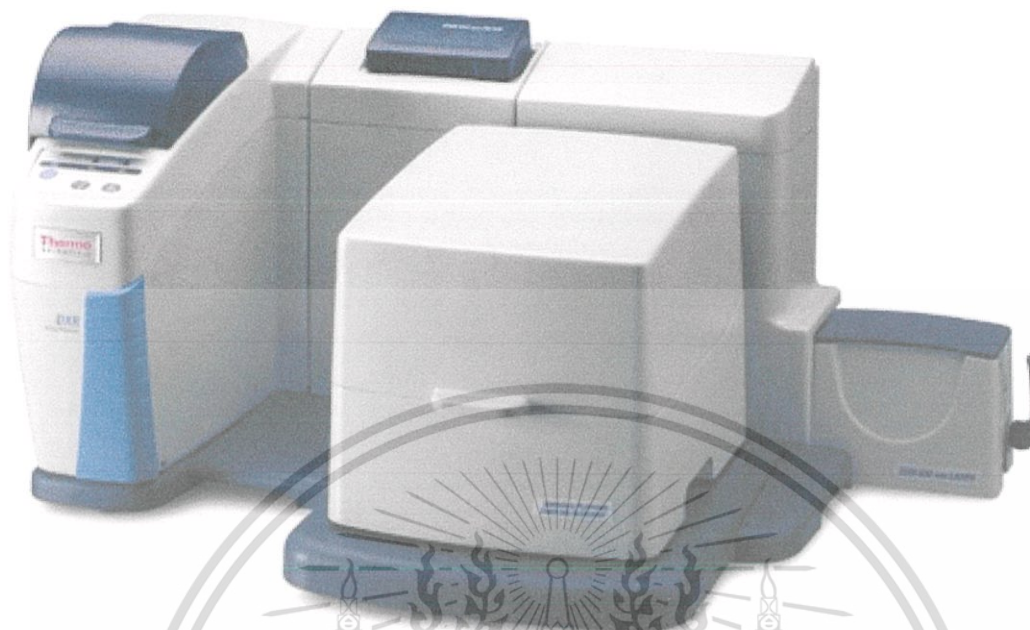


Figure 3.5 Raman spectrophotometer [6].

3.3.2 Phase formation

Powder XRD was carried out in micro-diffraction mode with $\text{CuK}\alpha$ radiation ($\lambda = 1.5428 \text{ \AA}$) on a D8 Advanced powder diffractometer (Bruker AXS, Karlsruhe, Germany), with θ/θ geometry, 0.5 mm beam size and a general area diffraction detector system (GADDS). The XRD data were collected at 40 kV and 40 mA. Samples were positioned using an xyz sample stage with a video microscope. Frames of data were collected for 1 min each, integrated and merged to produce a diffraction pattern from 10° to $80^\circ \theta$. DiffRACplus EVA 7.0 software was employed in data analysis. The crystalline phase was identified by comparing registered patterns in the powder diffraction files of the International Center for Diffraction Data (ICDD). The Scherer method was used to evaluate the crystallite size.

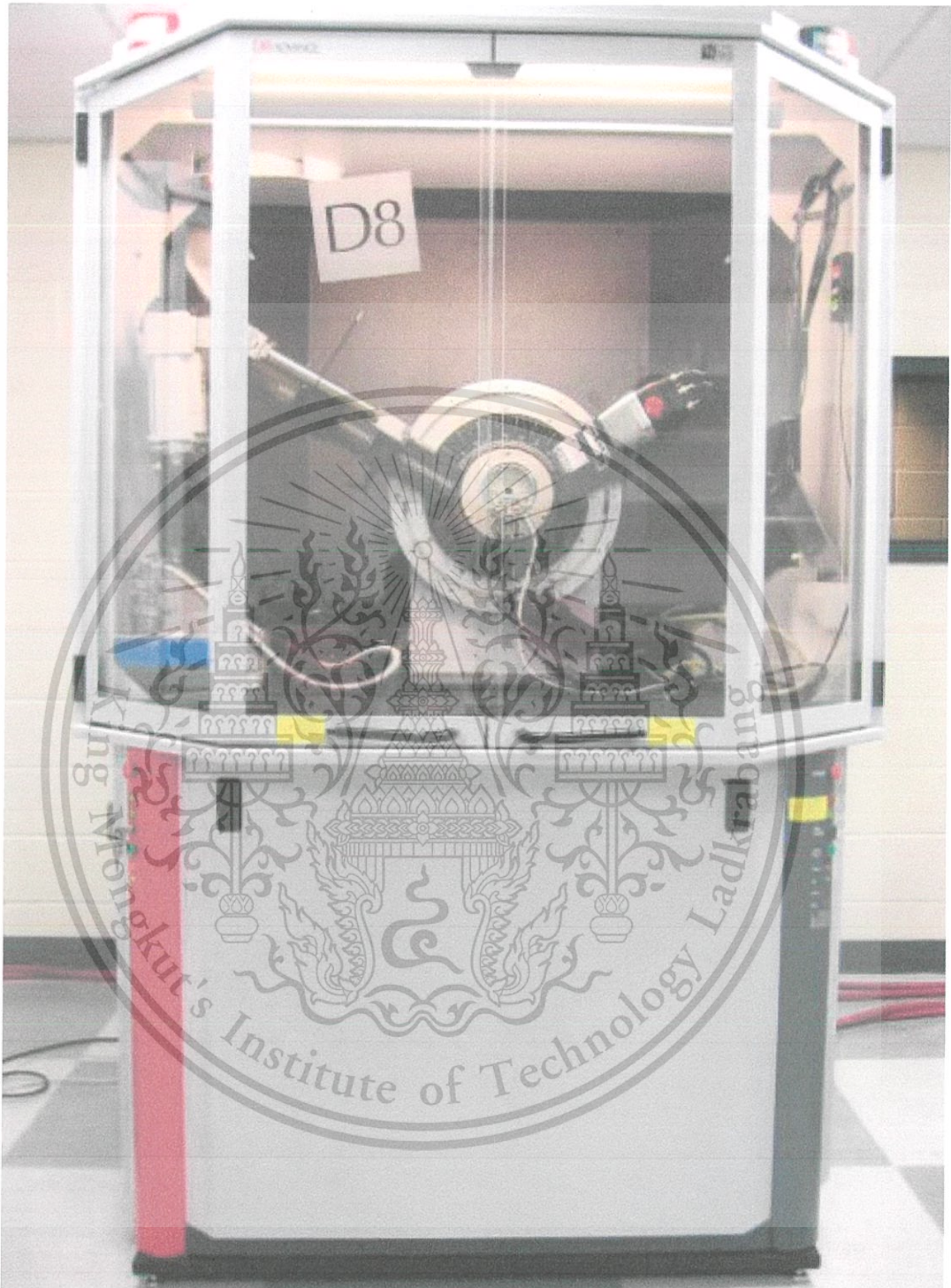


Figure 3.6 X-ray diffractometer [7].

This material is reserved for educational use only, not allowed for commercial use.

Forbidden to modify the content, and cite the document when use.

3.3.3 Structure refinement

The phases were identified cautiously, with the first parameters examining the unit cell and space group. The unit cell of a crystal is the smallest three-dimensional imaginary parallel-sided region, from which the entire crystal can be built by translation. It is described by the lattice parameters, a , b and c , for edge lengths, and α , β and γ for angles between the faces [8]. In this work, determination of this first characteristic of each sample was carried out with the FULLPROF package [9]. A pseudo-Voigt shape function was adequate for obtaining good fits for experimental data. The initial model was taken from parameters in Calvo's research [10]. A refinement program for diffraction patterns uses an iterative least square refinement method, and its equation is shown in the equation below (3.3):

$$M = \sum_i W_i (\sin^2 \theta^{obs} - \sin^2 \theta^{cal})^2 \quad (3.3)$$

where W_i is the weighting factor,

M is the minimized weighted difference observed in 2θ data.

The raw data file was read and reflection peaks were selected for refinement against theoretical values, as well as reflections based on the lattice parameters and space group obtained from a model found in the literature. This useful tool gave quick confirmation of whether or not this phase was expected. However, full Rietveld refinement is necessary for complete structural refinement, which takes all impurities into account.

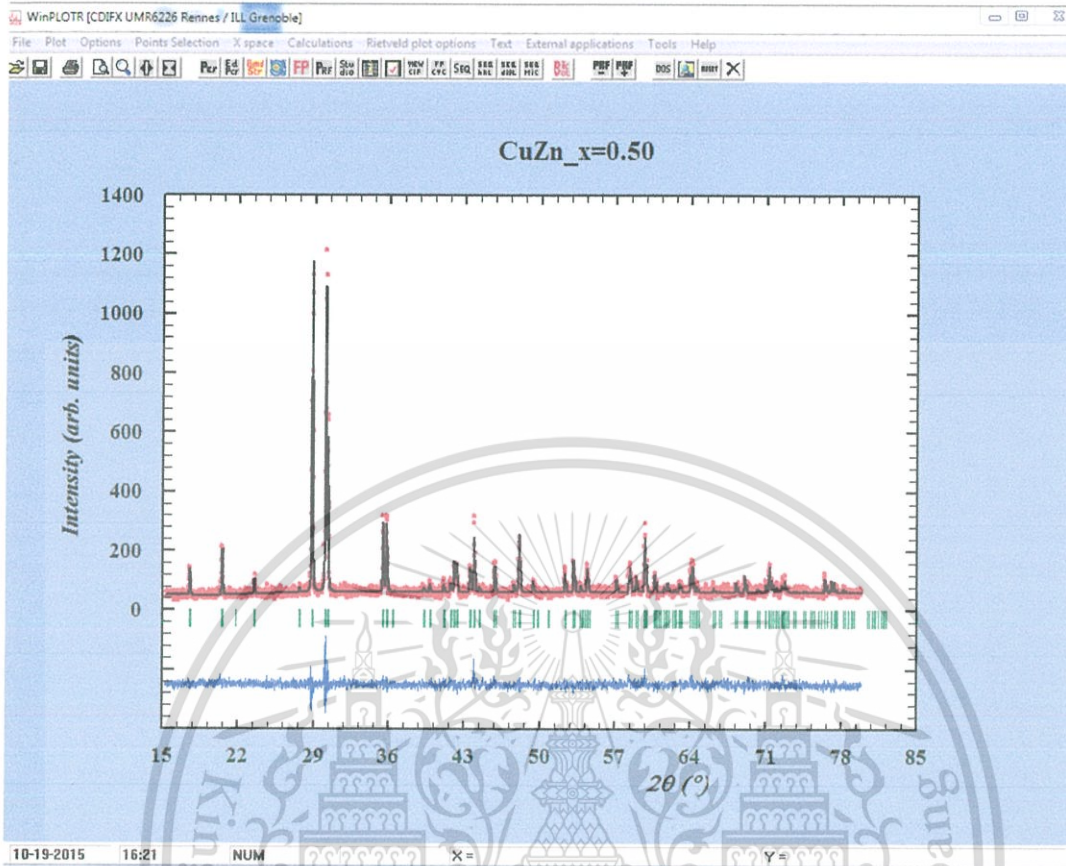


Figure 3.7 Fullprof program page.

3.3.4 Dielectric properties

Permittivity, relative to that of free space (ϵ_0), is often reported as relative permittivity (ϵ_r) or the dielectric constant. It is calculated from measured capacitance values of the sample by using the formula:

$$C = \frac{\epsilon_0 \epsilon_r A}{d} \quad (3.4)$$

where C is the measured capacitance, d is the sample thickness, A is the surface area, and ϵ_0 is the permittivity of free space, taken as 8.854×10^{-12} F/m.

In this work, dielectric property measurement allows for the determination of permittivity value, which reflects atomic rearrangement in the crystal structure. Dielectric properties were performed using a programmable furnace with an LCR analyzer (HP – 4284, Hewlett Packard Inc.), and the temperature varied between 25 – 250°C, with a heating rate of 2°C/min. Prior to making dielectric measurements, the sample was polished on both sides, as for an electrode, before being fired at 750°C for 30 minutes, with a heating rate of 5°C/min.

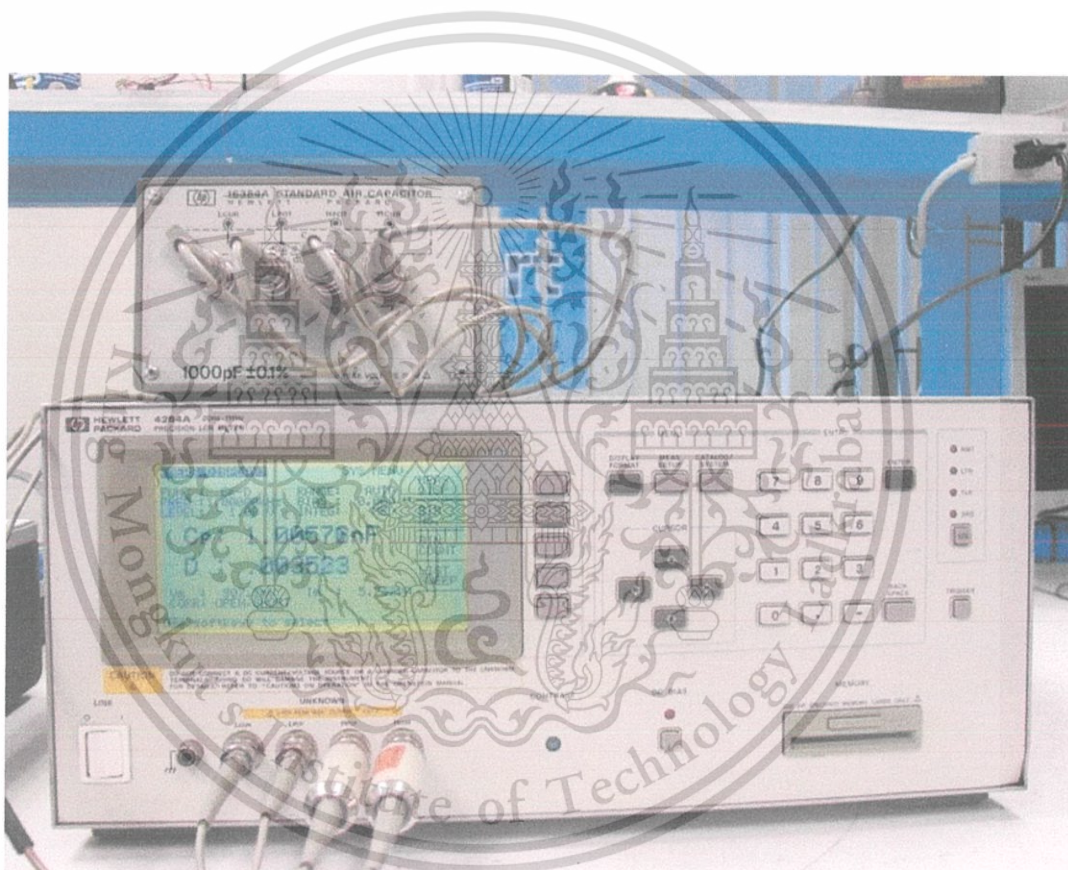


Figure 3.8 Dielectric measurement system [11].

3.3.5 Optical properties

The optical property of the powder samples were studied by the coloration method, which performs measurement of color as a function of composition using a calibrated Image staked SONY IMX214 CMOS sensor. The color data were transformed to CIE coordination, which can estimate the absorbed and transmitted wavelength of the samples.



Figure 3.9 Image staked SONY IMX214 CMOS sensor [12].

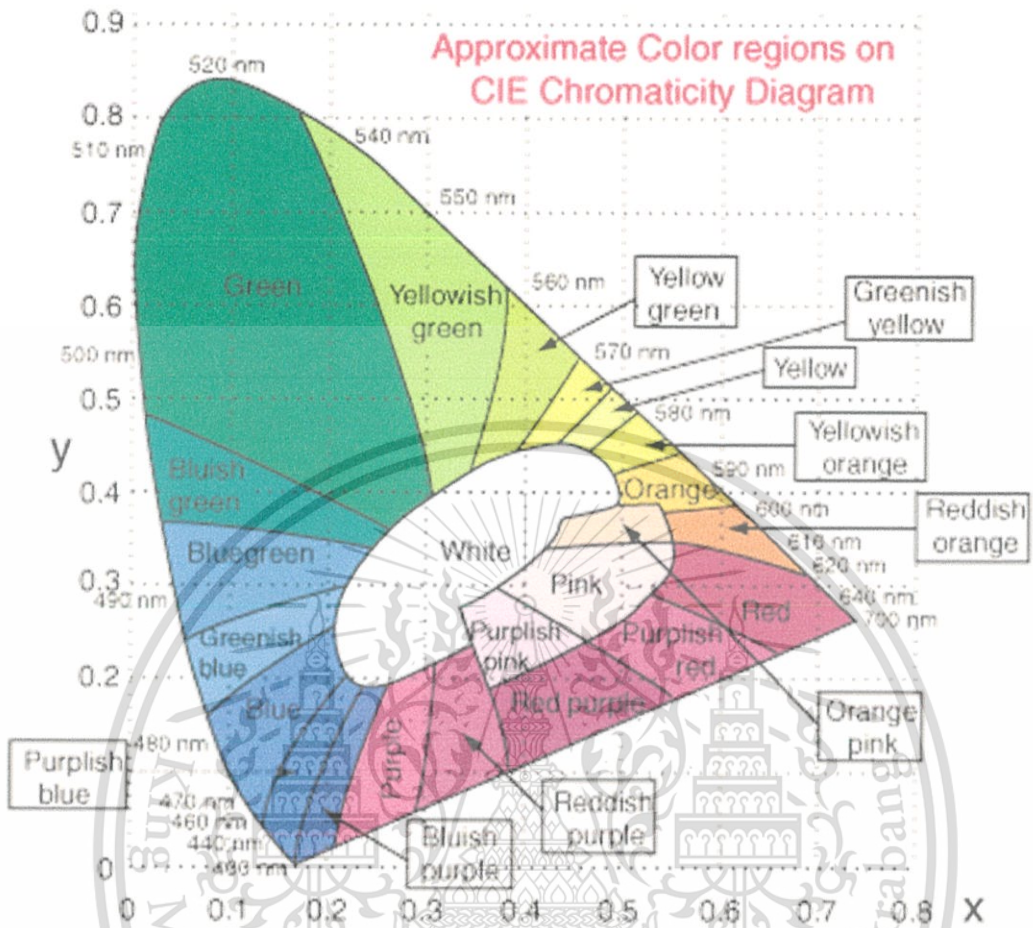


Figure 3.10 CIE chromaticity diagram [13].

This material is reserved for educational use only, not allowed for commercial use.

Forbidden to modify the content, and cite the document when use.

REFERENCES

- [1] Holdiag. "Thermogravimetry," <http://www.holodiag.com/tga.php>.
- [2] Ravel B, Newville M: ATHENA, ARTEMIS, HEPHAESTUS: data analysis for X-ray absorption spectroscopy using IFEFFIT. *Journal of Synchrotron Radiation*. 2005;12: 537-541.
- [3] Rehr JJ, Albers RC: Theoretical approaches to x-ray absorption fine structure. *Reviews of Modern Physics*. 2000;72: 621-654.
- [4] Vcharkarn, *Synchrotron Light*, 2013.
- [5] University NCK. "FT-IR spectrophotometer," <http://www.ncku.edu.tw/rrmrc/instruments-cht.htm>.
- [6] Scientific T: Raman spectrophotometer. 2012.
- [7] University of Vienna, *Research*, 2014.
- [8] Kauffman GB: Inorganic Chemistry (Shriver, Duward F.; Atkins, P. W.; Cooper, H. Langford). *Journal of Chemical Education*. 1990;67: A221.
- [9] Rodriguez-Carvajal J: Recent advances in magnetic structure determination by neutron powder diffraction + FullProf. *Physica B: Condensed Matter*. 1993;192: Pages 55–6.
- [10] Calvo BERA G: Crystal structure of β - $\text{Cu}_2\text{P}_2\text{O}_7$. *Canadian Journal of Chemistry*. 1968;46.
- [11] Wotol. "LCR analyzer," http://www.wotol.com/1-hewlett-packard-hp-4284a-precision-lcr-meter/second-hand-machinery/prod_id/778591.
- [12] Tradeindia: SONY IMX214 CMOS sensor. 2016.
- [13] Nave R: CIE chromaticity diagram. 2016.

CHAPTER 4

PHASE FORMATION AND EVOLUTION OF Cu:Zn
PARTIALS IN BINARY METAL PYROPHOSPHATES

Based on article published in *Thermochimica Acta* 596 (2014) 21-28

This chapter reported the phase formation and the evolution of Cu:Zn partials in the CuZnP_2O_7 compound. Binary metal pyrophosphate powders were prepared by the solid state reaction method and subsequently calcined at 400, 500, 600, 700, and 800 °C. Synchrotron X-ray absorption, X-ray diffraction, Raman, FT-IR spectroscopy, and Thermogravimetry analysis were used in this investigation. The results showed that complicated mixtures contributed to the reaction of synthesis temperature. The reaction comprised $3\text{CuO} \cdot 2\text{P}_2\text{O}_5 \cdot 0.3\text{NH}_3 \cdot 0.2\text{H}_2\text{O}$, $\text{Cu}_2\text{P}_2\text{O}_7$, $\text{Zn}_2\text{P}_2\text{O}_7$, and $\text{Zn}_2\text{P}_2\text{O}_7 \cdot 3\text{H}_2\text{O}$ intermediates. Decreasing percentage of $3\text{CuO} \cdot 2\text{P}_2\text{O}_5 \cdot 0.3\text{NH}_3 \cdot 0.2\text{H}_2\text{O}$ intermediates was related directly to an increasing final product. Cu:Zn contents changed in $\text{Cu}_{(2-x)}\text{Zn}_{(x)}\text{P}_2\text{O}_7$ in the temperature range of 400-600°C, when $x \approx 1$ clearly was related linearly to the reaction temperature. The final product was confirmed by EXAFS fitting spectra as solid solution between the Cu and Zn atom in the CuZnP_2O_7 structure, and it indicated environment around metal atoms.

4.1 Introduction

Metal pyrophosphates have had a wide range of applications such as microwave dielectric materials, chelating agents, corrosion-resistant coatings, glass ceramics, biomedical cements, and high-quality fertilizers [1-3]. The metal pyrophosphate, $\text{M}_2\text{P}_2\text{O}_7$, has been reported as various phase types [4]. An M radius structure greater than 0.97 Å has been observed as a dichromate type ($\text{M} = \text{Ba}^{2+}$, Cd^{2+} , Ca^{2+} , Sr^{2+} , and Pb^{2+}), in which a pair of $\text{P}_2\text{O}_7^{4-}$ groups crystallize in eclipsed conformation around the center of symmetry, with bridging O atoms extending towards each other. When the M radius is less than 0.97 Å ($\text{M} = \text{Mg}^{2+}$, Mn^{2+} , Co^{2+} , Cu^{2+} , Ni^{2+} , and Zn^{2+}), the

This material is reserved for educational use only, not allowed for commercial use.

Forbidden to modify the content, and cite the document when use.

structure is a thortveitite type, in which $P_2O_7^{4-}$ exists in staggered conformation. Furthermore, metal pyrophosphates were classified into two groups by stable phase temperatures [5]. They included alpha-phases, which are stable at low temperatures and beta-phases at high temperatures. Alpha and beta phases can be alternated at a critical temperature. In addition, different syntheses exhibited many phases such as $\text{glass} \rightarrow X \rightarrow Y \rightarrow \beta \leftrightarrow \alpha$ phases [6]. Binary copper zinc pyrophosphate ceramic has different physicochemical, mechanical and biological properties because of different processes.

Most studies of metal phosphate focused on the synthesis and characterizations of both bulk [7, 8] and nano particles [9], kinetics and the thermodynamics of reaction [10, 11], and their properties [12, 13]. However, the study of phase formation and atomic evolution of the final product, and intermediate substance relating phase, is not widely understood, and is therefore of interest. The objective of this study was to investigate Cu:Zn evolution of possible binary copper zinc pyrophosphate formation in a solid state reaction at different temperatures. In order to investigate the ideality of a solid solution fully, the probe needs to be more local. X-ray absorption spectroscopy (XAS), using synchrotron radiation, is an extremely suitable technique for studying local atomic and electronic structures of mixed metal phosphates, such as $CuZnP_2O_7$, and using extended X-ray absorption fine structure (EXAFS) measurements for probing structure of the final product.

4.2 Experimental procedure

Synthesis of $CuZnP_2O_7$ was conducted using traditional solid-state reaction techniques. High purity ZnO (99.9%), CuO (99.9%), and $(NH_4)_2HPO_4$ (99%) were used as raw materials. Stoichiometric mixtures of starting materials were homogenized by ball milling with ZrO_2 media in ethanol for 24 hrs, and batching was calcine for 2 hrs at 400, 500, 600, 700, and 800°C. The phase content of the prepared samples was studied by X-ray powder diffraction using a D8 Advanced powder diffractometer (Bruker AXS, Karlsruhe, Germany) with Cu $K\alpha$ radiation ($\lambda = 0.1546$ nm). Room temperature FT-IR spectra were recorded in the range of 4000–400 cm^{-1} with eight scans on a Perkin-Elmer Spectrum GX spectrometer with the resolution of 4 cm^{-1} . Raman spectra were recorded in the range of 1300–100 cm^{-1} with eight scans on a thermo scientific DXR Raman microscope. Thermal analysis measurements (thermogravimetry, TG; derivative

This material is reserved for educational use only, not allowed for commercial use.

Forbidden to modify the content, and cite the document when use.

thermogravimetry, DTG) were taken using a Perkin-Elmer, TGA Pyris 1. Experiments were conducted at room temperature on the beam line (BL8) of the National Synchrotron Research Center (Thailand), with a double crystal Ge(220) for the EXAFS monochromator. X-ray absorption (XAS) spectra at the Cu and Zn K-edge were obtained in transmission mode with air chambers. In addition, substitutional solid solutions, in accordance with the Hume-Rothery rules, may form if the solute and solvent have: similar atomic radii; $R_{\text{Cu(II)}} = 0.73 \text{ \AA}$ and $R_{\text{Zn(II)}} = 0.74 \text{ \AA}$ [14], similar electronegativities; Cu = 1.90 and Zn = 1.65, similar valency; Cu = 2+ and Zn = 2+. And same crystal structure; $\beta\text{-Cu}_2\text{P}_2\text{O}_7 = \text{Monoclinic, } C2/m$ and $\beta\text{-Zn}_2\text{P}_2\text{O}_7 = \text{Monoclinic, } C2/m$. These data show high possibility of substitutional solid solution between Cu and Zn ions in pyrophosphate compound.

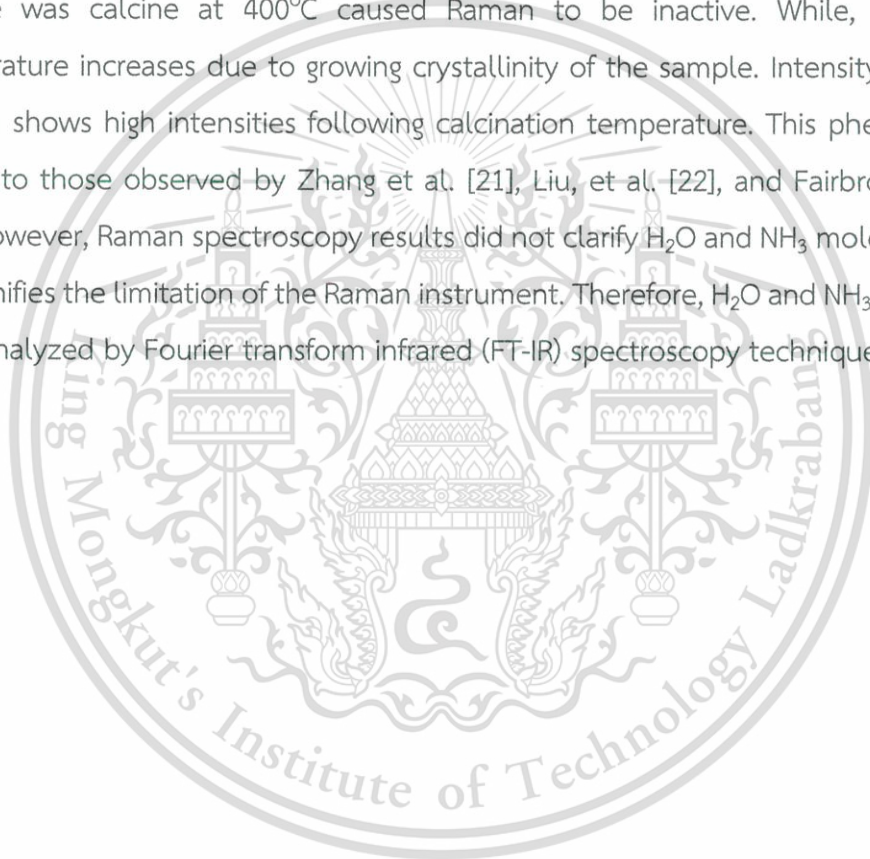
4.3 Results and Discussion

4.3.1 Functional group analysis

Infrared and Raman spectroscopy are two powerful methods used to analyze compound bonding. These popular techniques are used to observe vibrational, rotational, and other low-frequency modes in the phosphates system. Figure 4.1 shows Raman shift spectra when $x \approx 1$. Powders were calcine at different batch temperatures (400, 500, 600, 700, and 800°C) using the solid state reaction method. Raman spectra were assigned as relating to the vibration unit; PO_4^{3-} , $\text{P}_2\text{O}_7^{4-}$, P_2O_5 clusters and metal oxide (M-O) bond. The samples were calcine at 600, 700, and 800°C. The peak bands were similar. It is noticeably clear that the studied compounds exhibit more splitting and sharpness, especially in the low-frequency region ($1400\text{-}100 \text{ cm}^{-1}$), indicating polymerization of $[\text{PO}_4^{3-}]$ to $[\text{P}_2\text{O}_7^{4-}]$ [15, 16]. The strong vibration bands around $1000\text{-}1100 \text{ cm}^{-1}$ are attributed to stretching of the PO_4^{3-} unit. The bending vibration of the PO_4^{3-} unit is observed at about $450\text{-}650 \text{ cm}^{-1}$. These vibration bands were shown to remain in the phosphates group. The asymmetric and symmetric stretch of the P-O-P bridge in the $[\text{P}_2\text{O}_7^{4-}]$ unit for this sample were observed at around $930\text{-}970$ and $680\text{-}760 \text{ cm}^{-1}$ respectively, while P-O-P bending vibration is expected in the area $600\text{-}500 \text{ cm}^{-1}$ (PO_2^{2-} radical) and $500\text{-}370 \text{ cm}^{-1}$ (P-O-P bridge). These peaks were confirmed as characteristic of pyrophosphate compounds. In addition, the PO_3 deformation and rocking modes, P-O-P deformations, and torsional and external mode were found in

This material is reserved for educational use only, not allowed for commercial use.

the 430-180 cm^{-1} region. Metal–O stretching usually appears in the bending mode region, as the bending modes of the P–O–P bridge and absorption bands associated with these vibrations are usually very weak [17]. The weak band of approximately 1220 cm^{-1} exhibits a high temperature phase in pyrophosphate groups. These binary metal phosphates closely resemble those of the $\beta\text{-Zn}_2\text{P}_2\text{O}_7$ with a monoclinic structure and space group C2/m [18]. A wave number of 630 cm^{-1} for sample powders was calcine at 500°C, and assigned to asymmetric stretching of P–O in the P_2O_5 cluster [19]. The sample was calcine at 400°C, which unable to be observed any peak. Generally, Raman spectroscopy only detect crystalline of compounds [20]. The very low crystallinity of sample was calcine at 400°C caused Raman to be inactive. While, calcination temperature increases due to growing crystallinity of the sample. Intensity of Raman spectra shows high intensities following calcination temperature. This phenomena is similar to those observed by Zhang et al. [21], Liu, et al. [22], and Fairbrother et al. [23]. However, Raman spectroscopy results did not clarify H_2O and NH_3 molecules, and this signifies the limitation of the Raman instrument. Therefore, H_2O and NH_3 molecules were analyzed by Fourier transform infrared (FT-IR) spectroscopy techniques.



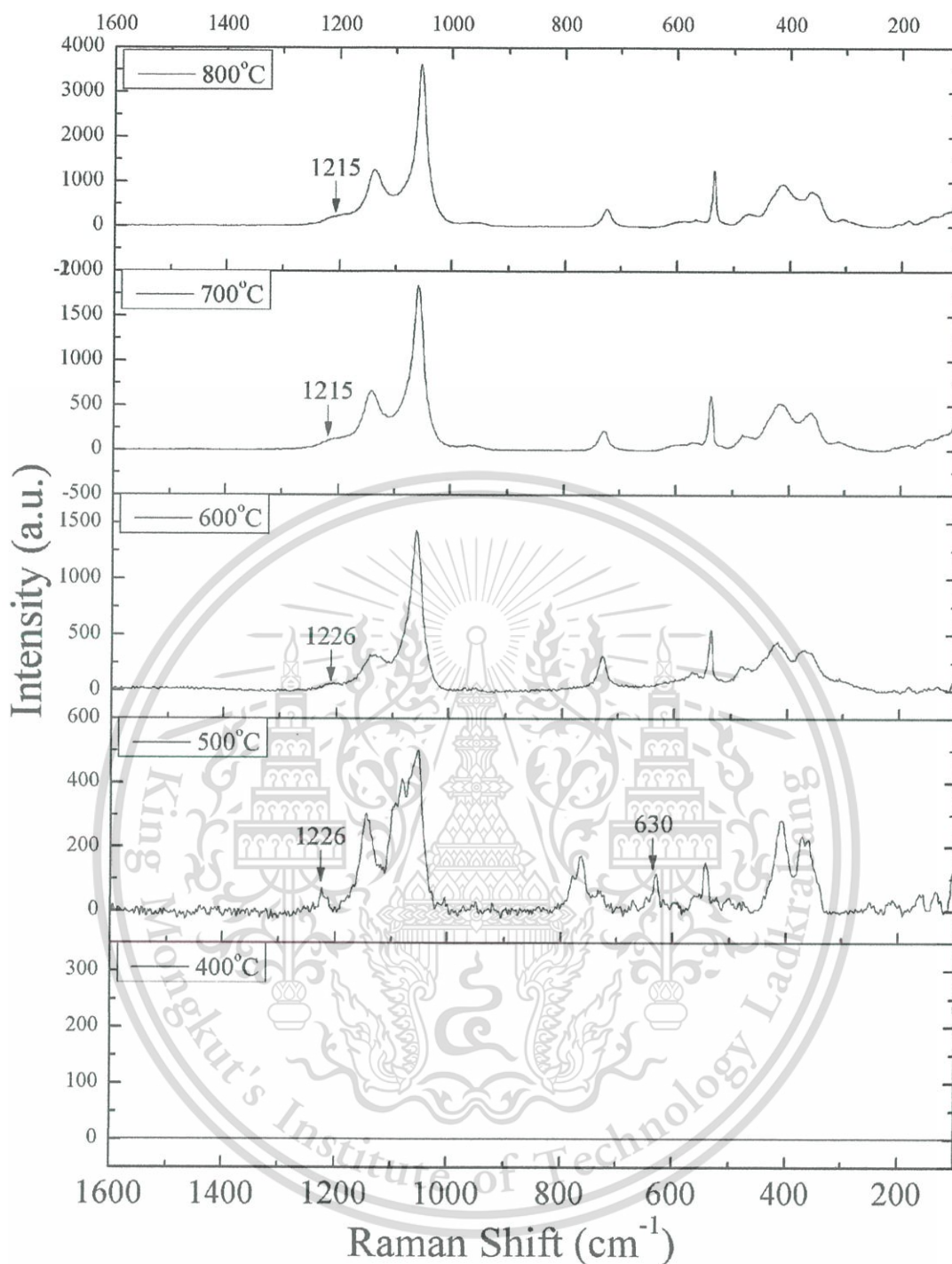


Figure 4.1 Raman spectra of $\text{Cu}_{(2-x)}\text{Zn}_x\text{P}_2\text{O}_7$; $x \approx 1.00$, subsequently calcine at 400, 500, 600, 700, and 800°C.

This material is reserved for educational use only, not allowed for commercial use.

Forbidden to modify the content, and cite the document when use.

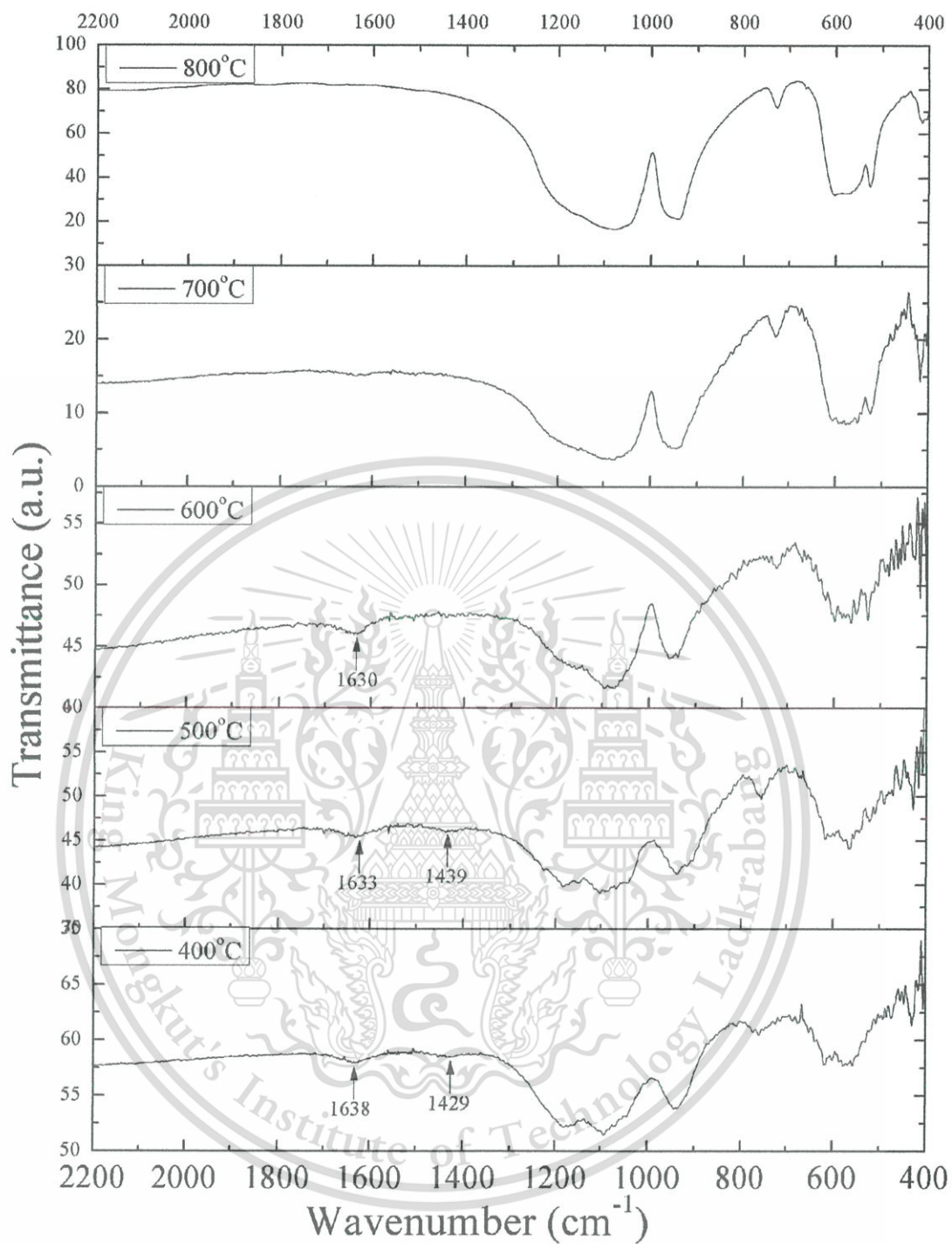


Figure 4.2 FTIR spectra of $\text{Cu}_{(2-x)}\text{Zn}_x\text{P}_2\text{O}_7$; $x \approx 1.00$, subsequently calcine at 400, 500, 600, 700, and 800°C.

The FT-IR spectra of samples are shown in Figure 4.2. All strong vibration bands were attributed to the phosphates group according to Raman results. However, medium peaks in the range of $1630\text{-}1640\text{ cm}^{-1}$ were referred to as the bending vibration of water for samples calcine at 400, 500, and 600°C . In addition, FT-IR spectra show a weak band at about 1430 cm^{-1} , particularly when calcine at 400 and 500°C , and there is asymmetric bending vibration of ammonia molecules in $3\text{CuO}\cdot 2\text{P}_2\text{O}_5\cdot 0.3\text{NH}_3\cdot 0.2\text{H}_2\text{O}$ compound [24].

4.3.2 Mechanism of phase formation

The XRD patterns of samples are shown in Figure 4.3. This technique can be investigated by both qualitative and quantitative analysis. X-ray diffraction is used often to semi-quantitatively determine the weight fraction of constituents, which can be identified by comparing the integrated intensities of the diffraction peaks from each of the known phases. In addition, complex mixtures containing more than two phases also can be quantified. Even if one phase is amorphous, diffraction can still yield a relative amount of each phase. The diffraction pattern includes information of peak positions and intensity. The peak positions are indicative of the crystal structure and symmetry of the contributing phase. The peak intensities reflect total scattering from each plane in the crystal structure of the phase, and are dependent directly on the distribution of particular atoms in the structure [25]. Thus, intensities are ultimately related to both the structure and composition of the phase.

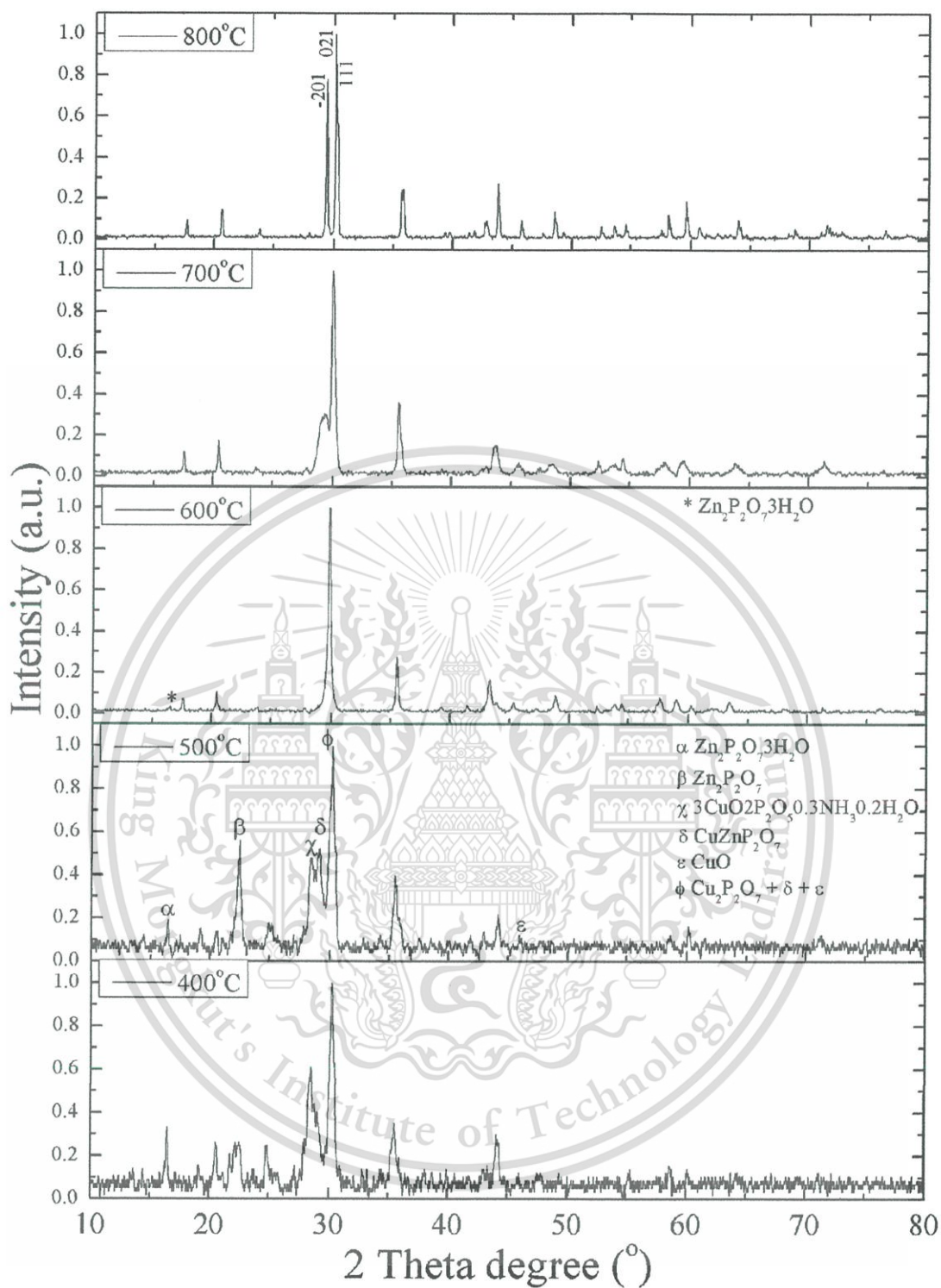


Figure 4.3 XRD patterns of $\text{Cu}_{(2-x)}\text{Zn}_x\text{P}_2\text{O}_7$; $x \approx 1.00$, subsequently calcine at 400, 500, 600, 700, and 800°C.

This material is reserved for educational use only, not allowed for commercial use.

Forbidden to modify the content, and cite the document when use.

The diffraction intensity equation has been studied many times [26-29], and is summarized below;

$$I_{(hkl)\alpha} = \frac{I_0 \lambda^3}{64\pi r} \left(\frac{e^2}{m_e c^2} \right)^2 \frac{M_{(hkl)}}{V_\alpha^2} |F_{(hkl)\alpha}|^2 \left(\frac{1 + \cos^2(2\theta) \cos^2(2\theta_m)}{\sin^2 \theta \cos \theta} \right)_{hkl} \frac{v_\alpha}{\mu_s} \quad (1)$$

where:

$I_{(hkl)\alpha}$: Intensity of reflection of hkl in phase α .

I_0 : Incident beam intensity.

r : distance from specimen to detector.

λ : X-ray wavelength.

$(e^2/m_e c^2)^2$: square of classical electron radius.

μ_s : linear absorption coefficient of the specimen.

v_α : volume fraction of phase α .

$M_{(hkl)}$: multiplicity of reflection hkl of phase α .

0 : Lorentz-polarization (and monochromator) correction $\left(\frac{1 + \cos^2(2\theta) \cos^2(2\theta_m)}{\sin^2 \theta \cos \theta} \right)$.

V_α : volume of the unit cell of phase α .

$2\theta_m$: diffraction angle of the monochromator.

$F_{(hkl)\alpha}$: structure factor for reflection hkl of phase α (i.e., the vector sum of scattering intensities of all atoms contributing to that reflection).

In recognizing that many of these terms are consistent for a particular experimental setup, the experimental constant, K_e , can be defined. The constant, $K_{(hkl)\alpha}$, can be defined for a given phase that is in effect equal to the structure factor term for phase α . In substituting the weight fraction (X_w) for the volume fraction, the density of the phase (ρ_α) for the volume, and the mass absorption coefficient of the specimen (μ/ρ)_s for the linear absorption coefficient, yields the following equation:

$$I_{(hkl)\alpha} = \frac{K_e K_{(hkl)\alpha} X_\alpha}{\rho_\alpha (\mu/\rho)_s} \quad (2)$$

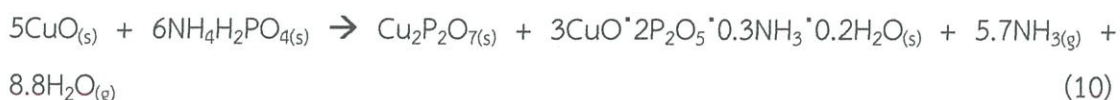
This equation describes the intensity for peak hkl in phase α in similar terms. The weight fraction, f_1 , could be described as follows:

$$f_1 = \frac{(I_1^{mix} / I_1^{pure}) A_2}{A_1 - (I_1^{mix} / I_1^{pure})(A_1 - A_2)} \quad (3)$$

where I_1^{mix} and I_1^{pure} are the phase 1 intensities in the mixture and pure material, respectively, and A_1 and A_2 are the mass absorption coefficients. Based on probability analysis, it is believed that the formation path of the CuZnP_2O_7 phase could be described as follows:



It is highly probable that all reactions proceeded together. In equation 4 and 5 reaction was competitive to reactions as follows:



Part of $\text{Zn}_2\text{P}_2\text{O}_7 \cdot 3\text{H}_2\text{O}$ was decomposed to $\text{Zn}_2\text{P}_2\text{O}_7$ and H_2O molecules, as in equation 8, while the $\text{Cu}_2\text{P}_2\text{O}_7$ and $\text{Zn}_2\text{P}_2\text{O}_7$ molecules were forced somewhat to fuse together by heating, as in equation 9. Products calcine at 400°C represented the

reaction at about 400°C. The result exhibited the complication of mixed phases, which included CuO (JCPDS no. 80-1917), α -Cu₂P₂O₇ (JCPDS no. 44-0182), 3CuO·2P₂O₅·0.3NH₃·0.2H₂O (JCPDS no. 49-1004), α -Zn₂P₂O₇ (JCPDS no. 49-1240), Zn₂P₂O₇·3H₂O (JCPDS no. 51-0201), and Cu_(2-x)Zn_(x)P₂O₇ when $x \approx 1$. All product contents (%wt) are shown in Table 4.1. The chemical reaction process is proposed in equation 11.

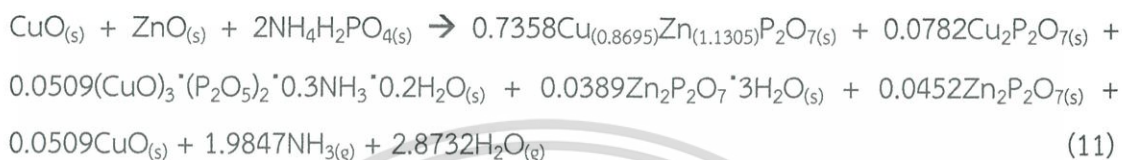
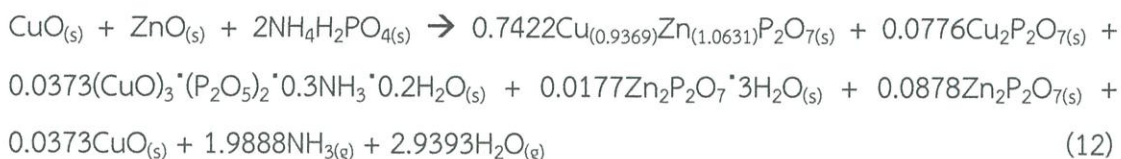


Table 4.1 Approximation of percentage by weigh from XRD results.

Temperature (°C)	Percentage of compounds (%wt)					
	CuO	3CuO·2P ₂ O ₅ ·0.3NH ₃ ·0.2H ₂ O	Cu ₂ P ₂ O ₇	Zn ₂ P ₂ O ₇	Zn ₂ P ₂ O ₇ ·3H ₂ O	Cu _(2-x) Zn _(x) P ₂ O ₇
800	-	-	-	-	-	100.00
700	-	-	-	-	-	100.00
600	-	-	-	-	2.03	97.97
500	2.97	19.83	23.37	26.74	6.36	20.71
400	4.05	27.08	23.54	13.78	13.95	17.61

Since starting reaction at room temperature until 400°C, the total mass loss was 21.89% of NH₃ and H₂O (gas phases). The sample calcine at 500°C, represented the reaction moment. This stage clearly shows decreasing content of 3CuO·2P₂O₅·0.3NH₃·0.2H₂O and CuO compounds because the rate of reaction between CuO and 3CuO·2P₂O₅·0.3NH₃·0.2H₂O to Cu₂P₂O₇ was increasing, while

$\text{Cu}_2\text{P}_2\text{O}_7$ reacted with $\text{Zn}_2\text{P}_2\text{O}_7$ to $\text{Cu}_{(2-x)}\text{Zn}_{(x)}\text{P}_2\text{O}_7$; $x \approx 1$ to bring increasing $\text{Cu}_{(2-x)}\text{Zn}_{(x)}\text{P}_2\text{O}_7$ and decreasing $\text{Cu}_2\text{P}_2\text{O}_7$. This stage is the proposed reaction in equation 12 as follows:



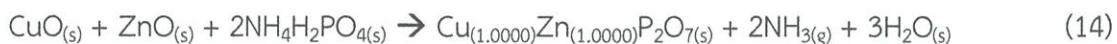
Total mass loss in NH_3 and H_2O gas phases at this stage was 22.21%, when the calcine temperature reached 600°C . The result detected only $\text{Cu}_{(2-x)}\text{Zn}_{(x)}\text{P}_2\text{O}_7$; $x \approx 1$ and the trace quantity of $\text{Zn}_2\text{P}_2\text{O}_7 \cdot 3\text{H}_2\text{O}$ phases. This effect exhibited temperatures below 600°C , and CuO and $3\text{CuO} \cdot 2\text{P}_2\text{O}_5 \cdot 0.3\text{NH}_3 \cdot 0.2\text{H}_2\text{O}$ were a complete reaction. A majority of $\text{Zn}_2\text{P}_2\text{O}_7 \cdot 3\text{H}_2\text{O}$ was decomposed to $\text{Zn}_2\text{P}_2\text{O}_7$ and reacted with $\text{Cu}_2\text{P}_2\text{O}_7$ to $\text{Cu}_{(2-x)}\text{Zn}_{(x)}\text{P}_2\text{O}_7$; $x \approx 1$. This stage proposed the following reaction in equation 8 and 9, the total mass loss was 22.52%.



According to IR results, no peak was detectable at around 1430 cm^{-1} of asymmetric bending vibration of ammonia ($\delta_{as}\text{NH}_4$) clusters. However, IR observed a weak band at about 1630 cm^{-1} , which indicated bending vibration of a water molecule for $\text{Zn}_2\text{P}_2\text{O}_7 \cdot 3\text{H}_2\text{O}$. The CuZnP_2O_7 sample was a complete reaction at a temperature of about 700°C . XRD results showed a single phase of $\text{Cu}_{(2-x)}\text{Zn}_{(x)}\text{P}_2\text{O}_7$; $x = 1$. Diffraction patterns of the sample were similar to those obtained from individual $\beta\text{-M}_2\text{P}_2\text{O}_7$ [5, 30]. The sample was calcine above 700°C . The XRD pattern showed only a single phase of CuZnP_2O_7 , and peak (-201), (021), and (111) clearly were separated. These affects caused atomic arrangement that brought long ordering in the crystal structure. In this state, the total mass loss was equal to that in the previous state. The reaction could be concluded as follows:

This material is reserved for educational use only, not allowed for commercial use.

Forbidden to modify the content, and cite the document when use.



Intermediates of all of states included $\alpha\text{-Cu}_2\text{P}_2\text{O}_7$, $3\text{CuO} \cdot 2\text{P}_2\text{O}_5 \cdot 0.3\text{NH}_3 \cdot 0.2\text{H}_2\text{O}$, $\alpha\text{-Zn}_2\text{P}_2\text{O}_7$, and $\text{Zn}_2\text{P}_2\text{O}_7 \cdot 3\text{H}_2\text{O}$, of which $\text{Zn}_2\text{P}_2\text{O}_7 \cdot 3\text{H}_2\text{O}$ was the strongest intermediate substance, because the heating energy it requires to reach temperatures higher than 600°C breaks all bonds in $\text{Zn}_2\text{P}_2\text{O}_7 \cdot 3\text{H}_2\text{O}$ molecules.

4.3.3 Atomic evolution

When evaluation of Zn and Cu atoms to CuZnP_2O_7 structure is considered, the relationship of the atomic partial, Cu:Zn, versus reaction temperature is shown in Figure 4.4. This result was classified into two parts. Firstly, a reaction temperature of below 600°C was included, and secondly a reaction temperature above 600°C . In the former, the increasing relationship of Cu or decreasing Zn clearly occupied a linear relationship with;

$$b = 0.0003a + 0.2949 \quad (15)$$

and strong linear regression of $R^2 = 0.9996$, when b is the atomic partial, and a the reaction temperature ($^\circ\text{C}$). These relationships predict occupancies between Cu and Zn atoms in $\text{Cu}_{(2-x)}\text{Zn}_{(x)}\text{P}_2\text{O}_7$; $x \approx 1$ structure at different temperatures. In the latter, atomic occupancy was close to 1. This range of temperature was close to a complete reaction. The other phases were fused to $\beta\text{-Cu}_2\text{P}_2\text{O}_7$ and $\beta\text{-Zn}_2\text{P}_2\text{O}_7$ (high temperature phases) before being assembled into one structure. A similar crystal structure with a monoclinic system, and C2/m space group, was above two compounds. Normally, low temperature is called alpha phases, $\alpha\text{-Cu}_2\text{P}_2\text{O}_7$ is a crystal structure with a monoclinic system and C2/c space group, $Z=4$, and $\alpha\text{-Zn}_2\text{P}_2\text{O}_7$ is a crystal structure with a monoclinic system and I2/c space group, $Z=12$. Meanwhile, $\beta\text{-Cu}_2\text{P}_2\text{O}_7$ and $\beta\text{-Zn}_2\text{P}_2\text{O}_7$ phases are finally intermediate and easily phased for formation of CuZnP_2O_7 compound. In addition, the mechanisms of the proposed CuZnP_2O_7 phase formation were supported by the result of Thermogravimetric analysis (TGA).

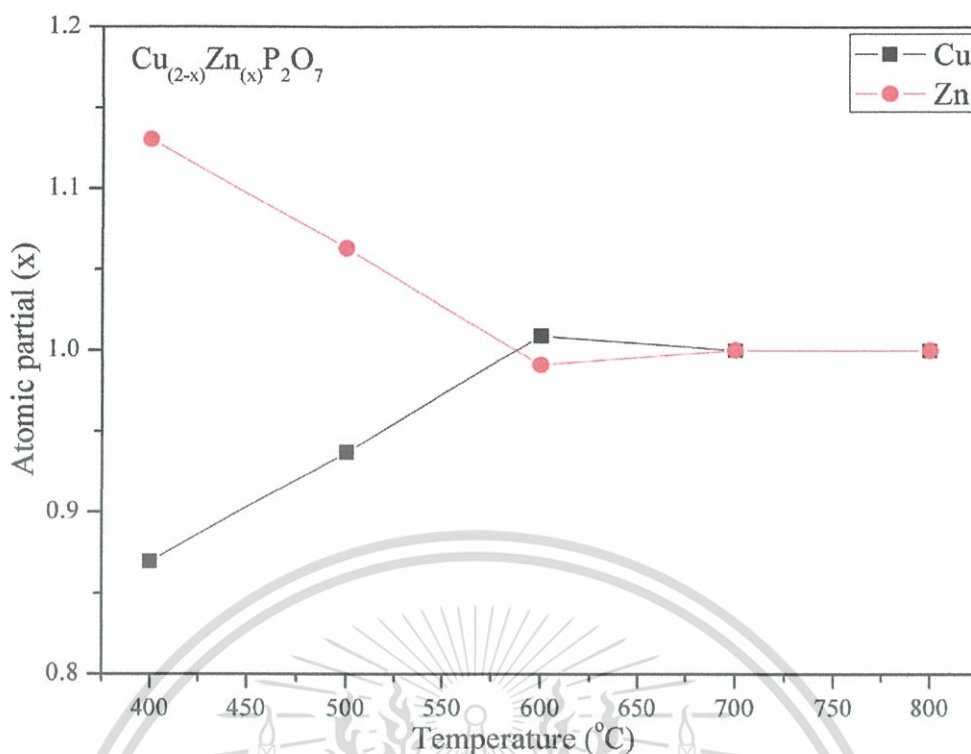


Figure 4.4 Plots of the relationship of the atomic partial, Cu:Zn, versus reaction temperature.

The thermal property of the studied compound was investigated on a TG-DTG (Thermogravimetry, TG; Derivative Thermogravimetry, DTG). The TG curve in Figure 4.5 shows the mass loss of between 30 and 800°C, which is a related multi-stage decomposition. On the basis of TG data, the final decomposed product seemed to occur at a temperature above 700°C and the water and ammonia content were determined. The first mass loss was 18.24% in the range of 50–400°C. The second to fifth mass loss was 19.88, 21.09, 21.79, and 21.79%, in the range of 400–500, 500–600, 600–700 and 700–800°C, respectively. All stages corresponded in continuum with the elimination of three molecules of crystallized water and two molecules of crystallized ammonia. The total mass loss of 21.81% was close to the XRD values. The retained mass of about 78% was comparable with the value expected for the formation of CuZnP_2O_7 , thus verified by XRD, Raman, and FT-IR measurements. Comparison values between the proposed TGA and XRD mass loss, which are close, are shown in Table 4.2.

This material is reserved for educational use only, not allowed for commercial use.

Forbidden to modify the content, and cite the document when use.

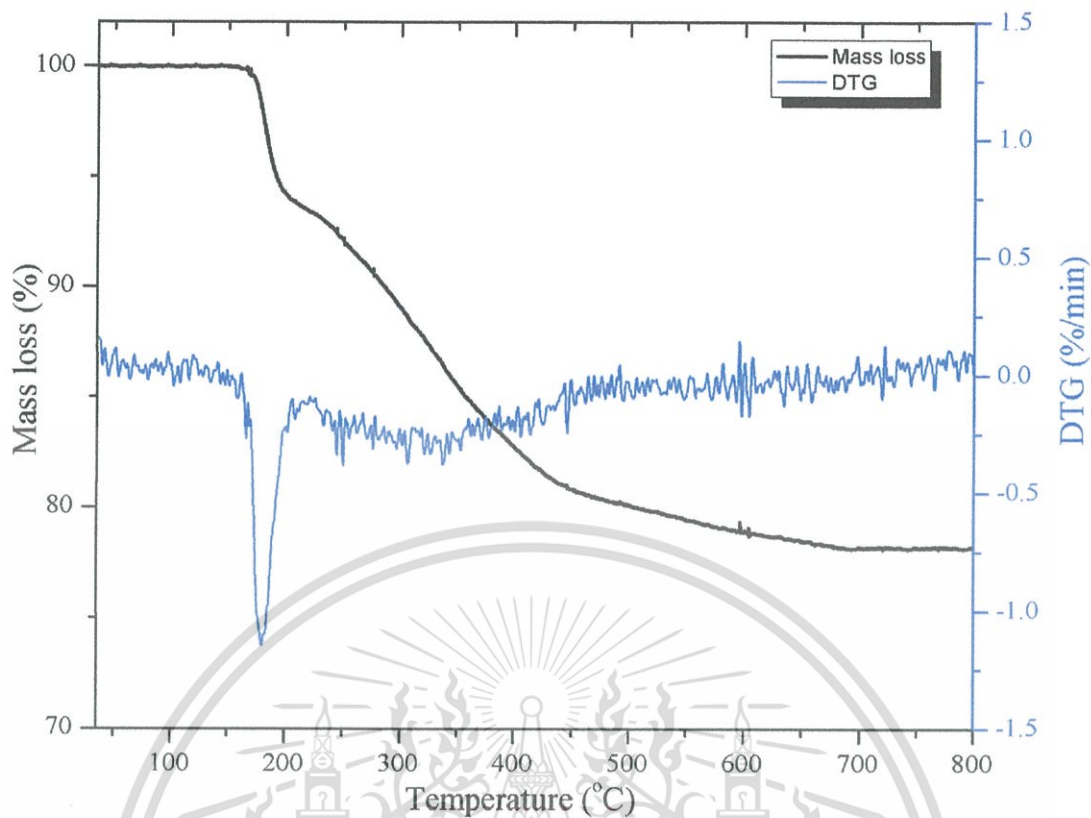


Figure 4.5 TG/DTG of CuZnP_2O_7 precursor powder.

Table 4.2 Comparison values between the proposed TGA and XRD mass loss.

Temperature (°C)	Mass loss (%)	
	XRD	TGA
400	21.89	18.24
500	22.21	19.88
600	22.52	21.09
700	22.54	21.78
800	22.54	21.81

As extended X-ray absorption fine structure (EXAFS) is very sensitive to change in local geometry, spectra collected at both edges could help in understanding Fourier transform evolutions. The EXAFS results were used for support XRD results of substitutional solid solution between Cu and Zn ions in the binary metal pyrophosphate compound. Therefore, EXAFS data were supported. The data set were then analyzed by 'data processing' with ATHENA software [31]. Accurate details of EXAFS such as interatomic distances and coordination numbers were obtained by 'curve fitting' (figure 4.6) through ARTEMIS software [31]. The details of shell which were presented in table 4.3. Cu K-edge and Zn K-edge were considered. In the case of Cu K-edge, the primitive EXAFS model was taken from parameters obtained from the Calvo's research [30]. The results of fitting were demonstrated the asymmetry of CuO_6 octahedral. The first shell to be modeled was the one consisting of four equatorial oxygen atoms, (Cu-O_{eq}) with interatomic distances of 1.96081 Å. Then the two axial oxygen atoms were taken into account (Cu-O_{ax}) with interatomic distances of 2.26967 Å, introducing the Jahn-Teller distortion effect undergone by the copper octahedral centered site into the model. The next shell was then added to the model to describe the combination of Cu-M (M=Cu/Zn), and Cu-P interaction. Addition of fourth shell did not improve the quality of the fitting. Zn K-edge were similar to the Cu K-edge fitting, the initial EXAFS model was taken from parameters obtained from the Calvo's research [5]. Zn K-edge EXAFS spectrum was identified, as in the case of Cu, with interatomic distances of 2.03230 and 2.35242 Å for first and second shell, respectively. The peak shifted to a high radial distance, due to a larger atomic radius. These show that $\text{Zn}_2\text{P}_2\text{O}_7$ is a completely solid solution with $\text{Cu}_2\text{P}_2\text{O}_7$ being brought to a CuZnP_2O_7 structure.

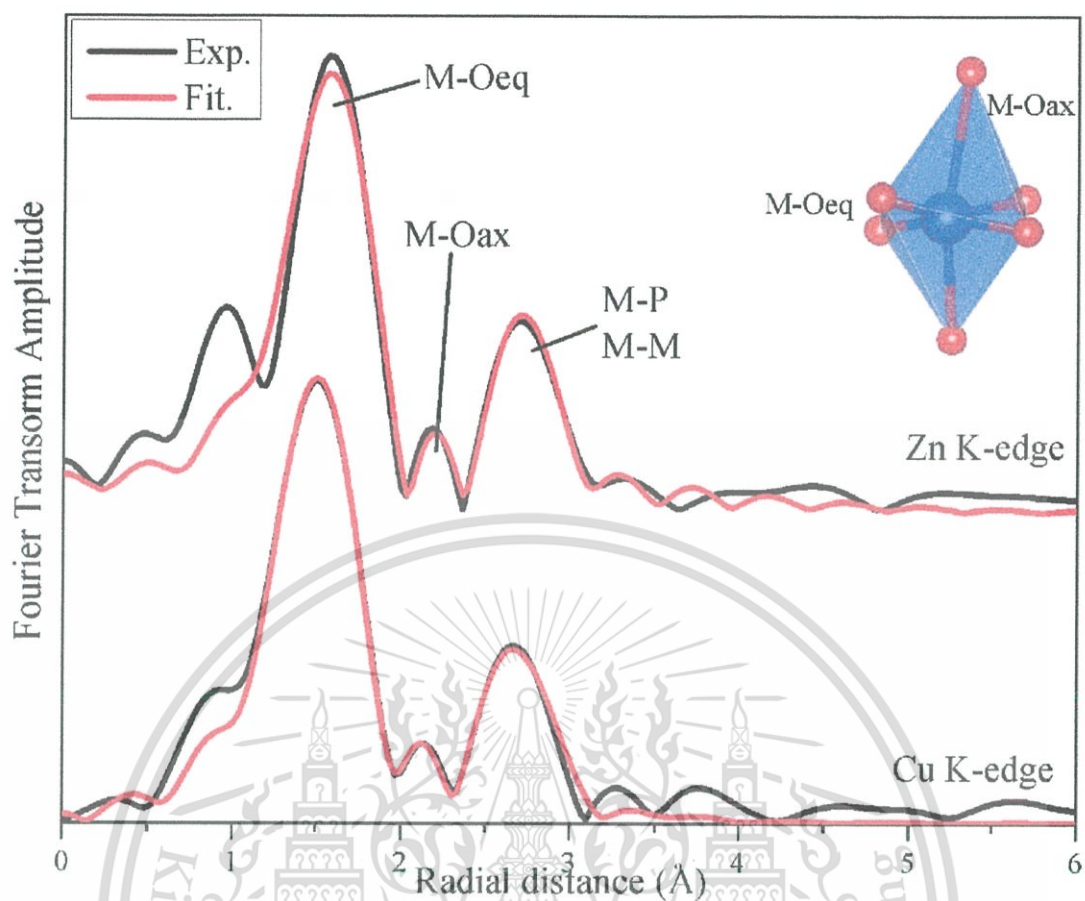


Figure 4.6 Experiment (Black line) and fitted EXAFS data (Red line) at Cu and Zn K-edge of CuZnP_2O_7 .

Table 4.3 Results obtained by EXAFS fitting analysis.

Sample	Path	Shell	CN	R(Å)	$\sigma^2(\text{Å}^2)$	R-factor
CuZnP ₂ O ₇	Cu-Oeq	1	4	1.96081	0.00704	0.0061
	Cu-Oax	2	2	2.26967	0.01537	
	Cu-Cu	3	1	3.01409	0.00738	
	Cu-P1	3	2	3.07768	0.05747	0.0113
	Cu-P2	3	2	3.11544	0.04976	
	Zn-Oeq	1	4	2.03230	0.00796	
	Zn-Oax	2	2	2.35242	0.07798	
	Zn-Zn	3	1	3.12398	0.01144	
	Zn-P1	3	2	3.18988	0.04815	
	Zn-P2	3	2	3.22903	0.00469	

4.4 Summary

Phase formation of the binary metal pyrophosphate, CuZnP₂O₇, was studied at different temperatures in the range of 400–800°C. Samples were obtained by solid state reaction using stoichiometry of CuO, ZnO and NH₄H₂PO₄ at ambient temperature to 800°C. Intermediate substances of reaction were observed by FT-IR, Raman, and XRD measurements that included α -Cu₂P₂O₇, α -Zn₂P₂O₇, 3CuO·2P₂O₅·0.3NH₃·0.2H₂O, and Zn₂P₂O₇·3H₂O, of which Zn₂P₂O₇·3H₂O was the strongest intermediate substance. The CuZnP₂O₇ sample completely reacted at a temperature of about 700°C, but with low crystallinity. When the temperature increased to about 800°C, the structure had an ordering atomic arrangement, which was brought to long range order and increased crystallinity. Cu:Zn evolution in the structure was separated into two parts with increasing temperature that started below 600°C. Thus, increasing Cu and decreasing

This material is reserved for educational use only, not allowed for commercial use.

Zn contents had clear linear relationships. When the temperature rose above 600°C, the range of reaction was close to completion. The final product confirmed the solid solution between Cu and Zn atoms by EXAFS fitting spectra. Distances between Cu/Zn-O_{eq} and Cu/Zn-O_{ax} (distorted) in the first and second shell were 1.96081 and 2.26967 Å for Cu K-edge and 2.03230 and 2.35242 Å for Zn K-edge. The third shell was then added to the model to describe the combination of M-M (M=Cu/Zn), and M-P interaction. The results of EXAFS analysis shows that Zn₂P₂O₇ is a completely solid solution with Cu₂P₂O₇ being brought to a CuZnP₂O₇ structure.



REFERENCES

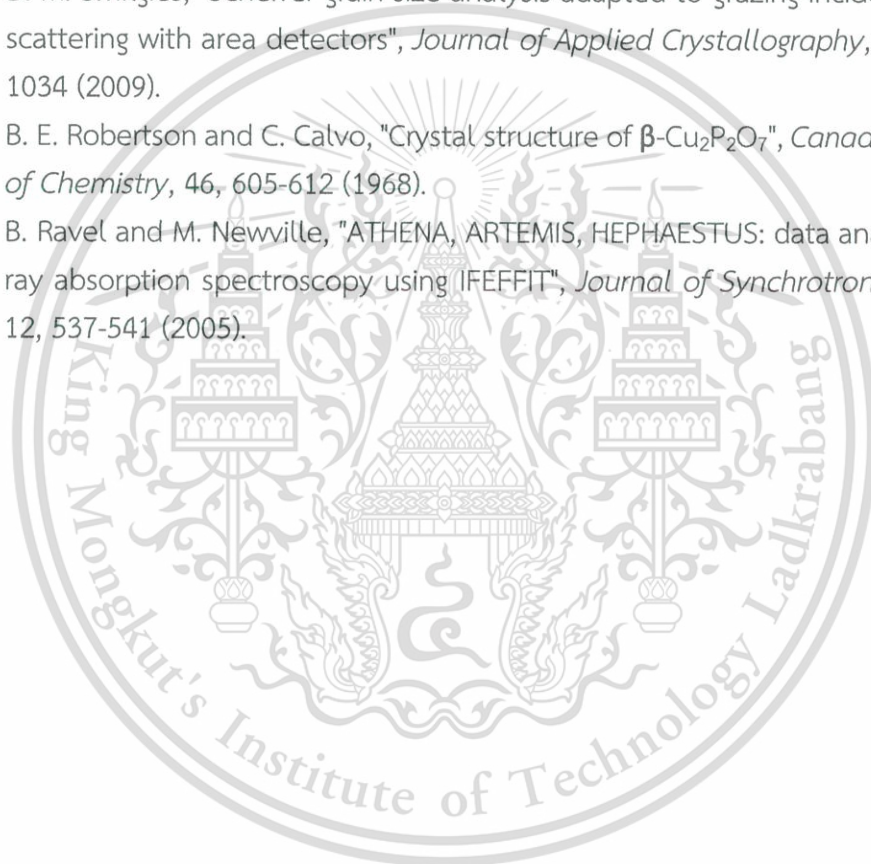
- [1] J. J. Bian, D. W. Kim and K. S. Hong, "Microwave dielectric properties of $A_2P_2O_7$ ($A = Ca, Sr, Ba; Mg, Zn, Mn$)", *Japanese Journal of Applied Physics, Part 1: Regular Papers and Short Notes and Review Papers*, 43, 3521-3525 (2004).
- [2] J. Bian, D. Kim and K. Hong, "Microwave dielectric properties of $(Ca_{1-x}Zn_x)_2P_2O_7$ ", *Materials Letters*, 59, 257-260 (2005).
- [3] W. Wenwei, F. Yanjin, W. Xuehang, L. Sen and L. Shushu, "Preparation via solid-state reaction at room temperature and characterization of layered nanocrystalline $NH_4MnPO_4 \cdot H_2O$ ", *Journal of Physics and Chemistry of Solids*, 70, 584-587 (2009).
- [4] M. Weil and B. Stöger, "Crystal chemistry of transition metal diarsenates $M_2As_2O_7$ ($M = Mn, Co, Ni, Zn$): Variants of the thortveitite structure", *Acta Crystallographica Section B: Structural Science*, 66, 603-614 (2010).
- [5] C. Calvo, "THE CRYSTAL STRUCTURE AND PHASE TRANSITIONS OF β - $Zn_2P_2O_7$ ", *Canadian Journal of Chemistry*, 43, 1147-1153 (1965).
- [6] M. A. Petrova, V. I. Shitova, G. A. Mikirticheva, V. F. Popova and A. E. Malshikov, "New data on $Zn_2P_2O_7$ phase transformations", *Journal of Solid State Chemistry*, 119, 219-223 (1995).
- [7] Z. W. Xiao, G. R. Hu, Z. D. Peng, K. Du and X. G. Gao, "Solid state synthesis and characterization of iron(II) pyrophosphate $Fe_2P_2O_7$ ", *Chinese Chemical Letters*, 18, 1525-1527 (2007).
- [8] A. Bensalem, M. Ahluwalia, T. V. Vijayaraghavan and Y. H. Ko, "Synthesis of amorphous $MgHPO_4 \cdot x(R)$ [$R = Ethanol; Ethylene glycol$] in anhydrous media", *Materials Research Bulletin*, 32, 1473-1483 (1997).
- [9] C. Díaz, M. L. Valenzuela, V. Lavayen, K. Mendoza, D. O. Peña and C. O'Dwyer, "Nanostructured copper oxides and phosphates from a new solid-state route", *Inorganica Chimica Acta*, 377, 5-13 (2011).
- [10] D. Brandová, M. Trojan, M. Arnold, F. Paulik and J. Paulik, "Mechanism of dehydration and condensation of $CuHPO_4 \cdot H_2O$ ", *Journal of Thermal Analysis*, 34, 1449-1454 (1988).
- [11] D. Brandová, M. Trojan, F. Paulik and J. Paulik, "Mechanism of dehydration of $ZnHPO_4 \cdot H_2O$ ", *Journal of Thermal Analysis*, 32, 1923-1928 (1987).
- [12] A. Jouini, J. C. Gâcon, M. Ferid and M. Trabelsi-Ayadi, "Luminescence and scintillation properties of praseodymium poly and diphosphates", *Optical Materials*, 24, 175-180 (2003).
- [13] T. Yang and J. Lin, "Hydrothermal syntheses and low temperature magnetic

- behaviors of $ACo_3(P_2O_7)_2$ (A=Ca, Sr, Ba, Pb)", *Journal of Solid State Chemistry*, 198, 1-5 (2013).
- [14] R. Shannon, "Revised effective ionic radii and systematic studies of interatomic distances in halides and chalcogenides", *Acta Crystallographica Section A*, 32, 751-767 (1976).
- [15] E. Steger and B. Käßner, "Die infrarotspektren von wasserfreien schwermetall-diphosphaten", *Spectrochimica Acta Part A: Molecular Spectroscopy*, 24, 447-456 (1968).
- [16] B. Boonchom and R. Baitahe, "Synthesis and characterization of nanocrystalline manganese pyrophosphate $Mn_2P_2O_7$ ", *Mater Lett*, 63, 2218-2220 (2009).
- [17] B. Boonchom, M. Thongkam, S. Kongtaweelert and N. Vittayakorn, "Flower-like microparticles and novel superparamagnetic properties of new binary $Co_{1/2}Fe_{1/2}(H_2PO_4)_{(2)}2H_{(2)}O$ obtained by a rapid solid state route at ambient temperature", *Mater Res Bull*, 44, 2206-2210 (2009).
- [18] K. Pogorzelec-Glaser, A. Pietraszko, B. Hilczer and M. Polomska, "Structure and phase transitions in $Cu_2P_2O_7$ ", *Phase Transit*, 79, 535-544 (2006).
- [19] K. Meyer, "Characterization of the structure of binary zinc ultraphosphate glasses by infrared and Raman spectroscopy", *Journal of Non-Crystalline Solids*, 209, 227-239 (1997).
- [20] L. Jin-bing, J. Zhi-quan, Q. Kun and H. Wei-xin, "Effect of Calcination Temperature on Surface Oxygen Vacancies and Catalytic Performance Towards CO Oxidation of Co_3O_4 Nanoparticles Supported on SiO_2 ", *Chinese Journal of Chemical Physics*, 25, 103 (2012).
- [21] S. Zhang, C. Zhang, H. Yang and Y. Zhu, "Formation and performances of porous $InVO_4$ films", *Journal of Solid State Chemistry*, 179, 873-882 (2006).
- [22] F. M. Liu, J. H. Ye, B. Ren, Z. L. Yang, Y. Y. Liao, A. See, L. Chan and Z. Q. Tian, "Raman spectroscopic studies of the formation processes of cobalt silicide thin films", *Thin Solid Films*, 471, 257-263 (2005).
- [23] A. Fairbrother, X. Fontané, V. Izquierdo-Roca, M. Espíndola-Rodríguez, S. López-Marino, M. Placidi, L. Calvo-Barrio, A. Pérez-Rodríguez and E. Saucedo, "On the formation mechanisms of Zn-rich Cu_2ZnSnS_4 films prepared by sulfurization of metallic stacks", *Solar Energy Materials and Solar Cells*, 112, 97-105 (2013).
- [24] G. Berhault, P. Afanasiev, H. Loboue, C. Geantet, T. Cseri, C. Pichon, C. Guillot-Deudon and A. Lafond, "In Situ XRD, XAS, and Magnetic Susceptibility Study of the Reduction of Ammonium Nickel Phosphate $NiNH_4PO_4 \cdot H_2O$ into Nickel Phosphide", *Inorg Chem*, 48, 2985-2992 (2009).
- [25] P. Y. Z. Vitalij K. Pecharsky, *Fundamentals of Powder Diffraction and Structural Characterization of Materials*, 2nd ed ed, Springer, 2009.

This material is reserved for educational use only, not allowed for commercial use.

Forbidden to modify the content, and cite the document when use.

- [26] H. P. Klug and L. E. Alexander, *X-ray diffraction procedures for polycrystalline and amorphous materials*, 2d ed, New York,, Wiley, 1974.
- [27] J. I. Langford and A. J. C. Wilson, "Scherrer after sixty years: A survey and some new results in the determination of crystallite size", *Journal of Applied Crystallography*, 11, 102-113 (1978).
- [28] S. Calvin, S. X. Luo, C. Caragianis-Broadbridge, J. K. McGuinness, E. Anderson, A. Lehman, K. H. Wee, S. A. Morrison and L. K. Kurihara, "Comparison of extended x-ray absorption fine structure and Scherrer analysis of x-ray diffraction as methods for determining mean sizes of polydisperse nanoparticles", *Applied Physics Letters*, 87, - (2005).
- [29] D.-M. Smilgies, "Scherrer grain-size analysis adapted to grazing-incidence scattering with area detectors", *Journal of Applied Crystallography*, 42, 1030-1034 (2009).
- [30] B. E. Robertson and C. Calvo, "Crystal structure of β - $\text{Cu}_2\text{P}_2\text{O}_7$ ", *Canadian Journal of Chemistry*, 46, 605-612 (1968).
- [31] B. Ravel and M. Newville, "ATHENA, ARTEMIS, HEPHAESTUS: data analysis for X-ray absorption spectroscopy using IFEFFIT", *Journal of Synchrotron Radiation*, 12, 537-541 (2005).



CHAPTER 5

CORRELATION BETWEEN THE CHROMATICITY, DIELECTRIC PROPERTIES AND STRUCTURE OF THE BINARY METAL PYROPHOSPHATES, $\text{Cu}_{(2-x)}\text{Zn}_x\text{P}_2\text{O}_7$

Based on article published in RSC Advances 5 (2015) 88890 - 88899

This chapter reported the correlation between the chromaticity, dielectric properties and structure of the binary metal pyrophosphates, $\text{Cu}_{(2-x)}\text{Zn}_x\text{P}_2\text{O}_7$. The binary metal pyrophosphates, $\text{Cu}_{(2-x)}\text{Zn}_x\text{P}_2\text{O}_7$; $x = 0.50 - 1.50$, were synthesized *via* solid state reaction in order to obtain information on their solid solution phase formation. Characteristic peaks of β -phase were detected under UV/Vis light emission in the range of $1,200\text{-}1,250\text{ cm}^{-1}$. The $\text{P}_2\text{O}_7^{4-}$ ion, analyzed by vibration, carried the O–P–O radical, P–O–P bridge, and approximate M–O bond stretching, and was identified using Raman and Fourier transform infrared (FT-IR) spectra. The corrected dielectric constant (ϵ_r) of samples showed a similar value when Cu^{2+} was replaced by Zn^{2+} in the $\text{Cu}_2\text{P}_2\text{O}_7$ structure. However, a slightly decreasing ϵ_r could still be seen when composition x increased. The color of samples with $x = 0.00 - 1.50$ exhibits a greenish hue, except for the composition $x = 2.00$, which presents a colourless powder. The CIE chromaticity coordinates of $\text{Cu}_{(2-x)}\text{Zn}_x\text{P}_2\text{O}_7$; $x = 0.50$ to 1.50 , shifted from $(0.303, 0.366)$ to $(0.292, 0.388)$, thus corresponding to the visible wavelength that shifted from about 506 to 512 nm , and 561 nm for $x = 0.00$. The phenomena of both dielectric and optical properties resulted from the changing crystal structure of the respective $\text{P}_2\text{O}_7^{4-}$ cluster and octahedral M-O_6 site. Investigation of the crystal structure was carried out by using Rietveld refinement analysis, with support from the extended X-ray absorption fine structure (EXAFS) fitting technique. Furthermore, this study revealed the relationships for binary metal pyrophosphates between their structure and dielectric properties, and the correlation between their structure and optical properties, which was confirmed by the reduction in chemical bonding, bond angle, number of clusters, and distortion of the octahedral MO_6 .

5.1 Introduction

Generally, divalent metal pyrophosphate salts ($\text{M}_2\text{P}_2\text{O}_7$; M = metal element), have a polymorphic structure. The crystal structure consists of two main parts, which consist of six oxygen atoms around a metal atom, or octahedral MO_6 , and a $\text{P}_2\text{O}_7^{4-}$. This material is reserved for educational use only, not allowed for commercial use.

Forbidden to modify the content, and cite the document when use.

cluster that is caused by the polymerization of two $[\text{PO}_4]^{3-}$ ions clustering to $[\text{P}_2\text{O}_7]^{4-}$ [1, 2]. These phosphates have two crystallization conformations. The first is a dichromate type, with an M radius in the structure of greater than 0.97 Å in, for example, $\text{Ca}_2\text{P}_2\text{O}_7$, $\text{Sr}_2\text{P}_2\text{O}_7$, $\text{Ba}_2\text{P}_2\text{O}_7$, $\text{Pb}_2\text{P}_2\text{O}_7$, and $\text{Cd}_2\text{P}_2\text{O}_7$ [3]. The $\text{P}_2\text{O}_7^{4-}$ cluster, in an eclipsed conformation, crystallizes in this group at about the center of the symmetry and P–O–P bridge, which spread towards each other. The second is a thortveitite type, with an M radius of less than 0.97 Å in, for example, $\text{Cu}_2\text{P}_2\text{O}_7$, $\text{Zn}_2\text{P}_2\text{O}_7$, $\text{Ni}_2\text{P}_2\text{O}_7$, $\text{Mn}_2\text{P}_2\text{O}_7$, $\text{Co}_2\text{P}_2\text{O}_7$, and $\text{Mg}_2\text{P}_2\text{O}_7$. This type of $\text{P}_2\text{O}_7^{4-}$ cluster occurs in a staggered conformation. On the other hand, the metal pyrophosphate compounds are separated by a stable phase structure at different temperatures, which includes $\alpha\text{-M}_2\text{P}_2\text{O}_7$, and $\beta\text{-M}_2\text{P}_2\text{O}_7$ phases (low and high temperature, respectively) [4]. Generally, the α -phase is the stable phase of $\text{Cu}_2\text{P}_2\text{O}_7$ at room temperature. The $\alpha\text{-Cu}_2\text{P}_2\text{O}_7$ phase exhibits the monoclinic space group, C2/c, with lattice parameters of $a = 6.876$ Å, $b = 8.113$ Å, $c = 9.162$ Å, and $\beta = 109.54^\circ$. High temperature analysis shows that the monoclinic C2/c transforms to monoclinic C2/m ($\beta\text{-Cu}_2\text{P}_2\text{O}_7$ phase), with lattice parameters of $a = 6.827$ Å, $b = 8.118$ Å, $c = 4.576$ Å, and $\beta = 108.85^\circ$. The transition temperature of $\alpha \rightarrow \beta$ phase is about 100°C [5]. Regarding the $\text{Zn}_2\text{P}_2\text{O}_7$ structure, $\alpha\text{-Zn}_2\text{P}_2\text{O}_7$ has the monoclinic space group, I2/c, at room temperature, with unit cell parameters of $a = 20.068$ Å, $b = 8.259$ Å, $c = 9.099$ Å, and $\beta = 106.35^\circ$. The transition temperature of $\alpha\text{-Zn}_2\text{P}_2\text{O}_7$ to $\beta\text{-Zn}_2\text{P}_2\text{O}_7$ was found to be about 130°C . The $\beta\text{-Zn}_2\text{P}_2\text{O}_7$ phase displays the monoclinic space group, C2/m, with unit cell parameters of $a = 6.61$ Å, $b = 8.29$ Å, $c = 4.51$ Å, and $\beta = 105.4^\circ$ [6]. In addition, the crystal structure of $\text{Zn}_2\text{P}_2\text{O}_7$ was observed in other phases, such as x and y, which are metastable phases in the form of $2\text{ZnO}\cdot\text{P}_2\text{O}_5$ [7]. The $\delta\text{-Zn}_2\text{P}_2\text{O}_7$ phase is a poor crystalline, and the $\gamma\text{-Zn}_2\text{P}_2\text{O}_7$ phase is orthorhombic with a unit cell of $a = 4.950$ Å, $b = 13.335$ Å, and $c = 16.482$ Å. It is interesting to note that the $\beta\text{-Zn}_2\text{P}_2\text{O}_7$ and $\beta\text{-Cu}_2\text{P}_2\text{O}_7$ phases have the same space group in the monoclinic phase, which enables the high possibility of solid solution formation at high temperature.

A group of metal pyrophosphate compounds can be applied widely in, for example, biomedical cements, chelating agents, corrosion-resistant coatings, high-quality fertilizers, glass ceramics, and microwave dielectric materials [8-10]. Most research studies on this group of compounds often focus on synthesis and characterization, [11, 12] such as synthesis through wet chemical processing via metal ammonium phosphate hydrates ($\text{MNH}_4\text{PO}_4\cdot n\text{H}_2\text{O}$) or metal hydrogen phosphate hydrates ($\text{MHPO}_4\cdot n\text{H}_2\text{O}$) with calcination at different temperatures [2, 12] as follows:



This material is reserved for educational use only, not allowed for commercial use.

Forbidden to modify the content, and cite the document when use.

The kinetics and thermodynamics of phase formation were studied in order to explain the mechanism of the reaction, intermediate reaction, and energy of the reaction (ΔH^* , ΔS^* , and ΔG^* , respectively). [13-15]. In order to understand the crystal structure [5, 6] and its properties [16, 17], structural refinement of the final product was analyzed. However, the study of the relationship between the crystal structure and properties has not been widely performed. Therefore, this research aimed to study the relationship between the crystal structure and dielectric properties, and that between the crystal structure and optical properties of the binary metal pyrophosphates, $\text{Cu}_{(2-x)}\text{Zn}_x\text{P}_2\text{O}_7$; $x = 0.50 - 1.50$, by using Rietveld refinement and the extended X-ray absorption fine structure (EXAFS) fitting technique. Previously, Kim *et al.* [18] reported two important factors which caused polarization in the structure of metal pyrophosphate compounds. These factors consisted of shifting O atoms in the collinear P–O–P bridge and movement of M^{2+} ions in the octahedral MO_6 , but with relatively few details of the structure. Consequently, the effect of bond length, bond angle, bond strength, number of P–O–P clusters, average bond length, and distortion of the octahedral MO_6 site were considered in order to explain the relationship between the crystal structure, dielectric properties, and optical properties of $\text{Cu}_{(2-x)}\text{Zn}_x\text{P}_2\text{O}_7$; $x = 0.00 - 2.00$ metal pyrophosphate compounds, which produced the mechanism of the phase formation [19].

5.2 Experimental procedure

Powders with the compositions, $\text{Cu}_{(2-x)}\text{Zn}_x\text{P}_2\text{O}_7$; $x = 0.00 - 2.00$, were synthesized via solid state reaction using the reagent-grade metal oxides and hydrogen phosphate powders CuO (99.9%), ZnO (99.9%), and $(\text{NH}_4)_2\text{HPO}_4$ (99%). All of the raw materials were weighed in stoichiometric proportions and then mixed homogeneously by vibratory ball milling with stabilized zirconia balls for 24 h in anhydrous ethanol. The dried powders were calcined in crucibles at 800 °C for 24 h, then vibratory-milled again for 2 h. After that, each calcined powder was sieved and mixed with 5 wt% polyvinyl alcohol (PVA) solution and uniaxially pressed into green disks of 10 mm diameter. The sintering temperature was varied between 700–900 °C for 24 h in order to obtain optimum sintering conditions. In order to eliminate the extrinsic factors of electrical properties such as grain size and density, ceramics with more than 95% theoretical density and near average grain size of each composition were selected for investigating the electrical properties. The vibration group of the samples was examined at room temperature using Fourier transform infrared (FT-IR) spectroscopy in the range of 3000–400 cm^{-1} , with eight scans on a Perkin-Elmer Spectrum GX spectrometer and a resolution of 4 cm^{-1} . Raman spectra were measured in the

This material is reserved for educational use only, not allowed for commercial use.

Forbidden to modify the content, and cite the document when use.

wavenumber range of 100-1600 cm^{-1} , with eight scans on a Thermo Scientific DXR Raman microscope, using the 532 nm excitation line of a He-Ne laser in order to support the identification of crystal structured ceramics. The dielectric properties were measured at 1 MHz via the use of an LCR meter (HP4284A; Hewlett-Packard, Palo Alto, CA). An image stacked SONY IMX214 CMOS sensor collected the colors of the samples, and matched them with CIE chromaticity diagrams in order to approximate the tendency of the absorption wavelength. Details of the crystal structure were studied through X-ray diffraction (XRD) of the powders, using a D8 Advanced powder diffractometer (Bruker AXS, Karlsruhe, Germany), with Cu K_{α} radiation ($\lambda = 0.1546$ nm); and X-ray absorption spectroscopy (XAS) was conducted on the beam line (BL8) of the National Synchrotron Research Center (Thailand). A double crystal Ge(220) was used for the EXAFS mono-chromator. X-ray absorption (XAS) spectra were collected in transmission mode at the Cu and Zn K-edge.

5.3 Results and Discussion

5.3.1 Functional group analysis

FT-IR and Raman spectroscopy (Raman) are powerful methods for analyzing the chemical bonding of vibration, rotational, and other low-frequency modes in the phosphate system. $M_2P_2O_7$ has a monoclinic structure with zone-center (C-point) phonons in the lattice vibration of these metal pyrophosphates, and it can be characterized by irreducible representation of the spectroscopic group, C_{2h} . Factor group analysis was conducted by using the procedure of Kroumova *et al* [20]. The single metal pyrophosphate, $\alpha\text{-Cu}_2\text{P}_2\text{O}_7$ ($x = 0.00$), showed four formula units in the unit cell ($Z = 4$). Cu and P atoms were attributed to the 8f position, and O atoms to both the 8f and 4e positions (Wyckoff notation). In order to remove the 3 acoustic modes ($\Gamma_{\text{acoustic}} = A_u + 2B_u$) from the total number ($N_{\text{tot}} = 66$) of vibrations, the optical modes of the lattice vibration were represented by

$$\Gamma_{\text{optic}} = 16A_g + 15A_u + 17B_g + 15B_u \quad (5.2)$$

The odd (un-gerade; A_u and B_u) vibration represents infrared-active modes (Γ_{IR}), as presented in the following equation:

$$\Gamma_{\text{IR}} = 15A_u + 15B_u \quad (5.3)$$

In addition, all even (gerade; A_g and B_g) vibrations are in Raman-active modes (Γ_{Raman}), as exhibited in the following equation:

$$\Gamma_{\text{Raman}} = 16A_g + 17B_g \quad (5.4)$$

The binary metal pyrophosphates, $\text{Cu}_{(2-x)}\text{Zn}_x\text{P}_2\text{O}_7$; $x = 0.50, 1.00, \text{ and } 1.50$, showed two formula units in the unit cell ($Z = 2$). The Cu and Zn atoms are distributed in the 4h position, and P atoms are attributed to the 4i position. The O atoms are attributed to three positions that include 2a, 4i, and 8j. IR-active and Raman-active modes, but not acoustic modes, are shown in the following equations:

$$\Gamma_{\text{IR}} = 6A_u + 9B_u \quad (5.5)$$

$$\Gamma_{\text{Raman}} = 8A_g + 7B_g \quad (5.6)$$



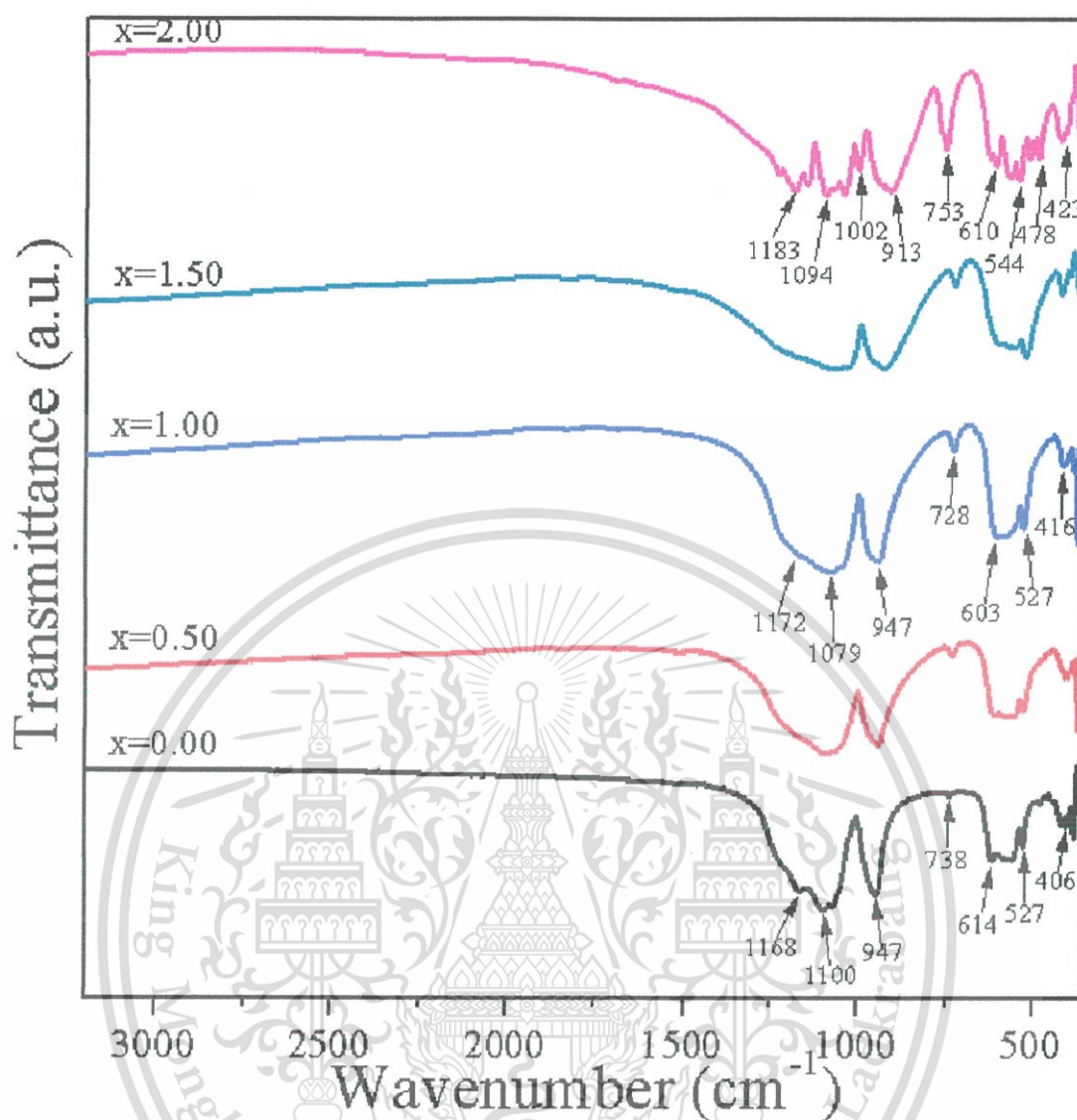


Figure 5.1 FT-IR spectra of $\text{Cu}_{(2-x)}\text{Zn}_x\text{P}_2\text{O}_7$; $x = 0.00 - 2.00$.

In addition, the single metal pyrophosphate, $\alpha\text{-Zn}_2\text{P}_2\text{O}_7$ ($x = 2.00$), exhibited twelve formula units in the unit cell ($Z = 12$) that were quite complex in structure. Zn and P atoms were attributed to the $8f$ position, and O atoms to both $8f$ and $4e$ positions. IR-active and Raman-active modes, but not acoustic modes, are determined by the following equations:

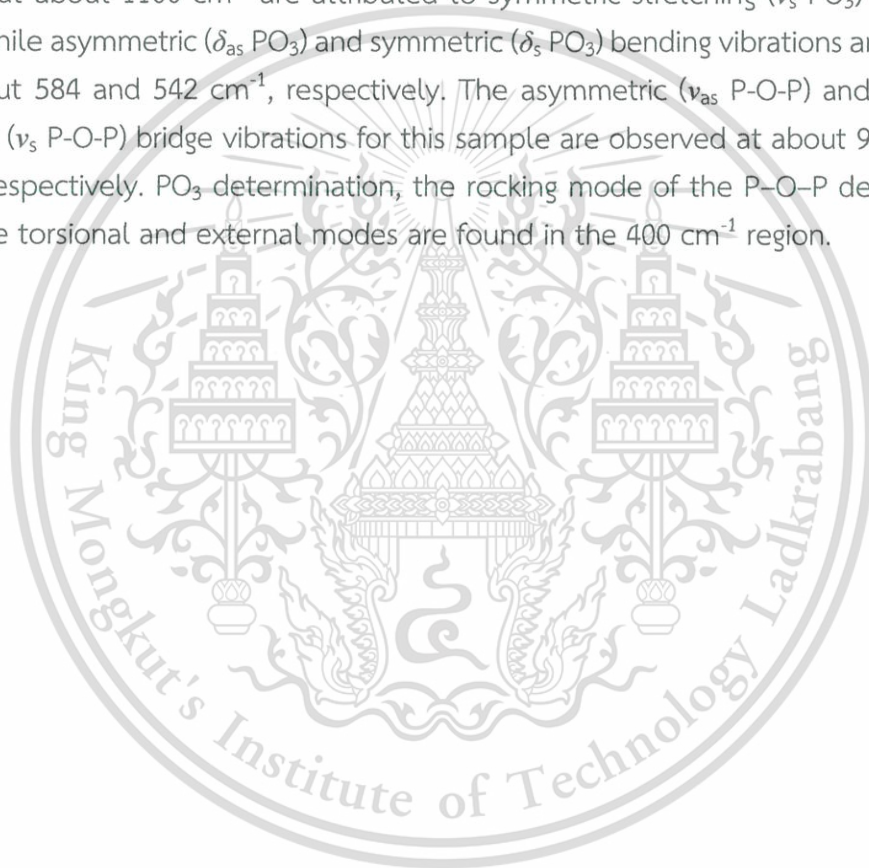
$$\Gamma_{\text{IR}} = 48A_u + 48B_u \quad (5.7)$$

$$\Gamma_{\text{Raman}} = 49A_g + 50B_g \quad (5.8)$$

This material is reserved for educational use only, not allowed for commercial use.

Forbidden to modify the content, and cite the document when use.

As a result, the number of peaks appeared to be greater in both the FT-IR and Raman spectra of α -Zn₂P₂O₇ than in other compounds. A number of peaks were detected using the Raman and IR techniques that related to the symmetry of the crystal structure in the pyrophosphate form. This resulted in the absorption of different resonant frequencies from the frequency of the absorbed radiation, which matches the transition of the energy in the vibrating bond or group. It can be proposed that bonding in the structure is different, as it appears in many of the peaks. The FT-IR spectra of the samples, which closely resemble those of the M₂P₂O₇ pyrophosphate compounds (M = Cu, Cd, Fe, Mn, Ni), are shown in Figure 5.1 [1, 21]. The strong vibration bands at about 1190 and 1060 cm⁻¹ are attributed to asymmetric (ν_{as} PO₃). Vibration bands at about 1100 cm⁻¹ are attributed to symmetric stretching (ν_s PO₃) of the PO₃ unit, while asymmetric (δ_{as} PO₃) and symmetric (δ_s PO₃) bending vibrations are observed at about 584 and 542 cm⁻¹, respectively. The asymmetric (ν_{as} P-O-P) and symmetric stretch (ν_s P-O-P) bridge vibrations for this sample are observed at about 960 and 740 cm⁻¹, respectively. PO₃ deformation, the rocking mode of the P-O-P deformations, and the torsional and external modes are found in the 400 cm⁻¹ region.



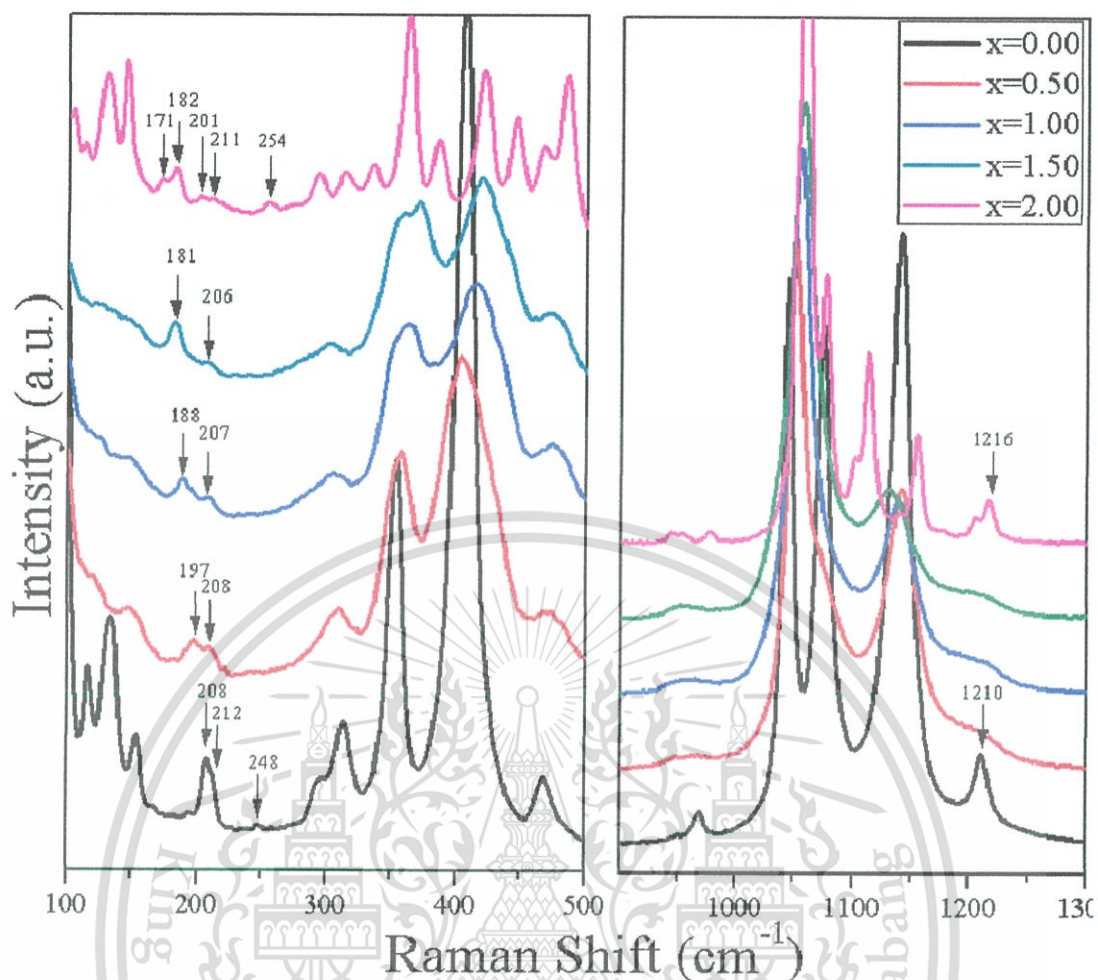


Figure 5.2 Raman spectra of $\text{Cu}_{(2-x)}\text{Zn}_x\text{P}_2\text{O}_7$; $x = 0.00 - 2.00$.

The number of bands in this spectral region confirms the existence of distinct nonequivalent [22, 23]. Additionally, a strong (ν_s P-O-P) band (730 cm^{-1}) was seen in the FT-IR spectrum of the samples, and is known to be the most striking feature of polyphosphate spectra. Most of the FT-IR data showed details of the functional group of the phosphates. Therefore, the support of Raman spectroscopy was used to analyze the metal oxide stretching (M-O) and the phase characteristics (α -, β -phase) of the pyrophosphate compounds at low frequencies. The Raman spectra of the samples are shown in Fig. 5.2 and tabulated in Table 5.1, the result corresponds well with the FT-IR result. Furthermore, the Raman results show a b-phase form in the pyrophosphate groups [24] through a detectably weak peak at approximately 1210 cm^{-1} . The single metal pyrophosphates ($x = 0.00$ and $x = 2.00$), and three distinct peaks that originate from the $\nu_{as}(\text{PO}_3)$ vibrations, are visible at about 1210 , 1140 and 1080 cm^{-1} .

Table 5.1 Vibrational assignment of the samples

Wave number (cm ⁻¹)	FT-IR	Raman	Assignment
1250 - 1200	-	w	α -phase characteristic
1200 - 1100	vs	vs	$\nu_{as}(\text{PO}_3)$
1100 - 1050	vs	vs	$\nu_s(\text{PO}_3)$
1050 - 1000	vs	vs	$\nu_{as}(\text{PO}_3)$
980 - 950	s	vw	$\nu_{as}(\text{POP})$
760 - 730	m	w	$\nu_s(\text{POP})$
650 - 280	s	s	$\delta(\text{OPO}) + \nu(\text{M-O})$
160 - 260	-	w	$\nu(\text{M-O})$
200-100	-	m	lattice vibration

vw: very weak, w: weak, m: medium, s: strong, vs: very strong

The peaks remain at 1140 and 1080 cm⁻¹ in the samples with $x = 0.50$, 1.00, and 1.50, or binary metal pyrophosphates, but the peak at 1210 cm⁻¹ disappears. This indicates that the binary metal phosphates closely resemble the β -Cu₂P₂O₇ phase, with a monoclinic structure and the space group, C2/m. In addition, single metal pyrophosphates exhibited an alpha phase (α -phase). The Cu²⁺ ion is replaced by Zn²⁺ in the Cu_(2-x)Zn_(x)P₂O₇ structure. The M–O stretching band at around 200 cm⁻¹ shifts to a lower wavenumber, and the interatomic distance between the metal and oxygen atom affects the bond strength and absorbs energy also at a lower wavenumber. The single metal pyrophosphates were observed with M–O stretching and peak splitting at 208, 212, and 248 cm⁻¹ for $x = 0.00$. The spectrum of the sample with $x = 2.00$ was observed to have five splitting peaks at 171, 182, 201, 211, and 254 cm⁻¹. These results show that the crystal structure of the sample with $x = 2.00$ has a lower symmetry than that of $x = 0.00$, due to the number of splitting peaks, which causes a different M–O bond length. Regarding binary metal pyrophosphates, splitting peaks were detected in only two regions in each of three samples: 197 and 208 cm⁻¹ for $x = 0.50$, 188 and 207 cm⁻¹ for $x = 1.00$, and 181 and 206 cm⁻¹ for $x = 1.50$. It should be pointed out that the crystal structure of the binary metal pyrophosphates has higher symmetry than the single metal pyrophosphate compound, which is proven using the structural analysis from Rietveld refinement and EXAFS fitting.

5.3.2 Dielectric and optical properties

The mean static atomic dielectric constant of the $\text{Cu}_{(2-x)}\text{Zn}_x\text{P}_2\text{O}_7$; $x = 0.00 - 2.00$ compounds were estimated using the well-known Clausius-Mossotti equation as follows [25]:

$$\varepsilon_r = \left(\frac{3V_m + 8\pi\alpha_D}{3V_m - 4\pi\alpha_D} \right) \quad (5.9)$$

where ε_r is the mean static atomic dielectric constant, α_D is the sum of the dielectric polarizabilities of individual ions, and V_m is the molar volume. The dielectric constant as a function of the composition x is presented in Fig. 5.3, which shows the comparison between calculated data (red bars), and measured results (green bars). The single metal pyrophosphates show a dielectric constant (ε_r) of about 13, which is higher than the ε_r of 10 in binary metal pyrophosphates. The Clausius-Mossotti equation focuses on only the dielectric constant from atomic polarization (electron cloud bias in the electric field). Indeed, the samples were measured at a frequency of 1 MHz for the decreasing extrinsic factor, and the polarization caused the cations (Cu^{2+} , Zn^{2+} , and P^{5+}) and anions (O^{2-}) in the structure to move. The moving ions in the electric field are the cause of the increased dielectric constant compared to the calculated data using the Clausius-Mossotti equation, as considered in this study using the bond angle, bond length, and volume of the octahedral MO_6 .

The coordination complexes have color properties such as green for $[\text{CoF}_6]^{3-}$, red for $[\text{Co}(\text{NH}_3)_5\text{H}_2\text{O}]^{3+}$, and blue for $[\text{Cu}(\text{NH}_3)_4\text{H}_2\text{O}]^{2+}$. The phenomenon of color is explained by crystal field theory (CFT) [26, 27], from which $\text{Cu}_{(2-x)}\text{Zn}_x\text{P}_2\text{O}_7$; $x = 0.00 - 2.00$ compounds show a greenish color, except for the composition with $x = 2.00$, which exhibits a colorless powder. The optical properties and corresponding CIE chromatic coordinates [26, 28, 29] of these samples are shown in Fig. 5.4.

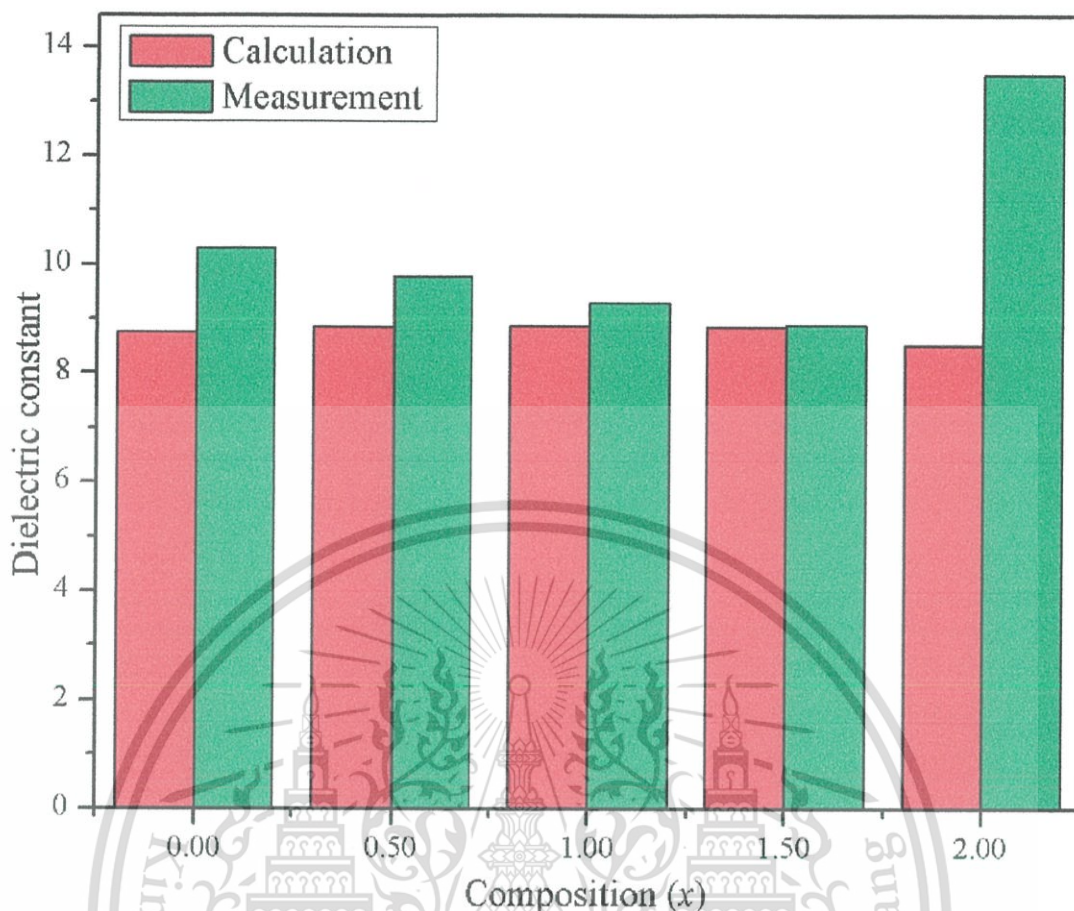


Figure 5.3 Dielectric constant plots of $\text{Cu}_{(2-x)}\text{Zn}_x\text{P}_2\text{O}_7$; $x = 0.00 - 2.00$.

The results of the composition with $x = 0.00$, illustrated a yellowish-green color, while the binary metal compounds ($x = 0.50-1.50$) presented color tones that changed from bluish-green to green. The composition with $x = 2.00$, was seen as colorless. The CIE chromaticity diagram can approximate roughly a visible and an absorption wavelength (nm). The CIE chromaticity coordinates of $\text{Cu}_{(2-x)}\text{Zn}_x\text{P}_2\text{O}_7$; $x = 0.50 - 1.50$ shift from (0.303, 0.366) to (0.292, 0.388) with increasing x , which corresponds to the visible wavelength and shifts from about 506 to 512 nm. The coordinates of $\alpha\text{-Cu}_2\text{P}_2\text{O}_7$ are (0.3454, 0.4081), which corresponds to a wavelength of about 561 nm. This leads to an octahedral crystal field splitting energy (Δ_o) that illustrates z-axis expansion of the octahedral site, with its length calculated using Rietveld refinement analysis and the EXAFS fitting technique.

This material is reserved for educational use only, not allowed for commercial use.

Forbidden to modify the content, and cite the document when use.

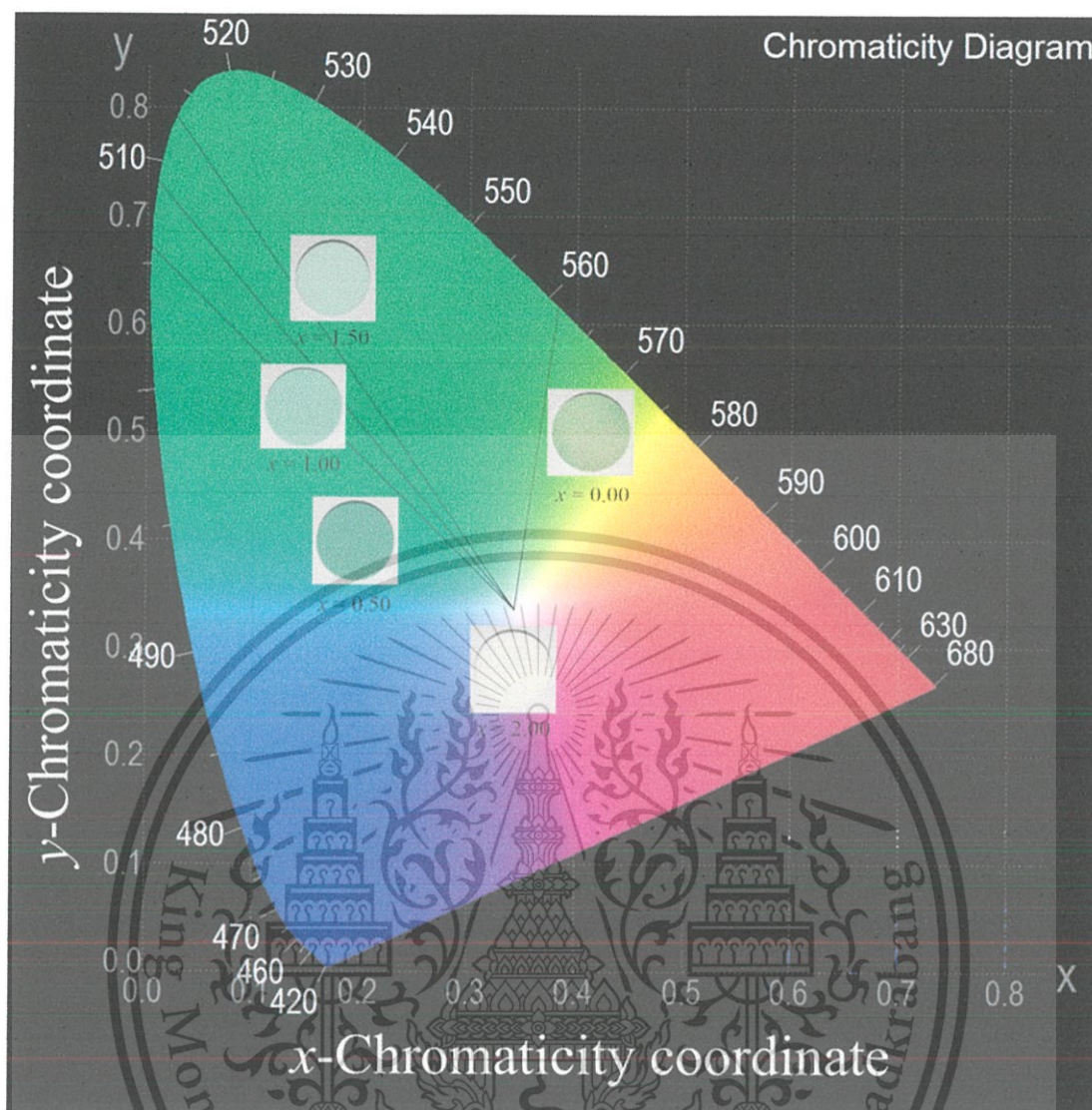


Figure 5.4 CIE chromatic coordinates of $\text{Cu}_{(2-x)}\text{Zn}_x\text{P}_2\text{O}_7$; $x = 0.00 - 2.00$.

5.3.3 Structure analysis

Structural refinement was performed through Rietveld refinement analysis [30] using the FULLPROF package [31]. A pseudo-Voigt shape function was adequate at all times for obtaining good fits for experimental data. The initial model was taken from parameters in the research of Calvo [32]. Factors for the P–O–P bond angle, M–O bond length, and quality of fit (χ^2) were obtained from the Rietveld refinement analysis and are summarized in Table 5.2. Fig. 5.5 shows the calculated (Y_{cal}) and observed (Y_{obs}) diffraction patterns and different ($Y_{\text{obs}} - Y_{\text{cal}}$) peaks of the samples. The refinement plot gives the evolution of the X-ray diffraction (XRD) patterns in the various $\text{Cu}_{(2-x)}\text{Zn}_x\text{P}_2\text{O}_7$; $x = 0.00 - 2.00$ compositions, and their synthesized pyrophosphates show that single-phase compounds constitute solid solutions. Similarity in the XRD patterns (peak

This material is reserved for educational use only, not allowed for commercial use.

positions) is an indication of only small variations in the unit cell parameters, for example, the small difference in size between the Cu^{2+} ion ($R = 0.73 \text{ \AA}$) and Zn^{2+} ion ($R = 0.74 \text{ \AA}$) [33]. Data collected from the Rietveld refinement analysis and the XRD of the powders confirmed the monoclinic system for the metal pyrophosphate compounds, $\text{Cu}_{(2-x)}\text{Zn}_x\text{P}_2\text{O}_7$; $x = 0.00$ (space group $C2/c$ (15), $Z = 4$), $x = 0.50 - 1.00$ (space group $C2/m$ (12), $Z = 2$), and $x = 2.00$ (space group $I2/c$ (15), $Z = 12$). The relationship between the reflection planes (hkl) of $\alpha\text{-Zn}_2\text{P}_2\text{O}_7$, $\alpha\text{-Cu}_2\text{P}_2\text{O}_7$, and $\text{Cu}_{(2-x)}\text{Zn}_x\text{P}_2\text{O}_7$; $x = 0.50 - 1.50$ in Fig. 5.5 projects the lattice size. The results show that the crystal structure size of the binary metal pyrophosphates is smaller than that of single metal pyrophosphates. Also, the long range ordering of the binary metal pyrophosphates is wider than that for single metal pyrophosphates, which was considered to be the (111) plane of $\text{Cu}_{(2-x)}\text{Zn}_x\text{P}_2\text{O}_7$; $x = 0.50 - 1.50$, (112) plane of $\alpha\text{-Cu}_2\text{P}_2\text{O}_7$, and (312) plane of $\alpha\text{-Zn}_2\text{P}_2\text{O}_7$. Furthermore, the refined data showed that the space group of $\text{Cu}_2\text{P}_2\text{O}_7$ had increased ordering the monoclinic system with $C2/c$ to that with $C2/m$, when Cu^{2+} was replaced by Zn^{2+} in the pyrophosphate structure. The final refinement demonstrated the P–O–P bridge and asymmetry of the octahedral MO_6 . Furthermore, the P–O–P bond angle was expanded from 155 to 180. The calculated number of P–O–P clusters decreased from 4 to 2 clusters per unit cell, and the number of octahedral MO_6 sites decreased from 8 to 4 sites per unit cell, due to the increased long range ordering and decreased number of unit cells, which had a direct effect on the electrical properties of the matter. The changing M–O bond length in the binary metal pyrophosphates was exhibited through the color of the matter, which resulted from the changing crystal field splitting [26] in the $3d^9$ -orbital Cu^{2+} ion, and this was observed in Raman spectroscopy.

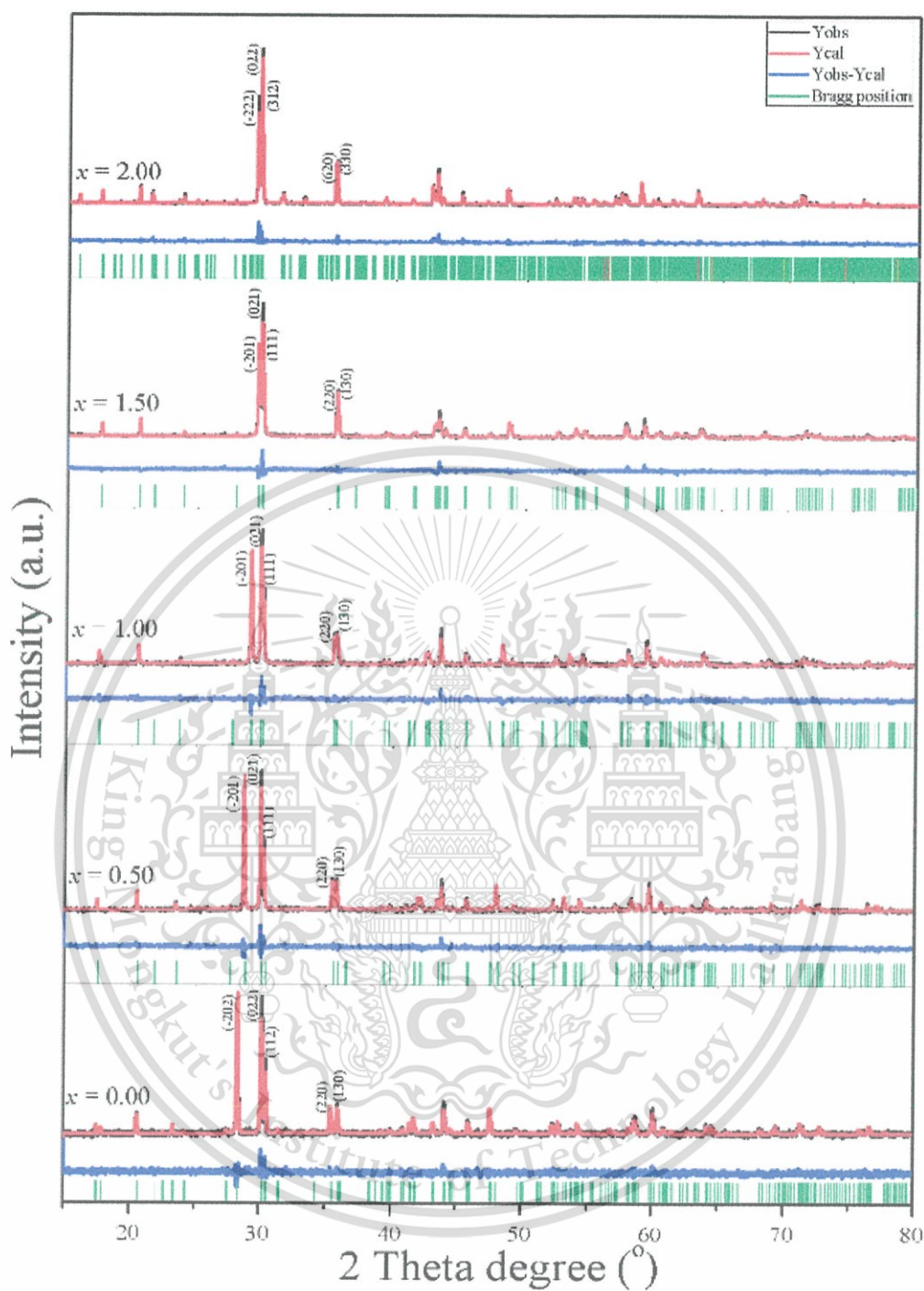


Figure 5.5 Rietveld refinement patterns of $\text{Cu}_{(2-x)}\text{Zn}_x\text{P}_2\text{O}_7$; $x = 0.00 - 2.00$.

Table 5.2 Bond angle and bond length from Rietveld refinement for samples

Sample	x = 0.00	x = 0.50	x = 1.00	x = 1.50	x = 2.00		
POP Angle (°)	154.6 (10)	180.0 (11)	180.0 (11)	180.0 (11)	138.00 (30)	159.00 (30)	
M-O bond length (Å)	M-O1	1.980 (5)	2.016 (2)	2.037 (6)	2.047 (7)	3.135 (15)	2.196 (11) 1.976 (11)
	M-O2	1.942 (6)	1.971 (4)	2.012 (5)	1.999 (2)	1.997 (13)	2.017 (11) 2.010 (12)
	M-O3	2.354 (9)	2.540 (2)	2.476 (3)	2.422 (3)	2.052 (13)	2.371 (16) 1.920 (11)
	M-O3	2.920 (9)	2.540 (2)	2.476 (3)	2.422 (3)	2.181 (15)	2.079 (11) 2.102 (14)
Space group	C2/c	C2/m	C2/m	C2/m	I2/c		
Z	4	2	2	2	12		
χ^2	1.21	1.21	1.33	1.58	1.6		
Lattice parameter	a (Å)	6.8811 (4)	6.7904 (3)	6.7257 (3)	6.6672 (4)	20.1098 (6)	
	b (Å)	8.1173 (4)	8.1576 (3)	8.1986 (3)	8.2413 (4)	8.2732 (2)	
	c (Å)	9.1614 (5)	4.5579 (2)	4.54312 (3)	4.5307 (3)	9.1067 (3)	
	β (°)	109.523 (3)	108.429 (2)	107.464 (3)	106.473 (3)	106.326 (2)	
	V (Å ³)	482.308 (43)	239.538 (17)	238.971 (24)	238.733 (27)	1454.012 (74)	
	R-factor (%)	R _p	9.27	10.0	11.50	14.20	15.70
R _{wp}		11.70	12.70	14.40	17.90	23.10	
R _{exp}		10.68	11.57	13.49	14.43	18.27	

The relationship between the M–O bond length and Raman shift is tabulated in Table 5.3. The Cu²⁺ ion was replaced by Zn²⁺ in the Cu_(2-x)Zn_(x)P₂O₇, which appeared in the M–O stretching band at around 210 cm⁻¹. The stretching band shifted to a lower wavenumber, due to the increased interatomic distance between the metal and oxygen atom, thus affecting the bond strength and energy absorbance. Table 5.3 shows the band position of the M–O bond stretching compared with Rietveld refinement results and an approximation of the calculated frequencies using a fundamental equation. This analysis focused on the tendency of the Raman band shift; therefore, the factors used in the calculation contained only the atomic mass. The results of the calculations were obtained in *k* terms.

This material is reserved for educational use only, not allowed for commercial use.

Forbidden to modify the content, and cite the document when use.

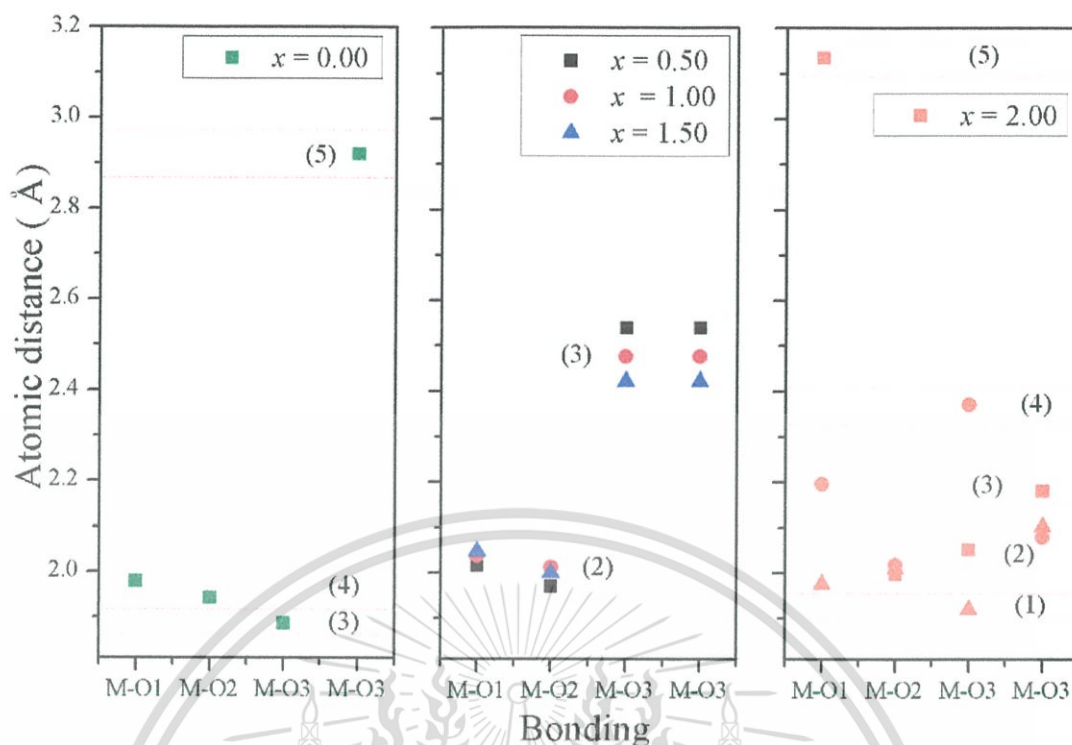


Figure 5.6 The approximate grouping of M-O bonding of $\text{Cu}_{(2-x)}\text{Zn}_x\text{P}_2\text{O}_7$; $x = 0.00 - 2.00$.

Each M-O bond absorbs energy at a different frequency, which brings about a peak in a different position in the Raman shift. The close M-O bond lengths exhibited close peak positions and this developed into an observation band. Thus, the close M-O bond lengths are grouped in Fig. 5.6, with the number of groups corresponding to that of the band in the Raman. All of the results are consistent with compositions with increasing x that correspond to a decreasing average M-O bond length and decreasing observation frequencies in both the Raman shift and fundamental frequency calculation. In addition, the crystal structure and bonding character of the materials were considered. The average bond strength ($\langle S_{P-O} \rangle$) of P^{5+} and O^{2-} in the $[\text{O}_3\text{P}-\text{O}-\text{PO}_3]^{4-}$ or $[\text{P}_2\text{O}_7]^{4-}$ cluster and the bond valence sum ($\langle V_{P-O} \rangle$) were calculated according to the procedure reported by Brown [34].

The average bond strength (Table 5.3) can be estimated from the average sum of the bond valence divided by the average cation coordination numbers, from which the bond valence can be defined by

$$V_{P-O} = \exp\left(\frac{R_0 - R}{B}\right) \quad (5.10)$$

This material is reserved for educational use only, not allowed for commercial use.

Forbidden to modify the content, and cite the document when use.

where R is the length of a bond between P and O atoms. R_0 and B are parameters determined empirically, by which the B parameter must use a universal value for the empirical parameter B ; $B = 0.37 \text{ \AA}$, which makes a one-parameter model relating to the formal valence V , bond length R , and coordination number N . Therefore, the sum of the bond valence is defined by

$$V_i = \sum_j^N \exp\left(\frac{(R_i - R_{ij})}{0.37}\right) \quad (5.11)$$

In divergence, the average bond strength of a single metal pyrophosphate is lower than that in binary metal pyrophosphates. Bond energies and force constants decrease with average bond strength. Determination of a quantitative correlation with the same type of bonding is complex. [35].

Table 5.3 The approximate grouping of M-O bonding and bond strength of samples

Composition	Observed	(1)	(2)	(3)	(4)	(5)
$x = 0.00$	Ra (cm^{-1})	-	-	208	212	248
	Avg D (\AA)	-	-	1.886	1.961	2.92
	Cal.	203.72k				
	$\langle S_{P-O} \rangle$	1.1232				
$x = 0.50$	Ra (cm^{-1})	-	197	208	-	-
	Avg D (\AA)	-	1.994	2.54	-	-
	Cal.	203.57k				
	$\langle S_{P-O} \rangle$	1.2840				
$x = 1.00$	Ra (cm^{-1})	-	188	207	-	-
	Avg D (\AA)	-	2.024	2.476	-	-
	Cal.	203.42k				
	$\langle S_{P-O} \rangle$	1.2938				
$x = 1.50$	Ra (cm^{-1})	-	181	206	-	-
	Avg D (\AA)	-	2.023	2.422	-	-
	Cal.	203.28k				
	$\langle S_{P-O} \rangle$	1.3011				
$x = 2.00$	Ra (cm^{-1})	171	182	201	211	254
	Avg D (\AA)	1.976	2.033	2.188	2.371	3.135
	Cal.	203.14k				
	$\langle S_{P-O} \rangle$	1.0969				

This material is reserved for educational use only, not allowed for commercial use.

Forbidden to modify the content, and cite the document when use.

Ra: Raman shift (cm^{-1})

Avg D: Average atomic distance (\AA)

The EXAFS spectra of the samples for the Cu K-edge and Zn K-edge are shown in Figure 5.7a and 5.7b, respectively. In order to study the environment around Cu atoms, a primitive EXAFS model was taken from parameters obtained from the Rietveld refinement of each sample. The details of EXAFS spectroscopic fitting are summarized in Table 5.4. The results exhibited distortion of octahedral CuO_6 . The sample with $x = 0.00$ showed three main shells, of which the first shell of the spectrum was modeled in consistence with four oxygen atoms that had interatomic distances of 1.9050 \AA and 1.9643 \AA for Cu–O1 and Cu–O2, respectively. Then, the second shell detected only one oxygen atom; Cu–O3, which had an interatomic distance of 2.3001 \AA . The last shell detected the oxygen atom of octahedral CuO_6 , which had an interatomic distance of 2.9136 \AA that combined a scattering phosphorus atom, Cu–P and metal copper atom, as well as Cu–M interaction. In the case of binary metal pyrophosphate samples ($x = 0.50 - 1.50$), the Cu–O3 interatomic distances shortened, and were included in the second shell. As a result, the second shell intensity of the binary metal pyrophosphate samples was seen to be higher than that in $\text{Cu}_2\text{P}_2\text{O}_7$ ($x = 0.00$). The addition of a fourth shell did not improve the quality of fit, and fitting of the Zn K-edge EXAFS was related to that of the Cu K-edge, with the curve shifting to a high radial distance due to a larger atomic radius. The EXAFS spectrum of Zn–O is shown by a single oscillation from four oxygen atoms surrounding the central Zn atom in the first shell, while Zn consists of two oxygen atoms in the second shell. The next shell described the combination of Cu–M (M = Cu/Zn), and Cu–P interaction. The difference in radial distances between Rietveld refinement and EXAFS fitting may be caused by the type of measurement in each technique, in which X-ray diffraction investigated the global structure, and X-ray absorption probed into details of the Cu/Zn local structure [36, 37]. The fitting statistic (R-factor) of the Zn K-edge is worse than that of the Cu K-edge because of two factors. Firstly, the crystal structure of $\alpha\text{-Zn}_2\text{P}_2\text{O}_7$ showed lower symmetry when compared with other samples, and Zn exhibited three different types of atomic position in the unit cell. Secondly, there was a limitation in the instrument, in which the absorption edge of Zn (9659 eV) approached the maximum energy range (1,250 – 10,000 eV) of the BL8 station.

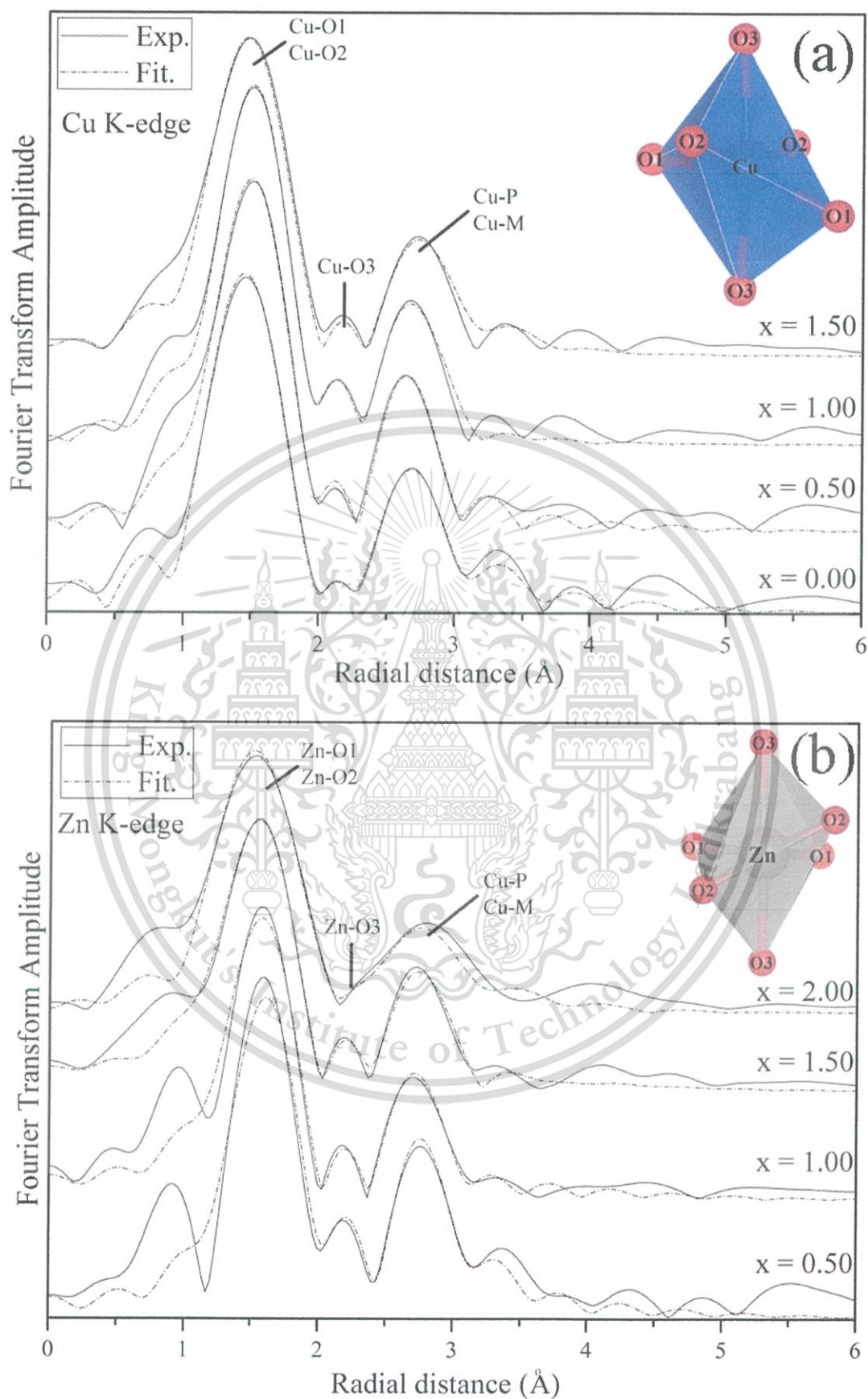


Figure 5.7 EXAFS fitting curves of $\text{Cu}_{(2-x)}\text{Zn}_x\text{P}_2\text{O}_7$; $x = 0.00$ – 2.00 .

This material is reserved for educational use only, not allowed for commercial use.

Forbidden to modify the content, and cite the document when use.

Table 5.4 Bond length from EXAFS fitting for the samples

Composition (x)	Path	Shell	CN	R (Å)	σ^2 (Å ²)	R-factor
0.00	Cu-O1	1	2	1.90505	0.00508	0.00369
	Cu-O2	1	2	1.96427	0.00499	
	Cu-O3	2	1	2.30075	0.03223	
	Cu-O3	3	1	2.91358	0.00796	
0.50	Cu-O1	1	2	1.93460	0.00775	0.00519
	Cu-O2	1	2	1.97180	0.00996	
	Cu-O3	2	2	2.32395	0.02004	
	Zn-O1	1	2	1.98304	0.02336	
	Zn-O2	1	2	2.02117	0.00034	
	Zn-O3	2	2	2.38214	0.03426	
1.00	Cu-O1	1	2	1.93087	0.00575	0.01085
	Cu-O2	1	2	1.97205	0.00647	
	Cu-O3	2	2	2.28269	0.02209	
	Zn-O1	1	2	1.98889	0.02117	
	Zn-O2	1	2	2.03131	0.00406	
	Zn-O3	2	2	2.35128	0.07393	
1.50	Cu-O1	1	2	1.94951	0.00611	0.00763
	Cu-O2	1	2	1.99453	0.25154	
	Cu-O3	2	2	2.26768	0.0392	
	Zn-O1	1	2	2.00714	0.01068	
	Zn-O2	1	2	2.05349	0.01074	
	Zn-O3	2	2	2.33473	0.04422	
2.00	Zn-O1	1	2	1.96928	0.00176	0.02072
	Zn-O2	1	2	2.05357	0.00823	
	Zn-O3	2	1	2.11171	0.00931	
	Zn-O3	3	1	2.58544	0.06587	

The refinement results from P–O–P bond angles can be classified into two groups. The first group includes a P–O–P bond angle of less than 180° such as the compositions with $x = 0.00$ and $x = 2.00$, or single metal pyrophosphates. The sample with $x = 0.00$ had a P–O–P bond angle of 154.6°, and appeared with 4 clusters per unit cell and symmetric P–O bond lengths of 1.574 Å. The composition with $x = 2.00$ showed two different P–O–P bond angles, including 159.0°, which appeared with 8 clusters per unit cell and asymmetric P–O bond lengths of 1.770 Å and 1.390 Å, and

the P–O–P bond angle of 138.0° appeared with 4 clusters per unit cell and a symmetric P–O bond length of 1.640 Å. The second group had a P–O–P bond angle equal to 180°, which contained the compositions with $x = 0.50$, 1.00, and 1.50, or binary metal pyrophosphates. All of the compositions in this group exhibited a P–O–P bond angle equal to 180.0° and appeared with 4 clusters per unit cell and symmetric P–O bond lengths of 1.524 Å, 1.521 Å, and 1.519 Å for $x = 0.50$, 1.00, and 1.50, respectively. However, when compared to an equal space volume, the number of P–O–P clusters in each composition was equal. As a result, the number of P–O–P clusters did not affect the polarization of the samples. The single metal pyrophosphates showed outstanding dielectric constants, while all of the binary metal pyrophosphates presented lower and similar dielectric constants. It was highly possible that high polarization caused a narrow P–O–P bond angle, as analyzed through the dielectric constants of the metal pyrophosphate compounds. In addition, the long P–O bond length of $x = 2.00$ (weak bonding) led to the better polarization of $x = 0.00$, 0.50, 1.00, and 1.50. The binary metal pyrophosphates ($x = 0.50$, 1.00, and 1.50) exhibited a similar dielectric constant, due to all of the P–O–P bond angles being equal. However, the dielectric constant tends to decrease slightly when the component x increases. Results from the final refinement showed decreasing average M–O bond lengths in the octahedral MO_6 site, of which short length bonding caused hard polarization. Additionally, the volume of selected octahedral coordinations was calculated using the method reported by Swanson *et al.* [38] for highlighting the relationship between the polarization and metal oxide bonding. Besides, the distortion index (D) was used to describe the distortion of the structure. Baur [39] described D based on bond lengths in the distortion index as

$$D = \frac{1}{n} \sum_{i=1}^n \frac{|l_i - l_{av}|}{l_{av}} \quad (5.12)$$

where l_{av} is the average bond length, and l_i is the atomic distance from the central atom to the i th coordinating atom.

Table 5.5 The evolution of average bond length, octahedral volume, and distortion index of samples

Composition (x)	Average bond length (Å)	Octahedral volume (Å ³)	Distortion index
0.50	2.1758	12.6629	0.1117
1.00	2.1720	12.5791	0.0935
1.50	2.1659	12.4106	0.0821

Table 5.6 Approximate wavelength of energy absorption

Composition (x)	Wavelength (nm)		Δ_o (kJ/mol)	Cu-O3 (Å) bond length	
	Observed	Absorbed		XRD	XAS
	0.00	561	403	297	2.92
0.50	506	660	181	2.54	2.32
1.00	508	665	180	2.48	2.28
1.50	512	675	177	2.42	2.27
2.00	-	-	-	-	-

These results are tabulated in Table 5.5. All of the data showed decreasing average bond lengths, octahedral volume and distortion index, which exhibited decreasing polarization (dielectric constant, ϵ_r) when the component x increased. These analyses show that polarization of the $\text{Cu}_{(2-x)}\text{Zn}_x\text{P}_2\text{O}_7$; $x = 0.00 - 2.00$ system occurred due to two factors, with shifting O atoms in the collinear P–O–P bridge probably being the main factor in a narrow bond angle that causes high polarization and a high dielectric constant. The movement of M^{2+} ions in the octahedral MO_6 is a supplementary factor, in which the longer average M–O bond length and larger octahedral volume lead to high polarization and the high dielectric constants of metal pyrophosphate compounds.

The distortion of octahedral CuO_6 exhibited decreasing Cu–O3 bond lengths in going from $x = 0.00$ to 1.50, which corresponded to a decreasing octahedral crystal field splitting energy (Δ_o) (Table 5.6). As a result, Zn^{2+} increased this value when the Cu^{2+} in the $\text{Cu}_2\text{P}_2\text{O}_7$ compound was replaced. The color of the compounds illustrated that its hue changes from bluish-green to green. The colorless composition, when $x =$

This material is reserved for educational use only, not allowed for commercial use.

Forbidden to modify the content, and cite the document when use.

2.00 or $\text{Zn}_2\text{P}_2\text{O}_7$, caused a state of fulfillment in the octet rule of the Zn^{2+} ions ($[\text{Ar}] 3d^{10}$) in the structure, despite distortion appearing in the octahedral ZnO_6 site. The octahedral splitting diagram of $\text{Cu}_{(2-x)}\text{Zn}_x\text{P}_2\text{O}_7$; $x = 0.00 - 1.50$ is shown and summarized in Fig. 5.8. Total interpretations showed that a distorted octahedral MO_6 affects both the color of the matter and the polarization of the octahedral unit, as reflected by the dielectric constant.

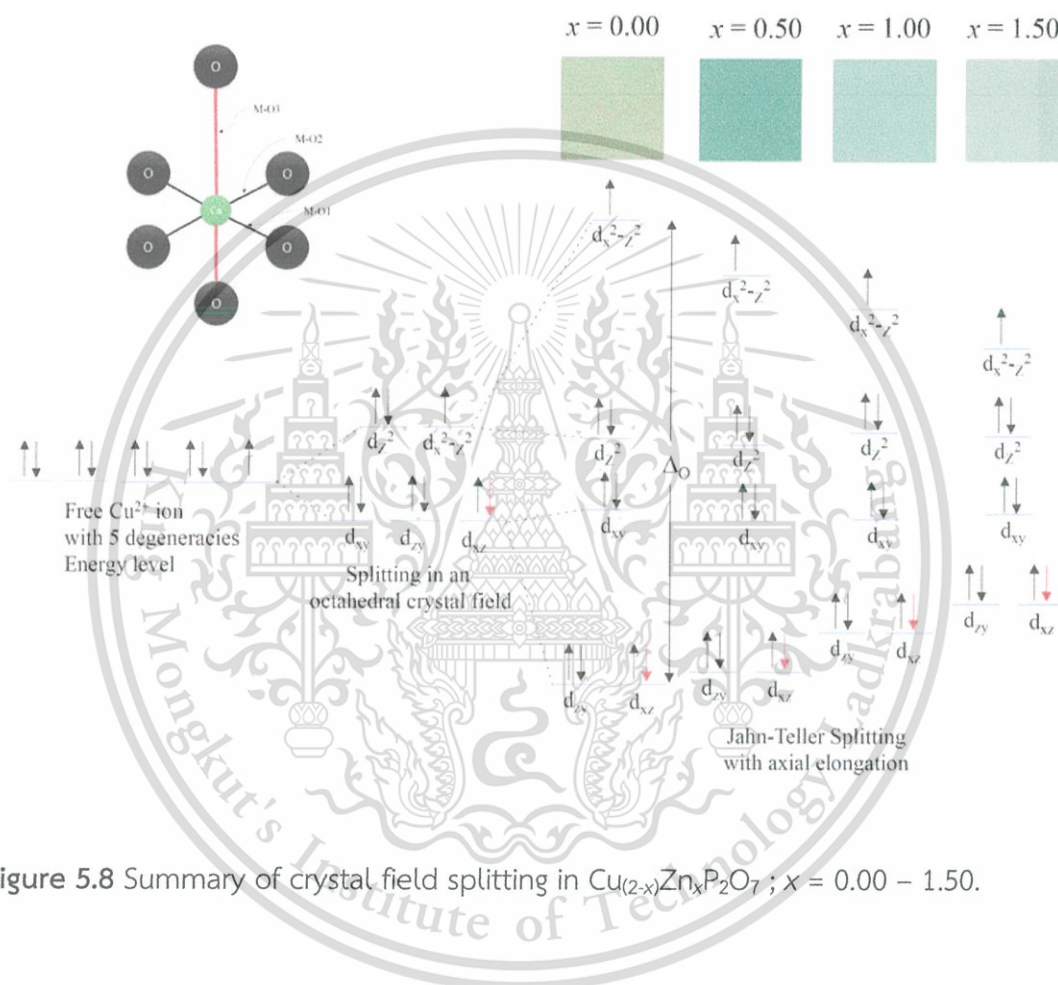


Figure 5.8 Summary of crystal field splitting in $\text{Cu}_{(2-x)}\text{Zn}_x\text{P}_2\text{O}_7$; $x = 0.00 - 1.50$.

5.4 Summary

The single metal pyrophosphates, $\alpha\text{-Cu}_2\text{P}_2\text{O}_7$ and $\alpha\text{-Zn}_2\text{P}_2\text{O}_7$, and binary metal pyrophosphates, $\text{Cu}_{(2-x)}\text{Zn}_x\text{P}_2\text{O}_7$; $x = 0.00 - 1.50$, were synthesized successfully via solid state reaction from metal oxides and ammonium hydrogen phosphate. All of the samples exhibited a single-phase monoclinic system with the $C2/c$ space group for $\alpha\text{-Cu}_2\text{P}_2\text{O}_7$ and $\alpha\text{-Zn}_2\text{P}_2\text{O}_7$ ($I2/c$), and $C2/m$ space group for the binary metal pyrophosphates, which showed that the binary metal pyrophosphates had more structural symmetry than the single metal pyrophosphates. Rietveld refinement

This material is reserved for educational use only, not allowed for commercial use.

Forbidden to modify the content, and cite the document when use.

presented the P–O–P bond angle and P–O bond length in the $P_2O_7^{4-}$ ions, and also details of the octahedral MO_6 including the average bond length, octahedral volume, and distortion index. The addition of Zn^{2+} ions in the $Cu_2P_2O_7$ structure caused distortion of the crystal structure, which led to a change in the bond length and bond angle of the P–O–P clusters in the $P_2O_7^{4-}$ ions, and changed the octahedral volume and average bond lengths of the octahedral MO_6 site. Shifting O atoms in the collinear P–O–P bridge is probably the main factor in ionic polarization, in which a narrow bond angle caused high polarization and high dielectric constants. The movement of M^{2+} ions in octahedral MO_6 is a supplementary factor, in which the longer average M–O bond length and larger octahedral volume led to the high polarization and high dielectric constants of metal pyrophosphate compounds. The color of the samples changed from bluish-green to green when the Zn component increased because the absorption wavelength increased and corresponded to the decrease in z-axis expansion. The final results showed that the distortion of the octahedral MO_6 caused a direct effect on the color of the metal pyrophosphate compounds, while the change of the P–O–P bridge affected the dielectric properties.



REFERENCES

- [1] E. Steger and B. Käßner, "Die infrarotspektren von wasserfreien schwermetall-diphosphaten", *Spectrochimica Acta Part A: Molecular Spectroscopy*, 24, 447-456 (1968).
- [2] B. Boonchom and R. Baitahe, "Synthesis and characterization of nanocrystalline manganese pyrophosphate $Mn_2P_2O_7$ ", *Materials Letters*, 63, 2218-2220 (2009).
- [3] M. Weil and B. Stöger, "Crystal chemistry of transition metal diarsenates $M_2As_2O_7$ (M = Mn, Co, Ni, Zn): Variants of the thortveitite structure", *Acta Crystallographica Section B: Structural Science*, 66, 603-614 (2010).
- [4] A. Durif, *Crystal chemistry of condensed phosphates*, New York, Plenum Press, 1995.
- [5] B. E. Robertson and C. Calvo, "The crystal structure and phase transformation of α - $Cu_2P_2O_7$ ", *Acta Crystallographica*, 22, 665-672 (1967).
- [6] C. Calvo, "THE CRYSTAL STRUCTURE AND PHASE TRANSITIONS OF β - $Zn_2P_2O_7$ ", *Canadian Journal of Chemistry*, 43, 1147-1153 (1965).
- [7] M. A. Petrova, V. I. Shitova, G. A. Mikirticheva, V. F. Popova and A. E. Malshikov, "New data on $Zn_2P_2O_7$ phase transformations", *Journal of Solid State Chemistry*, 119, 219-223 (1995).
- [8] J. I. Bian, D. W. Kim and K. S. Hong, "Microwave dielectric properties of $A_2P_2O_7$ (A = Ca, Sr, Ba; Mg, Zn, Mn)", *Jpn J Appl Phys* 1, 43, 3521-3525 (2004).
- [9] J. J. Bian, D. Kim and K. S. Hong, "Microwave dielectric properties of $(Zn_{1-x}Mn_x)_2P_2O_7$ ", *J Mater Sci*, 40, 1801-1803 (2005).
- [10] W. Wenwei, F. Yanjin, W. Xuehang, L. Sen and L. Shushu, "Preparation via solid-state reaction at room temperature and characterization of layered nanocrystalline $NH_4MnPO_4 \cdot H_2O$ ", *Journal of Physics and Chemistry of Solids*, 70, 584-587 (2009).
- [11] Z. W. Xiao, G. R. Hu, Z. D. Peng, K. Du and X. G. Gao, "Solid state synthesis and characterization of iron(II) pyrophosphate $Fe_2P_2O_7$ ", *Chinese Chemical Letters*, 18, 1525-1527 (2007).
- [12] A. Bensalem, M. Ahluwalia, T. V. Vijayaraghavan and Y. H. Ko, "Synthesis of amorphous $MgHPO_4 \cdot x(R)$ [R = Ethanol; Ethylene glycol] in anhydrous media", *Materials Research Bulletin*, 32, 1473-1483 (1997).
- [13] D. Brandová, M. Trojan, M. Arnold, F. Paulik and J. Paulik, "Mechanism of dehydration and condensation of $CuHPO_4 \cdot H_2O$ ", *Journal of Thermal Analysis*, 34, 1449-1454 (1988).

- [14] D. Brandová, M. Trojan, F. Paulik and J. Paulik, "Mechanism of dehydration of $\text{ZnHPO}_4 \cdot \text{H}_2\text{O}$ ", *Journal of Thermal Analysis*, 32, 1923-1928 (1987).
- [15] B. Boonchom, R. Baitahe, S. Kongtaweelert and N. Vittayakorn, "Kinetics and Thermodynamics of Zinc Phosphate Hydrate Synthesized by a Simple Route in Aqueous and Acetone Media", *Industrial & Engineering Chemistry Research*, 49, 3571-3576 (2010).
- [16] A. Jouini, J. C. Gâcon, M. Ferid and M. Trabelsi-Ayadi, "Luminescence and scintillation properties of praseodymium poly and diphosphates", *Optical Materials*, 24, 175-180 (2003).
- [17] T. Yang and J. Lin, "Hydrothermal syntheses and low temperature magnetic behaviors of $\text{ACo}_3(\text{P}_2\text{O}_7)_2$ (A=Ca, Sr, Ba, Pb)", *Journal of Solid State Chemistry*, 198, 1-5 (2013).
- [18] C. H. Kim and H. S. Yim, "The effect of tetravalent metal on dielectric property in ZrP_2O_7 and TiP_2O_7 ", *Solid State Communications*, 110, 137-142 (1999).
- [19] R. Baitahe and N. Vittayakorn, "Phase formation and evolution of Cu:Zn partials in binary metal pyrophosphates $\text{Cu}_{(2-x)}\text{Zn}_x\text{P}_2\text{O}_7$; $x \approx 1$ ", *Thermochimica Acta*, 596, 21-28 (2014).
- [20] E. Kroumova, M. I. Aroyo, J. M. Perez-Mato, A. Kirov, C. Capillas, S. Ivantchev and H. Wondratschek, "Bilbao Crystallographic Server : Useful Databases and Tools for Phase-Transition Studies", *Phase Transitions*, 76, 155-170 (2003).
- [21] B. Boonchom and N. Phuvongpha, "Synthesis of new binary cobalt iron pyrophosphate CoFeP_2O_7 ", *Materials Letters*, 63, 1709-1711 (2009).
- [22] O. Pawlig and R. Trettin, "Synthesis and characterization of a-hopeite, $\text{Zn}_3(\text{PO}_4)_2 \cdot 4\text{H}_2\text{O}$ ", *Materials Research Bulletin*, 34, 1959-1966 (1999).
- [23] O. Pawlig, V. Schellenschläger, H. D. Lutz and R. Trettin, "Vibrational analysis of iron and zinc phosphate conversion coating constituents", *Spectrochimica Acta Part A: Molecular and Biomolecular Spectroscopy*, 57, 581-590 (2001).
- [24] K. Pogorzelec-Glaser, A. Pietraszko, B. Hilczer and M. Polomska, "Structure and phase transitions in $\text{Cu}_2\text{P}_2\text{O}_7$ ", *Phase Transitions*, 79, 535-544 (2006).
- [25] M. T. Sebastian, *Dielectric materials for wireless communication*, Amsterdam ; Boston, Elsevier, 2008.
- [26] A. El Jazouli, B. Tbib, A. Demourgues and M. Gaudon, "Structure and colour of diphosphate pigments with square pyramid environment around chromophore ions (Co^{2+} , Ni^{2+} , Cu^{2+})", *Dyes and Pigments*, 104, 67-74 (2014).
- [27] L.-T. Chen, C.-S. Hwang, I. L. Sun and I.-G. Chen, "Luminescence and chromaticity of alkaline earth aluminate $\text{M}_x\text{Sr}_{1-x}\text{Al}_2\text{O}_4:\text{Eu}^{2+}$ (M: Ca, Ba)", *Journal of Luminescence*, 118, 12-20 (2006).

- [28] B. Kukliński, D. Wileńska, S. Mahlik, K. Szczodrowski, M. Grinberg and A. M. Klonkowski, "Luminescent $\text{GeO}_2\text{-Pb-Bi}_2\text{O}_3$ glasses co-doped with Tb^{3+} and Eu^{3+} : Excitation energy transfer and color chromaticity", *Optical Materials*, 36, 633-638 (2014).
- [29] B.-K. Kim and R.-H. Park, "Detection and correction of purple fringing using color desaturation in the xy chromaticity diagram and the gradient information", *Image and Vision Computing*, 28, 952-964 (2010).
- [30] H. Rietveld, "A profile refinement method for nuclear and magnetic structures", *Journal of Applied Crystallography*, 2, 65-71 (1969).
- [31] J. Rodríguez-Carvajal, "Recent advances in magnetic structure determination by neutron powder diffraction", *Physica B: Condensed Matter*, 192, 55-69 (1993).
- [32] B. E. Robertson and C. Calvo, "Crystal structure of $\beta\text{-Cu}_2\text{P}_2\text{O}_7$ ", *Canadian Journal of Chemistry*, 46, 605-612 (1968).
- [33] R. Shannon, "Revised effective ionic radii and systematic studies of interatomic distances in halides and chalcogenides", *Acta Crystallographica Section A*, 32, 751-767 (1976).
- [34] I. Brown, "Predicting bond lengths in inorganic crystals", *Acta Crystallographica Section B*, 33, 1305-1310 (1977).
- [35] I. Brown, "Chemical and steric constraints in inorganic solids", *Acta Crystallographica Section B*, 48, 553-572 (1992).
- [36] V. I. Voronin, I. F. Berger, V. A. Cherepanov, L. Y. Gavrilova, A. N. Petrov, A. I. Ancharov, B. P. Tolochko and S. G. Nikitenko, "Neutron diffraction, synchrotron radiation and EXAFS spectroscopy study of crystal structure peculiarities of the lanthanum nickelates $\text{La}^{n+1}\text{Ni}^n\text{O}_y$ ($n=1,2,3$)", *Nuclear Instruments and Methods in Physics Research Section A: Accelerators, Spectrometers, Detectors and Associated Equipment*, 470, 202-209 (2001).
- [37] Y. L. B. Hulyageqi, W. Haschaolu, Z. Song, O. Tegus and I. Nakai, "EXAFS study of $\text{Mn}_{1.28}\text{Fe}_{0.67}\text{P}_{0.46}\text{Si}_{0.54}$ compound with first-order phase transition", *Journal of Electron Spectroscopy and related Phenomena*, 196, 104-109 (2014).
- [38] D. K. Swanson and R. C. Peterson, "Polyhedral volume calculations", *The Canadian Mineralogist*, 18, 153-156 (1980).
- [39] W. Baur, "The geometry of polyhedral distortions. Predictive relationships for the phosphate group", *Acta Crystallographica Section B*, 30, 1195-1215 (1974).

CHAPTER 6

DIELECTRIC PROPERTIES AND CHARACTERIZATIONS OF BINARY $\text{Cu}_{(2-x)}\text{Mg}_x\text{P}_2\text{O}_7$ PYROPHOSPHATES

Based on article published in *Ferroelectrics* 490 (2016) 174-183

This chapter presented the structure-dielectric properties relationship of binary $\text{Cu}_{(2-x)}\text{Mg}_x\text{P}_2\text{O}_7$ pyrophosphates. Samples of the binary metal pyrophosphate, $\text{Cu}_{(2-x)}\text{Mg}_x\text{P}_2\text{O}_7$ ($x = 0.00 - 2.00$) were prepared via solid state conventional method. Vibrational bands of $[\text{P}_2\text{O}_7]^{4-}$ anion which contains the O–P–O radical ($[\text{PO}_2]^-$) and the P–O–P bridge ($[\text{OPO}]^-$) and approximate M–O stretching were identified by Raman scattering. A strong P–O–P band was observed clearly in Raman spectra, which indicated the formation of solid solution. The purity of synthetic powders were characterized by X-ray diffraction (XRD). The XRD patterns indicated that all the samples exhibited a single monoclinic phase structure. The complete solid solutions in the $\text{Cu}_{(2-x)}\text{Mg}_x\text{P}_2\text{O}_7$ ($x = 0.00 - 2.00$) system were obtained. The unit cell volume changed, due to the difference between the final product structure and $\text{Cu}_2\text{P}_2\text{O}_7$. X-ray absorption near the edge structure (XANES) technique was used to confirm oxidation state of copper in the $\text{Cu}_{(2-x)}\text{Mg}_x\text{P}_2\text{O}_7$. The relative permittivity and dielectric loss of the samples were measured. The bond length and bond angle were analyzed by EXAFS and Raman techniques. The relative permittivity was seen to maintain temperature by substituting Mg^{2+} with $\text{Cu}_2\text{P}_2\text{O}_7$. These results were used to explain the crystal structure of materials in order to change the bond which affects dielectric phenomena.

6.1 Introduction

Metal phosphate ($\text{M}_x(\text{PO}_4^{3-})_y$ species) materials show interesting properties nowadays because of their wide applications in microwave dielectric materials, corrosion-resistant coatings, biomedical cements, chelating agents, glass ceramics, and high-quality fertilizers [1-3]. The pyrophosphate $\text{M}_2\text{P}_2\text{O}_7$ compounds have been reported to possess good dielectric loss properties as well as a relatively low sintering temperature [1]. It has been observed that an M radius structure greater than 0.97 Å [4] is a dichromate type ($\text{M} = \text{Ca}^{2+}, \text{Sr}^{2+}, \text{Ba}^{2+}, \text{Pb}^{2+},$ and Cd^{2+}), in which a pair of $\text{P}_2\text{O}_7^{4-}$ groups in eclipsed conformation crystallize at about the center of symmetry, with

This material is reserved for educational use only, not allowed for commercial use.

Forbidden to modify the content, and cite the document when use.

bridging O atoms spreading towards each other. When the M radius is less than 0.97 Å ($M = \text{Ni}^{2+}, \text{Mg}^{2+}, \text{Zn}^{2+}, \text{Co}^{2+}, \text{Cu}^{2+}, \text{and } \text{Mn}^{2+}$), the structure is a thortveitite type, in which $\text{P}_2\text{O}_7^{4-}$ occurs in staggered conformation, and thortveitite-type pyrophosphate α - $\text{Cu}_2\text{P}_2\text{O}_7$ or α - $\text{Mg}_2\text{P}_2\text{O}_7$ exhibits a rather low sintering temperature when compared with metal oxides. However, single pyrophosphates groups (such as $\text{Cu}_2\text{P}_2\text{O}_7$, $\text{Mg}_2\text{P}_2\text{O}_7$, $\text{Zn}_2\text{P}_2\text{O}_7$, and $\text{Co}_2\text{P}_2\text{O}_7$) still show phase transition when changing temperature. Therefore, this primary research aimed to modify the structure of these materials in order to decrease dielectric loss and manipulate the relative permittivity to constant variations with temperature.

Most studies of metal phosphate focused on the synthesis and characterizations of both bulk [5, 6] and nano particles [7], kinetics and the thermodynamics of reaction [8, 9], and their properties [10, 11]. Nevertheless, the study of the relationship between dielectric properties and crystal structure is not widely understood, and is therefore of interest. The secondary aim of this study was to probe the crystal structure which influence dielectric phenomena of binary metal pyrophosphate compounds. Dielectric properties of the metal pyrophosphate group are due to two effects that comprise movement of M^{2+} ions in the octahedral MO_6 and shift of O atoms in the collinear P–O–P bridge. If the collinear P–O–P bond of the pyrophosphate ion is distorted, some distortion of octahedral MO_6 also can occur, which would improve the dielectric property of the molecule by producing polarization [12]. It is well known that the highly relative permittivity of tetragonal perovskite BaTiO_3 comes from off-centred Ti^{4+} ions in octahedral TiO_6 . Putting a solid solution of Mg^{2+} into $\text{Cu}_2\text{P}_2\text{O}_7$ structure may bring about distortion of MO_6 and the collinear P–O–P bond and improve the dielectric properties of $\text{Cu}_2\text{P}_2\text{O}_7$ with a low sintering temperature. This research synthesized $\text{Cu}_{(2-x)}\text{Mg}_x\text{P}_2\text{O}_7$ ($x = 0.0 - 2.0$) before Raman, and XRD techniques investigated the crystal structure that affects dielectric properties. The phenomena of polarization in the crystal structure of compounds also were studied in order to characterize via bond length and bond angle.

6.2 Experimental procedure

Synthesis of $\text{Cu}_{(2-x)}\text{Mg}_x\text{P}_2\text{O}_7$ ($x = 0.00, 0.50, 1.00, 1.50, \text{ and } 2.00$) was conducted using the conventional method. High purity $(\text{NH}_4)_2\text{HPO}_4$ (99%) CuO (99.9%), and MgO (99.9%), were used as starting materials. Stoichiometric mixtures of raw materials were homogenized by vibratory milling with Yttria stabilized zirconia media in ethanol for 4 hrs. These were calcined at $800^\circ\text{C}/24$ hrs for $x = 0.00$, and $950^\circ\text{C}/3$ days for $x = 0.50 - 2.00$. The calcined powders were ball-milled again, pressed uniaxially into small pellets at the pressure of 1000 kg/cm^2 and sintered at 1000°C for 24h. The theoretical density of all ceramics observed was about 95–98%. Raman spectra were recorded in the range of $1300\text{--}100 \text{ cm}^{-1}$ with eight scans on a thermo scientific DXR Raman microscope. The samples were excited with 488 nm light from an Ar^+ ion laser and the power of the incident beam was 12.5 mW. The crystal structure and crystallite sizes of the prepared samples were studied by X-ray powder diffraction with $\text{Cu K}\alpha$ radiation ($\lambda = 0.1546 \text{ nm}$). using a Bruker D8 Advance X-ray diffractometer (Bruker AXS, Karlsruhe, Germany) The dielectric properties were measured as a function of frequency (1–1000 kHz) and temperature (room temperature to 150°C) using an LCR meter (HP4284A; Hewlett- Packard, Palo Alto, CA).

Furthermore, substitutional solid solutions, in accordance with the Hume-Rothery rules, may form if the solute and solvent have: similar atomic radii; $R_{\text{Cu(II)}} = 0.73 \text{ \AA}$ and $R_{\text{Mg(II)}} = 0.72 \text{ \AA}$ [13], similar electronegativities; $\text{Cu} = 1.90$ and $\text{Mg} = 1.31$, similar valency; $\text{Cu} = 2+$ and $\text{Mg} = 2+$. And same crystal structure; $\beta\text{-Cu}_2\text{P}_2\text{O}_7 = \text{Monoclinic, } C2/m$ and $\beta\text{-Mg}_2\text{P}_2\text{O}_7 = \text{Monoclinic, } C2/m$. These data show a high possibility of substitutional solid solution between Cu and Mg ions in pyrophosphate compounds. The X-ray absorption spectroscopy (XAS) was conducted on the beam line (BL8) of the National Synchrotron Research Center (Thailand). A double crystal $\text{Ge}(220)$ was used for the EXAFS monochromator. X-ray absorption (XAS) spectra at the Cu K-edge were collected in transmission mode. The Cu foil, Cu_2O , CuO were used as a reference materials for X-ray absorption near-edge spectroscopy (XANES) measurements. The data from XANES were analyzed by a ATHENA supporting program.

6.3 Results and Discussion

6.3.1 Functional group analysis

The Raman spectra of $\text{Cu}_{(2-x)}\text{Mg}_x\text{P}_2\text{O}_7$ are shown in Figure 6.1. It is clearly noticeable that the studied ceramics display more sharpness and splitting, especially in the low-frequency region ($1300\text{--}100\text{ cm}^{-1}$), indicating polymerization of $[\text{PO}_4^{3-}]$ to $[\text{P}_2\text{O}_7]^{4-}$. The vibration analysis of the $\text{P}_2\text{O}_7^{4-}$ ion which contains the O–P–O radical ($[\text{PO}_2]^-$) and the P–O–P bridge ($[\text{OPO}]^-$) and approximate M–O stretching band were exhibited in Raman spectra. The Raman spectra are similar to those observed by Boonchom *et al* [14]. The strong vibration bands around 1100 cm^{-1} are recognized to stretching of the PO_3 unit. The asymmetric ($\nu_{\text{asym}} \text{POP}$) and symmetric stretch ($\nu_{\text{sym}} \text{POP}$) bridge vibration for these samples are detected at about 960 and 730 cm^{-1} , respectively, while the asymmetric ($\delta_{\text{asym}} \text{PO}_3$) and symmetric ($\delta_{\text{sym}} \text{PO}_3$) bending vibration are observed at about 600 and 520 cm^{-1} , respectively. The metal oxide bonds are found in the $460\text{--}400\text{ cm}^{-1}$ region. When Cu^{2+} is replaced by Mg^{2+} in the $\text{Cu}_{(2-x)}\text{Mg}_x\text{P}_2\text{O}_7$ solid solutions, the Raman spectra show an important displacement of an absorption band found at about 420 cm^{-1} . This band can be assigned to the M–O bond lengths, which are responsible for the wave number increase from 411 to 458 cm^{-1} [15]. In composition $x = 0.00$ and 2.00 phases, three distinct bands that originate from the $\nu_{\text{asym}}(\text{PO}_3)$ vibrations are visible at 1214 , 1146 and 1080 cm^{-1} . In the composition of $x = 0.50$, 1.00 , and 1.50 phases, the bands remain at 1146 and 1080 cm^{-1} , but disappear at 1214 cm^{-1} . This indicates binary metal phosphates that closely resemble those of the $\beta\text{-Mg}_2\text{P}_2\text{O}_7$ phase, because the medium peak appears at around 1220 cm^{-1} only in the alpha phase [16].

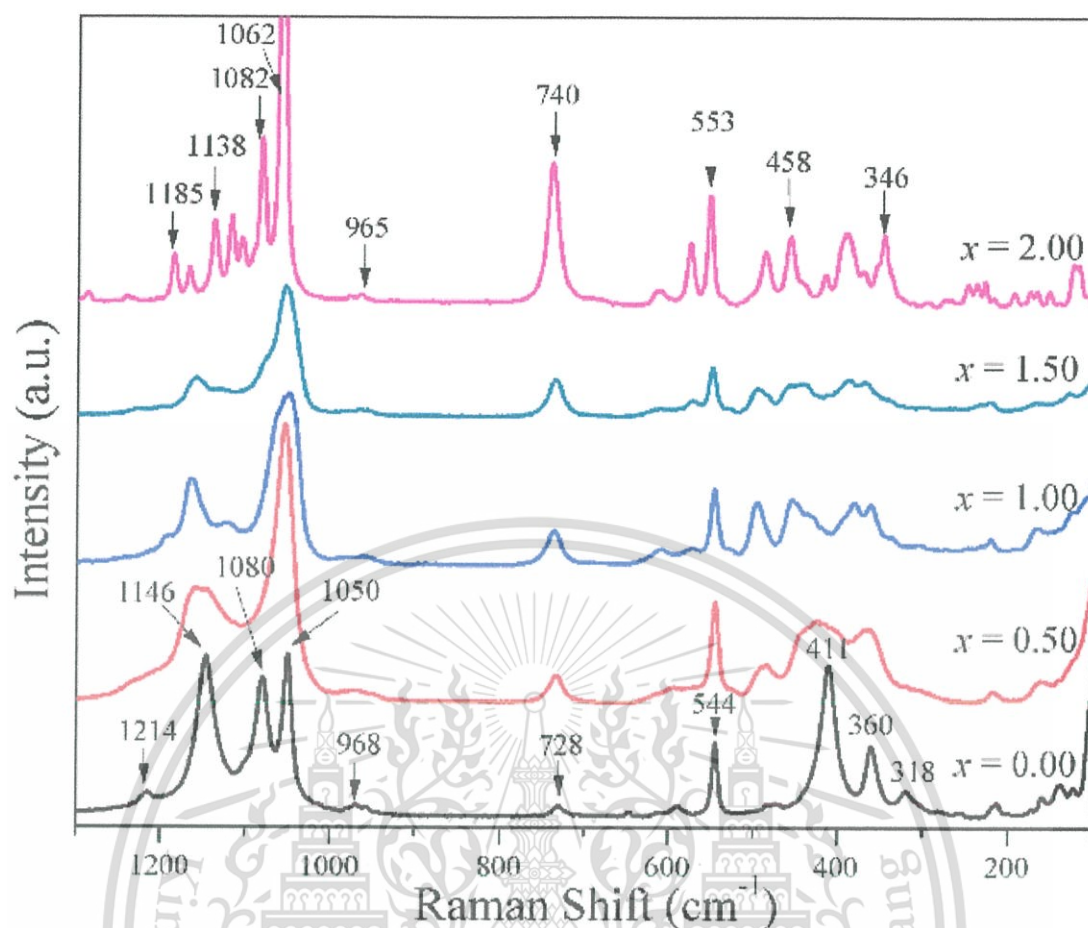


Figure 6.1 Raman spectra of $\text{Cu}_{(2-x)}\text{Mg}_x\text{P}_2\text{O}_7$; $x = 0.00 - 2.00$.

6.3.2 Crystal structure analysis

Figure 6.2 shows the XRD patterns of $\text{Cu}_{(2-x)}\text{Mg}_x\text{P}_2\text{O}_7$ ($x = 0.00, 0.50, 1.00, 1.50,$ and 2.00). Based on our analysis, the synthesized materials are solid solution and not a combination of the individual phases. These results indicate that the binary and the single metal compounds for $\text{X}_2\text{P}_2\text{O}_7$ ($X = \text{Ni}, \text{Mn}, \text{Zn}, \text{Mg}, \text{Cu}, \text{Co}$) types are isostructural. Consequently, all XRD pattern can be indexed distinctly based on a pure monoclinic phase with space group $\text{C2}/c$ ($Z=4$) for $\alpha\text{-Cu}_2\text{P}_2\text{O}_7$, $\text{P2}_1/c$ ($Z=4$) for $\alpha\text{-Mg}_2\text{P}_2\text{O}_7$, and $\text{C2}/m$ ($Z=2$) for the samples as a function of $x = 0.50 - 1.50$, which noted to be similar to those of the standard XRD patterns of $\text{M}_2\text{P}_2\text{O}_7$ (PDF no. 44-0180 for Cu, PDF no. 75-1055 for Mg and PDF no.82-0973 for CuMg), respectively.

This material is reserved for educational use only, not allowed for commercial use.

Forbidden to modify the content, and cite the document when use.

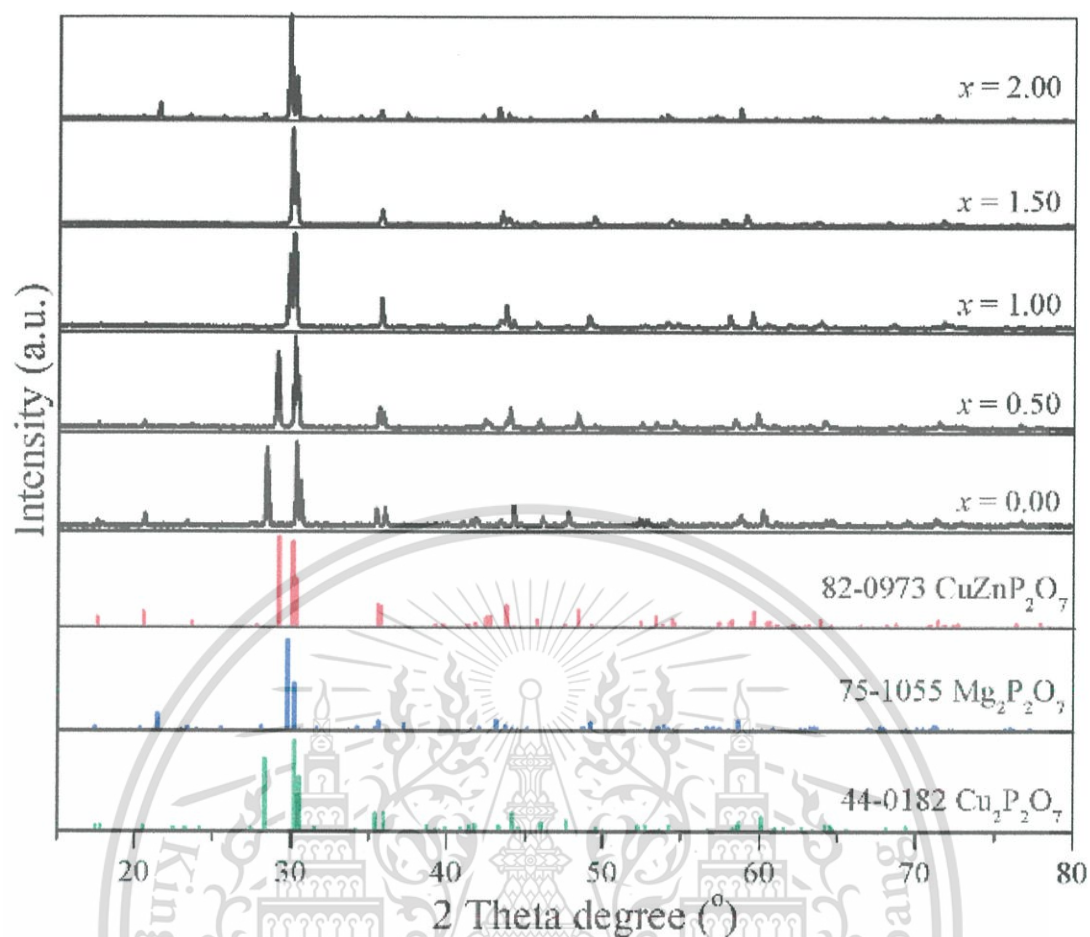


Figure 6.2 XRD patterns of $\text{Cu}_{(2-x)}\text{Mg}_x\text{P}_2\text{O}_7$; $x = 0.00 - 2.00$.

Table 6.1 Lattice parameters of $\text{Cu}_{(2-x)}\text{Mg}_x\text{P}_2\text{O}_7$; $x = 0.00 - 2.00$ calculated from XRD data.

Composition (x)	Systems	a (Å)	b (Å)	c (Å)	β (°)	V (Å) ³
0.00	PDF no. 44-0182	6.88(0)	8.11(3)	9.16(1)	109.52(1)	482.30(0)
0.50		6.75(1)	8.15(0)	4.54(4)	107.07(2)	238.75(2)
1.00	This work	6.64(0)	8.21(4)	4.50(0)	106.52(0)	235.19(0)
1.50		6.57(4)	8.24(1)	4.48(2)	105.50(0)	233.71(1)
2.00	PDF no. 75-1055	6.94(0)	8.28(0)	9.04(0)	113.79(4)	476.47(4)

Table 6.1 presents the variation in these unit cell parameters with x . The half decreasing of lattice parameter c due to changing of space symmetry elements in the molecules from c (glide plane axis perpendicular to principal axis) to m (mirror plane perpendicular to principal axis) which show that increase symmetry in crystal structure. The lattice parameters a , c and β decrease. Parameter b increases, but the volume shows little change, due to the similar ionic radii of Mg and Cu ($R_{\text{Cu(II)}} = 0.73 \text{ \AA}$ and $R_{\text{Mg(II)}} = 0.72 \text{ \AA}$). These results indicated that when the crystal structure of $\alpha\text{-Cu}_2\text{P}_2\text{O}_7$ was disturbed by different kinds of atom (Mg atoms). As a result the new crystal structure is stable at both low and high temperature. The average crystallite size of $72 \pm 10 \text{ nm}$ for $\alpha\text{-Cu}_2\text{P}_2\text{O}_7$ sample was calculated from X-ray line broadening of the reflections of (002), (-112), (-202), (022), (112), (220), and (130), using Scherrer equation;

$$D = 0.89\lambda/\beta\cos\theta \quad (1)$$

where D is the mean size of the ordered (crystalline) domain, which may be smaller or equal to the grain size, θ is the diffraction angle, λ is the wavelength of X-ray radiation, and β is the full width at half maximum (FWHM) [17], and were found to be $83 \pm 9 \text{ nm}$ for sample $\alpha\text{-Mg}_2\text{P}_2\text{O}_7$ was calculated from X-ray line broadening of the reflections of (111), (002), (020), (212), (410) and (-422). The average crystallite size of 79 ± 9 , 73 ± 6 , and $61 \pm 7 \text{ nm}$ for binary metal pyrophosphates at $x = 0.50$, 1.00 , and 1.50 , respectively, were calculated from X-ray line broadening of the reflections of (110), (001), (-201), (021), (111), (220), and (130). The data of Raman and XRD results confirms that to single phase.

Table 6.2 Energy positions of the absorption edges observed for measured samples.

Compounds	Threshold value (E ₀)
Cu(0)	8979.27
Cu(I)	8979.91
Cu(II)	8986.25
0.00	8986.08
0.50	8986.65
1.00	8986.45
1.50	8986.69

Normally, the oxidation state of Mg is two plus. However, the oxidation state of Cu can be one plus or two plus in phosphate form. So, X-ray absorption near the edge structure (XANES) technique was used to confirm oxidation state of copper in the $\text{Cu}_{(2-x)}\text{Mg}_x\text{P}_2\text{O}_7$ ($x = 0.0, 0.5, 1.0, \text{ and } 1.5$) compounds. As XANES is very sensitive to both changes in the local geometry and the oxidation state, spectra collected at both edges could help in understanding Fourier transform evolutions. The XANES spectra of samples, as shown at the Cu K-edge in Figure 6.3, remain identical to the signal observed for Cu(II)O (Table 6.2), whatever the Cu content. Copper atoms thus remain Cu^{2+} in a monoclinic symmetry.

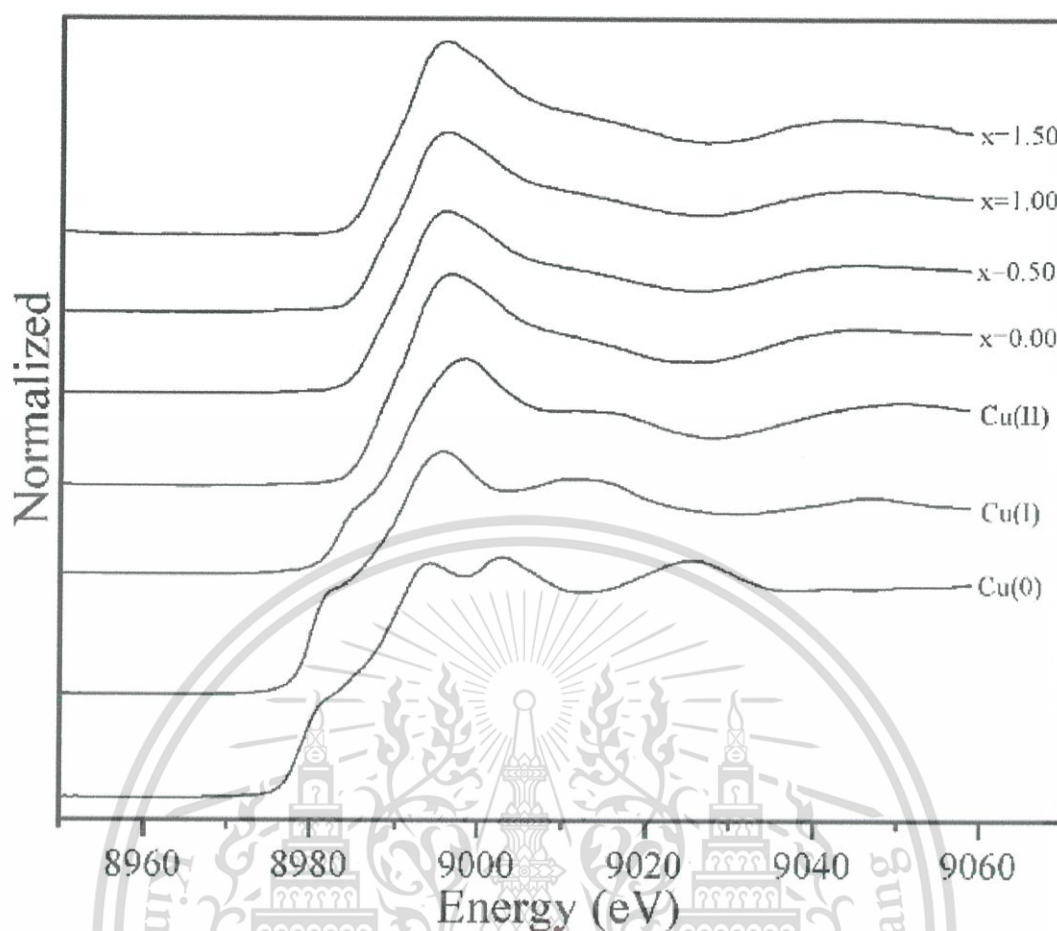


Figure 6.3 XANES spectra of $\text{Cu}_{(2-x)}\text{Mg}_x\text{P}_2\text{O}_7$; $x = 0.00 - 2.00$.

Table 6.3 Relative permittivity and dielectric loss of samples.

Composition (x)	%TD	Corrected relative permittivity			Dielectric loss		
		10k	100k	1000k	10k	100k	1000k
0.00	98.5	11.11	10.66	10.44	0.0432	0.0224	0.0091
0.50	96.7	9.64	9.46	9.36	0.0017	0.0045	0.0072
1.00	95.7	9.19	8.92	8.82	0.0196	0.0117	0.0055
1.50	96.4	6.67	6.43	8.19	0.0175	0.0095	0.0035
2.00	95.3	14.13	13.92	13.87	0.0105	0.0094	0.0076

This material is reserved for educational use only, not allowed for commercial use.

Forbidden to modify the content, and cite the document when use.

6.3.3 Dielectric properties

The relative permittivity (ϵ_r) and dielectric loss versus composition plots at 10, 100, and 1,000 kHz of $\text{Cu}_{(2-x)}\text{Mg}_x\text{P}_2\text{O}_7$ are shown in Figure 6.4. The effect of porosity on the permittivity was eliminated by applying the Bosman and Havinga's correction [18], shown in Eq. (2), which can be used for dense ceramics having porosity lower than 5%:

$$\epsilon_{r, \text{ corrected}} = \epsilon_{r, \text{ measured}}(1+1.5P) \quad (2)$$

where $\epsilon_{r, \text{ measured}}$ and $\epsilon_{r, \text{ corrected}}$ are the measured and corrected relative permittivity, respectively, and P is fractional porosity and tabulated in table 6.3. The bond angle and bond length were performed by the Raman scattering and EXAFS results for investigated phenomena of dielectric properties. Dielectric properties of the metal pyrophosphate group include two effects that comprise to shift of O atoms in the collinear P–O–P bridge and movement of M^{2+} ions in the octahedral MO_6 . In the part of shifting of O atoms in the collinear P–O–P bridge. The sample as a function of $x = 0.50 - 1.50$, all compositions have the space group C2/m . Previous researches reported that all of pyrophosphates compound which have monoclinic system with C2/m , the P–O–P angle are 180 degrees. Single metal pyrophosphates, $\alpha\text{-Cu}_2\text{P}_2\text{O}_7$ and $\alpha\text{-Mg}_2\text{P}_2\text{O}_7$ were exhibited the P–O–P angle to 157° [19] and 144° [20], respectively. In this case, the octahedral MO_6 site via bond strength or average bond length was considered by EXAFS data and supported by Raman spectra in the wavenumber about 420 cm^{-1} (M–O stretching). As extended X-ray absorption fine structure (EXAFS) is very sensitive to change in local geometry, spectra collected at both edges could help in understanding Fourier transform evolutions. The data set were then analyzed by 'data processing' with ATHENA software [21]. The structure parameters of this analysis included approximate interatomic distances. The results demonstrated the asymmetry of CuO_6 octahedral due to the occurred of the little peak around last part of 1^{st} shell introducing the Jahn-Teller distortion effect undergone by the copper octahedral centered site into the model or this peak may be the ghost peak [22]. The first shell was the consisting of six oxygen atoms, (M–O) with interatomic distances about 2.10 \AA . The next shell was described the combination of Cu–M (M=Cu/Mg), and Cu–P interaction. However, in this work was focus on 1^{st} shell of M– O_6 octahedral.

This material is reserved for educational use only, not allowed for commercial use.

Forbidden to modify the content, and cite the document when use.

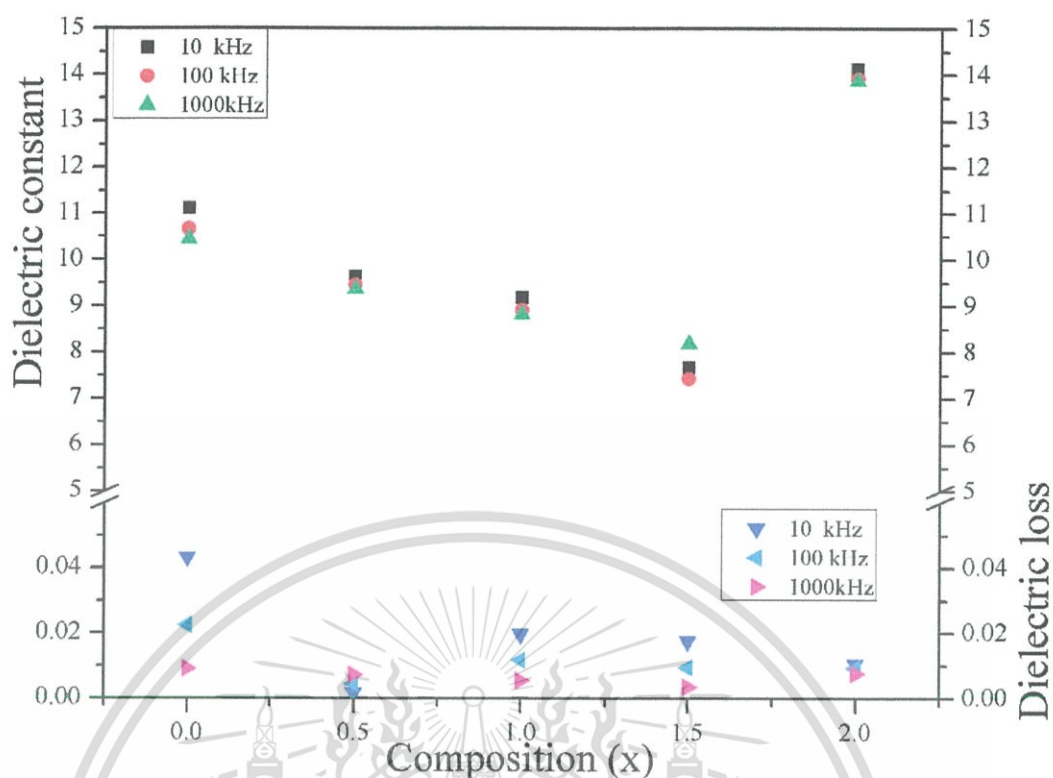


Figure 6.4 Plots of the relative permittivity and loss of $\text{Cu}_{(2-x)}\text{Mg}_x\text{P}_2\text{O}_7$; $x = 0.00 - 2.00$.

6.3.4 Correlation between structure and dielectric properties

The relation of POP angle, M-O atomic distances from Raman and EXAFS were tabulated in table 6.4. The average bond length of Mg-O₆ ($x = 2.00$) from XAS technic cannot be measured due to limitations of the instrument. Nevertheless, this data was supported by Raman result with increasing peak position which corresponded to decreasing bond length of EXAFS data. The single metal pyrophosphate, $x = 2.00$ ($\text{Mg}_2\text{P}_2\text{O}_7$) was shown to be the highest ϵ_r and the least of P-O-P angles is 144 degrees, while $x = 0.00$ ($\text{Cu}_2\text{P}_2\text{O}_7$) was shown second ϵ_r and the second lowest of P-O-P angle is 157 degrees. Binary metal pyrophosphates, $x = 0.50 - 1.50$ with P-O-P angle is 180 degrees which exhibited ϵ_r less than single metal pyrophosphate compounds. These results show that the P-O-P angle is probably main factor for polarization of pyrophosphates group, by means of small P-O-P angle cause good polarization and good dielectric properties.

This material is reserved for educational use only, not allowed for commercial use.

Forbidden to modify the content, and cite the document when use.

Table 6.4 Bond angle, M-O stretching position, and average bond length of samples

Composition (x)	POP angle		M-O ₆	
	Angle (°)	Peak position (cm ⁻¹)	Bond length (Å)	
0.00	157	411	2.18	
0.50	180	420	2.16	
1.00	180	431	2.13	
1.50	180	442	2.09	
2.00	144	458	-	

Secondly, compounds having the same P–O–P angle (180 degrees), average bond length were considered. The samples as a function of $x = 0.50, 1.00,$ and 1.50 displayed decreasing of ϵ_r when increasing Mg^{2+} compositions.

These as a result of average M-O bond length decrease polarization. Therefore, dielectric permittivity tends to increase with increasing bond length, since decreasing bond strength, shows better polarization. The changing of dielectric loss of binary metal pyrophosphates at high frequency tends to be decreasing when x increases. Due to pyrophosphates compound are quite responsive in the high frequency range (microwave dielectric properties). But low frequency, the dielectric loss changing were difference may be caused by the extrinsic factors. Generally, high dielectric permittivity causes high dielectric loss. The Mg having lower EN (Electronegativity) than Cu [23] is introduced, positively charged defects will be destroyed thus decreasing the density of defect states of binary metal pyrophosphates, $\text{Cu}_{(2-x)}\text{Mg}_x\text{P}_2\text{O}_7$ system as compared to pure $\text{Cu}_2\text{P}_2\text{O}_7$. The addition of Mg to $\text{Cu}_2\text{P}_2\text{O}_7$ build up the amount of charged defect states that might affect the dielectric loss. Since the dielectric loss of these compounds depends upon the total amount of localized sites, the decrease of dielectric loss and the increase of Mg component can be understood in terms of the decreased density of defects on summing up of Mg to $\text{Cu}_2\text{P}_2\text{O}_7$. Due to the decreased number of dipoles (D^- and D^+) at higher component of Mg, the dielectric loss is also expected to decrease with Mg component as found in this study.

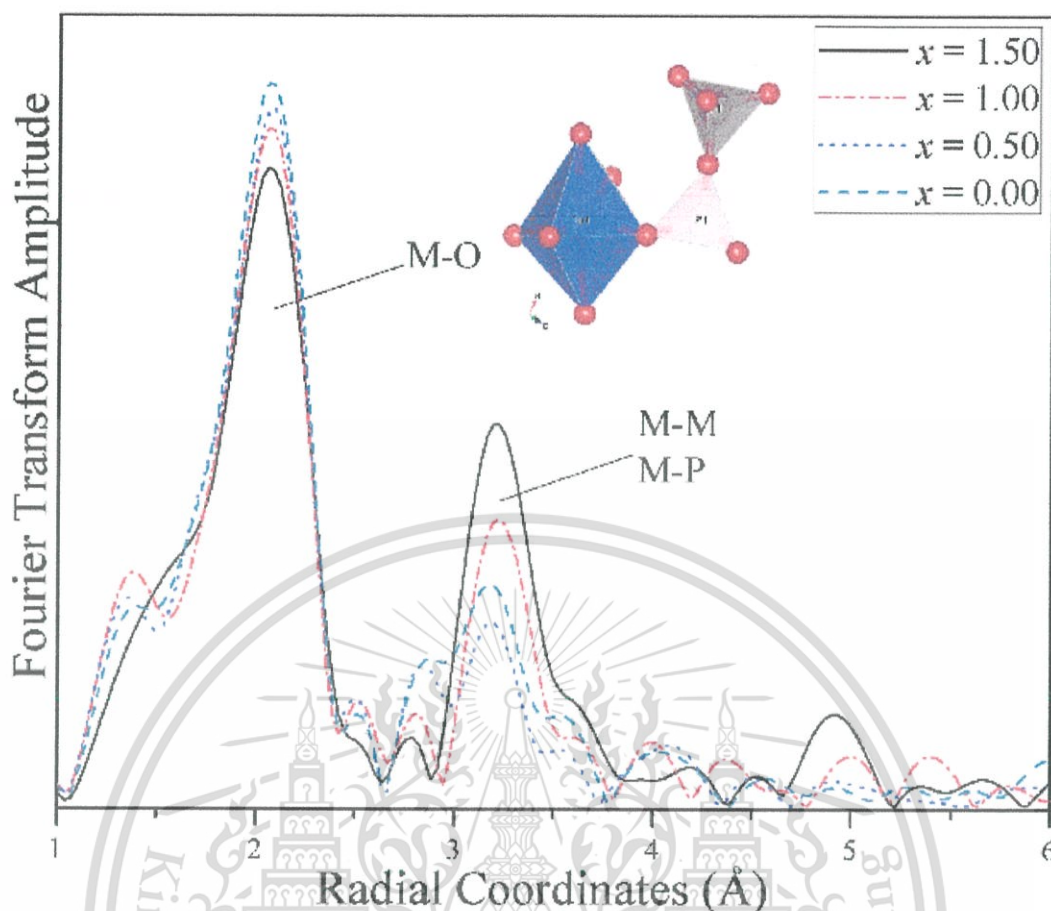


Figure 6.5 EXAFS patterns of $\text{Cu}_{(2-x)}\text{Mg}_x\text{P}_2\text{O}_7$; $x = 0.00 - 2.00$.

6.4 Summary

Metal pyrophosphates; $\text{Cu}_{(2-x)}\text{Mg}_x\text{P}_2\text{O}_7$ ($x = 0.0-2.0$) samples were prepared via solid state reaction to obtain information on solid solution formation, and characterized in the metal pyrophosphate group by Raman spectroscopy. XRD and Raman spectroscopy investigated the structure, which exhibited the compositions, $x = 0.50 - 1.50$, as a copy structure of high temperature phase, $\beta\text{-Cu}_2\text{P}_2\text{O}_7$, with space group $C2/m$ at both high and low temperature. The dielectric properties of the metal pyrophosphate group include two effects that comprise to shift of O atoms in the collinear P–O–P bridge and movement of M^{2+} ions in the octahedral MO_6 . The experimental results were shown that P–O–P angle in $\text{P}_2\text{O}_7^{4-}$ ions is the main factor. Narrow angles will cause more polarization than wide angles. Furthermore, increasing bond length in the octahedral site (M–O) increases polarization, because it affects the

This material is reserved for educational use only, not allowed for commercial use.

bond strength of octahedral MO_6 . The binary metal pyrophosphates have high dielectric permittivity and low dielectric loss, especially in $x = 0.50$.



This material is reserved for educational use only, not allowed for commercial use.

Forbidden to modify the content, and cite the document when use.

REFERENCE

- [1] J. I. Bian, D. W. Kim and K. S. Hong, "Microwave dielectric properties of $A_{(2)}P_{(2)}O_{(7)}$ (A = Ca, Sr, Ba; Mg, Zn, Mn)", *Jpn J Appl Phys* 1, 43, 3521-3525 (2004).
- [2] J. J. Bian, D. Kim and K. S. Hong, "Microwave dielectric properties of $(Zn_{1-x}Mn_x)_{(2)}P_2O_7$ ", *J Mater Sci*, 40, 1801-1803 (2005).
- [3] W. Wenwei, F. Yanjin, W. Xuehang, L. Sen and L. Shushu, "Preparation via solid-state reaction at room temperature and characterization of layered nanocrystalline $NH_4MnPO_4 \cdot H_2O$ ", *Journal of Physics and Chemistry of Solids*, 70, 584-587 (2009).
- [4] M. Weil and B. Stöger, "Crystal chemistry of transition metal diarsenates $M_2As_2O_7$ (M= Mn, Co, Ni, Zn): Variants of the thortveitite structure", *Acta Crystallographica Section B: Structural Science*, 66, 603-614 (2010).
- [5] Z. W. Xiao, G. R. Hu, Z. D. Peng, K. Du and X. G. Gao, "Solid state synthesis and characterization of iron(II) pyrophosphate $Fe_2P_2O_7$ ", *Chinese Chemical Letters*, 18, 1525-1527 (2007).
- [6] A. Bensalem, M. Ahluwalia, T. V. Vijayaraghavan and Y. H. Ko, "Synthesis of amorphous $MgHPO_4 \cdot x(R)$ [R = Ethanol; Ethylene glycol] in anhydrous media", *Materials Research Bulletin*, 32, 1473-1483 (1997).
- [7] C. Díaz, M. L. Valenzuela, V. Lavayen, K. Mendoza, D. O. Peña and C. O'Dwyer, "Nanostructured copper oxides and phosphates from a new solid-state route", *Inorganica Chimica Acta*, 377, 5-13 (2011).
- [8] D. Brandová, M. Trojan, M. Arnold, F. Paulik and J. Paulik, "Mechanism of dehydration and condensation of $CuHPO_4 \cdot H_2O$ ", *Journal of Thermal Analysis*, 34, 1449-1454 (1988).
- [9] D. Brandová, M. Trojan, F. Paulik and J. Paulik, "Mechanism of dehydration of $ZnHPO_4 \cdot H_2O$ ", *Journal of Thermal Analysis*, 32, 1923-1928 (1987).
- [10] A. Jouini, J. C. Gâcon, M. Ferid and M. Trabelsi-Ayadi, "Luminescence and scintillation properties of praseodymium poly and diphosphates", *Optical Materials*, 24, 175-180 (2003).
- [11] T. Yang and J. Lin, "Hydrothermal syntheses and low temperature magnetic

- behaviors of $\text{ACo}_3(\text{P}_2\text{O}_7)_2$ (A=Ca, Sr, Ba, Pb)", *Journal of Solid State Chemistry*, 198, 1-5 (2013).
- [12] C. H. Kim and H. S. Yim, "The effect of tetravalent metal on dielectric property in ZrP_2O_7 and TiP_2O_7 ", *Solid State Communications*, 110, 137-142 (1999).
- [13] R. Shannon, "Revised effective ionic radii and systematic studies of interatomic distances in halides and chalcogenides", *Acta Crystallographica Section A*, 32, 751-767 (1976).
- [14] B. Boonchom and N. Phuvongpha, "Synthesis of new binary cobalt iron pyrophosphate CoFeP_2O_7 ", *Mater Lett*, 63, 1709-1711 (2009).
- [15] H. Bih, I. Saadoune, H. Ehrenberg and H. Fuess, "Crystal structure, magnetic and infrared spectroscopy studies of the $\text{LiCr}_y\text{Fe}_{1-y}\text{P}_2\text{O}_7$ solid solution", *Journal of Solid State Chemistry*, 182, 821-826 (2009).
- [16] K. Pogorzelec-Glaser, A. Pietraszko, B. Hilczer and M. Połomska, "Structure and phase transitions in $\text{Cu}_2\text{P}_2\text{O}_7$ ", *Phase Transitions*, 79, 535-544 (2006).
- [17] B. D. Cullity, *Elements of X-ray Diffraction*, 2nd ed. ed, London, Addison-Wesley Publishing, 1977.
- [18] A. J. Bosman and E. E. Havinga, "Temperature Dependence of Dielectric Constants of Cubic Ionic Compounds", *Physical Review*, 129, 1593-1600 (1963).
- [19] B. E. Robertson and C. Calvo, "The crystal structure and phase transformation of $\alpha\text{-Cu}_2\text{P}_2\text{O}_7$ ", *Acta Crystallographica*, 22, 665-672 (1967).
- [20] B. E. Robertson and C. Calvo, "Crystal structure of $\beta\text{-Cu}_2\text{P}_2\text{O}_7$ ", *Canadian Journal of Chemistry*, 46, 605-612 (1968).
- [21] B. Ravel and M. Newville, "ATHENA, ARTEMIS, HEPHAESTUS: data analysis for X-ray absorption spectroscopy using IFEFFIT", *Journal of Synchrotron Radiation*, 12, 537-541 (2005).
- [22] J. A. Gomes, M. H. Sousa, G. J. da Silva, F. A. Tourinho, J. Mestnik-Filho, R. Itri, G. d. M. Azevedo and J. Depeyrot, "Cation distribution in copper ferrite nanoparticles of ferrofluids: A synchrotron XRD and EXAFS investigation", *J. Magn. Mater.*, 300, e213-e216 (2006).
- [23] P. L., *The nature of chemical bond*, Oxford and IBH, Calcutta, 1969.

CHAPTER 7

CONCLUSIONS

7.1 General Conclusions

Phase formation of the binary metal pyrophosphate, CuZnP_2O_7 , was studied at different temperatures in the range of 400-800°C. Samples were obtained by solid state reaction using stoichiometry of CuO, ZnO and $\text{NH}_4\text{H}_2\text{PO}_4$ at ambient temperature to 800°C. Intermediate substances of reaction were observed by FT-IR, Raman, and XRD measurements that included $\alpha\text{-Cu}_2\text{P}_2\text{O}_7$, $\alpha\text{-Zn}_2\text{P}_2\text{O}_7$, $3\text{CuO}\cdot 2\text{P}_2\text{O}_5\cdot 0.3\text{NH}_3\cdot 0.2\text{H}_2\text{O}$, and $\text{Zn}_2\text{P}_2\text{O}_7\cdot 3\text{H}_2\text{O}$, of which $\text{Zn}_2\text{P}_2\text{O}_7\cdot 3\text{H}_2\text{O}$ was the strongest intermediate substance. The CuZnP_2O_7 sample completely reacted at a temperature of about 700°C, but with low crystallinity. When the temperature increased to about 800°C, the structure had an ordering atomic arrangement, which was brought to long range order and increased crystallinity. Cu:Zn evolution in the structure was separated into two parts with increasing temperature that started below 600°C. Thus, increasing Cu and decreasing Zn contents had clear linear relationships. When the temperature rose above 600°C, the range of reaction was close to completion. The final product confirmed the solid solution between Cu and Zn atoms by EXAFS fitting spectra. Distances between Cu/Zn- O_{eq} and Cu/Zn- O_{ax} (distorted) in the first and second shell were 1.96081 and 2.26967 Å for Cu K-edge and 2.03230 and 2.35242 Å for Zn K-edge. The third shell was then added to the model to describe the combination of M-M (M=Cu/Zn), and M-P interaction. The results of EXAFS analysis shows that $\text{Zn}_2\text{P}_2\text{O}_7$ is a completely solid solution with $\text{Cu}_2\text{P}_2\text{O}_7$ being brought to a CuZnP_2O_7 structure.

The single metal pyrophosphates, $\alpha\text{-Cu}_2\text{P}_2\text{O}_7$ and $\alpha\text{-Zn}_2\text{P}_2\text{O}_7$, and binary metal pyrophosphates, $\text{Cu}_{(2-x)}\text{Zn}_x\text{P}_2\text{O}_7$; $x = 0.00 - 1.50$, were synthesized successfully via solid state reaction from metal oxides and ammonium hydrogen phosphate. All of the samples exhibited a single-phase monoclinic system with the $C2/c$ space group for $\alpha\text{-Cu}_2\text{P}_2\text{O}_7$ and $\alpha\text{-Zn}_2\text{P}_2\text{O}_7$ ($I2/c$), and $C2/m$ space group for the binary metal pyrophosphates, which showed that the binary metal pyrophosphates had more structural symmetry than the single metal pyrophosphates. Rietveld refinement presented the P-O-P bond angle and P-O bond length in the $\text{P}_2\text{O}_7^{4-}$ ions, and also details of the octahedral MO_6 including the average bond length, octahedral volume, and distortion index. The addition of Zn^{2+} ions in the $\text{Cu}_2\text{P}_2\text{O}_7$ structure caused distortion of the crystal structure, which led to a

change in the bond length and bond angle of the P–O–P clusters in the $P_2O_7^{4-}$ ions, and changed the octahedral volume and average bond lengths of the octahedral MO_6 site. The color of the samples changed from bluish-green to green when the Zn component increased because the absorption wavelength increased and corresponded to the decrease in z-axis expansion. The final results showed that the distortion of the octahedral MO_6 caused a direct effect on the color of the metal pyrophosphate compounds, while the change of the P–O–P bridge affected the dielectric properties.

Metal pyrophosphates; $Cu_{(2-x)}Mg_xP_2O_7$ ($x = 0.0-2.0$) samples were prepared via solid state reaction to obtain information on solid solution formation, and characterized in the metal pyrophosphate group by Raman spectroscopy. XRD and Raman spectroscopy investigated the structure, which exhibited the compositions, $x = 0.50 - 1.50$, as a copy structure of high temperature phase, $\beta-Cu_2P_2O_7$, with space group $C2/m$ at both high and low temperature. The binary metal pyrophosphates have high dielectric permittivity and low dielectric loss, especially in $x = 0.50$.

The dielectric properties of the metal pyrophosphate group include two effects that comprise to shift of O atoms in the collinear P–O–P bridge and movement of M^{2+} ions in the octahedral MO_6 . The experimental results were shown that P–O–P angle in $P_2O_7^{4-}$ ions is the main factor. Narrow angles will cause more polarization than wide angles. Furthermore, increasing bond length in the octahedral site (M–O) increases polarization, because it affects the bond strength of octahedral MO_6 .

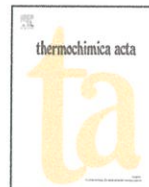
Table 7.1 Summary of all factors on the pyrophosphates in this study

Sample	Structure		POP bonding			M-O bonding			Dielectric properties		Optical properties			
	Space group	V (Å ³)	bond length (Å)	Bond angle (°)	Number	Bond length (Å)	MO ₆ Volume (Å ³)	Distortion index	ε _r	Atomic polarization	Ionic polarization	Obs. (nm)	Abs. (nm)	Δ ₀ (kJ/mol)
Cu ₂ P ₂ O ₇	C2/c	482.31	1.574	154.6	4	2.1794	12.6198	0.1400	10.53	8.76	1.77	562	753	159
CuZn050	C2/m	239.54	1.524	180.0	2	2.1758	12.6629	0.1117	9.88	8.86	1.02	506	669	179
CuZn100	C2/m	238.97	1.521	180.0	2	2.172	12.5791	0.0935	9.61	8.88	0.73	508	672	178
CuZn150	C2/m	238.73	1.519	180.0	2	2.1659	12.4106	0.0821	9.42	8.86	0.56	512	678	176
Zn ₂ P ₂ O ₇	I2/c	1454.01	1.59	140.4	12	2.2929	15.4633	0.1556	14.45	8.53	5.92	-	-	-
CuMg050	C2/m	238.75	1.522	180.0	2	2.1705	12.1405	0.1085	9.36	8.54	0.82	515	683	175
CuMg100	C2/m	235.19	1.512	180.0	2	2.1362	12.0986	0.0788	8.82	8.3	0.52	530	705	170
CuMg150	C2/m	233.71	1.489	180.0	2	2.0899	11.0903	0.0687	8.19	7.86	0.33	542	723	165
Mg ₂ P ₂ O ₇	P2 ₁ /c	476.47	1.605	144.0	4	2.1304	11.0222	0.0871	13.87	7.16	6.71	-	-	-



This material is reserved for educational use only, not allowed for commercial use.

Forbidden to modify the content, and cite the document when use.



Phase formation and evolution of Cu:Zn partials in binary metal pyrophosphates $\text{Cu}_{(2-x)}\text{Zn}_x\text{P}_2\text{O}_7$; $x \approx 1$

Rattana Baitahe^a, Naratip Vittayakorn^{a,b,*}

^a Electroceramic Research Laboratory, College of KMITL Nanotechnology, King Mongkut's Institute of Technology Ladkrabang, Bangkok 10520, Thailand

^b Advanced Materials Science Research Unit, Department of Chemistry, Faculty of Science, King Mongkut's Institute of Technology Ladkrabang, Bangkok 10520, Thailand



ARTICLE INFO

Article history:

Received 12 May 2014

Received in revised form 13 August 2014

Accepted 13 August 2014

Available online 28 September 2014

Keywords:

Phase formation

Metal pyrophosphates

X-ray absorption spectroscopy

ABSTRACT

Binary metal pyrophosphate powders were prepared by the solid state reaction method and subsequently calcined at 400, 500, 600, 700, and 800 °C in order to study Cu:Zn partial evolution to the final CuZnP_2O_7 product. Synchrotron X-ray absorption, X-ray diffraction, Raman, FT-IR spectroscopy, and thermogravimetric analysis were used in this investigation. Phase evolution of the reaction products was investigated systematically. The results showed that complicated mixtures contributed to the reaction of synthesis temperature. The reaction comprised $3\text{CuO} \cdot 2\text{P}_2\text{O}_5 \cdot 0.3\text{NH}_3 \cdot 0.2\text{H}_2\text{O}$, $\text{Cu}_2\text{P}_2\text{O}_7$, $\text{Zn}_2\text{P}_2\text{O}_7$, and $\text{Zn}_2\text{P}_2\text{O}_7 \cdot 3\text{H}_2\text{O}$ intermediates. Decreasing percentage of $3\text{CuO} \cdot 2\text{P}_2\text{O}_5 \cdot 0.3\text{NH}_3 \cdot 0.2\text{H}_2\text{O}$ intermediates was related directly to an increasing final product. Cu:Zn contents changed in $\text{Cu}_{(2-x)}\text{Zn}_x\text{P}_2\text{O}_7$ in the temperature range of 400–600 °C, when $x \approx 1$ clearly was related linearly to the reaction temperature. The final product was confirmed by EXAFS fitting spectra as solid solution between the Cu and Zn atom in the CuZnP_2O_7 structure, and it indicated environment around metal atoms.

© 2014 Elsevier B.V. All rights reserved.

1. Introduction

Metal pyrophosphates have had a wide range of applications such as microwave dielectric materials, chelating agents, corrosion-resistant coatings, glass ceramics, biomedical cements, and high-quality fertilizers [1–3]. The metal pyrophosphate, $\text{M}_2\text{P}_2\text{O}_7$, has been reported as various phase types [4]. An M radius structure greater than 0.97 Å has been observed as a dichromate type ($M = \text{Ba}^{2+}$, Cd^{2+} , Ca^{2+} , Sr^{2+} , and Pb^{2+}), in which a pair of $\text{P}_2\text{O}_7^{4-}$ groups crystallize in eclipsed conformation around the center of symmetry, with bridging O atoms extending towards each other. When the M radius is less than 0.97 Å ($M = \text{Mg}^{2+}$, Mn^{2+} , Co^{2+} , Cu^{2+} , Ni^{2+} , and Zn^{2+}), the structure is a thortveitite type, in which $\text{P}_2\text{O}_7^{4-}$ exists in staggered conformation. Furthermore, metal pyrophosphates were classified into two groups by stable phase temperatures [5]. They included alpha-phases, which are stable at low temperatures and beta-phases at high temperatures. Alpha and beta phases can be alternated at a critical temperature. In addition, different syntheses exhibited many phases such as $\text{glass} \rightarrow \text{X} \rightarrow \text{Y} \rightarrow \beta \leftrightarrow \alpha$

phases [6]. Binary copper zinc pyrophosphate ceramic has different physicochemical, mechanical and biological properties because of different processes.

Most studies of metal phosphate focused on the synthesis and characterizations of both bulk [7,8] and nano particles [9], kinetics and the thermodynamics of reaction [10,11], and their properties [12,13]. However, the study of phase formation and atomic evolution of the final product, and intermediate substance relating phase, is not widely understood, and is therefore of interest. The objective of this study was to investigate Cu:Zn evolution of possible binary copper zinc pyrophosphate formation in a solid state reaction at different temperatures. In order to investigate the ideality of a fully solid solution, the probe needs to be more local. X-ray absorption spectroscopy (XAS), using synchrotron radiation, is an extremely suitable technique for studying local atomic and electronic structures of mixed metal phosphates, such as CuZnP_2O_7 , and using extended X-ray absorption fine structure (EXAFS) measurements for probing structure of the final product.

2. Experimental procedure

Synthesis of CuZnP_2O_7 was conducted using traditional solid-state reaction techniques. High purity ZnO (99.9%), CuO (99.9%), and $(\text{NH}_4)_2\text{HPO}_4$ (99%) were used as raw materials. Stoichiometric mixtures of starting materials were homogenized by ball milling

* Corresponding author at: Advanced Materials Science Research Unit, Department of Chemistry, Faculty of Science, King Mongkut's Institute of Technology Ladkrabang, Bangkok 10520, Thailand. Fax: +66 2 326 4415.

E-mail address: naratipcmu@yahoo.com (N. Vittayakorn).

with ZrO_2 media in ethanol for 24 h, and batching was calcined for 2 h at 400, 500, 600, 700, and 800 °C. The phase content of the prepared samples was studied by X-ray powder diffraction using a Bruker D8 Advance X-ray Diffractometer (Bruker AXS, Karlsruhe, Germany) with $Cu\ K\alpha$ radiation ($\lambda = 0.1546\text{ nm}$). Room temperature Fourier transform infrared (FT-IR) spectra were recorded in the range of $4000\text{--}400\text{ cm}^{-1}$ with eight scans on a PerkinElmer Spectrum GX spectrometer with the resolution of 4 cm^{-1} . Raman spectra were recorded in the range of $1300\text{--}100\text{ cm}^{-1}$ with eight scans on a thermo scientific DXR Raman microscope. Thermal analysis measurements (thermogravimetry, TG; derivative thermogravimetry, DTG) were taken using a PerkinElmer, Pyris 1 TGA. Experiments were conducted at room temperature on the beam line (BL8) of the National Synchrotron Research Center (Thailand), with a double crystal Ge(220) for the EXAFS mono-chromator. X-ray absorption (XAS) spectra at the Cu and Zn K-edge were obtained in transmission mode with air chambers. In addition, complete substitutional solid solutions, in accordance with the Hume–Rothery rules, may form if the solute and solvent have: similar atomic radii; $R_{Cu(II)} = 0.73\text{ \AA}$ and $R_{Zn(II)} = 0.74\text{ \AA}$ [14], similar

electronegativities; $Cu = 1.90$ and $Zn = 1.65$, similar valency; $Cu = 2+$ and $Zn = 2+$ and same crystal structure; $\beta\text{-Cu}_2\text{P}_2\text{O}_7 = \text{monoclinic, } C_2/m$ and $\beta\text{-Zn}_2\text{P}_2\text{O}_7 = \text{monoclinic, } C_2/m$. These data show high possibility of substitutional solid solution between Cu and Zn ions in pyrophosphate compound.

3. Results and discussion

Infrared and Raman spectroscopy are two powerful methods used to analyze compound bonding. These popular techniques are used to observe vibrational, rotational, and other low-frequency modes in the phosphates system. Fig. 1 shows Raman shift spectra when $x \approx 1$. Powders were calcined at different batch temperatures (400, 500, 600, 700, and 800 °C) using the solid state reaction method. Raman spectra were assigned as relating to the vibration unit; PO_4^{3-} , $P_2O_7^{4-}$, P_2O_5 clusters and metal oxide (M–O) bond. The samples were calcined at 600, 700, and 800 °C. The peak bands were similar. It is noticeably clear that the studied compounds exhibit more splitting and sharpness, especially in the low-frequency region ($1400\text{--}100\text{ cm}^{-1}$), indicating polymerization of

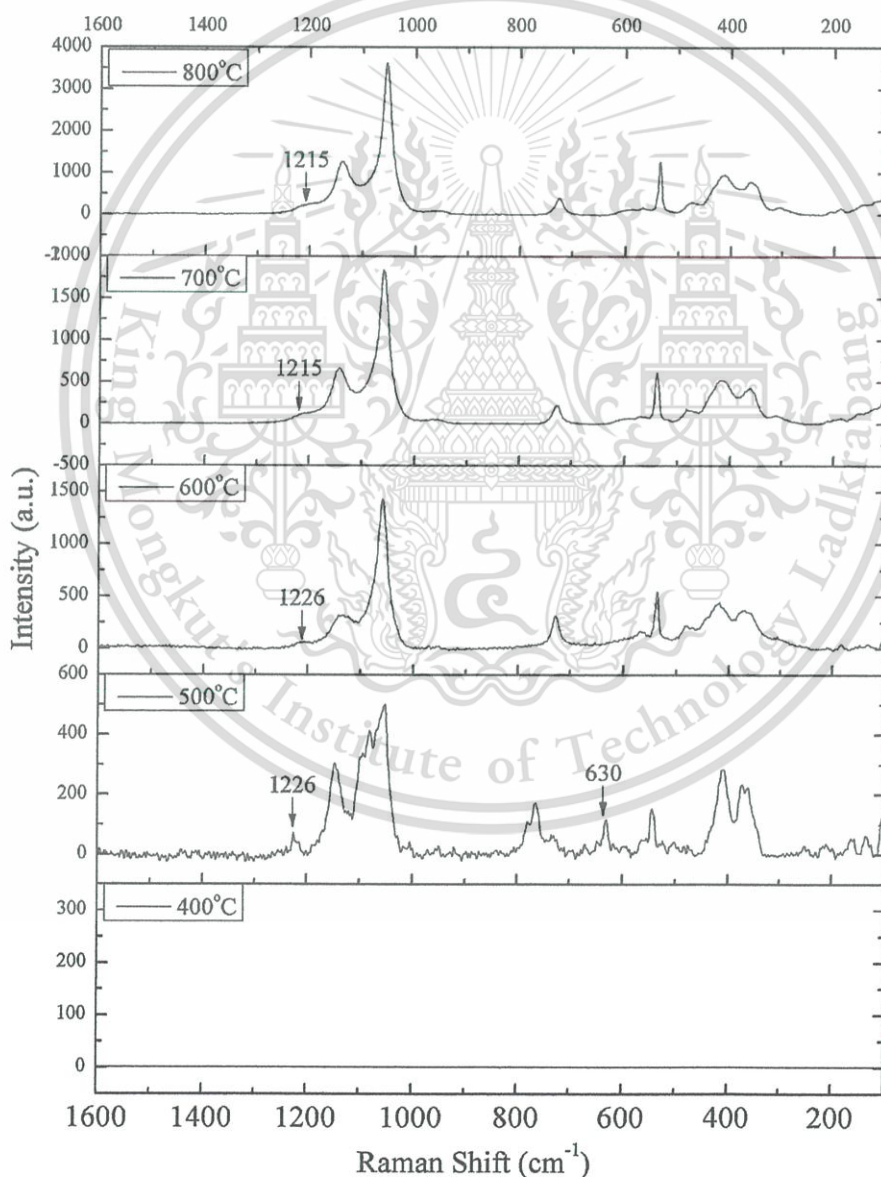


Fig. 1. Raman spectra of $Cu_{(2-x)}Zn_xP_2O_7$; $x \approx 1.00$, subsequently calcined at 400, 500, 600, 700, and 800 °C.

$[\text{PO}_4^{3-}]$ to $[\text{P}_2\text{O}_7]^{4-}$ [15,16]. The strong vibration bands around $1000\text{--}1100\text{ cm}^{-1}$ are attributed to stretching of the PO_4^{3-} unit. The bending vibration of the PO_4^{3-} unit is observed at about $450\text{--}650\text{ cm}^{-1}$. These vibration bands were shown to remain in the phosphates group. The asymmetric and symmetric stretch of the P–O–P bridge in the $[\text{P}_2\text{O}_7]^{4-}$ unit for this sample were observed at around $930\text{--}970$ and $680\text{--}760\text{ cm}^{-1}$ respectively, while P–O–P bending vibration is expected in the area $600\text{--}500\text{ cm}^{-1}$ (PO_2^{2-} radical) and $500\text{--}370\text{ cm}^{-1}$ (P–O–P bridge). These peaks were confirmed as characteristic of pyrophosphate compounds. In addition, the PO_3 deformation and rocking modes, P–O–P deformations, and torsional and external mode were found in the $430\text{--}180\text{ cm}^{-1}$ region. Metal–O stretching usually appears in the bending mode region, as the bending modes of the P–O–P bridge and absorption bands associated with these vibrations are usually very weak [17]. The weak band of approximately 1220 cm^{-1} exhibits a high temperature phase in pyrophosphate groups. These binary metal phosphates closely resemble those of the $\beta\text{-Zn}_2\text{P}_2\text{O}_7$ with a monoclinic structure and space group C_2/m [18]. A wave number of 630 cm^{-1} for sample

powders was calcined at 500°C , and assigned to asymmetric stretching of P–O in the P_2O_5 cluster [19]. The sample was calcined at 400°C , which unable to be observed any peak. Generally, Raman spectroscopy only detect crystalline of compounds [20]. The very low crystallinity of sample was calcined at 400°C caused Raman to be inactive. While, calcination temperature increases due to growing crystallinity of the sample. Intensity of Raman spectra shows high intensities following calcination temperature. This phenomena is similar to those observed by Zhang et al. [21], Liu et al. [22], and Fairbrother et al. [23]. However, Raman spectroscopy results did not clarify H_2O and NH_3 molecules, and this signifies the limitation of the Raman instrument. Therefore, H_2O and NH_3 molecules were analyzed by FT-IR spectroscopy techniques. The FT-IR spectra of samples are shown in Fig. 2. All strong vibration bands were attributed to the phosphates group according to Raman results. However, medium peaks in the range of $1630\text{--}1640\text{ cm}^{-1}$ were referred to as the bending vibration of water for samples calcined at 400 , 500 , and 600°C . In addition, FT-IR spectra show a weak band at about 1430 cm^{-1} , particularly when calcined at 400 and 500°C , and there is asymmetric bending

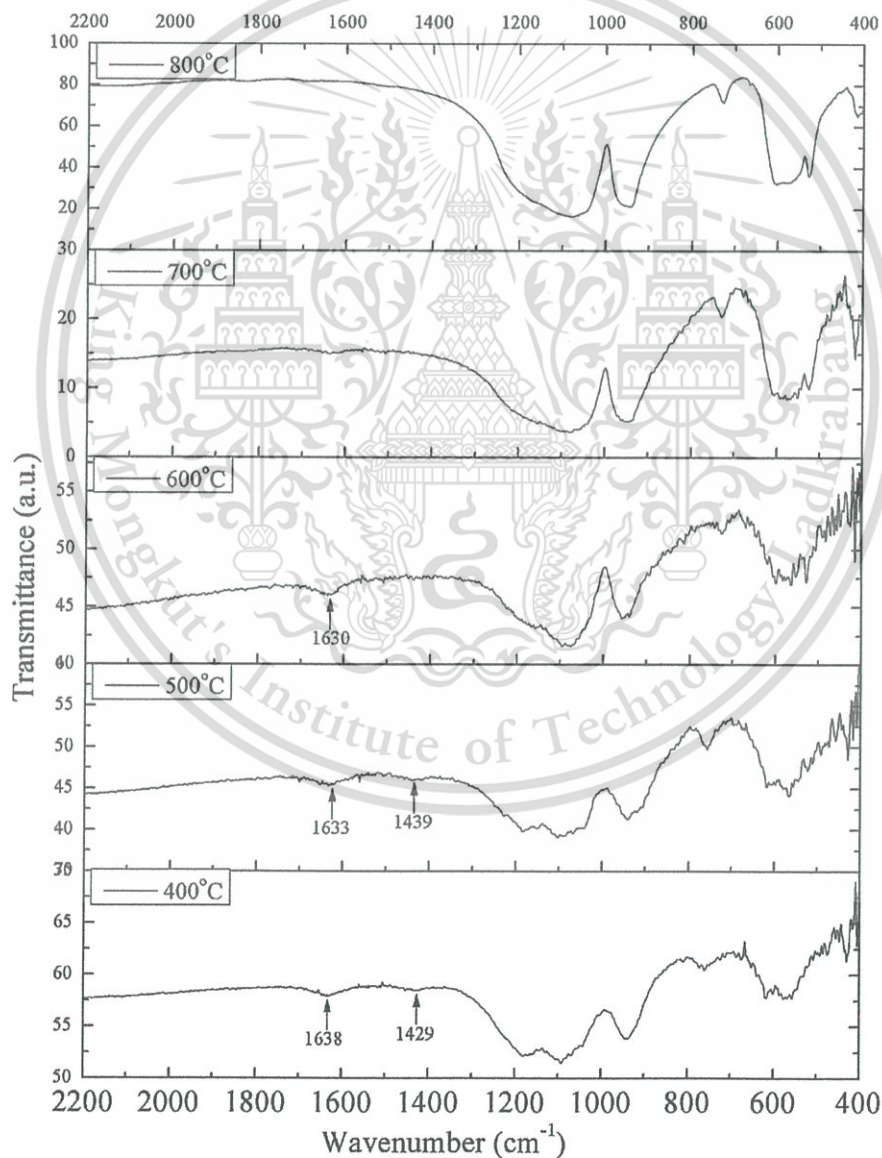


Fig. 2. FT-IR spectra of $\text{Cu}_{(2-x)}\text{Zn}_x\text{P}_2\text{O}_7$; $x \approx 1.00$, subsequently calcined at 400 , 500 , 600 , 700 , and 800°C .

vibration of ammonia molecules in $3\text{CuO}\cdot 2\text{P}_2\text{O}_5\cdot 0.3\text{NH}_3\cdot 0.2\text{H}_2\text{O}$ compound [24].

The XRD patterns of samples are shown in Fig. 3. This technique can be investigated by both qualitative and quantitative analysis. X-ray diffraction is used often to semi-quantitatively determine the weight fraction of constituents, which can be identified by comparing the integrated intensities of the diffraction peaks from each of the known phases. In addition, complex mixtures containing more than two phases also can be quantified. Even if one phase is amorphous, diffraction can still yield a relative amount of each phase. The diffraction pattern includes information of peak positions and intensity. The peak positions are indicative of the crystal structure and symmetry of the contributing phase. The peak intensities reflect total scattering from each plane in the crystal structure of the phase, and are dependent directly on the distribution of particular atoms in the structure [25]. Thus, intensities are ultimately related to both the structure and composition of the phase. The diffraction intensity equation has

been studied many times [26–29], and is summarized below;

$$I_{(hkl)\alpha} = \frac{I_0 \lambda^3}{64 \pi r} \left(\frac{e^2}{m_e c^2} \right)^2 \frac{M_{(hkl)}}{V_\alpha^2} |F_{(hkl)\alpha}|^2 \left(\frac{1 + \cos^2(2\theta) \cos^2(2\theta_m)}{\sin^2 \theta \psi \sigma \theta} \right) \frac{\nu_\alpha}{\mu_s} \quad (1)$$

where:

$I_{(hkl)\alpha}$: intensity of reflection of hkl in phase α .

I_0 : incident beam intensity.

r : distance from specimen to detector.

λ : X-ray wavelength.

$(e^2/m_e c^2)^2$: square of classical electron radius.

μ_s : linear absorption coefficient of the specimen.

ν_α : volume fraction of phase α .

$M_{(hkl)}$: multiplicity of reflection hkl of phase α .

0 : Lorentz-polarization (and monochromator) correction $\left(\frac{1 + \cos^2(2\theta) \cos^2(2\theta_m)}{\sin^2 \theta \psi \sigma \theta} \right)$.

V_α : volume of the unit cell of phase α .

$2\theta_m$: diffraction angle of the monochromator.

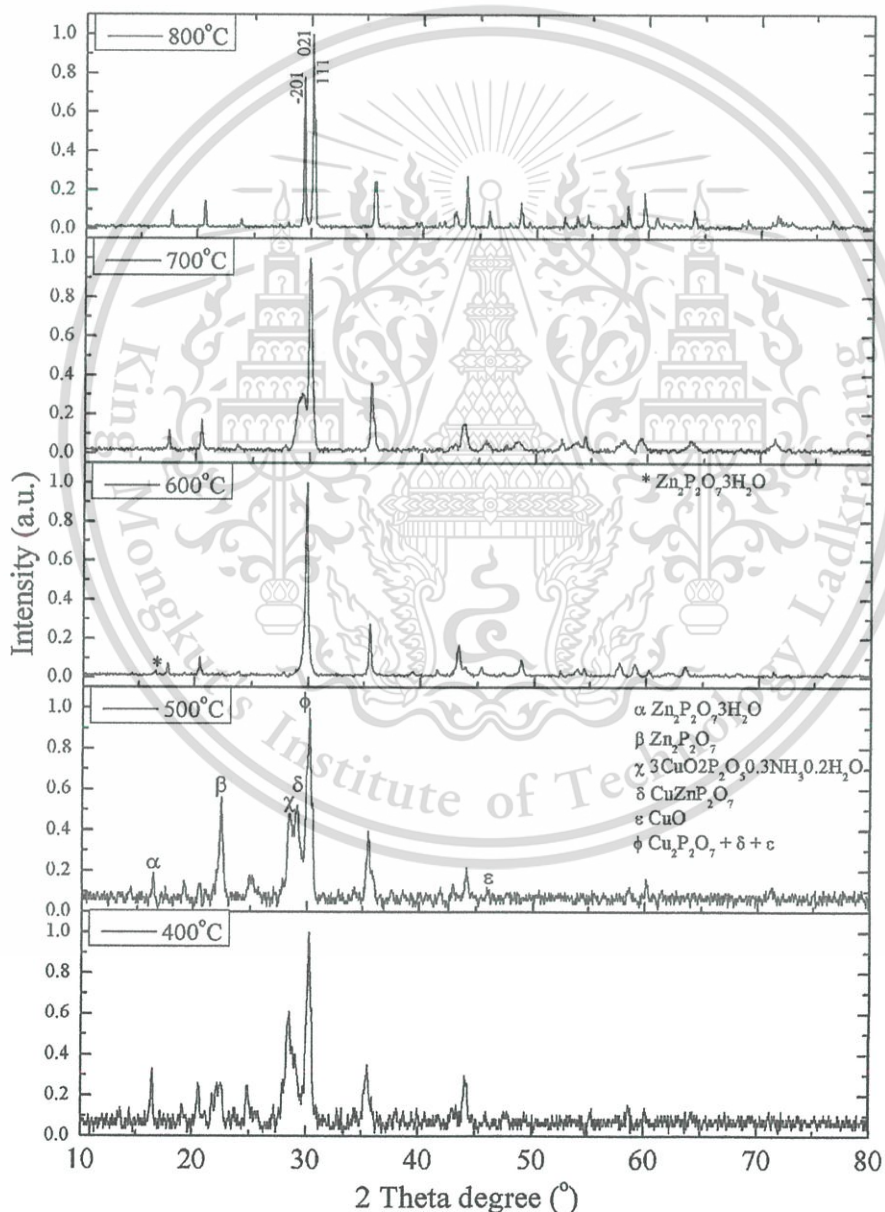


Fig. 3. XRD patterns of $\text{Cu}_{(2-x)}\text{Zn}_x\text{P}_2\text{O}_7$; $x \approx 1.00$, subsequently calcined at 400, 500, 600, 700, and 800 °C.

$F_{(hkl)\alpha}$: structure factor for reflection hkl of phase α (i.e., the vector sum of scattering intensities of all atoms contributing to that reflection).

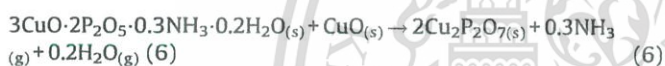
In recognizing that many of these terms are consistent for a particular experimental setup, the experimental constant, K_e , can be defined. The constant, $K_{(hkl)\alpha}$, can be defined for a given phase that is in effect equal to the structure factor term for phase α . In substituting the weight fraction (X_α) for the volume fraction, the density of the phase (ρ_α) for the volume, and the mass absorption coefficient of the specimen (μ/ρ)_s for the linear absorption coefficient, yields the following equation:

$$I_{(hkl)\alpha} = \frac{K_e K_{(hkl)\alpha} X_\alpha}{\rho_\alpha (\mu/\rho)_s} \quad (2)$$

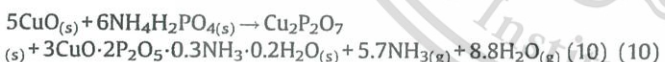
This equation describes the intensity for peak hkl in phase α in similar terms. The weight fraction, f_1 , could be described as follows:

$$f_1 = \frac{(I_1^{\text{mix}}/I_1^{\text{pure}})A_2}{A_1 - (I_1^{\text{mix}}/I_1^{\text{pure}})(A_1 - A_2)} \quad (3)$$

where I_1^{mix} and I_1^{pure} are the phase 1 intensities in the mixture and pure material, respectively, and A_1 and A_2 are the mass absorption coefficients. Based on probability analysis, it is believed that the formation path of the CuZnP_2O_7 phase could be described as follows:

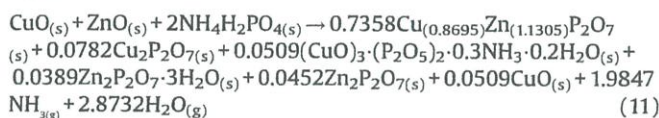


It is highly probable that all reactions proceeded together. In Eqs. (4) and (5) reaction was competitive to reactions as follows:

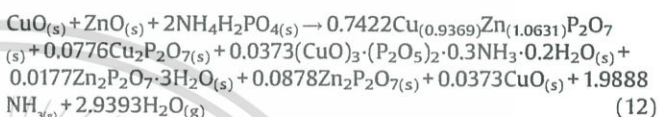


Part of $\text{Zn}_2\text{P}_2\text{O}_7 \cdot 3\text{H}_2\text{O}$ was decomposed to $\text{Zn}_2\text{P}_2\text{O}_7$ and H_2O molecules, as in Eq. (8), while the $\text{Cu}_2\text{P}_2\text{O}_7$ and $\text{Zn}_2\text{P}_2\text{O}_7$ molecules were forced somewhat to fuse together by heating, as in Eq. (9). Products calcined at 400 °C represented the reaction at about 400 °C. The result exhibited the complication of mixed phases, which included CuO (JCPDS no. 80-1917), $\alpha\text{-Cu}_2\text{P}_2\text{O}_7$ (JCPDS no.

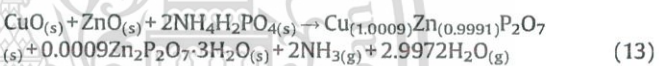
44-0182), $3\text{CuO} \cdot 2\text{P}_2\text{O}_5 \cdot 0.3\text{NH}_3 \cdot 0.2\text{H}_2\text{O}$ (JCPDS no. 49-1004), $\alpha\text{-Zn}_2\text{P}_2\text{O}_7$ (JCPDS no. 49-1240), $\text{Zn}_2\text{P}_2\text{O}_7 \cdot 3\text{H}_2\text{O}$ (JCPDS no. 51-0201), and $\text{Cu}_{(2-x)}\text{Zn}_{(x)}\text{P}_2\text{O}_7$ when $x \approx 1$. All product contents (%wt) are shown in Table 1. The chemical reaction process is proposed in Eq. (11).



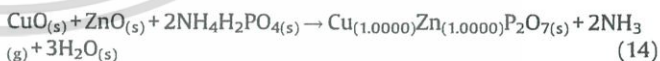
Since starting reaction at room temperature until 400 °C, the total mass loss was 21.89% of NH_3 and H_2O (gas phases). The sample calcined at 500 °C, represented the reaction moment. This stage clearly shows decreasing content of $3\text{CuO} \cdot 2\text{P}_2\text{O}_5 \cdot 0.3\text{NH}_3 \cdot 0.2\text{H}_2\text{O}$ and CuO compounds because the rate of reaction between CuO and $3\text{CuO} \cdot 2\text{P}_2\text{O}_5 \cdot 0.3\text{NH}_3 \cdot 0.2\text{H}_2\text{O}$ to $\text{Cu}_2\text{P}_2\text{O}_7$ was increasing, while $\text{Cu}_2\text{P}_2\text{O}_7$ reacted with $\text{Zn}_2\text{P}_2\text{O}_7$ to $\text{Cu}_{(2-x)}\text{Zn}_{(x)}\text{P}_2\text{O}_7$; $x \approx 1$ to bring increasing $\text{Cu}_{(2-x)}\text{Zn}_{(x)}\text{P}_2\text{O}_7$ and decreasing $\text{Cu}_2\text{P}_2\text{O}_7$. This stage is the proposed reaction in Eq. (12) as follows.



Total mass loss in NH_3 and H_2O gas phases at this stage was 22.21%, when the calcination temperature reached 600 °C. The result detected only $\text{Cu}_{(2-x)}\text{Zn}_{(x)}\text{P}_2\text{O}_7$; $x \approx 1$ and the trace quantity of $\text{Zn}_2\text{P}_2\text{O}_7 \cdot 3\text{H}_2\text{O}$ phases. This effect exhibited temperatures below 600 °C, and CuO and $3\text{CuO} \cdot 2\text{P}_2\text{O}_5 \cdot 0.3\text{NH}_3 \cdot 0.2\text{H}_2\text{O}$ were a complete reaction. A majority of $\text{Zn}_2\text{P}_2\text{O}_7 \cdot 3\text{H}_2\text{O}$ was decomposed to $\text{Zn}_2\text{P}_2\text{O}_7$ and reacted with $\text{Cu}_2\text{P}_2\text{O}_7$ to $\text{Cu}_{(2-x)}\text{Zn}_{(x)}\text{P}_2\text{O}_7$; $x \approx 1$. This stage proposed the following reaction in Eqs. (8) and (9), the total mass loss was 22.52%.



According to IR results, no peak was detectable at around 1430 cm^{-1} of asymmetric bending vibration of ammonia ($\delta_{as}\text{NH}_4$) clusters. However, IR observed a weak band at about 1630 cm^{-1} , which indicated bending vibration of a water molecule for $\text{Zn}_2\text{P}_2\text{O}_7 \cdot 3\text{H}_2\text{O}$. The CuZnP_2O_7 sample was a complete reaction at a temperature of about 700 °C. XRD results showed a single phase of $\text{Cu}_{(2-x)}\text{Zn}_{(x)}\text{P}_2\text{O}_7$; $x = 1$. Diffraction patterns of the sample were similar to those obtained from individual $\beta\text{-M}_2\text{P}_2\text{O}_7$ [5,30]. At the 700 °C, The XRD pattern showed only a single phase of CuZnP_2O_7 , and peak (-201) , (021) , and (111) clearly were separated. These affects caused atomic arrangement that brought long ordering in the crystal structure. In this state, the total mass loss was equal to that in the previous state. The reaction could be concluded as follows:



Intermediates of all of states included $\alpha\text{-Cu}_2\text{P}_2\text{O}_7$, $3\text{CuO} \cdot 2\text{P}_2\text{O}_5 \cdot 0.3\text{NH}_3 \cdot 0.2\text{H}_2\text{O}$, $\alpha\text{-Zn}_2\text{P}_2\text{O}_7$, and $\text{Zn}_2\text{P}_2\text{O}_7 \cdot 3\text{H}_2\text{O}$, of

Table 1
Approximation of percentage by weigh from XRD results.

Temperature (°C)	Percentage of compounds (%wt)					
	CuO	$3\text{CuO} \cdot 2\text{P}_2\text{O}_5 \cdot 0.3\text{NH}_3 \cdot 0.2\text{H}_2\text{O}$	$\text{Cu}_2\text{P}_2\text{O}_7$	$\text{Zn}_2\text{P}_2\text{O}_7$	$\text{Zn}_2\text{P}_2\text{O}_7 \cdot 3\text{H}_2\text{O}$	$\text{Cu}_{(2-x)}\text{Zn}_{(x)}\text{P}_2\text{O}_7$
800	–	–	–	–	–	100.00
700	–	–	–	–	–	100.00
600	–	–	–	–	2.03	97.97
500	2.97	19.83	23.37	26.74	6.36	20.71
400	4.05	27.08	23.54	13.78	13.95	17.61

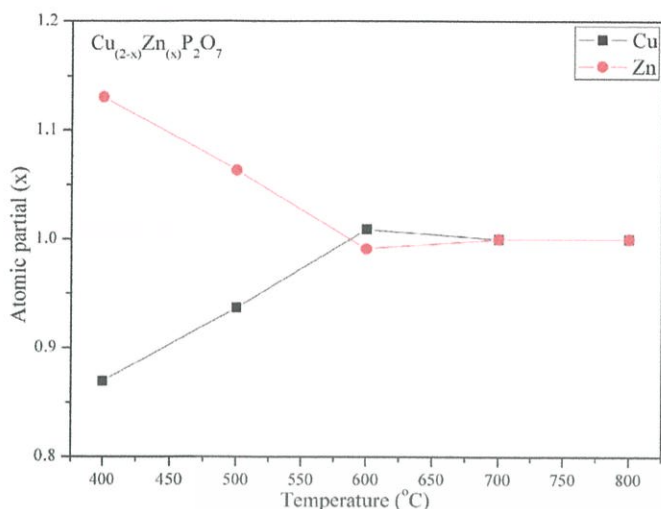


Fig. 4. Plots of the relationship of the atomic partial, Cu:Zn, versus reaction temperature.

which $\text{Zn}_2\text{P}_2\text{O}_7 \cdot 3\text{H}_2\text{O}$ was the strongest intermediate substance, because the heating energy it requires to reach temperatures higher than 600°C breaks all bonds in $\text{Zn}_2\text{P}_2\text{O}_7 \cdot 3\text{H}_2\text{O}$ molecules.

When evaluation of Zn and Cu atoms to CuZnP_2O_7 structure is considered, the relationship of the atomic partial, Cu:Zn, versus reaction temperature is shown in Fig. 4. This result was classified into two parts. Firstly, a reaction temperature of below 600°C was included, and secondly a reaction temperature above 600°C . In the former, the increasing relationship of Cu or decreasing Zn clearly occupied a linear relationship with:

$$b = 0.0003a + 0.2949 \quad (15)$$

and strong linear regression of $R^2 = 0.9996$, when b is the atomic partial, and a the reaction temperature ($^\circ\text{C}$). These relationships predict occupancies between Cu and Zn atoms in $\text{Cu}_{(2-x)}\text{Zn}_x\text{P}_2\text{O}_7$; $x \approx 1$ structure at different temperatures. In the latter, atomic occupancy was close to 1. This range of temperature was close to a complete reaction. The other phases were fused to $\beta\text{-Cu}_2\text{P}_2\text{O}_7$ and $\beta\text{-Zn}_2\text{P}_2\text{O}_7$ (high temperature phases) before being assembled into one structure. A similar crystal structure with a monoclinic system, and C_2/m space group, was above two compounds. Normally, low temperature is called alpha phases, $\alpha\text{-Cu}_2\text{P}_2\text{O}_7$ is a crystal structure with a monoclinic system and C_2/c space group, $Z=4$, and $\alpha\text{-Zn}_2\text{P}_2\text{O}_7$ is a crystal structure with a monoclinic system and $I2/c$ space group, $Z=12$. Meanwhile, $\beta\text{-Cu}_2\text{P}_2\text{O}_7$ and $\beta\text{-Zn}_2\text{P}_2\text{O}_7$ phases are finally intermediate and easily phased for formation of CuZnP_2O_7 compound. In addition, the mechanisms of the proposed CuZnP_2O_7 phase formation were supported by the result of Thermogravimetric analysis (TGA).

The thermal property of the studied compound was investigated on a TG-DTG (Thermogravimetry, TG; Derivative Thermogravimetry, DTG). The TG curve in Fig. 5 shows the mass loss of between 30 and 800°C , which is a related multi-stage decomposition. On the basis of TG data, the final decomposed product seemed to occur at a temperature above 700°C and the water and ammonia content were determined. The first mass loss was 18.24% in the range of $50\text{--}400^\circ\text{C}$. The second to fifth mass loss was 19.88, 21.09, 21.79, and 21.79%, in the range of $400\text{--}500$, $500\text{--}600$, $600\text{--}700$ and $700\text{--}800^\circ\text{C}$, respectively. All stages corresponded in continuum with the elimination of three molecules of crystallized water and two molecules of crystallized ammonia. The total mass loss of 21.81% was close to the XRD values. The retained mass of

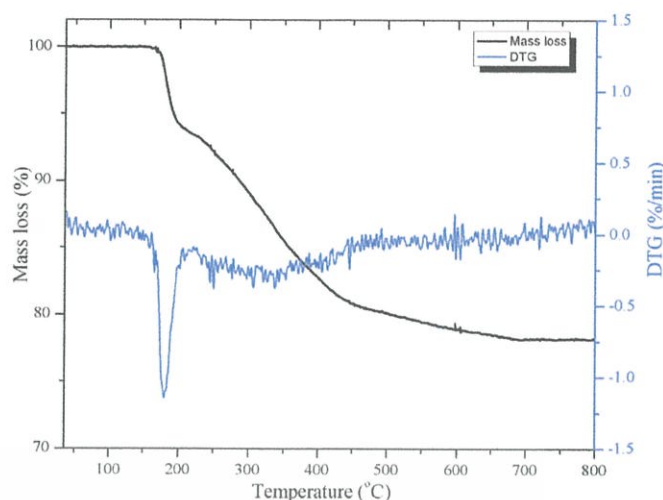


Fig. 5. TG/DTG of CuZnP_2O_7 precursor powder.

about 78% was comparable with the value expected for the formation of CuZnP_2O_7 , thus verified by XRD, Raman, and FT-IR measurements. Comparison values between the proposed TGA and XRD mass loss, which are close, are shown in Table 2.

As extended X-ray absorption fine structure (EXAFS) is very sensitive to change in local geometry, spectra collected at both edges could help in understanding Fourier transform evolutions. The EXAFS results were used for support XRD results of substitutional solid solution between Cu and Zn ions in the binary metal pyrophosphate compound. Therefore, EXAFS data were supported. The data set were then analyzed by 'data processing' with ATHENA software [31]. Accurate details of EXAFS such as interatomic distances and coordination numbers were obtained by 'curve fitting' (Fig. 6) through ARTEMIS software [31]. The details of shell which were presented in Table 3. Cu K-edge and Zn K-edge were considered. In the case of Cu K-edge, the primitive EXAFS model was taken from parameters obtained from Robertson et al. [30]. The results of fitting were demonstrated the asymmetry of CuO_6 octahedral. The first shell to be modeled was the one consisting of four equatorial oxygen atoms, ($\text{Cu}\text{--}\text{O}_{\text{eq}}$) with interatomic distances of 1.96081 Å. Then the two axial oxygen atoms were taken into account ($\text{Cu}\text{--}\text{O}_{\text{ax}}$) with interatomic distances of 2.26967 Å, introducing the Jahn-Teller distortion effect undergone by the copper octahedral centered site into the model. The next shell was then added to the model to describe the combination of $\text{Cu}\text{--}\text{M}$ ($\text{M}=\text{Cu}/\text{Zn}$), and $\text{Cu}\text{--}\text{P}$ interaction. Addition of fourth shell did not improve the quality of the fitting. Zn K-edge were similar to the Cu K-edge fitting, the initial EXAFS model was taken from parameters obtained from Calvo [5]. Zn K-edge EXAFS spectrum was identified, as in the case of Cu, with interatomic distances of 2.03230 and 2.35242 Å for first and second shell, respectively. The peak shifted to a high radial distance, due to a larger atomic radius. These results clearly confirmed that the

Table 2

Comparison values between the proposed TGA and XRD mass loss.

Temperature ($^\circ\text{C}$)	Mass loss (%)	
	XRD	TGA
400	21.89	18.24
500	22.21	19.88
600	22.52	21.09
700	22.54	21.78
800	22.54	21.81

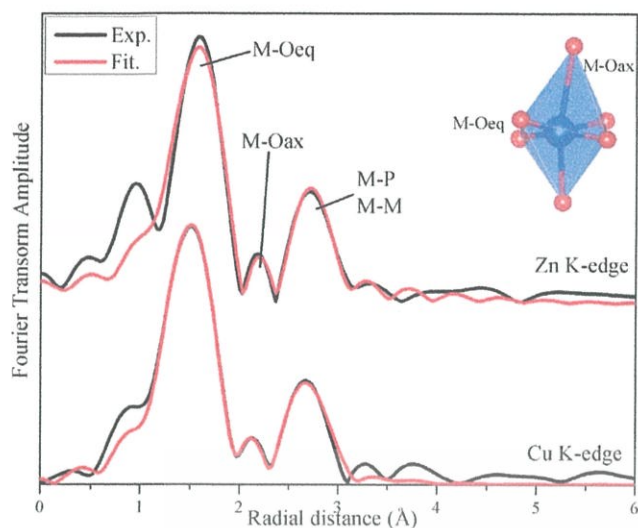


Fig. 6. Experiment (Black line) and fitted EXAFS data (Red line) at Cu and Zn K-edge of CuZnP_2O_7 . (For interpretation of the references to color in this figure legend, the reader is referred to the web version of this article.)

Table 3
Results obtained by EXAFS fitting analysis.

Sample	Path	Shell	CN	R(Å)	$\sigma^2(\text{Å}^2)$	R-factor
CuZnP_2O_7	Cu-Oeq	1	4	1.96081	0.00704	0.0061
	Cu-Oax	2	2	2.26967	0.01537	
	Cu-Cu	3	1	3.01409	0.00738	
	Cu-P1	3	2	3.07768	0.05747	
	Cu-P2	3	2	3.11544	0.04976	
	Zn-Oeq	1	4	2.03230	0.00796	
	Zn-Oax	2	2	2.35242	0.07798	
	Zn-Zn	3	1	3.12398	0.01144	
	Zn-P1	3	2	3.18988	0.04815	
	Zn-P2	3	2	3.22903	0.00469	

$\text{Zn}_2\text{P}_2\text{O}_7$ is a completely solid solution with $\text{Cu}_2\text{P}_2\text{O}_7$ being brought to a CuZnP_2O_7 compound.

4. Conclusion

Phase formation of the binary metal pyrophosphate, CuZnP_2O_7 , was studied at different temperatures in the range of 400–800 °C. Samples were obtained by solid state reaction using stoichiometry of CuO, ZnO and $\text{NH}_4\text{H}_2\text{PO}_4$ at ambient temperature to 800 °C. Intermediate substances of reaction were observed by FT-IR, Raman, and XRD measurements that included $\alpha\text{-Cu}_2\text{P}_2\text{O}_7$, $\alpha\text{-Zn}_2\text{P}_2\text{O}_7$, $3\text{CuO}\cdot 2\text{P}_2\text{O}_5\cdot 0.3\text{NH}_3\cdot 0.2\text{H}_2\text{O}$, and $\text{Zn}_2\text{P}_2\text{O}_7\cdot 3\text{H}_2\text{O}$, of which $\text{Zn}_2\text{P}_2\text{O}_7\cdot 3\text{H}_2\text{O}$ was the strongest intermediate substance. The CuZnP_2O_7 sample completely reacted at a temperature of about 700 °C, with low crystallinity. When the temperature increased to about 800 °C, the structure had an ordering atomic arrangement, which was brought to long range order and increased crystallinity. Cu:Zn evolution in the structure was separated into two parts with increasing temperature that started below 600 °C. Thus, increasing Cu and decreasing Zn contents had clear linear relationships. When the temperature rose above 600 °C, the range of reaction was close to completion. The calcination temperature has been found to have a pronounced effect on phase formation and chemical composition of the calcined CuZnP_2O_7 powders. The complete solid solution was clearly confirmed by EXAFS fitting spectra.

Acknowledgements

This work has partially been supported by the National Nanotechnology Center (NANOTEC), NSTDA, Ministry of Science and Technology, Thailand, through its program of Center of Excellence Network, the Synchrotron Light Research Institute (Public Organization) for EXAFS measurement and the Thailand Research Fund (TRF) under Grant No. BRG5680006.

References

- [1] J.J. Bian, D.W. Kim, K.S. Hong, Microwave dielectric properties of $\text{A}_2\text{P}_2\text{O}_7$ (A = Ca, Sr Ba; Mg, Zn, Mn), *Jpn. J. Appl. Phys.* 43 (2004) 3521–3525.
- [2] J.J. Bian, D.W. Kim, K.S. Hong, Microwave dielectric properties of $(\text{Ca}_{1-x}\text{Zn}_x)_2\text{P}_2\text{O}_7$, *Mater. Lett.* 59 (2005) 257–260.
- [3] W. Wenwei, F. Yanjin, W. Xuehang, L. Sen, L. Shushu, Preparation via solid-state reaction at room temperature and characterization of layered nanocrystalline $\text{NH}_4\text{MnPO}_4\cdot\text{H}_2\text{O}$, *J. Phys. Chem. Solids* 70 (2009) 584–587.
- [4] M. Weil, B. Stöger, Crystal chemistry of transition metal diarsenates $\text{M}_2\text{As}_2\text{O}_7$ (M = Mn, Co, Ni, Zn): variants of the thortveitite structure, *Acta Crystallogr. B* 66 (2010) 603–614.
- [5] C. Calvo, The crystal structure and phase transition of $\beta\text{-Zn}_2\text{P}_2\text{O}_7$, *Can. J. Chem.* 43 (1965) 1147–1153.
- [6] M.A. Petrova, V.I. Shitova, G.A. Mikirticheva, V.F. Popova, A.E. Malshikov, New data on $\text{Zn}_2\text{P}_2\text{O}_7$ phase transformations, *J. Solid State Chem.* 119 (1995) 219–223.
- [7] Z.W. Xiao, G.R. Hu, Z.D. Peng, K. Du, X.G. Gao, Solid state synthesis and characterization of iron(II) pyrophosphate $\text{Fe}_2\text{P}_2\text{O}_7$, *Chin. Chem. Lett.* 18 (2007) 1525–1527.
- [8] A. Bensalem, M. Ahluwalia, T.V. Vijayaraghavan, Y.H. Ko, Synthesis of amorphous $\text{MgHPO}_4\cdot x(\text{R})$ [R = ethanol; ethylene glycol] in anhydrous media, *Mater. Res. Bull.* 32 (1997) 1473–1483.
- [9] C. Díaz, M.I. Valenzuela, V. Lavayen, K. Mendoza, D.O. Peña, C. O'Dwyer, Nanostructured copper oxides and phosphates from a new solid-state route, *Inorg. Chim. Acta* 377 (2011) 5–13.
- [10] D. Brandová, M. Trojan, M. Arnold, F. Paulik, J. Paulik, Mechanism of dehydration and condensation of $\text{CuHPO}_4\cdot\text{H}_2\text{O}$, *J. Therm. Anal.* 34 (1988) 1449–1454.
- [11] D. Brandová, M. Trojan, F. Paulik, J. Paulik, Mechanism of dehydration of $\text{ZnHPO}_4\cdot\text{H}_2\text{O}$, *J. Therm. Anal.* 32 (1978) 1923–1928.
- [12] A. Jotimi, J.C. Gácon, M. Ferid, M. Trabelsi-Ayadi, Luminescence and scintillation properties of praseodymium poly and diphosphates, *Opt. Mater.* 24 (2003) 175–180.
- [13] T. Yang, J. Lin, Hydrothermal syntheses and low temperature magnetic behaviors of $\text{ACo}_3(\text{P}_2\text{O}_7)_2$ (A = Ca, Sr Ba, Pb), *J. Solid State Chem.* 198 (2013) 1–5.
- [14] R. Shannon, Revised effective ionic radii and systematic studies of interatomic distances in halides and chalcogenides, *Acta Crystallogr. A* 32 (1976) 751–767.
- [15] E. Steger, B. Käbner, Die infrarotspektren von wasserfreien schwermetall-diphosphaten, *Spectrochim. Acta A* 24 (1968) 447–456.
- [16] B. Boonchom, R. Baitahe, Synthesis and characterization of nanocrystalline manganese pyrophosphate $\text{Mn}_2\text{P}_2\text{O}_7$, *Mater. Lett.* 63 (2009) 2218–2220.
- [17] B. Boonchom, M. Thongkam, S. Kongtaweelert, N. Vittayakorn, Flower-like microparticles and novel superparamagnetic properties of new binary $\text{Co}_{1/2}\text{Fe}_{1/2}(\text{H}_2\text{PO}_4)_2\cdot 2\text{H}_2\text{O}$ obtained by a rapid solid state route at ambient temperature, *Mater. Res. Bull.* 44 (2009) 2206–2210.
- [18] K. Pogorzalec-Glaser, A. Pietraszko, B. Hlilczar, M. Polomska, Structure and phase transitions in $\text{Cu}_2\text{P}_2\text{O}_7$, *Phase Transit.* 79 (2006) 535–544.
- [19] K. Meyer, Characterization of the structure of binary zinc ultraphosphate glasses by infrared and Raman spectroscopy, *J. Non-Cryst. Solids* 209 (1997) 227–239.
- [20] L. Jin-bing, J. Zhi-quan, Q. Kun, H. Wei-xin, Effect of calcination temperature on surface oxygen vacancies and catalytic performance towards CO oxidation of Co_3O_4 nanoparticles supported on SiO_2 , *Chin. J. Chem. Phys.* 25 (2012) 103.
- [21] S. Zhang, C. Zhang, H. Yang, Y. Zhu, Formation and performances of porous InVO_4 films, *J. Solid State Chem.* 179 (2006) 873–882.
- [22] F.M. Liu, J.H. Ye, B. Ren, Z.L. Yang, Y.Y. Liao, A. See, L. Chan, Z.Q. Tian, Raman spectroscopic studies of the formation processes of cobalt silicide thin films, *Thin Solid Films* 471 (2005) 257–263.
- [23] A. Fairbrother, X. Fontané, V. Izquierdo-Roca, M. Espíndola-Rodríguez, S. López-Marino, M. Placidi, L. Calvo-Barrio, A. Pérez-Rodríguez, E. Saucedo, On the formation mechanisms of Zn-rich $\text{Cu}_2\text{ZnSnS}_4$ films prepared by sulfuration of metallic stacks, *Sol. Energ. Mat. Sol. C* 112 (2013) 97–105.
- [24] G. Berhault, P. Afanasiev, H. Loboue, C. Geantet, T. Cseri, C. Pichon, C. Guillot-Deudon, A. Lafond, In Situ XRD XAS, and magnetic susceptibility study of the reduction of ammonium nickel phosphate $\text{NiNH}_4\text{PO}_4\cdot\text{H}_2\text{O}$ into nickel phosphide, *Inorg. Chem.* 48 (2009) 2985–2992.
- [25] P.Y.Z.K. Vitalij Pecharsky, Fundamentals of Powder Diffraction and Structural Characterization of Materials, 2nd ed., Springer, 2009, 2014.
- [26] H.P. Klug, L.E. Alexander, X-ray Diffraction Procedures for Polycrystalline and Amorphous Materials, 2nd ed., Wiley, New York, 1974.
- [27] J.I. Langford, A.J.C. Wilson, Scherrer after sixty years: a survey and some new results in the determination of crystallite size, *J. Appl. Crystallogr.* 11 (1978) 102–113.

- [28] S. Calvin, S.X. Luo, C. Caragianis-Broadbridge, J.K. McGuinness, E. Anderson, A. Lehman, K.H. Wee, S.A. Morrison, L.K. Kurihara, Comparison of extended X-ray absorption fine structure and Scherrer analysis of X-ray diffraction as methods for determining mean sizes of polydisperse nanoparticles, *Appl. Phys. Lett.* 87 (2005) .
- [29] D.-M. Smilgies, Scherrer grain-size analysis adapted to grazing-incidence scattering with area detectors, *J. Appl. Crystallogr.* 42 (2009) 1030–1034.
- [30] B.E. Robertson, C. Calvo, Crystal structure of β - $\text{Cu}_2\text{P}_2\text{O}_7$, *Can. J. Chem.* 46 (1968) 605–612.
- [31] B. Ravel, M. Newville, Athena, Artemis, Hephaestus, data analysis for X-ray absorption spectroscopy using IFEFFIT, *J. Synchrotron Radiat.* 12 (2005) 537–541.



This material is reserved for educational use only, not allowed for commercial use.

Forbidden to modify the content, and cite the document when use.

Cite this: *RSC Adv.*, 2015, 5, 88890

Correlation between the chromaticity, dielectric properties and structure of the binary metal pyrophosphates, $\text{Cu}_{(2-x)}\text{Zn}_x\text{P}_2\text{O}_7$

Rattana Baitahe,^a Naratip Vittayakorn^{*ab} and Santi Maensiri^c

The binary metal pyrophosphates, $\text{Cu}_{(2-x)}\text{Zn}_x\text{P}_2\text{O}_7$; $x = 0.50$ – 1.50 , were synthesized *via* solid state reaction in order to obtain information on their solid solution phase formation. Characteristic peaks of the β -phase were detected under UV/Vis light emission in the range of 1200 – 1250 cm^{-1} . The $\text{P}_2\text{O}_7^{4-}$ ion, analyzed through vibration, carried the O–P–O radical, P–O–P bridge, and approximate M–O bond stretching, and was identified using Raman and Fourier transform infrared (FT-IR) spectra. The corrected dielectric constant (ϵ_r) of the samples showed a similar value when Cu^{2+} was replaced by Zn^{2+} in the $\text{Cu}_2\text{P}_2\text{O}_7$ structure. However, a slightly decreasing ϵ_r could still be seen when the component x increased. The color of the samples with $x = 0.00$ – 1.50 exhibit a greenish hue, except for the composition with $x = 2.00$, which presents a colourless powder. The CIE chromaticity coordinates of $\text{Cu}_{(2-x)}\text{Zn}_x\text{P}_2\text{O}_7$; $x = 0.50$ to 1.50 , shifted from $(0.303, 0.366)$ to $(0.292, 0.388)$, thus corresponding to a visible wavelength that shifted from about 506 to 512 nm , and 561 nm for $x = 0.00$. The phenomena of both dielectric and optical properties resulted from the changing crystal structure of the respective $\text{P}_2\text{O}_7^{4-}$ cluster and octahedral M–O₆ site. Investigation of the crystal structure was carried out by using Rietveld refinement analysis, with support from the extended X-ray absorption fine structure (EXAFS) fitting technique. Furthermore, this study revealed the relationships for binary metal pyrophosphates between their structure and dielectric properties, and the correlation between their structure and optical properties, which was confirmed by the reduction in chemical bonding, bond angle, number of clusters, and distortion of the octahedral MO₆.

Received 11th June 2015
Accepted 30th September 2015

DOI: 10.1039/c5ra11103j

www.rsc.org/advances

1. Introduction

Generally, divalent metal pyrophosphate salts ($\text{M}_2\text{P}_2\text{O}_7$; M = metal element), have a polymorphic structure. The crystal structure consists of two main parts, which consist of six oxygen atoms around a metal atom, or octahedral MO₆, and a $\text{P}_2\text{O}_7^{4-}$ cluster that is caused by the polymerization of two $[\text{PO}_4]^{3-}$ ions clustering to $[\text{P}_2\text{O}_7]^{4-}$.^{1,2} These phosphates have two crystallization conformations. The first is a dichromate type, with an M radius in the structure of greater than 0.97 \AA in, for example, $\text{Ca}_2\text{P}_2\text{O}_7$, $\text{Sr}_2\text{P}_2\text{O}_7$, $\text{Ba}_2\text{P}_2\text{O}_7$, $\text{Pb}_2\text{P}_2\text{O}_7$, and $\text{Cd}_2\text{P}_2\text{O}_7$.³ The $\text{P}_2\text{O}_7^{4-}$ cluster, in an eclipsed conformation, crystallizes in this group at about the center of the symmetry and P–O–P bridge, which spread towards each other. The second is a thortveitite type, with an M radius of less than 0.97 \AA in, for example, $\text{Cu}_2\text{P}_2\text{O}_7$,

$\text{Zn}_2\text{P}_2\text{O}_7$, $\text{Ni}_2\text{P}_2\text{O}_7$, $\text{Mn}_2\text{P}_2\text{O}_7$, $\text{Co}_2\text{P}_2\text{O}_7$, and $\text{Mg}_2\text{P}_2\text{O}_7$. This type of $\text{P}_2\text{O}_7^{4-}$ cluster occurs in a staggered conformation. On the other hand, the metal pyrophosphate compounds are separated by a stable phase structure at different temperatures, which includes α - $\text{M}_2\text{P}_2\text{O}_7$ and β - $\text{M}_2\text{P}_2\text{O}_7$ phases (low and high temperature, respectively).⁴ Generally, the α -phase is the stable phase of $\text{Cu}_2\text{P}_2\text{O}_7$ at room temperature. The α - $\text{Cu}_2\text{P}_2\text{O}_7$ phase exhibits the monoclinic space group, $C2/c$, with lattice parameters of $a = 6.876\text{ \AA}$, $b = 8.113\text{ \AA}$, $c = 9.162\text{ \AA}$, and $\beta = 109.54^\circ$. High temperature analysis shows that the monoclinic $C2/c$ transforms to monoclinic $C2/m$ (β - $\text{Cu}_2\text{P}_2\text{O}_7$ phase), with lattice parameters of $a = 6.827\text{ \AA}$, $b = 8.118\text{ \AA}$, $c = 4.576\text{ \AA}$, and $\beta = 108.85^\circ$. The transition temperature of $\alpha \rightarrow \beta$ phase is about 100°C .⁵ Regarding the $\text{Zn}_2\text{P}_2\text{O}_7$ structure, α - $\text{Zn}_2\text{P}_2\text{O}_7$ has the monoclinic space group, $I2/c$, at room temperature, with unit cell parameters of $a = 20.068\text{ \AA}$, $b = 8.259\text{ \AA}$, $c = 9.099\text{ \AA}$, and $\beta = 106.35^\circ$. The transition temperature of α - $\text{Zn}_2\text{P}_2\text{O}_7$ to β - $\text{Zn}_2\text{P}_2\text{O}_7$ was found to be about 130°C . The β - $\text{Zn}_2\text{P}_2\text{O}_7$ phase displays the monoclinic space group, $C2/m$, with unit cell parameters of $a = 6.61\text{ \AA}$, $b = 8.29\text{ \AA}$, $c = 4.51\text{ \AA}$, and $\beta = 105.4^\circ$.⁶ In addition, the crystal structure of $\text{Zn}_2\text{P}_2\text{O}_7$ was observed in other phases, such as x and y , which are metastable phases in the form of $2\text{ZnO} \cdot \text{P}_2\text{O}_5$.⁷ The δ - $\text{Zn}_2\text{P}_2\text{O}_7$ phase is poorly crystalline, and the

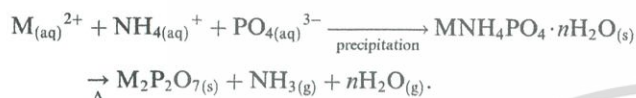
^aElectroceramic Research Laboratory, College of Nanotechnology, King Mongkut's Institute of Technology Ladkrabang, Bangkok 10520, Thailand. E-mail: naratipcmu@yahoo.com; Fax: +66-2-326-4415

^bDepartment of Chemistry, Faculty of Science, King Mongkut's Institute of Technology Ladkrabang, Bangkok 10520, Thailand

^cSchool of Physics, Institute of Science, Suranaree University of Technology, Nakhon Ratchasima 30000, Thailand

γ - $\text{Zn}_2\text{P}_2\text{O}_7$ phase is orthorhombic with a unit cell of $a = 4.950 \text{ \AA}$, $b = 13.335 \text{ \AA}$, and $c = 16.482 \text{ \AA}$. It is interesting to note that the β - $\text{Zn}_2\text{P}_2\text{O}_7$ and β - $\text{Cu}_2\text{P}_2\text{O}_7$ phases have the same space group in the monoclinic phase, which enables the high possibility of solid solution formation at high temperature.

A group of metal pyrophosphate compounds can be applied widely in, for example, biomedical cements, chelating agents, corrosion-resistant coatings, high-quality fertilizers, glass ceramics, and microwave dielectric materials.^{8–10} Most research studies on this group of compounds often focus on synthesis and characterization,^{11,12} such as synthesis through wet chemical processing *via* metal ammonium phosphate hydrates ($\text{MNH}_4\text{PO}_4 \cdot n\text{H}_2\text{O}$) or metal hydrogen phosphate hydrates ($\text{MHPO}_4 \cdot n\text{H}_2\text{O}$) with calcination at different temperatures^{2,12} as follows:



The kinetics and thermodynamics of phase formation were studied in order to explain the mechanism of the reaction, intermediate reaction, and energy of the reaction (ΔH^* , ΔS^* , and ΔG^* , respectively).^{13–15} In order to understand the crystal structure^{5,6} and its properties,^{16,17} structural refinement of the final product was analyzed. However, the study of the relationship between the crystal structure and properties has not been widely performed. Therefore, this research aimed to study the relationship between the crystal structure and dielectric properties, and that between the crystal structure and optical properties of the binary metal pyrophosphates, $\text{Cu}_{(2-x)}\text{Zn}_x\text{P}_2\text{O}_7$; $x = 0.50$ – 1.50 , by using Rietveld refinement analysis and the extended X-ray absorption fine structure (EXAFS) fitting technique. Previously, Kim *et al.*¹⁸ reported two important factors which caused polarization in the structure of metal pyrophosphate compounds. These factors consisted of shifting O atoms in the collinear P–O–P bridge and movement of M^{2+} ions in the octahedral MO_6 , but with relatively few details of the structure. Consequently, the effect of bond length, bond angle, bond strength, number of P–O–P clusters, average bond length, and distortion of the octahedral MO_6 site were considered in order to explain the relationship between the crystal structure, dielectric properties, and optical properties of $\text{Cu}_{(2-x)}\text{Zn}_x\text{P}_2\text{O}_7$; $x = 0.00$ – 2.00 metal pyrophosphate compounds, which produced the mechanism of the phase formation.¹⁹

2. Experimental procedure

Powders with the compositions, $\text{Cu}_{(2-x)}\text{Zn}_x\text{P}_2\text{O}_7$; $x = 0.00$ – 2.00 , were synthesized *via* solid state reaction using the reagent-grade metal oxides and hydrogen phosphate powders CuO (99.9%), ZnO (99.9%), and $(\text{NH}_4)_2\text{HPO}_4$ (99%). All of the raw materials were weighed in stoichiometric proportions and then mixed homogeneously by vibratory ball milling with stabilized zirconia balls for 24 h in anhydrous ethanol. The dried powders were calcined in crucibles at $800 \text{ }^\circ\text{C}$ for 24 h, then vibratory-

milled again for 2 h. After that, each calcined powder was sieved and mixed with 5 wt% polyvinyl alcohol (PVA) solution and uniaxially pressed into green disks of 10 mm diameter. The sintering temperature was varied between 700 – $900 \text{ }^\circ\text{C}$ for 24 h in order to obtain optimum sintering conditions. In order to eliminate the extrinsic factors of electrical properties such as grain size and density, ceramics with more than 95% theoretical density and near average grain size of each composition were selected for investigating the electrical properties. The vibration group of the samples was examined at room temperature using Fourier transform infrared (FT-IR) spectroscopy in the range of 3000 – 400 cm^{-1} , with eight scans on a Perkin-Elmer Spectrum GX spectrometer and a resolution of 4 cm^{-1} . Raman spectra were measured in the wavenumber range of 100 – 1600 cm^{-1} , with eight scans on a Thermo Scientific DXR Raman microscope, using the 532 nm excitation line of a He–Ne laser in order to support the identification of crystal structured ceramics. The dielectric properties were measured at 1 MHz *via* the use of an LCR meter (HP4284A; Hewlett-Packard, Palo Alto, CA). An image stacked SONY IMX214 CMOS sensor collected the colors of the samples, and matched them with CIE chromaticity diagrams in order to approximate the tendency of the absorption wavelength. Details of the crystal structure were studied through X-ray diffraction (XRD) of the powders, using a D8 Advanced powder diffractometer (Bruker AXS, Karlsruhe, Germany), with Cu K_α radiation ($\lambda = 0.1546 \text{ nm}$); and X-ray absorption spectroscopy (XAS) was conducted on the beam line (BL8) of the National Synchrotron Research Center (Thailand). A double crystal Ge(220) was used for the EXAFS mono-chromator. X-ray absorption (XAS) spectra were collected in transmission mode at the Cu and Zn K-edge.

3. Results and discussion

Functional group analysis

FT-IR and Raman spectroscopy (Raman) are powerful methods for analyzing the chemical bonding of vibration, rotational, and other low-frequency modes in the phosphate system. $\text{M}_2\text{P}_2\text{O}_7$ has a monoclinic structure with zone-center (C -point) phonons in the lattice vibration of these metal pyrophosphates, and it can be characterized by irreducible representation of the spectroscopic group, C_{2h} . Factor group analysis was conducted by using the procedure of Kroumova *et al.*²⁰ The single metal pyrophosphate, α - $\text{Cu}_2\text{P}_2\text{O}_7$ ($x = 0.00$), showed four formula units in the unit cell ($Z = 4$). Cu and P atoms were attributed to the $8f$ position, and O atoms to both the $8f$ and $4e$ positions (Wyckoff notation). In order to remove the 3 acoustic modes ($\Gamma_{\text{acoustic}} = A_u + 2B_u$) from the total number ($N_{\text{tot}} = 66$) of vibrations, the optical modes of the lattice vibration were represented by

$$\Gamma_{\text{optic}} = 16A_g + 15A_u + 17B_g + 15B_u$$

The odd (un-gerade; A_u and B_u) vibration represents infrared-active modes (Γ_{IR}), as presented in the following equation:

$$\Gamma_{\text{IR}} = 15A_u + 15B_u$$

In addition, all even (gerade; A_g and B_g) vibrations are in Raman-active modes (Γ_{Raman}), as exhibited in the following equation:

$$\Gamma_{\text{Raman}} = 16A_g + 17B_g$$

The binary metal pyrophosphates, $\text{Cu}_{(2-x)}\text{Zn}_x\text{P}_2\text{O}_7$; $x = 0.50$, 1.00, and 1.50, showed two formula units in the unit cell ($Z = 2$). The Cu and Zn atoms are distributed in the 4h position, and P atoms are attributed to the 4i position. The O atoms are attributed to three positions that include 2a, 4i, and 8j. IR-active and Raman-active modes, but not acoustic modes, are shown in the following equations:

$$\Gamma_{\text{IR}} = 6A_u + 9B_u$$

$$\Gamma_{\text{Raman}} = 8A_g + 7B_g$$

In addition, the single metal pyrophosphate, $\alpha\text{-Zn}_2\text{P}_2\text{O}_7$ ($x = 2.00$), exhibited twelve formula units in the unit cell ($Z = 12$) that were quite complex in structure. Zn and P atoms were attributed to the 8f position, and O atoms to both the 8f and 4e positions. IR-active and Raman-active modes, but not acoustic modes, are determined by the following equations:

$$\Gamma_{\text{IR}} = 48A_u + 48B_u$$

$$\Gamma_{\text{Raman}} = 49A_g + 50B_g$$

As a result, the number of peaks appeared to be greater in both the FT-IR and Raman spectra of $\alpha\text{-Zn}_2\text{P}_2\text{O}_7$ than in other compounds. A number of peaks were detected using the Raman and IR techniques that related to the symmetry of the crystal structure in the pyrophosphate form. This resulted in the absorption of different resonant frequencies from the frequency of the absorbed radiation, which matches the transition of the energy in the vibrating bond or group. It can be proposed that bonding in the structure is different, as it appears in many of the peaks. The FT-IR spectra of the samples, which closely resemble those of the $\text{M}_2\text{P}_2\text{O}_7$ pyrophosphate compounds ($\text{M} = \text{Cu}, \text{Cd}, \text{Fe}, \text{Mn}, \text{Ni}$), are shown in Fig. 1.^{1,24} The strong vibration bands at about 1190 and 1060 cm^{-1} are attributed to asymmetric ($\nu_{\text{as}} \text{PO}_3$). Vibration bands at about 1100 cm^{-1} are attributed to symmetric stretching ($\nu_{\text{s}} \text{PO}_3$) of the PO_3 unit, while asymmetric ($\delta_{\text{as}} \text{PO}_3$) and symmetric ($\delta_{\text{s}} \text{PO}_3$) bending vibrations are observed at about 584 and 542 cm^{-1} , respectively. The asymmetric ($\nu_{\text{as}} \text{P-O-P}$) and symmetric stretch ($\nu_{\text{s}} \text{P-O-P}$) bridge vibrations for this sample are observed at about 960 and 740 cm^{-1} , respectively. PO_3 determination, the rocking mode of the P-O-P deformations, and the torsional and external modes are found in the 400 cm^{-1} region. The number of bands in this spectral region confirms the existence of distinct nonequivalent

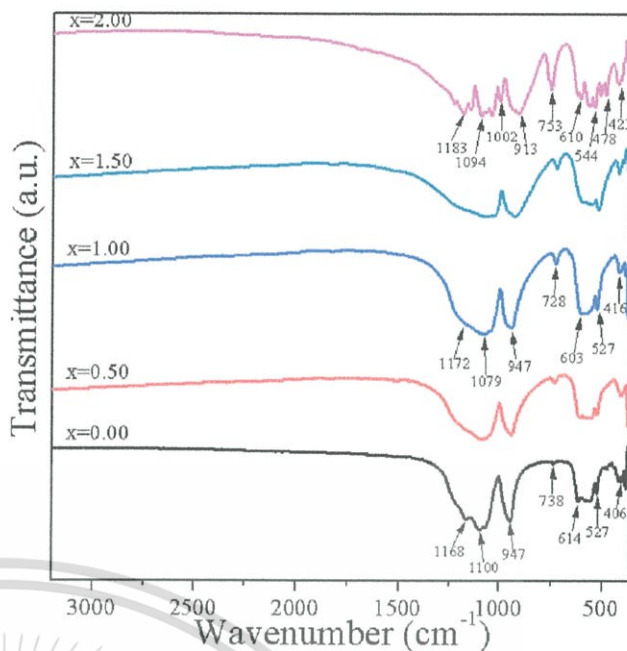


Fig. 1 FT-IR spectra of $\text{Cu}_{(2-x)}\text{Zn}_x\text{P}_2\text{O}_7$; $x = 0.00$ – 2.00 .

phosphate units in each structure and loss of degeneracy in the vibration modes, which were confirmed using factor group analysis.^{22,23} Additionally, a strong ($\nu_{\text{s}} \text{P-O-P}$) band (730 cm^{-1}) was seen in the FT-IR spectrum of the samples, and is known to be the most striking feature of polyphosphate spectra. Most of the FT-IR data showed details of the functional group of the phosphates. Therefore, the support of Raman spectroscopy was used to analyze the metal oxide stretching (M-O) and the phase-characteristics (α -, β -phase) of the pyrophosphate compounds at low frequencies. The Raman spectra of the samples are shown in Fig. 2 and tabulated in Table 1, the result corresponds well with the FT-IR result. Furthermore, the Raman results show a β -phase form in the pyrophosphate groups²⁴ through a detectably weak peak at approximately 1210 cm^{-1} . The single metal pyrophosphates ($x = 0.00$ and $x = 2.00$), and three distinct peaks that originate from the $\nu_{\text{as}}(\text{PO}_3)$ vibrations, are visible at about 1210, 1140 and 1080 cm^{-1} . The peaks remain at 1140 and 1080 cm^{-1} in the samples with $x = 0.50$, 1.00, and 1.50, or binary metal pyrophosphates, but the peak at 1210 cm^{-1} disappears. This indicates that the binary metal phosphates closely resemble the $\beta\text{-Cu}_2\text{P}_2\text{O}_7$ phase, with a monoclinic structure and the space group, $C2/m$. In addition, single metal pyrophosphates exhibited an alpha phase (α -phase). The Cu^{2+} ion is replaced by Zn^{2+} in the $\text{Cu}_{(2-x)}\text{Zn}_x\text{P}_2\text{O}_7$ structure. The M-O stretching band at around 200 cm^{-1} shifts to a lower wavenumber, and the interatomic distance between the metal and oxygen atom affects the bond strength and absorbs energy also at a lower wavenumber. The single metal pyrophosphates were observed with M-O stretching and peak splitting at 208, 212, and 248 cm^{-1} for $x = 0.00$. The spectrum of the sample with $x = 2.00$ was observed to have five splitting peaks at 171, 182, 201, 211, and 254 cm^{-1} . These results show that the crystal structure of the sample with $x = 2.00$ has a lower symmetry than

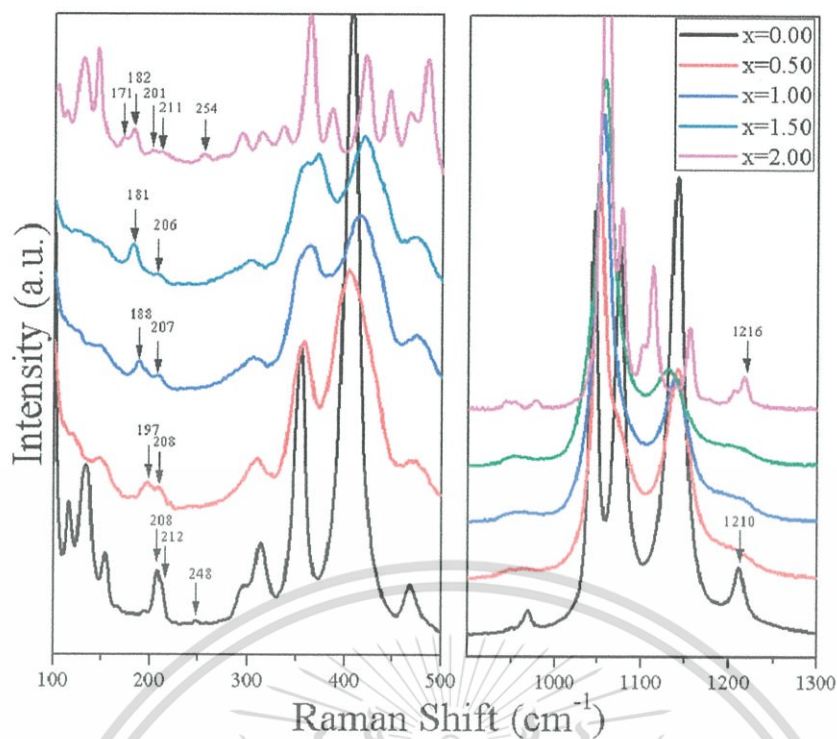


Fig. 2 Raman spectra of $\text{Cu}_{(2-x)}\text{Zn}_x\text{P}_2\text{O}_7$; $x = 0.00-2.00$.

that of $x = 0.00$, due to the number of splitting peaks, which causes a different M–O bond length. Regarding binary metal pyrophosphates, splitting peaks were detected in only two regions in each of three samples: 197 and 208 cm^{-1} for $x = 0.50$, 188 and 207 cm^{-1} for $x = 1.00$, and 181 and 206 cm^{-1} for $x = 1.50$. It should be pointed out that the crystal structure of the binary metal pyrophosphates has higher symmetry than the single metal pyrophosphate compound, which is proven using the structural analysis from Rietveld refinement and EXAFS fitting.

Dielectric and optical properties

The mean static atomic dielectric constants of the $\text{Cu}_{(2-x)}\text{Zn}_x\text{P}_2\text{O}_7$; $x = 0.00-2.00$ compounds were estimated using the well-known Clausius–Mossotti equation:²⁵

$$\epsilon_r = \frac{(3V_m + 8\pi\alpha_D)}{(3V_m - 4\pi\alpha_D)}$$

where ϵ_r is the mean static atomic dielectric constant, α_D is the sum of the dielectric polarizabilities of the individual ions, and V_m is the molar volume. The dielectric constant as a function of the composition x is presented in Fig. 3, which shows the comparison between calculated data (red bars), and measured results (green bars). The single metal pyrophosphates show a dielectric constant (ϵ_r) of about 13, which is higher than the ϵ_r

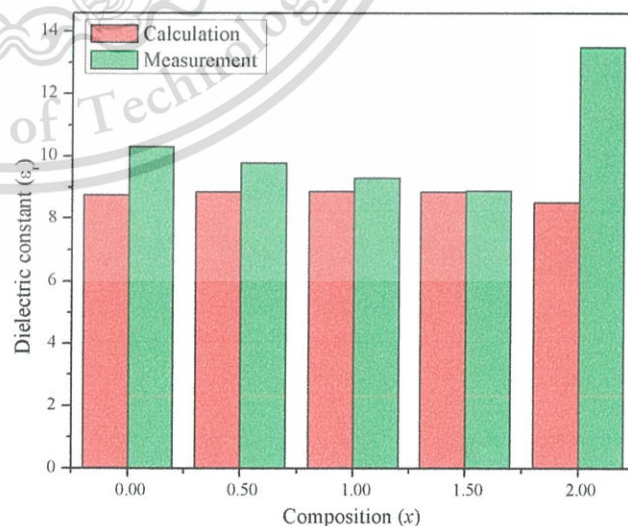


Fig. 3 Dielectric constant plots of $\text{Cu}_{(2-x)}\text{Zn}_x\text{P}_2\text{O}_7$; $x = 0.00-2.00$.

Table 1 Vibrational assignment of the samples^a

Wavenumber (cm^{-1})	FT-IR	Raman	Assignment
1250–1200	—	w	α -Phase characteristic
1200–1100	vs	vs	$\nu_{\text{as}}(\text{PO}_3)$
1100–1050	vs	vs	$\nu_{\text{s}}(\text{PO}_3)$
1050–1000	vs	vs	$\nu_{\text{as}}(\text{PO}_3)$
980–950	s	vw	$\nu_{\text{as}}(\text{POP})$
760–730	m	w	$\nu_{\text{s}}(\text{POP})$
650–280	s	s	$\delta(\text{OPO}) + \nu(\text{M-O})$
160–260	—	w	$\nu(\text{M-O})$
200–100	—	m	Lattice vibration

^a vw: very weak, w: weak, m: medium, s: strong, vs: very strong.

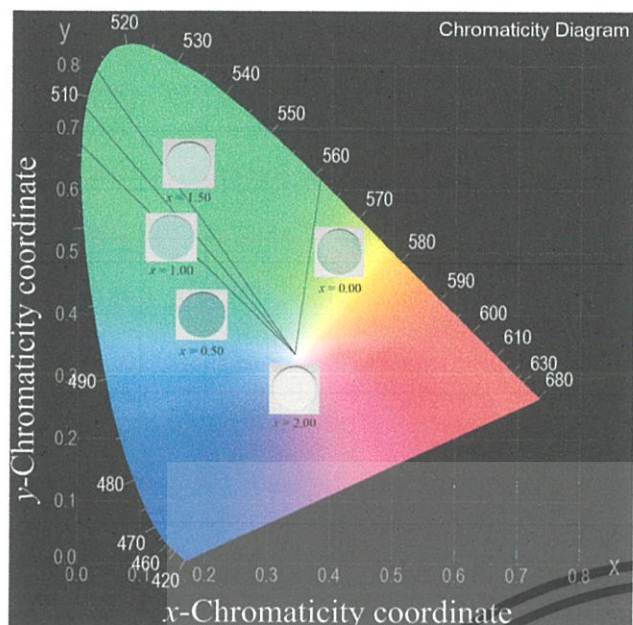


Fig. 4 CIE chromatic coordinates of $\text{Cu}_{(2-x)}\text{Zn}_x\text{P}_2\text{O}_7$; $x = 0.00$ – 2.00 .

of 10 in binary metal pyrophosphates. The Clausius–Mossotti equation focuses on only the dielectric constant from atomic polarization (electron cloud bias in the electric field). Indeed, the samples were measured at a frequency of 1 MHz for the decreasing extrinsic factor, and the polarization caused the cations (Cu^{2+} , Zn^{2+} , and P^{5+}) and anions (O^{2-}) in the structure to move. The moving ions in the electric field are the cause of the increased dielectric constant compared to the calculated data using the Clausius–Mossotti equation, as considered in this study using the bond angle, bond length, and volume of the octahedral MO_6 .

The coordination complexes have color properties such as green for $[\text{CoF}_6]^{3-}$, red for $[\text{Co}(\text{NH}_3)_5\text{H}_2\text{O}]^{3+}$, and blue for $[\text{Cu}(\text{NH}_3)_4(\text{H}_2\text{O})_2]^{2+}$. The phenomenon of color is explained by crystal field theory (CFT),^{26,27} from which $\text{Cu}_{(2-x)}\text{Zn}_x\text{P}_2\text{O}_7$; $x =$

0.00 – 2.00 compounds show a greenish color, except for the composition with $x = 2.00$, which exhibits a colorless powder. The optical properties and corresponding CIE chromatic coordinates^{26,28,29} of these samples are shown in Fig. 4. The results of the composition with $x = 0.00$, illustrated a yellowish-green color, while the binary metal compounds ($x = 0.50$ – 1.50) presented color tones that changed from bluish-green to green. The composition with $x = 2.00$, was seen as colorless. The CIE chromaticity diagram can approximate roughly a visible and an absorption wavelength (nm). The CIE chromaticity coordinates of $\text{Cu}_{(2-x)}\text{Zn}_x\text{P}_2\text{O}_7$; $x = 0.50$ – 1.50 shift from (0.303, 0.366) to (0.292, 0.388) with increasing x , which corresponds to the visible wavelength and shifts from about 506 to 512 nm. The coordinates of $\alpha\text{-Cu}_2\text{P}_2\text{O}_7$ are (0.3454, 0.4081), which corresponds to a wavelength of about 561 nm. This leads to an octahedral crystal field splitting energy (Δ_o) that illustrates z-axis expansion of the octahedral site, with its length calculated using Rietveld refinement analysis and the EXAFS fitting technique.

Structural analysis

Structural refinement was performed through Rietveld refinement analysis³⁰ using the FULLPROF package.³¹ A pseudo-Voigt shape function was adequate at all times for obtaining good fits for the experimental data. The initial model was taken from parameters in the research of Calvo.³² Factors for the P–O–P bond angle, M–O bond length, and quality of fit (χ^2) were obtained from the Rietveld refinement analysis and are summarized in Table 2. Fig. 5 shows the calculated (Y_{cal}) and observed (Y_{obs}) diffraction patterns and different ($Y_{\text{obs}} - Y_{\text{cal}}$) peaks of the samples. The refinement plot gives the evolution of the X-ray diffraction (XRD) patterns in the various $\text{Cu}_{(2-x)}\text{Zn}_x\text{P}_2\text{O}_7$; $x = 0.00$ – 2.00 compositions, and their synthesized pyrophosphates show that single-phase compounds constitute solid solutions. Similarity in the XRD patterns (peak positions) is an indication of only small variations in the unit cell parameters, for example, the small difference in size between the Cu^{2+} ion ($R = 0.73 \text{ \AA}$) and Zn^{2+} ion ($R = 0.74 \text{ \AA}$).³³ Data collected from the Rietveld

Table 2 Bond angle and bond length from Rietveld refinement for the samples

Sample		$x = 0.00$	$x = 0.50$	$x = 1.00$	$x = 1.50$	$x = 2.00$	
POP angle ($^\circ$)		154.6 (10)	180.0 (11)	180.0 (11)	180.0 (11)	138.00 (30)	159.00 (30)
M–O bond length (\AA)	M–O1	1.980 (5)	2.016 (2)	2.037 (6)	2.047 (7)	3.135 (15)	2.196 (11)
	M–O2	1.942 (6)	1.971 (4)	2.012 (5)	1.999 (2)	1.997 (13)	2.017 (11)
	M–O3	1.886 (5)	2.540 (2)	2.476 (3)	2.422 (3)	2.052 (13)	2.371 (16)
	M–O3	2.920 (9)	2.540 (2)	2.476 (3)	2.422 (3)	2.181 (15)	2.079 (11)
Space group		$C2/c$	$C2/m$	$C2/m$	$C2/m$		$I2/c$
Z		4	2	2	2		12
χ^2		1.21	1.21	1.33	1.58		1.6
Lattice parameter	a (\AA)	6.8811 (4)	6.7904 (3)	6.7257 (3)	6.6672 (4)		20.1098 (6)
	b (\AA)	8.1173 (4)	8.1576 (3)	8.1986 (3)	8.2413 (4)		8.2732 (2)
	c (\AA)	9.1614 (5)	4.5579 (2)	4.54312 (3)	4.5307 (3)		9.1067 (3)
	β ($^\circ$)	109.523 (3)	108.429 (2)	107.464 (3)	106.473 (3)		106.326 (2)
	V (\AA^3)	482.308 (43)	239.538 (17)	238.971 (24)	238.733 (27)		1454.012 (74)
R-factor (%)	R_p	9.27	10.0	11.50	14.20		15.70
	R_{wp}	11.70	12.70	14.40	17.90		23.10
	R_{exp}	10.68	11.57	13.49	14.43		18.27

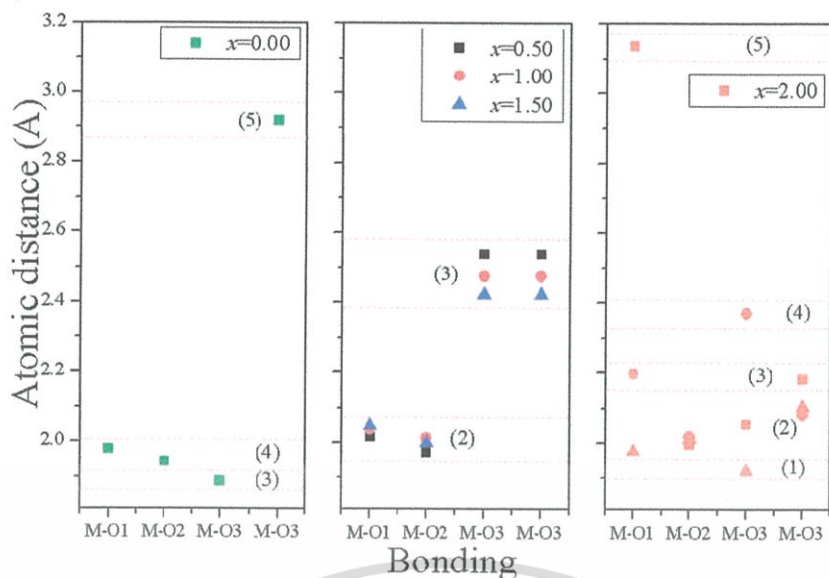


Fig. 6 The approximate grouping of the M–O bonding of $\text{Cu}_{(2-x)}\text{Zn}_x\text{P}_2\text{O}_7$; $x = 0.00\text{--}2.00$.

$$V_{\text{P-O}} = \exp\left(\frac{R_0 - R}{B}\right)$$

where R is the length of a bond between P and O atoms. R_0 and B are parameters determined empirically, by which the B parameter must use a universal value for the empirical parameter B ; $B = 0.37 \text{ \AA}$, which makes a one-parameter model relating to the formal valence V , bond length R , and coordination number N . Therefore, the sum of the bond valence is defined by

$$V_i = \sum_j^N \exp\left(\frac{(R_1 - R_{ij})}{0.37}\right)$$

In divergence, the average bond strength of a single metal pyrophosphate is lower than that in binary metal pyrophosphates. Bond energies and force constants decrease with average bond strength. Determination of a quantitative correlation with the same type of bonding is complex.³⁵ The EXAFS fitting technique was used in support of the structural refinement analysis.

The EXAFS spectra of the samples for the Cu K-edge and Zn K-edge are shown in Fig. 7a and b, respectively. In order to study the environment around the Cu atoms, a primitive EXAFS model was taken from parameters obtained from the Rietveld refinement of each sample. The details of the EXAFS spectroscopic fitting are summarized in Table 4. The results exhibited distortion of the octahedral CuO_6 . The sample with $x = 0.00$ showed three main shells, of which the first shell of the spectrum was modeled in consistency with four oxygen atoms that had interatomic distances of 1.9050 \AA and 1.9643 \AA for Cu–O1 and Cu–O2, respectively. Then, the second shell detected only one oxygen atom; Cu–O3, which had an interatomic distance of 2.3001 \AA . The last shell detected the oxygen atom of octahedral CuO_6 , which had an interatomic distance of 2.9136 \AA that combined scattering from a phosphorus atom, Cu–P bond and

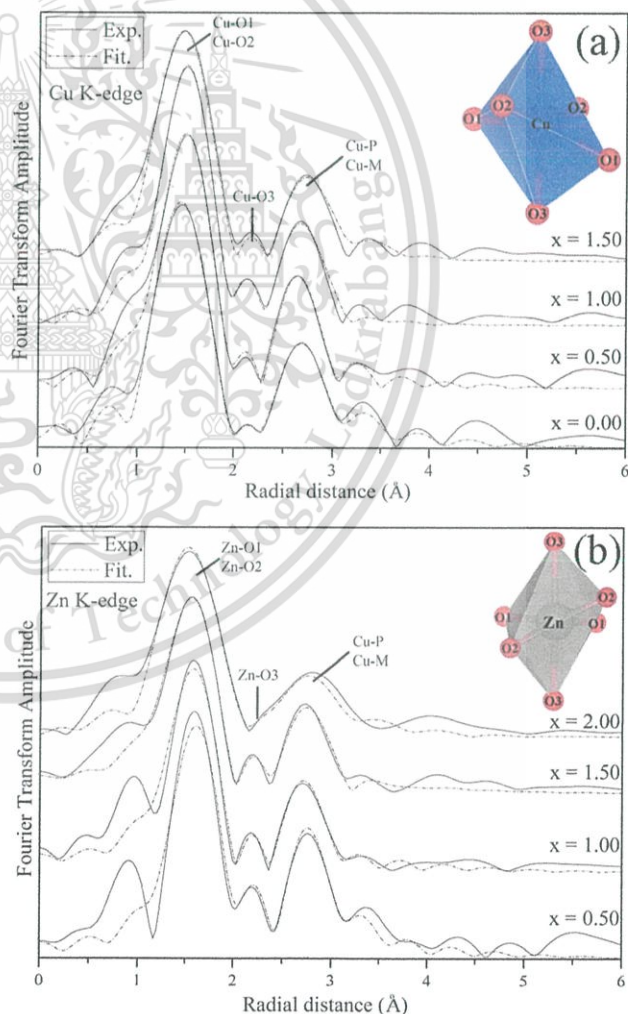


Fig. 7 EXAFS fitting curves of $\text{Cu}_{(2-x)}\text{Zn}_x\text{P}_2\text{O}_7$; $x = 0.00\text{--}2.00$.

Table 4 Bond length from EXAFS fitting for the samples

Composition (x)	Path	Shell	CN	R (Å)	σ^2 (Å ²)	R-factor
0.00	Cu-O1	1	2	1.90505	0.00508	0.00369
	Cu-O2	1	2	1.96427	0.00499	
	Cu-O3	2	1	2.30075	0.03223	
	Cu-O3	3	1	2.91358	0.00796	
0.50	Cu-O1	1	2	1.93460	0.00775	0.00519
	Cu-O2	1	2	1.97180	0.00996	
	Cu-O3	2	2	2.32395	0.02004	
	Zn-O1	1	2	1.98304	0.02336	0.01175
	Zn-O2	1	2	2.02117	0.00034	
	Zn-O3	2	2	2.38214	0.03426	
1.00	Cu-O1	1	2	1.93087	0.00575	0.00514
	Cu-O2	1	2	1.97205	0.00647	
	Cu-O3	2	2	2.28269	0.02209	
	Zn-O1	1	2	1.98889	0.02117	0.01085
	Zn-O2	1	2	2.03131	0.00406	
	Zn-O3	2	2	2.35128	0.07393	
1.50	Cu-O1	1	2	1.94951	0.00611	0.00763
	Cu-O2	1	2	1.99453	0.25154	
	Cu-O3	2	2	2.26768	0.0392	
	Zn-O1	1	2	2.00714	0.01068	0.00393
	Zn-O2	1	2	2.05349	0.01074	
	Zn-O3	2	2	2.33473	0.04422	
2.00	Zn-O1	1	2	1.96928	0.00176	0.02072
	Zn-O2	1	2	2.05357	0.00823	
	Zn-O3	2	1	2.11171	0.00931	
	Zn-O3	3	1	2.58544	0.06587	

copper metal atom, as well as a Cu-M interaction. In the case of the binary metal pyrophosphate samples ($x = 0.50-1.50$), the Cu-O3 interatomic distances shortened, and were included in the second shell. As a result, the second shell intensity of the binary metal pyrophosphate samples was seen to be higher than that in $\text{Cu}_2\text{P}_2\text{O}_7$ ($x = 0.00$). The addition of a fourth shell did not improve the quality of fit, and fitting of the Zn K-edge EXAFS was related to that of the Cu K-edge, with the curve shifting to a high radial distance due to a larger atomic radius. The EXAFS spectrum of Zn-O is shown by a single oscillation from four oxygen atoms surrounding the central Zn atom in the first shell, while Zn consists of two oxygen atoms in the second shell. The next shell described the combination of Cu-M ($M = \text{Cu}/\text{Zn}$), and the Cu-P interaction. The difference in radial distances between the Rietveld refinement and EXAFS fitting may be caused by the type of measurement in each technique, in which X-ray diffraction was used to investigate the global structure, and X-ray absorption was used to probe the details of the Cu/Zn local structure.^{36,37} The fitting statistic (*R*-factor) of the Zn K-edge is worse than that of the Cu K-edge because of two factors. Firstly, the crystal structure of $\alpha\text{-Zn}_2\text{P}_2\text{O}_7$ showed lower symmetry when compared with other samples, and the Zn exhibited three different types of atomic position in the unit cell. Secondly, there was a limitation of the instrument, in which the absorption edge of Zn (9659 eV) approached the maximum energy range (1250–10 000 eV) of the BL8 station.

The refinement results from P-O-P bond angles can be classified into two groups. The first group includes a P-O-P bond angle of less than 180° such as the compositions with $x =$

0.00 and $x = 2.00$, or single metal pyrophosphates. The sample with $x = 0.00$ had a P-O-P bond angle of 154.6°, and appeared with 4 clusters per unit cell and symmetric P-O bond lengths of 1.574 Å. The composition with $x = 2.00$ showed two different P-O-P bond angles, including 159.0°, which appeared with 8 clusters per unit cell and asymmetric P-O bond lengths of 1.770 Å and 1.390 Å, and the P-O-P bond angle of 138.0° appeared with 4 clusters per unit cell and a symmetric P-O bond length of 1.640 Å. The second group had a P-O-P bond angle equal to 180°, which contained the compositions with $x = 0.50, 1.00$, and 1.50, or binary metal pyrophosphates. All of the compositions in this group exhibited a P-O-P bond angle equal to 180.0° and appeared with 4 clusters per unit cell and symmetric P-O bond lengths of 1.524 Å, 1.521 Å, and 1.519 Å for $x = 0.50, 1.00$, and 1.50, respectively. However, when compared to an equal space volume, the number of P-O-P clusters in each composition was equal. As a result, the number of P-O-P clusters did not affect the polarization of the samples. The single metal pyrophosphates showed outstanding dielectric constants, while all of the binary metal pyrophosphates presented lower and similar dielectric constants. It was highly possible that high polarization caused a narrow P-O-P bond angle, as analyzed through the dielectric constants of the metal pyrophosphate compounds. In addition, the long P-O bond length of $x = 2.00$ (weak bonding) led to the better polarization of $x = 0.00, 0.50, 1.00$, and 1.50. The binary metal pyrophosphates ($x = 0.50, 1.00$, and 1.50) exhibited a similar dielectric constant, due to all of the P-O-P bond angles being equal. However, the dielectric constant tends to decrease slightly when the component x increases. Results from the final refinement showed decreasing average M-O bond lengths in the octahedral MO_6 site, of which short length bonding caused hard polarization. Additionally, the volume of selected octahedral coordinations was calculated using the method reported by Swanson *et al.*³⁸ for highlighting the relationship between the polarization and metal oxide bonding. Besides, the distortion index (*D*) was used to describe the distortion of the structure. Baur³⁹ described *D* based on bond lengths in the distortion index as

$$D = \frac{1}{n} \sum_{i=1}^n \frac{|l_i - l_{av}|}{l_{av}}$$

where l_{av} is the average bond length, and l_i is the atomic distance from the central atom to the i th coordinating atom. These results are tabulated in Table 5. All of the data showed decreasing average bond lengths, octahedral volume and distortion index, which exhibited decreasing polarization (dielectric constant, ϵ_r) when the component x increased. These

Table 5 The evolution of average bond length, octahedral volume, and distortion index of the samples

Composition (x)	Average bond length (Å)	Octahedral volume (Å ³)	Distortion index
0.50	2.1758	12.6629	0.1117
1.00	2.1720	12.5791	0.0935
1.50	2.1659	12.4106	0.0821

Table 6 Approximate wavelength of the energy absorption

Composition (x)	Wavelength (nm)		Δ_o (kJ mol ⁻¹)	Cu-O3 (Å) bond length	
	Observed	Absorbed		XRD	EXAFS
0.00	561	403	297	2.92	2.91
0.50	506	660	181	2.54	2.32
1.00	508	665	180	2.48	2.28
1.50	512	675	177	2.42	2.27
2.00	—	—	—	—	—

analyses show that polarization of the $\text{Cu}_{(2-x)}\text{Zn}_x\text{P}_2\text{O}_7$; $x = 0.00$ – 2.00 system occurred due to two factors, with shifting O atoms in the collinear P–O–P bridge probably being the main factor in a narrow bond angle that causes high polarization and a high dielectric constant. The movement of M^{2+} ions in the octahedral MO_6 is a supplementary factor, in which the longer average M–O bond length and larger octahedral volume lead to high polarization and the high dielectric constants of metal pyrophosphate compounds.

The distortion of octahedral CuO_6 exhibited decreasing Cu–O3 bond lengths in going from $x = 0.00$ to 1.50 , which corresponded to a decreasing octahedral crystal field splitting energy (Δ_o) (Table 6). As a result, Zn^{2+} increased this value when the Cu^{2+} in the $\text{Cu}_2\text{P}_2\text{O}_7$ compound was replaced. The color of the compounds illustrated that its hue changes from bluish-green to green. The colorless composition, when $x = 2.00$ or $\text{Zn}_2\text{P}_2\text{O}_7$, caused a state of fulfillment in the octet rule of the Zn^{2+} ions ([Ar] $3d^{10}$) in the structure, despite distortion appearing in the octahedral ZnO_6 site. The octahedral splitting

diagram of $\text{Cu}_{(2-x)}\text{Zn}_x\text{P}_2\text{O}_7$; $x = 0.00$ – 1.50 is shown and summarized in Fig. 8. Total interpretations showed that a distorted octahedral MO_6 affects both the color of the matter and the polarization of the octahedral unit, as reflected by the dielectric constant.

4. Conclusion

The single metal pyrophosphates, α - $\text{Cu}_2\text{P}_2\text{O}_7$ and α - $\text{Zn}_2\text{P}_2\text{O}_7$, and binary metal pyrophosphates, $\text{Cu}_{(2-x)}\text{Zn}_x\text{P}_2\text{O}_7$; $x = 0.00$ – 1.50 , were synthesized successfully *via* solid state reaction from metal oxides and ammonium hydrogen phosphate. All of the samples exhibited a single-phase monoclinic system with the $C2/c$ space group for α - $\text{Cu}_2\text{P}_2\text{O}_7$ and α - $\text{Zn}_2\text{P}_2\text{O}_7$ ($I2/c$), and the $C2/m$ space group for the binary metal pyrophosphates, which showed that the binary metal pyrophosphates had more structural symmetry than the single metal pyrophosphates. Rietveld refinement and EXAFS fitting data presented the P–O–P bond angle and P–O bond length in the $\text{P}_2\text{O}_7^{4-}$ ions, and also details of the octahedral MO_6 including the average bond length, octahedral volume, and distortion index. The addition of Zn^{2+} ions in the $\text{Cu}_2\text{P}_2\text{O}_7$ structure caused distortion of the crystal structure, which led to a change in the bond length and bond angle of the P–O–P clusters in the $\text{P}_2\text{O}_7^{4-}$ ions, and changed the octahedral volume and average bond lengths of the octahedral MO_6 site. Shifting O atoms in the collinear P–O–P bridge is probably the main factor in ionic polarization, in which a narrow bond angle caused high polarization and high dielectric constants. The movement of M^{2+} ions in octahedral MO_6 is a supplementary factor, in which the longer average M–O bond length and larger octahedral volume led to the high polarization and high dielectric constants of metal

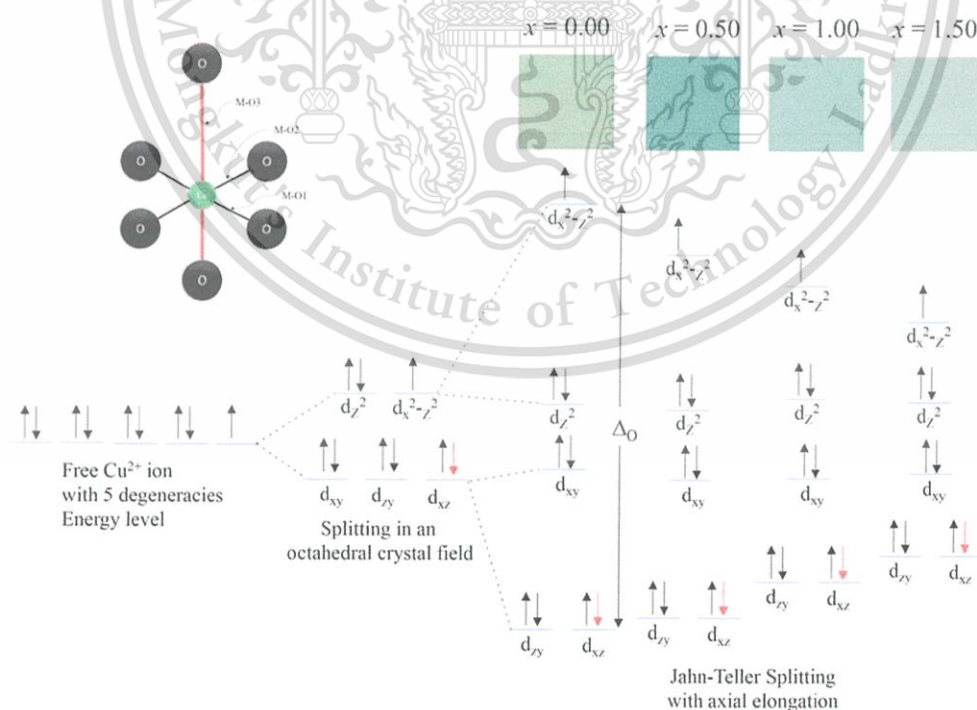


Fig. 8 Summary of the crystal field splitting in $\text{Cu}_{(2-x)}\text{Zn}_x\text{P}_2\text{O}_7$; $x = 0.00$ – 1.50 .

pyrophosphate compounds. The color of the samples changed from bluish-green to green when the Zn component increased because the absorption wavelength increased and corresponded to the decrease in z-axis expansion. The final results showed that the distortion of the octahedral MO₆ caused a direct effect on the color of the metal pyrophosphate compounds, while the change of the P–O–P bridge affected the dielectric properties.

Acknowledgements

This work was supported by the Thailand Research Fund (TRF) under the TRF Senior Research Scholar, Grant no. RTA5680008 and The National Nanotechnology Center (NANOTEC), NSTDA, Ministry of Science and Technology, Thailand, through its program of Center of Excellence Network. The authors also would like to thank the Synchrotron Light Research Institute (Public Organization) for the XAS measurements.

References

- 1 E. Steger and B. Käßner, *Spectrochim. Acta, Part A*, 1968, **24**, 447–456.
- 2 B. Boonchom and R. Baitahe, *Mater. Lett.*, 2009, **63**, 2218–2220.
- 3 M. Weil and B. Stöger, *Acta Crystallogr., Sect. B: Struct. Sci.*, 2010, **66**, 603–614.
- 4 A. Durif, *Crystal chemistry of condensed phosphates*, Plenum Press, New York, 1995.
- 5 B. E. Robertson and C. Calvo, *Acta Crystallogr.*, 1967, **22**, 665–672.
- 6 C. Calvo, *Can. J. Chem.*, 1965, **43**, 1147–1153.
- 7 M. A. Petrova, V. I. Shitova, G. A. Mikirticheva, V. F. Popova and A. E. Malshikov, *J. Solid State Chem.*, 1995, **119**, 219–223.
- 8 J. I. Bian, D. W. Kim and K. S. Hong, *Jpn. J. Appl. Phys., Part 1*, 2004, **43**, 3521–3525.
- 9 J. J. Bian, D. Kim and K. S. Hong, *J. Mater. Sci.*, 2005, **40**, 1801–1803.
- 10 W. Wenwei, F. Yanjin, W. Xuehang, L. Sen and L. Shushu, *J. Phys. Chem. Solids*, 2009, **70**, 584–587.
- 11 Z. W. Xiao, G. R. Hu, Z. D. Peng, K. Du and X. G. Gao, *Chin. Chem. Lett.*, 2007, **18**, 1525–1527.
- 12 A. Bensalem, M. Ahluwalia, T. V. Vijayaraghavan and Y. H. Ko, *Mater. Res. Bull.*, 1997, **32**, 1473–1483.
- 13 D. Brandová, M. Trojan, M. Arnold, F. Paulik and J. Paulik, *J. Therm. Anal.*, 1988, **34**, 1449–1454.
- 14 D. Brandová, M. Trojan, F. Paulik and J. Paulik, *J. Therm. Anal.*, 1987, **32**, 1923–1928.
- 15 B. Boonchom, R. Baitahe, S. Kongtaweelert and N. Vittayakorn, *Ind. Eng. Chem. Res.*, 2010, **49**, 3571–3576.
- 16 A. Jouini, J. C. Gâcon, M. Ferid and M. Trabelsi-Ayadi, *Opt. Mater.*, 2003, **24**, 175–180.
- 17 T. Yang and J. Lin, *J. Solid State Chem.*, 2013, **198**, 1–5.
- 18 C. H. Kim and H. S. Yim, *Solid State Commun.*, 1999, **110**, 137–142.
- 19 R. Baitahe and N. Vittayakorn, *Thermochim. Acta*, 2014, **596**, 21–28.
- 20 E. Kroumova, M. I. Aroyo, J. M. Perez-Mato, A. Kirov, C. Capillas, S. Ivantchev and H. Wondratschek, *Phase Transitions*, 2003, **76**, 155–170.
- 21 B. Boonchom and N. Phuvongpha, *Mater. Lett.*, 2009, **63**, 1709–1711.
- 22 O. Pawlig and R. Trettin, *Mater. Res. Bull.*, 1999, **34**, 1959–1966.
- 23 O. Pawlig, V. Schellenschläger, H. D. Lutz and R. Trettin, *Spectrochim. Acta, Part A*, 2001, **57**, 581–590.
- 24 K. Pogorzelec-Glaser, A. Pietraszko, B. Hilczer and M. Polomska, *Phase Transitions*, 2006, **79**, 535–544.
- 25 M. T. Sebastian, *Dielectric materials for wireless communication*, Elsevier, Amsterdam, Boston, 2008.
- 26 A. El Jazouli, B. Tbib, A. Demourgues and M. Gaudon, *Dyes Pigm.*, 2014, **104**, 67–74.
- 27 L.-T. Chen, C.-S. Hwang, I. L. Sun and I.-G. Chen, *J. Lumin.*, 2006, **118**, 12–20.
- 28 B. Kukliński, D. Wileńska, S. Mahlik, K. Szczodrowski, M. Grinberg and A. M. Klonkowski, *Opt. Mater.*, 2014, **36**, 633–638.
- 29 B.-K. Kim and R.-H. Park, *Image and Vision Computing*, 2010, **28**, 952–964.
- 30 H. Rietveld, *J. Appl. Crystallogr.*, 1969, **2**, 65–71.
- 31 J. Rodriguez-Carvajal, *Physica B: Condensed Matter*, 1993, **192**, 55–69.
- 32 B. E. Robertson and C. Calvo, *Can. J. Chem.*, 1968, **46**, 605–612.
- 33 R. Shannon, *Acta Crystallogr., Sect. A: Cryst. Phys., Diffr., Theor. Gen. Crystallogr.*, 1976, **32**, 751–767.
- 34 I. Brown, *Acta Crystallogr., Sect. B: Struct. Crystallogr. Cryst. Chem.*, 1977, **33**, 1305–1310.
- 35 I. Brown, *Acta Crystallogr., Sect. B: Struct. Crystallogr. Cryst. Chem.*, 1992, **48**, 553–572.
- 36 V. I. Voronin, I. F. Berger, V. A. Cherepanov, L. Y. Gavrilova, A. N. Petrov, A. I. Ancharov, B. P. Tolochko and S. G. Nikitenko, *Nucl. Instrum. Methods Phys. Res., Sect. A*, 2001, **470**, 202–209.
- 37 L. Yingjie, B. Huliyaqeqi, W. Haschaolu, Z. Song, O. Tegus and I. Nakai, *J. Electron Spectrosc. Relat. Phenom.*, 2014, **196**, 104–109.
- 38 D. K. Swanson and R. C. Peterson, *Can. Mineral.*, 1980, **18**, 153–156.
- 39 W. Baur, *Acta Crystallogr., Sect. B: Struct. Crystallogr. Cryst. Chem.*, 1974, **30**, 1195–1215.

Dielectric Properties and Characterizations of Binary $\text{Cu}_{(2-x)}\text{Mg}_x\text{P}_2\text{O}_7$ Pyrophosphates

RATTANAIBAITAHE¹ AND NARATIP VITTAYAKORN^{1,2,3,4,*}

¹Electroceramics Research Laboratory, College of Nanotechnology, King Mongkut's Institute of Technology Ladkrabang, Bangkok 10520, Thailand

²Advanced Materials Research Unit, Faculty of Science, King Mongkut's Institute of Technology Ladkrabang, Bangkok 10520, Thailand

³Department of Chemistry, Faculty of Science, King Mongkut's Institute of Technology Ladkrabang, Bangkok 10520, Thailand

⁴Nano-KMITL Center of Excellence on Nanoelectronic Devices, KMITL, Ladkrabang, Bangkok 10520, Thailand

Samples of the binary metal pyrophosphate, $\text{Cu}_{(2-x)}\text{Mg}_x\text{P}_2\text{O}_7$ ($x = 0.00 - 2.00$), were prepared via solid state reaction. Vibrational bands of $[\text{P}_2\text{O}_7]^{4-}$ anion which contains the O–P–O radical ($[\text{PO}_2]^-$) and the P–O–P bridge ($[\text{OPO}]^-$) and approximate M–O stretching were identified by Raman scattering. A strong P–O–P band was observed clearly in Raman spectra, which indicated the formation of solid solution. The purity of synthetic powders were characterized by X-ray diffraction (XRD). The XRD patterns indicated that all the samples exhibited a single monoclinic phase structure. The complete solid solutions in the $\text{Cu}_{(2-x)}\text{Mg}_x\text{P}_2\text{O}_7$ ($x = 0.00 - 2.00$) system were obtained. The unit cell volume changed, due to the difference between the final product structure and $\text{Cu}_2\text{P}_2\text{O}_7$. X-ray absorption near the edge structure (XANES) technique was used to confirm oxidation state of copper in the $\text{Cu}_{(2-x)}\text{Mg}_x\text{P}_2\text{O}_7$. The relative permittivity and dielectric loss of the samples were measured. The bond length and bond angle were analyzed by EXAFS and Raman techniques. The relative permittivity was seen to maintain temperature by substituting Mg^{2+} with $\text{Cu}_2\text{P}_2\text{O}_7$. These results were used to explain the crystal structure of materials in order to change the bond which affects dielectric phenomena.

Keywords Binary metal pyrophosphates; relative permittivity; EXAFS analysis

1. Introduction

Metal phosphate ($\text{M}_x(\text{PO}_4^{3-})_y$ species) materials show interesting properties nowadays because of their wide applications in microwave dielectric materials, corrosion-resistant coatings, biomedical cements, chelating agents, glass ceramics, and high-quality fertilizers [1–3]. The pyrophosphate $\text{M}_2\text{P}_2\text{O}_7$ compounds have been reported to possess good dielectric loss properties as well as a relatively low sintering temperature [1]. It has been observed that an M radius structure greater than 0.97 Å [4] is a dichromate type (M =

Received October 26, 2014; in final form February 15, 2015.

*Corresponding author. E-mail: naratipcmu@yahoo.com

Color versions of one or more figures in this article can be found online at www.tandfonline.com/gfer.

[686]/174

Ca^{2+} , Sr^{2+} , Ba^{2+} , Pb^{2+} , and Cd^{2+}), in which a pair of $\text{P}_2\text{O}_7^{4-}$ groups in eclipsed conformation crystallize at about the center of symmetry, with bridging O atoms spreading towards each other. When the M radius is less than 0.97 Å ($\text{M} = \text{Ni}^{2+}$, Mg^{2+} , Zn^{2+} , Co^{2+} , Cu^{2+} , and Mn^{2+}), the structure is a thortveitite type, in which $\text{P}_2\text{O}_7^{4-}$ occurs in staggered conformation, and thortveitite-type pyrophosphate $\alpha\text{-Cu}_2\text{P}_2\text{O}_7$ or $\alpha\text{-Mg}_2\text{P}_2\text{O}_7$ exhibits a rather low sintering temperature when compared with metal oxides. However, single pyrophosphates groups (such as $\text{Cu}_2\text{P}_2\text{O}_7$, $\text{Mg}_2\text{P}_2\text{O}_7$, $\text{Zn}_2\text{P}_2\text{O}_7$, and $\text{Co}_2\text{P}_2\text{O}_7$) still show phase transition when changing temperature. Therefore, this primary research aimed to modify the structure of these materials in order to decrease dielectric loss and manipulate the relative permittivity to constant variations with temperature.

Most studies of metal phosphate focused on the synthesis and characterizations of both bulk [5, 6] and nano particles [7], kinetics and the thermodynamics of reaction [8, 9], and their properties [10, 11]. Nevertheless, the study of the relationship between dielectric properties and crystal structure is not widely understood, and is therefore of interest. The secondary aim of this study was to probe the crystal structure which influence dielectric phenomena of binary metal pyrophosphate compounds. Dielectric properties of the metal pyrophosphate group are due to two effects that comprise movement of M^{2+} ions in the octahedral MO_6 and shift of O atoms in the collinear P–O–P bridge. If the collinear P–O–P bond of the pyrophosphate ion is distorted, some distortion of octahedral MO_6 also can occur, which would improve the dielectric property of the molecule by producing polarization [12]. It is well known that the highly relative permittivity of tetragonal perovskite BaTiO_3 comes from off-centred Ti^{4+} ions in octahedral TiO_6 . Putting a solid solution of Mg^{2+} into $\text{Cu}_2\text{P}_2\text{O}_7$ structure may bring about distortion of MO_6 and the collinear P–O–P bond and improve the dielectric properties of $\text{Cu}_2\text{P}_2\text{O}_7$ with a low sintering temperature. This research synthesized $\text{Cu}_{(2-x)}\text{Mg}_x\text{P}_2\text{O}_7$ ($x = 0.0 - 2.0$) before Raman, and XRD techniques investigated the crystal structure that affects dielectric properties. The phenomena of polarization in the crystal structure of compounds also were studied in order to characterize via bond length and bond angle.

2. Experimental Procedure

Synthesis of $\text{Cu}_{(2-x)}\text{Mg}_x\text{P}_2\text{O}_7$ ($x = 0.00, 0.50, 1.00, 1.50, \text{ and } 2.00$) was conducted using the conventional method. High purity $(\text{NH}_4)_2\text{HPO}_4$ (99%) CuO (99.9%), and MgO (99.9%), were used as starting materials. Stoichiometric mixtures of raw materials were homogenized by vibratory milling with Ytria stabilized zirconia media in ethanol for 4 hrs. These were calcined at $800^\circ\text{C}/24$ hrs for $x = 0.00$, and $950^\circ\text{C}/3$ days for $x = 0.50 - 2.00$. The calcined powders were ball-milled again, pressed uniaxially into small pellets at the pressure of 1000 kg/cm^2 and sintered at 1000°C for 24h. The theoretical density of all ceramics observed was about 95–98%. Raman spectra were recorded in the range of $1300\text{--}100 \text{ cm}^{-1}$ with eight scans on a thermo scientific DXR Raman microscope. The samples were excited with 488 nm light from an Ar^+ ion laser and the power of the incident beam was 12.5 mW. The crystal structure and crystallite sizes of the prepared samples were studied by X-ray powder diffraction with Cu K_α radiation ($\lambda = 0.1546 \text{ nm}$). using a Bruker D8 Advance X-ray diffractometer (Bruker AXS, Karlsruhe, Germany) The dielectric properties were measured as a function of frequency (1–1000 kHz) and temperature (room temperature to 150°C) using an LCR meter (HP4284A; Hewlett-Packard, Palo Alto, CA).

Furthermore, substitutional solid solutions, in accordance with the Hume-Rothery rules, may form if the solute and solvent have: similar atomic radii; $R_{\text{Cu(II)}} = 0.73 \text{ \AA}$ and

$R_{Mg(M)} = 0.72 \text{ \AA}$ [13], similar electronegativities; Cu = 1.90 and Mg = 1.31, similar valency; Cu = : 2+ and Mg = 2+. And same crystal structure; $\beta\text{-Cu}_2\text{P}_2\text{O}_7 = \text{Monoclinic, C2/m}$ and $\beta\text{-Mg}_2\text{P}_2\text{O}_7 = \text{Monoclinic, C2/m}$. These data show a high possibility of substitutional solid solution between Cu and Mg ions in pyrophosphate compounds. The X-ray absorption spectroscopy (XAS) was conducted on the beam line (BL8) of the National Synchrotron Research Center (Thailand). A double crystal Ge(220) was used for the EXAFS mono-chromator. X-ray absorption (XAS) spectra at the Cu K-edge were collected in transmission mode. The Cu foil, Cu_2O , CuO were used as a reference materials for X-ray absorption near-edge spectroscopy (XANES) measurements. The data from XANES were analyzed by aATHENA supporting program.

3. Results and Discussion

The Raman spectra of $\text{Cu}_{(2-x)}\text{Mg}_x\text{P}_2\text{O}_7$ are shown in Figure 1. It is clearly noticeable that the studied ceramics display more sharpness and splitting, especially in the low-frequency region ($1300\text{-}100 \text{ cm}^{-1}$), indicating polymerization of $[\text{PO}_4]^{3-}$ to $[\text{P}_2\text{O}_7]^{4-}$. The vibration analysis of the $\text{P}_2\text{O}_7^{4-}$ ion which contains the O–P–O radical ($[\text{PO}_2]^-$) and the P–O–P bridge ($[\text{OPO}]^-$) and approximate M–O stretching band were exhibited in Raman spectra. The Raman spectra are similar to those observed by Boonchom *et al.* [14]. The strong vibration bands around 1100 cm^{-1} are recognized to stretching of the PO_3 unit. The asymmetric ($\nu_{\text{asym}} \text{POP}$) and symmetric stretch ($\nu_{\text{sym}} \text{POP}$) bridge vibration for these samples are detected at about 960 and 730 cm^{-1} , respectively, while the asymmetric ($\delta_{\text{asym}} \text{PO}_3$) and symmetric ($\delta_{\text{sym}} \text{PO}_3$) bending vibration are observed at about 600 and 520 cm^{-1} , respectively. The metal oxide bonds are found in the $460\text{-}400 \text{ cm}^{-1}$ region. When Cu^{2+} is replaced by Mg^{2+} in the $\text{Cu}_{(2-x)}\text{Mg}_x\text{P}_2\text{O}_7$ solid solutions, the Raman spectra show an important displacement of an absorption band found at about 420 cm^{-1} . This band can be assigned to the M–O bond lengths, which are responsible for the wave number increase from 411 to 458 cm^{-1} [15]. In composition $x = 0.00$ and 2.00 phases, three distinct bands that originate from the $\nu_{\text{asym}}(\text{PO}_3)$ vibrations are visible at 1214 , 1146 and 1080 cm^{-1} . In

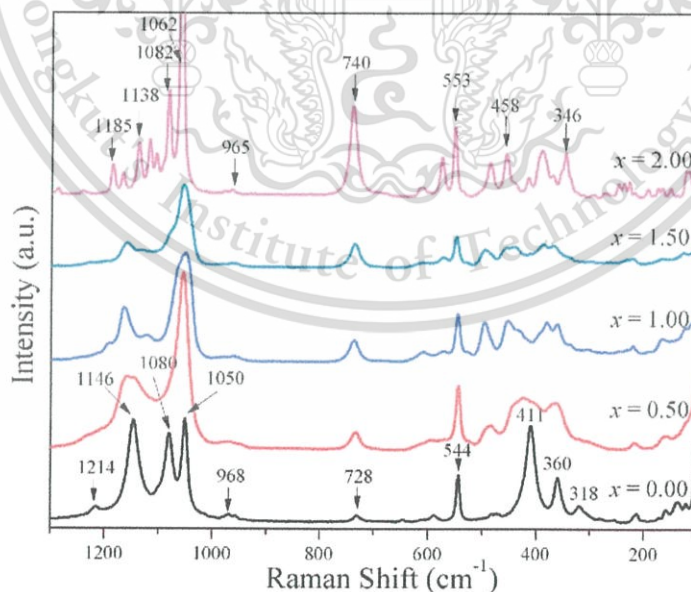


Figure 1. Raman spectra of $\text{Cu}_{(2-x)}\text{Mg}_x\text{P}_2\text{O}_7$; $x = 0.00\text{-}2.00$.

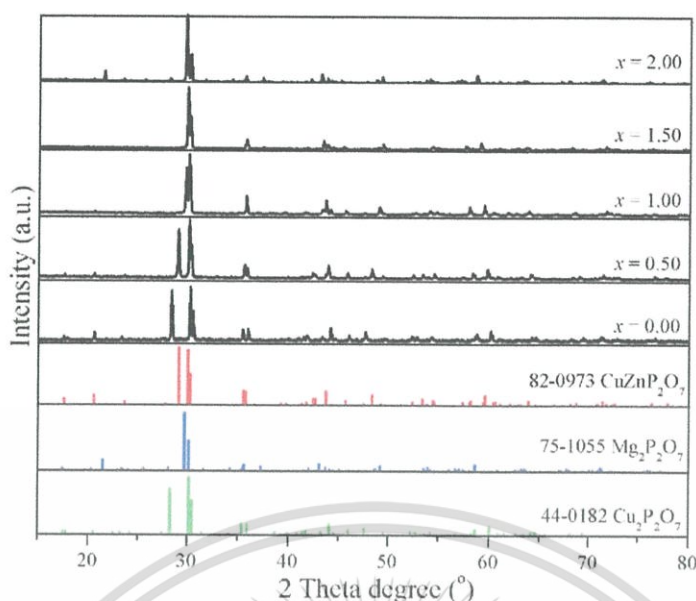


Figure 2. XRD patterns of $\text{Cu}_{(2-x)}\text{Mg}_x\text{P}_2\text{O}_7$; $x = 0.00 - 2.00$.

the composition of $x = 0.50$, 1.00 , and 1.50 phases, the bands remain at 1146 and 1080 cm^{-1} , but disappear at 1214 cm^{-1} . This indicates binary metal phosphates that closely resemble those of the β - $\text{Mg}_2\text{P}_2\text{O}_7$ phase, because the medium peak appears at around 1220 cm^{-1} only in the alpha phase [16].

Figure 2 shows the XRD patterns of $\text{Cu}_{(2-x)}\text{Mg}_x\text{P}_2\text{O}_7$ ($x = 0.00, 0.50, 1.00, 1.50$, and 2.00). Based on our analysis, the synthesized materials are solid solution and not a combination of the individual phases. These results indicate that the binary and the single metal compounds for $\text{X}_2\text{P}_2\text{O}_7$ ($\text{X} = \text{Ni}, \text{Mn}, \text{Zn}, \text{Mg}, \text{Cu}, \text{Co}$) types are isostructural. Consequently, all XRD pattern can be indexed distinctly based on a pure monoclinic phase with space group $\text{C}2/c$ ($Z = 4$) for α - $\text{Cu}_2\text{P}_2\text{O}_7$, $\text{P}2_1/c$ ($Z = 4$) for α - $\text{Mg}_2\text{P}_2\text{O}_7$, and $\text{C}2/m$ ($Z = 2$) for the samples as a function of $x = 0.50 - 1.50$, which noted to be similar to those of the standard XRD patterns of $\text{M}_2\text{P}_2\text{O}_7$ (PDF no. 44-0180 for Cu, PDF no. 75-1055 for Mg and PDF no.82-0973 for CuMg), respectively.

Table 1 presents the variation in these unit cell parameters with x . The half decreasing of lattice parameter c due to changing of space symmetry elements in the molecules from c (glide plane axis perpendicular to principal axis) to m (mirror plane perpendicular to principal axis) which show that increase symmetry in crystal structure. The lattice parameters a , c and β decrease. Parameter b increases, but the volume shows little change, due to the similar ionic radii of Mg and Cu ($R_{\text{Cu(II)}} = 0.73$ Å and $R_{\text{Mg(II)}} = 0.72$ Å). These results indicated that when the crystal structure of α - $\text{Cu}_2\text{P}_2\text{O}_7$ was disturbed by different kinds of atom (Mg atoms). As a result the new crystal structure is stable at both low and high temperature. The average crystallite size of 72 ± 10 nm for α - $\text{Cu}_2\text{P}_2\text{O}_7$ sample was calculated from X-ray line broadening of the reflections of (002), (-112), (-202), (022), (112), (220), and (130), using Scherrer equation;

$$D = 0.89\lambda / \beta \cos\theta \quad (1)$$

where D is the mean size of the ordered (crystalline) domain, which may be smaller or equal to the grain size, θ is the diffraction angle, λ is the wavelength of X-ray radiation,

Table 1
Lattice parameters of $\text{Cu}_{(2-x)}\text{Mg}_x\text{P}_2\text{O}_7$; $x = 0.00 - 2.00$ calculated from XRD data

Composition (x)	Systems	a Å	b Å	c Å	β °	V Å ³
0.00	PDF no. 44-0182	6.88(0)	8.11(3)	9.16(1)	109.52(1)	482.30(0)
0.50	This work	6.75(1)	8.15(0)	4.54(4)	107.07(2)	238.75(2)
1.00		6.64(0)	8.21(4)	4.50(0)	106.52(0)	235.19(0)
1.50		6.57(4)	8.24(1)	4.48(2)	105.50(0)	233.71(1)
2.00	PDF no. 75-1055	6.94(0)	8.28(0)	9.04(0)	113.79(4)	476.47(4)

and β is the full width at half maximum (FWHM) [17], and were found to be 83 ± 9 nm for sample $\alpha\text{-Mg}_2\text{P}_2\text{O}_7$ was calculated from X-ray line broadening of the reflections of (111), (002), (020), (212), (410) and (-422) . The average crystallite size of 79 ± 9 , 73 ± 6 , and 61 ± 7 nm for binary metal pyrophosphates at $x = 0.50$, 1.00 , and 1.50 , respectively, were calculated from X-ray line broadening of the reflections of (110), (001), (-201) , (021), (111), (220), and (130). The data of Raman and XRD results confirms that to single phase.

Normally, the oxidation state of Mg is two plus. However, the oxidation state of Cu can be one plus or two plus in phosphate form. So, X-ray absorption near the edge structure (XANES) technique was used to confirm oxidation state of copper in the $\text{Cu}_{(2-x)}\text{Mg}_x\text{P}_2\text{O}_7$ ($x = 0.0, 0.5, 1.0$, and 1.5) compounds. As XANES is very sensitive to both changes in the local geometry and the oxidation state, spectra collected at both edges could help in understanding Fourier transform evolutions. The XANES spectra of samples, as shown at the Cu K-edge in Figure 3, remain identical to the signal observed for

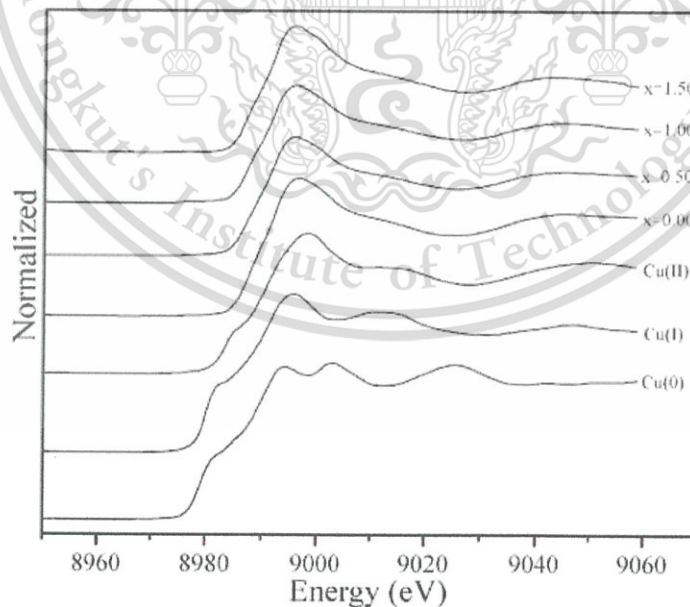


Figure 3. XANES spectra of $\text{Cu}_{(2-x)}\text{Mg}_x\text{P}_2\text{O}_7$; $x = 0.00 - 2.00$.

Table 2
Energy positions of the absorption edges observed for measured samples

Compounds	Threshold value (E0)
Cu(0)	8979.27
Cu(I)	8979.91
Cu(II)	8986.25
0.00	8986.08
0.50	8986.65
1.00	8986.45
1.50	8986.69

Cu(II)O (Table 2), whatever the Cu content. Copper atoms thus remain Cu^{2+} in a monoclinic symmetry.

The relative permittivity (ϵ_r) and dielectric loss versus composition plots at 10, 100, and 1,000 kHz of $\text{Cu}_{(2-x)}\text{Mg}_x\text{P}_2\text{O}_7$ are shown in Figure 4. The effect of porosity on the permittivity was eliminated by applying the Bosman and Havinga's correction [18], shown in Eq. (2), which can be used for dense ceramics having porosity lower than 5%:

$$\epsilon_{r, \text{corrected}} = \epsilon_{r, \text{measured}}(1 + 1.5P) \quad (2)$$

where $\epsilon_{r, \text{measured}}$ and $\epsilon_{r, \text{corrected}}$ are the measured and corrected relative permittivity, respectively, and P is fractional porosity and tabulated in Table 3. The bond angle and bond length were performed by the Raman scattering and EXAFS results for investigated phenomena of dielectric properties. Dielectric properties of the metal pyrophosphate group include two effects that comprise to shift of O atoms in the collinear P–O–P bridge and movement of M^{2+} ions in the octahedral MO_6 . In the part of shifting of O atoms in the collinear P–O–P bridge. The sample as a function of $x = 0.50 - 1.50$, all compositions

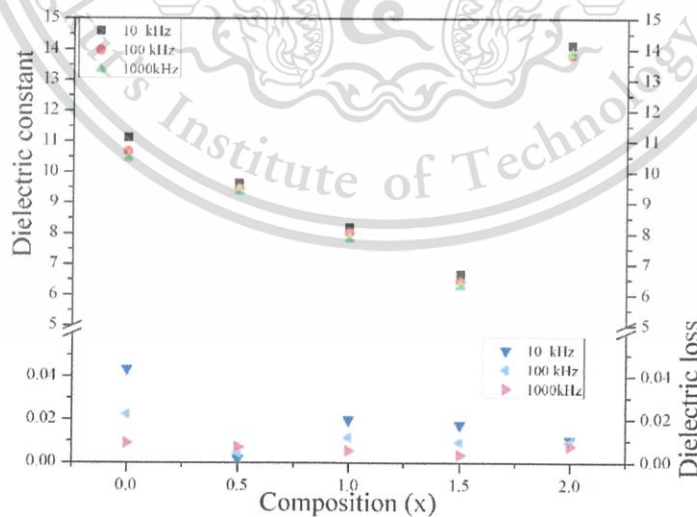


Figure 4. Plots of the relative permittivity and loss of $\text{Cu}_{(2-x)}\text{Mg}_x\text{P}_2\text{O}_7$; $x = 0.00 - 2.00$.

Table 3
Relative permittivity and dielectric loss of samples

Composition (x)	%TD	Corrected relative permittivity			Dielectric loss		
		10k	100k	1000k	10k	100k	1000k
0.00	98.5	11.11	10.66	10.44	0.0432	0.0224	0.0091
0.50	96.7	9.64	9.46	9.36	0.0017	0.0045	0.0072
1.00	95.7	8.19	8.02	7.82	0.0196	0.0117	0.0055
1.50	96.4	6.67	6.43	6.29	0.0175	0.0095	0.0035
2.00	95.3	14.13	13.82	13.87	0.0105	0.0094	0.0076

have the space group $C2/m$. Previous researches reported that all of pyrophosphates compound which have monoclinic system with $C2/m$, the P–O–P angle are 180 degrees. Single metal pyrophosphates, α - $Cu_2P_2O_7$ and α - $Mg_2P_2O_7$ were exhibited the P–O–P angle to 157° [19] and 144° [20], respectively. In this case, the octahedral MO_6 site via bond strength or average bond length was considered by EXAFS data (Figure 5) and supported by Raman spectra in the wavenumber about 420 cm^{-1} (M–O stretching). As extended X-ray absorption fine structure (EXAFS) is very sensitive to change in local geometry, spectra collected at both edges could help in understanding Fourier transform evolutions. The data set were then analyzed by ‘data processing’ with ATHENA software [21]. The structure parameters of this analysis included approximate interatomic distances. The results demonstrated the asymmetry of CuO_6 octahedral due to the occurred of the little peak around last part of 1st shell introducing the Jahn-Teller distortion effect undergone by the copper octahedral centered site into the model or this peak may be the ghost peak [22]. The first shell was the consisting of six oxygen atoms, (M–O) with interatomic distances about 2.10 \AA . The next shell was described the combination of Cu–M (M = Cu/Mg), and Cu–P interaction. However, in this work was focus on 1st shell of $M-O_6$ octahedral. The relation of POP angle, M–O atomic distances from Raman and EXAFS were tabulated in Table 4. The average bond length of Mg– O_6 ($x = 2.00$) from XAS technic cannot be measured due to limitations of the instrument. Nevertheless, this data was supported by Raman result with increasing peak position which corresponded to decreasing bond length of EXAFS data Figure 5. The single metal pyrophosphate, $x = 2.00$ ($Mg_2P_2O_7$)

Table 4
Bond angle, M–O stretching position, and average bond length of samples

Composition (x)	POP angle	M– O_6	
	Angle($^\circ$)	Peak position (cm^{-1})	Bond length(\AA)
0.00	157	411	2.18
0.50	180	420	2.16
1.00	180	431	2.13
1.50	180	442	2.09
2.00	144	458	—

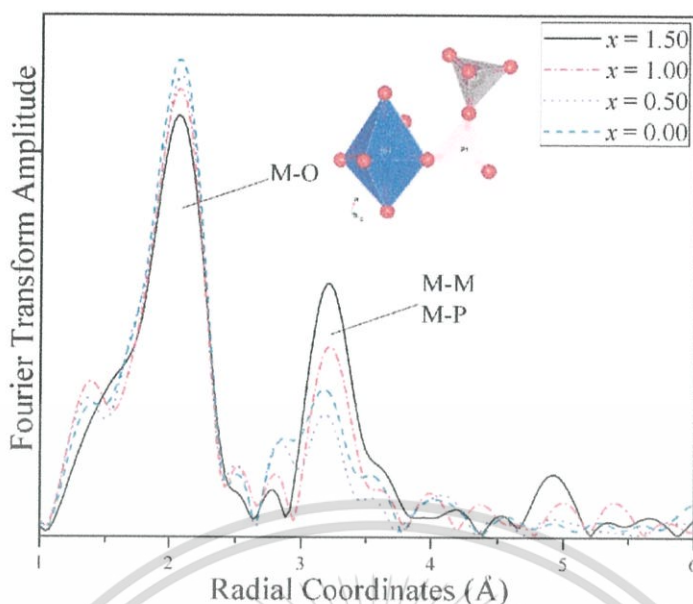


Figure 5. EXAFS patterns of $\text{Cu}_{(2-x)}\text{Mg}_x\text{P}_2\text{O}_7$; $x = 0.00 - 2.00$.

was shown to be the highest ϵ_r and the least of P–O–P angles is 144 degrees, while $x = 0.00$ ($\text{Cu}_2\text{P}_2\text{O}_7$) was shown second ϵ_r and the second lowest of P–O–P angle is 157 degrees. Binary metal pyrophosphates, $x = 0.50 - 1.50$ with P–O–P angle is 180 degrees which exhibited ϵ_r less than single metal pyrophosphate compounds. These results show that the P–O–P angle is probably main factor for polarization of pyrophosphates group, by means of small P–O–P angle cause good polarization and good dielectric properties. Secondly, compounds having the same P–O–P angle (180 degrees), average bond length were considered. The samples as a function of $x = 0.50, 1.00,$ and 1.50 displayed decreasing of ϵ_r when increasing Mg^{2+} compositions. These as a result of average M–O bond length decrease polarization. Therefore, dielectric permittivity tends to increase with increasing bond length, since decreasing bond strength, shows better polarization. The changing of dielectric loss of binary metal pyrophosphates at high frequency tends to be decreasing when x increases. Due to pyrophosphates compound are quite responsive in the high frequency range (microwave dielectric properties). But low frequency, the dielectric loss changing were difference may be caused by the extrinsic factors. Generally, high dielectric permittivity causes high dielectric loss. The Mg having lower EN (Electronegativity) than Cu [23] is introduced, positively charged defects will be destroyed thus decreasing the density of defect states of binary metal pyrophosphates, $\text{Cu}_{(2-x)}\text{Mg}_x\text{P}_2\text{O}_7$ system as compared to pure $\text{Cu}_2\text{P}_2\text{O}_7$. The addition of Mg to $\text{Cu}_2\text{P}_2\text{O}_7$ build up the amount of charged defect states that might affect the dielectric loss. Since the dielectric loss of these compounds depends upon the total amount of localized sites, the decrease of dielectric loss and the increase of Mg component can be understood in terms of the decreased density of defects on summing up of Mg to $\text{Cu}_2\text{P}_2\text{O}_7$. Due to the decreased number of dipoles (D^- and D^+) at higher component of Mg, the dielectric loss is also expected to decrease with Mg component as found in this study.

4. Conclusion

Metal pyrophosphates; $\text{Cu}_{(2-x)}\text{Mg}_x\text{P}_2\text{O}_7$ ($x = 0.0-2.0$) samples were prepared via solid state reaction to obtain information on solid solution formation, and characterized in the metal pyrophosphate group by Raman spectroscopy. XRD and Raman spectroscopy investigated the structure, which exhibited the compositions, $x = 0.50-1.50$, as a copy structure of high temperature phase, $\beta\text{-Cu}_2\text{P}_2\text{O}_7$, with space group $C2/m$ at both high and low temperature. The dielectric properties of the metal pyrophosphate group include two effects that comprise to shift of O atoms in the collinear P–O–P bridge and movement of M^{2+} ions in the octahedral MO_6 . The experimental results were shown that P–O–P angle in $\text{P}_2\text{O}_7^{4-}$ ions is the main factor. Narrow angles will cause more polarization than wide angles. Furthermore, increasing bond length in the octahedral site (M–O) increases polarization, because it affects the bond strength of octahedral MO_6 . The binary metal pyrophosphates have high dielectric permittivity and low dielectric loss, especially in $x = 0.50$.

Acknowledgment

We would like to thank the Synchrotron Light Research Institute (Public Organization) for XAS measurement.

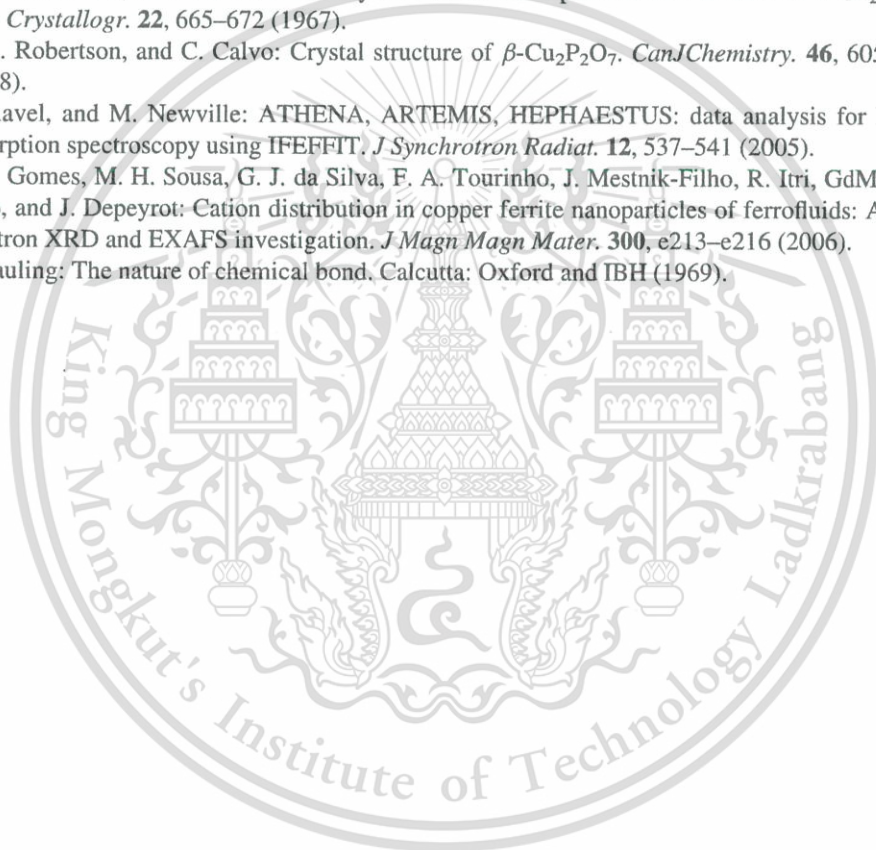
Funding

This work was partially supported by the Thailand Research Fund (TRF) under Grant No. BRG5680006.

References

1. J. I. Bian, D. W. Kim, and K. S. Hong: Microwave dielectric properties of $\text{A}_{(2)}\text{P}_{(2)}\text{O}_{(7)}$ ($\text{A} = \text{Ca}, \text{Sr}, \text{Ba}; \text{Mg}, \text{Zn}, \text{Mn}$). *Jpn J Appl Phys.* **43**, 3521–3525 (2004).
2. J. I. Bian, D. Kim, and K. S. Hong: Microwave dielectric properties of $(\text{Zn}_{1-x}\text{Mn}_x)_{(2)}\text{P}_2\text{O}_7$. *J Mater Sci.* **40**, 1801–1803 (2005).
3. W. Wenwei, F. Yanjin, W. Xuehang, L. Sen, and L. Shushu: Preparation via solid-state reaction at room temperature and characterization of layered nanocrystalline $\text{NH}_4\text{MnPO}_4 \cdot \text{H}_2\text{O}$. *J Phys Chem Solids.* **70**, 584–587 (2009).
4. M. Weil, B: Stöger Crystal chemistry of transition metal diarsenates $\text{M}_2\text{As}_2\text{O}_7$ ($\text{M} = \text{Mn}, \text{Co}, \text{Ni}, \text{Zn}$): Variants of the thortveitite structure. *Acta Crystallographica Section B: Structural Science.* **66**, 603–614 (2010).
5. Z. W Xiao, G. R. Hu, Z. D. Peng, K. Du, and X. G. Gao: Solid state synthesis and characterization of iron(II) pyrophosphate $\text{Fe}_2\text{P}_2\text{O}_7$. *Chinese Chem Lett.* **18**, 1525–1527 (2007).
6. A. Bensalem, M. Ahluwalia, T. V. Vijayaraghavan, and YH Ko: Synthesis of amorphous $\text{MgHPO}_4 \cdot x(\text{R})$ [$\text{R} = \text{Ethanol}; \text{Ethylene glycol}$] in anhydrous media. *Mater Res Bull.* **32**, 1473–1483 (1997).
7. C. Díaz, M. L. Valenzuela, V Lavayen, K Mendoza, DO Peña, and O'Dwyer C: Nanostructured copper oxides and phosphates from a new solid-state route. *Inorg Chim Acta.* **377**, 5–13 (2011).
8. D. Brandová, M. Trojan, M. Arnold, F. Paulik, and J. Paulik: Mechanism of dehydration and condensation of $\text{CuHPO}_4 \cdot \text{H}_2\text{O}$. *J Therm Anal.* **34**, 1449–1454 (1988).
9. D. Brandová, M. Trojan, F. Paulik, and J. Paulik: Mechanism of dehydration of $\text{ZnHPO}_4 \cdot \text{H}_2\text{O}$. *J Therm Anal.* **32**, 1923–1928 (1987).
10. A. Jouini, J. C. Gâcon, M. Ferid, and M. Trabelsi-Ayadi: Luminescence and scintillation properties of praseodymium poly and diphosphates. *Opt Mater.* **24**, 175–180 (2003).

11. T. Yang, and J. Lin: Hydrothermal syntheses and low temperature magnetic behaviors of $\text{ACo}_3(\text{P}_2\text{O}_7)_2$ ($A = \text{Ca}, \text{Sr}, \text{Ba}, \text{Pb}$). *J Solid State Chem.* **198**, 1–5 (2013).
12. C. H. Kim, and H. S. Yim: The effect of tetravalent metal on dielectric property in ZrP_2O_7 and TiP_2O_7 . *Solid State Commun.* **110**, 137–142 (1999).
13. R. Shannon: Revised effective ionic radii and systematic studies of interatomic distances in halides and chalcogenides. *Acta Crystallogr A.* **32**, 751–767 (1976).
14. B. Boonchom, and N. Phuvongpha: Synthesis of new binary cobalt iron pyrophosphate CoFeP_2O_7 . *Mater Lett.* **63**, 1709–1711 (2009).
15. H. Bih, I. Saadoune, H. Ehrenberg, and H. Fuess: Crystal structure, magnetic and infrared spectroscopy studies of the $\text{LiCr}_y\text{Fe}_{1-y}\text{P}_2\text{O}_7$ solid solution. *J Solid State Chem.* **182**, 821–826 (2009).
16. K. Pogorzalet-Glaser, A. Pietraszko, B. Hilczer, and M. Połomska: Structure and phase transitions in $\text{Cu}_2\text{P}_2\text{O}_7$. *Phase Transit.* **79**, 535–544 (2006).
17. B. D. Cullity: Elements of X-ray Diffraction. London: Addison-Wesley Publishing (1977).
18. A. J. Bosman, EE Havinga: Temperature Dependence of Relative permittivities of Cubic Ionic Compounds. *Phys Rev.* **129**, 1593–1600 (1963).
19. B. E. Robertson, and C. Calvo: The crystal structure and phase transformation of $\alpha\text{-Cu}_2\text{P}_2\text{O}_7$. *Acta Crystallogr.* **22**, 665–672 (1967).
20. B. E. Robertson, and C. Calvo: Crystal structure of $\beta\text{-Cu}_2\text{P}_2\text{O}_7$. *CanJChemistry.* **46**, 605–612 (1968).
21. B. Ravel, and M. Newville: ATHENA, ARTEMIS, HEPHAESTUS: data analysis for X-ray absorption spectroscopy using IFEFFIT. *J Synchrotron Radiat.* **12**, 537–541 (2005).
22. J. A. Gomes, M. H. Sousa, G. J. da Silva, F. A. Tourinho, J. Mestnik-Filho, R. Itri, GdM Azevedo, and J. Depeyrot: Cation distribution in copper ferrite nanoparticles of ferrofluids: A synchrotron XRD and EXAFS investigation. *J Magn Magn Mater.* **300**, e213–e216 (2006).
23. L. Pauling: The nature of chemical bond. Calcutta: Oxford and IBH (1969).



CURRICULUM VITAE

1. Name: Rattanaï Baitahe
2. Nationality: Thai
3. Date of Birth: 18 February 1986
4. Sex: male
5. E-mail Address: hadee1234@gmail.com
6. Tel.: 0846969241
7. Province: Surat Thani
8. Education:
 - 2005 - 2009 B.Sc. Industrial Chemistry - Analytical Instrumentation, Faculty of Science, Department of Chemistry, King Mongkut's Institute of Technology Ladkrabang, Bangkok, Thailand
 - Subjects studied: Major studies: General Chemistry, Analytical Chemistry, Organic Chemistry, Inorganic Chemistry, Biomolecular Chemistry, Physical Chemistry, Calculus, Mathematics for Chemical Industry, Elementary Statistics, Petrochemical Industry, Material Science, Applied Computer for Scientists, Industrial Chemicals Processes, Experimental Design and Quality Control, Quality Assurance and Chemical Laboratory Standards, Chemical Analysis and Product Quality Control, Instrumentation Calibration. Industrial Chemicals Analysis, Analytical Instrumental Maintenance, Separation Techniques, Fundamental Physics.
 - Minor studies: Nuclear Chemistry and Radiochemical Analysis Techniques, Modern Analytical Instruments, Industrial Inorganic Chemistry, Analytical Spectroscopy, Applied Chemical Instrumental Analysis, Scientific Glass Equipment Production, Glass Blowing and Engineering Workshop, Engineering Drawing, Information Technology for Scientists, English.
 - Elective studies: Business Administration, Industrial and Labor Law, Thai Heritage for Tourism.
 - **Project:** Preparation and Characterization of Indium Tin Oxide by Chemical Processes.
 - **Graduated** with 3.42 GPA (First of class, Second class honors)

This material is reserved for educational use only, not allowed for commercial use.

Forbidden to modify the content, and cite the document when use.

2010 – 2016 PhD. Nanoscience and Nanotechnology. College of Nanotechnology, King Mongkut's Institute of Technology Ladkrabang, Bangkok, Thailand

- **Subjects studied:** Quantum Mechanics for Nanotechnology, Materials Characterization, Polymer Nanocomposites, Testing of Materials Properties, Nanostructure Optical Materials and Their Applications, Electroceramic Materials and Applications, Functional Organic Materials, Nanocomposite Materials.

- **Project:** Structure refinement, optical and dielectric properties of metal pyrophosphate groups

9. Publication:

- [1] Banjong Boonchom, and Rattanaï Baitahe "Synthesis and characterization of nanocrystalline manganese pyrophosphate $Mn_2P_2O_7$ " Materials Letters. Vol.63 (2009) 2218-2220. Impact Factor = 2.307.
- [2] Banjong Boonchom, Rattanaï Baitahe, Zongporn Joungmunkong, and Naratip Vittayakorn " Grass blade-like microparticle $MnPO_4 \cdot H_2O$ prepared by a simple precipitation at room temperature" Powder Technology. Vol.203 (2010) 310-314, Impact Factor = 2.080.
- [3] Banjong Boonchom, Rattanaï Baitahe, Samart Kongtaweelert, and Naratip Vittayakorn "Kinetics and Thermodynamics of Zinc Phosphate Hydrate Synthesized by a Simple Route in Aqueous and Acetone Media" Industrial & Engineering Chemistry Research. Vol.49 (2010) 3571-3576, Impact Factor = 2.237.
- [4] Rattanaï Baitahe, Naratip Vittayakorn, and Banjong Boonchom " Study on thermal transformation of $CuHPO_4 \cdot H_2O$ obtained by acetone-mediated synthesis at ambient temperature" Journal of Thermal Analysis and Calorimetry. Vol.110 (2012) 625-632, Impact Factor = 1.604.
- [5] Rattanaï Baitahe, Chanapa Kongmark, Rangson Muanghlua, Panpailin Seeharaj, and Naratip Vittayakorn "Dielectric Properties and Characterizations of Binary $Zn_{(2-x)}Cu_xP_2O_7$ Pyrophosphates" (Accepted) Integrated Ferroelectrics, Impact Factor = 0.300.

- [6] **Rattanaï Baitahe**, Chanapa Kongmark, Rangson Muanghlua, Panpailin Seeharaj, and Naratip Vittayakorn " X-ray Absorption Spectroscopy Studies of $\text{Cu}_{(2-x)}\text{Zn}_x\text{P}_2\text{O}_7$ Binary Pyrophosphates" *Ferroelectrics*. Vol.453 (2013) 100-105, Impact Factor = 0.391.
- [7] Rachanusorn Roongtao, **Rattanaï Baitahe**, Naratip Vittayakorn, Panpailin Seeharaj and Wanwilai C. Vittayakorn, "Influence of Mn Doping on the Magnetic Properties of CoFe_2O_4 ", *Ferroelectrics*. Vol.459 (2013) 119-127, Impact Factor = 0.391.
- [8] Rachanusorn Roongtao, **Rattanaï Baitahe**, Naratip Vittayakorn, Panpailin Seeharaj and Wanwilai C. Vittayakorn, "Structural and Magnetic Properties of Zn Doped CoFe_2O_4 ", *Integrated Ferroelectrics*. Vol.148 (2013) 145-152, Impact Factor = 0.300.
- [9] Piyanut Charoonsuk, **Rattanaï Baitahe**, Wanwilai Vittayakorn, Rangson Muanghua, Narin Atiwongsangthong, Panpailin Seeharaj, Naratip Vittayakorn, "Synthesis of Monodispersed Perovskite Barium Zirconate (BaZrO_3) by the Sonochemical Method" *Ferroelectrics*. Vol.453 (2013) 54-61, Impact Factor = 0.391.
- [10] **Rattanaï Baitahe**, Naratip Vittayakorn, "Phase formation and evolution of Cu:Zn partials in binary metal pyrophosphates $\text{Cu}_{(2-x)}\text{Zn}_x\text{P}_2\text{O}_7$; $x \approx 1$ " *Thermochimica Acta*. Vol.596 (2014) 21-28, Impact Factor = 2.105.
- [11] **Rattanaï Baitahe**, Naratip Vittayakorn, "Dielectric properties and characterizations of binary $\text{Cu}_{(2-x)}\text{Mg}_x\text{P}_2\text{O}_7$ pyrophosphates", (Accepted) *Ferroelectrics*. Impact Factor = 0.391.
- [12] Supamas Wirunchit, **Rattanaï Baitahe** and Naratip Vittayakorn, "The Effect of Zirconium on the Formation of Barium Zirconium Titanate Nanoparticles by Sonochemical Method", (Accepted) *Ferroelectrics*. Impact Factor = 0.391.
- [13] Jira Janbua, Jitkasame Mayamae, Supamas Wirunchit, **Rattanaï Baitahe** and Naratip Vittayakorn, "Direct synthesis, growth process and optical properties of monodispersed CaWO_4 microspheres via a sonochemical route", *RSC Advances*. Vol. 5 (2015) 19893-19899, Impact Factor = 3.840.
- [14] **Rattanaï Baitahe**, Naratip Vittayakorn and Santi Meansiti, "Correlation between the chromaticity, dielectric properties and the structure of binary

metal pyrophosphates, $\text{Cu}_{(2-x)}\text{Zn}_x\text{P}_2\text{O}_7$ ", RSC Advances. Vol. 5 (2015) 88890-88899, Impact Factor = 3.840.

10. Presentations

International Conferences:

- [1] **Rattanaï Baitahe**, Banjong Boonchom, and Naratip Vittayakorn "Study of transformation of ZnNH_4PO_4 via kinetic and thermodynamic" Siam Physics Congress (SPC2012) May 9-12, 2012, Phranakhon Si Ayutthaya, Thailand (oral presentation).
- [2] **Rattanaï Baitahe**, Rangson Muanghlua, Panpailin Seeharaj, Banjong Boonchom, and Naratip Vittayakorn, "Dielectric properties and characterizations of binary $\text{Zn}_{(2-x)}\text{Cu}_x\text{P}_2\text{O}_7$ pyrophosphates" Special international workshop and symposium on emerging frontiers in multiferroics and electronic metamaterials (INAMM) December 9-10, 2012 Pattaya Beach, Thailand (poster presentation).
- [3] **Rattanaï Baitahe**, Rangson Muanghlua, Panpailin Seeharaj, and Naratip Vittayakorn " X-ray Absorption Spectroscopy Studies of $\text{Cu}_{(2-x)}\text{Zn}_x\text{P}_2\text{O}_7$ Binary Pyrophosphates" The 8th Asian Meeting on Ferroelectrics (AMF-8) December 11-14, 2012 Amari Orchid Hotel, Pattaya, Thailand (oral presentation).
- [4] **Rattanaï Baitahe** and Naratip Vittayakorn "Dielectric Properties and Characterizations of Binary $\text{Cu}_{(2-x)}\text{Mg}_x\text{P}_2\text{O}_7$ Pyrophosphates" The 9th Asian Meeting on Ferroelectrics (AMF-AMEC-2014) October 26-30, 2014 Shanghai International Convention Center, Shanghai, China (Poster presentation).

National Conferences:

- [1] **Rattanaï Baitahe**, Naratip Vittayakorn, Rangson Muanghlua, and Banjong Boonchom "Synthesis and thermal behavior of Serrabrancaite ($\text{MnPO}_4 \cdot \text{H}_2\text{O}$)" The Congress on Science and Technology of Thailand (STT38) October 17 – 19, 2012 Chiang Mai University, Thailand (poster presentation).
- [2] Manoon suttapan, **Rattanaï Baitahe**, Naratip Vittayakorn and Banjong Boonchom " Synthesis and characterization of $\text{Mn}_{(2-x)}\text{Zn}_x\text{P}_2\text{O}_7$ compounds"

This material is reserved for educational use only, not allowed for commercial use.

Forbidden to modify the content, and cite the document when use.

The Congress on Science and Technology of Thailand (STT38) October 17 – 19,
2012 Chiang Mai University, Thailand (Oral representation).



This material is reserved for educational use only, not allowed for commercial use.

Forbidden to modify the content, and cite the document when use.